City Research Online

City, University of London Institutional Repository

Citation: Kumar, A. (2017). Investigation of in-nozzle flow characteristics of fuel injectors of IC engines. (Unpublished Doctoral thesis, City, University of London)

This is the accepted version of the paper.

This version of the publication may differ from the final published version.

Permanent repository link: https://openaccess.city.ac.uk/id/eprint/17583/

Link to published version:

Copyright: City Research Online aims to make research outputs of City, University of London available to a wider audience. Copyright and Moral Rights remain with the author(s) and/or copyright holders. URLs from City Research Online may be freely distributed and linked to.

Reuse: Copies of full items can be used for personal research or study, educational, or not-for-profit purposes without prior permission or charge. Provided that the authors, title and full bibliographic details are credited, a hyperlink and/or URL is given for the original metadata page and the content is not changed in any way.

City Research Online: http://openaccess.city.ac.uk/ publications@city.ac.uk

Investigation of in-nozzle flow characteristics of fuel injectors of IC engines

by

Aishvarya Kumar

Thesis submitted for the fulfilment of the requirements
for the degree of doctor of philosophy
of the

CITY
UNIVERSITY OF LONDON
EST 1894

Department of Mechanical Engineering & Aeronautics
School of Mathematics, Computer Science & Engineering

May 2017

Declarations

I hereby declare that all work produced in this document is entirely my own work, except where otherwise indicated, and has not been submitted in whole or in part to any other University.

I grant powers of discretion to the University Librarian to allow this thesis to be copied in whole or in part without further reference to me. This permission covers only single copies made for study purposes, subject to normal conditions of acknowledgement.

Signed: ....

Dedicated to my mother
Neelam,
my sister
Anshul,
&
to my late father
Ashok

An expert is a person who has made all the mistakes that can be made in a very narrow field

Niels Bohr

Abstract

Almost all automotive fuel injection systems are experiencing some form of cavitation within their nozzle under different operating conditions. In-nozzle cavitation initiates in various forms and directly influences the emerging spray. Experimental studies have shown that cavitation in diesel injectors leads to smaller droplet formation, especially by the on-going trend towards higher injection pressures, which enhances fuel evaporation but also creates undesirable consequences due to transient nature of cavitation such as spray instabilities, erosion on internal surfaces, and hydraulic flip. Thus, the understanding of the internal flow of automotive fuel injectors is critical for injector design. On the other hand, biodiesel has emerged as one of the potential alternative fuel which can also be carbon neutral because it uptakes CO_2 during cultivation of its feedstock and can be used in existing diesel engines with little or no modifications. Therefore, the present study is focussed on assessing and outlining cost-effective methods to analyse internal flow in fuel injectors for diesel and biodiesel fuel applications.

In the present study, RANS-based (Reynolds-averaged Navier–Stokes) CFD (Computational fluid dynamics) approach has been chosen to simulate quasi-steady flows in the steady state test rigs of fuel injectors of IC engines. The RANS approach is selected over computationally expensive SAS (Scale Adaptive Simulations), DES (Detached Eddy Simulations) and LES (Large Eddy Simulations) because it was considered that these quasi-steady simulations could be performed within hours and with less computing resources using RANS rather using SAS, DES and LES which may require orders more time and computing resources. Cavitation models and RANS-based turbulence models have been evaluated for single-hole and multi-hole injectors operating on steady state test rigs. Furthermore, influences of liquid and vapour compressibility were also investigated. Influences of biodiesel properties such as higher viscosity and density on cavitation were also assessed. In the first part of the study, single-phase simulations have been carried out in the mini-sac type multi-hole (6) injector. Several two-equation turbulence and near wall models were assessed, amongst most appropriate for the application were identified. Predicted mean velocity and RMS velocity were compared with measurements and showed good agreements. Flow field analysis showed predictions of different types of vortices in the injector. Two main types of vortex structures were predicted: ‘Hole-to-hole’ connecting vortex and double ‘counter-rotating’ vortices emerging from the needle wall and entering the injector hole facing it. The latter create a complex 3D flow inside the injector hole when it interacts with the recirculation region at the entrance of the injector hole.

Cavitation simulations inside a single-hole injector were next performed. Simulations were assessed by comparing predicted vapour volume fraction with measurements. Influences of liquid

and vapour compressibility were also checked. The compressibility of vapour was modelled using ideal gas law and liquid compressibility was modelled using the Tait equation. Vapour compressibility resulted in an increase of vapour volume fraction at the low-pressure region and predictions were also in better agreements with experimental data. The liquid compressibility made no impact on the simulation results. The local sonic speed in the liquid-vapour mixture was computed using Wallis model which predicted a very low local sonic speed in the liquid-vapour mixture. Therefore, the local flow in liquid-vapour mixture became supersonic. A normal shock wave was predicted just downstream of the cavitation bubble cloud as local flow velocity was reduced from supersonic to subsonic.

Finally, the cavitation simulations were performed in the enlarged mini-sac type multi-hole (6) injector. Established turbulence, cavitation and compressibility models from above studies were used. Reasonable quantitative agreements with experimental data were obtained for the mean axial velocity and RMS velocity. Reasonable qualitative agreements were also achieved when predicted cavitation results were compared with high-speed digital images. Henceforth a parametric study to assess the influence of biodiesel fuel properties such as an increase in viscosity and density on the cavitation was performed. Viscosity and density of both phases in the fluid were parametrically increased by 20%. Results showed that cavitation was suppressed when the viscosity was increased because it increased the flow resistance, thus reduced the velocity. This caused a reduction in the size of recirculation region at the entrance of the injector hole and hence a smaller saturation pressure region was predicted. Cavitation was further suppressed when density was increased causing the reduction in the velocity at the same mass flow rate, which further reduced the recirculation region, therefore, reduced the saturation pressure region and consequently cavitation.

Acknowledgements

I would like to express my sincere gratitude to my supervisors, Prof. Jamshid Nouri and Prof. Ali Ghobadian, for their ongoing support during this project. I would especially like to thank Prof. Nouri for providing me with financial support to my PhD without which it would not have been possible. I would also like to thank him for being always accessible to share his knowledge. My journey started with Prof. Ghobadian with the MSc CFD project. I admire his attention to details and his push to raise my level - always asking me to ‘think’ critically. He always challenged me with interesting questions that helped me understand physical processes better.

Computational Fluid Dynamics needs computing resources. I would not have been able to complete simulations without the help of Dr Bob Edney and Mr Chris Marshall, who helped me use university clusters and whom I owe my hearty gratitude and thanks.

I would like to thank my parents especially my dad, Mr Ashok Kumar, who encouraged me to pursue this Ph.D., unfortunately, he passed away on 26th November 2013 leaving me with his dream. I would like to thank my mother, Mrs Neelam Kumar, and sister, Miss Anshul Kumar for their continuous encouragement.

I would like to thank my colleagues for their frequent help during this PhD. They are - Dr Sham Rane, Mr Milad Mirshahi, Dr Saeed Javdani, Mr Dhamotharan Veerasamy and Mr Hassan Kassem. It was an honour sharing the office them. I would like to thank many friends I met in London whose support kept me going. Some of them are - Mr Amin Sabeti, Miss Olga Riepar Garcia, Miss Jurga Zukovskaite, Miss Denise Lombardi, Mr Stephano Laudani, Miss Lisa Broomhall, Dr Sarah Goodwin, Mr Sumit Gajbhiye, Miss Priscilla Rampazzo, Mr Mahmoud Khader, Mr Milos Asanov, Miss Pallavi Rajnath, Mr Suresh Manvar, Mr Shrawasti Sahare, Miss Caledonia Maxwell, Mrs Asha Yadav, Mr Deepanjan Nag, Ven. Tejwant, and many more. Also, I thank Miss Krzysia Balinska and Mrs Bhagya Dasari for offering their support at unequal times.

I would especially like to thank Mr Sarvajeet Ram, Mr Mohammad Zama and Dr Uma Kant Prasad for taking care of my mother and sister in India at odd times. My special thank goes to Mr Gautam Chakravarty for providing me accommodation at the Ambedkar Center, Southall in the last year of the PhD. Also, I would especially like to thank all members of Shri Guru Ravidass Sabha, Southall for offering delicious meals whenever I popped in. Last but not the least, I owe my intellectual life to Dr B.R. Ambedkar, my ideal, whose memory kept me stand high during critical moments and who is the sole reason for me to be spirited in this endeavour.

Contents

Declarations iii

Abstract ix

Acknowledgements xi

List of Figures xxi

List of Tables xxxiii

1 Introduction 1

- 1.1 Motivation 1
- 1.2 Biodiesel 5
- 1.3 Why biodiesel? 6
- 1.4 Advantages and disadvantages of biodiesel fuel 9
  - 1.4.1 Advantages: 9
  - 1.4.2 Disadvantages: 10
- 1.5 Diesel injection systems 11
  - 1.5.1 Indirect injection 11
  - 1.5.2 Direct injection 12
    - 1.5.2.1 Fuel injector 13
    - 1.5.2.2 Injector geometries 14
- 1.6 Cavitation 14
  - 1.6.1 Cavitation in fuel injectors 15
- 1.7 Role of CFD on cavitation Modelling 17
- 1.8 Aims and objectives of this study 20
- 1.9 Thesis outline 20

2 Literature Review 23

2.1 Introduction . . . 23
2.2 Experimental fluid dynamics . . . 23
    2.2.1 Single-hole injectors . . . 23
    2.2.2 Multi-hole injectors . . . 28
    2.2.3 Cavitation damage . . . 33
    2.2.4 Biodiesel cavitation . . . 34
    2.2.5 Experimental studies for non-ICE application . . . 35
2.3 Numerical modelling . . . 35
    2.3.1 Single bubble dynamics . . . 35
    2.3.2 Cavitation Models . . . 36
    2.3.3 Rayleigh relation based cavitation models: . . . 36
    2.3.4 Empirical and semi-empirical models . . . 42
    2.3.5 Barotropic cavitation models . . . 44
    2.3.6 Eulerian-Langrangian models . . . 45
    2.3.7 Homogeneous Relaxation Model . . . 47
2.4 CFD simulations . . . 47
    2.4.1 Single-phase simulations . . . 47
    2.4.2 Cavitation simulations . . . 48
    2.4.3 Cavitation damage simulations . . . 49
2.5 Summary . . . 49

3 Governing equations 53

3.1 Favre-averaged Navier-Stokes . . . 53
3.2 Mixture model . . . 54
3.3 Conservations equations . . . 56
    3.3.1 Continuity equation: . . . 56
    3.3.2 Momentum equation: . . . 56
    3.3.3 Energy equation: . . . 56
3.4 Favre-averaged equations . . . 57
    3.4.1 Favre-averaged continuity equation . . . 57
    3.4.2 Favre-averaged momentum equation . . . 57

3.4.3 Favre-averaged energy equation . . . 57
3.5 Compressible flow closure approximations . . . 58
3.5.1 Reynolds stress tensor: . . . 58
3.5.2 Turbulent heat flux vector . . . 59
3.5.3 Heat diffusion flux . . . 59
3.5.4 Pressure-velocity correlation . . . 59
3.6 Cavitation models . . . 59
3.6.1 Schnerr and Sauer model . . . 59
3.6.1.1 Favre-averaged transport equation of vapour fraction . . . 61
3.6.2 Zwart-Gerber-Belamri model . . . 61
3.6.2.1 Favre-averaged transport equation of vapour fraction . . . 63
3.7 Turbulence models . . . 63
3.7.1 Standard $k - \epsilon$ model . . . 64
3.7.2 Realizable $k - \epsilon$ model . . . 65
3.7.3 Launder and Sharma $k - \epsilon$ model . . . 66
3.7.4 Standard $k - \omega$ model . . . 66
3.7.4.1 Low-Reynolds-Number correction . . . 67
3.7.4.2 Modelling turbulence production . . . 68
3.7.4.3 Modelling turbulence dissipation . . . 68
3.7.4.4 Compressibility correction . . . 69
3.7.4.5 Model constants . . . 69
3.7.5 SST $k - \omega$ model . . . 69
3.7.5.1 Modelling the turbulence production . . . 71
3.7.5.2 Modelling the turbulence dissipation . . . 71
3.7.5.3 Cross diffusion modification . . . 72
3.7.5.4 Model constants . . . 72
3.8 Wall functions . . . 72
3.8.1 Standard Wall Function . . . 72
3.8.2 Launder-Spalding Wall function . . . 73
3.8.3 Enhanced Wall Treatment method . . . 74

4 Single-phase simulations in an enlarged multi-hole injector 75

4.1 Introduction 75

4.2 Description of test cases: 75

4.2.0.1 Description of the test rig 79

4.3 Boundary condition error analysis 80

4.3.0.2 Case setup 80

4.3.0.3 Results 82

4.3.0.4 Discussions: 83

4.4 Grid sensitivity analysis 83

4.4.1 Case setup 83

4.4.2 Results: lower needle lift (1.6 mm) 85

4.4.3 Discussion: lower needle lift 87

4.4.4 Results: nominal needle lift (6.0 mm) 87

4.4.5 Discussion: nominal needle lift 89

4.5 Physical modelling errors 89

4.5.1 Turbulence models comparison 89

4.5.1.1 Case setup 89

4.5.1.2 Results 91

4.5.1.3 Discussion: models comparison 94

4.5.2 Near wall modelling 95

4.5.2.1 Case setup 95

4.5.2.2 Results 95

4.5.2.3 Discussion: near wall modelling 96

4.6 Validation at the nominal needle-lift 98

4.6.0.4 Results: 99

4.6.0.5 Discussion: nominal needle lift 101

4.7 Flow field analysis: 101

4.7.1 Lower needle lift (1.6 mm) flow field: 102

4.7.1.1 ‘Hole-to-hole’ connecting vortex 106

4.7.1.2 ‘Counter-rotating’ vortices originating from the needle wall and entering the injector hole facing it 111

4.7.2 Nominal needle lift (6.0 mm) flow field 116

4.7.3 Discussions . . . 124
4.8 Summary . . . 125
4.8.0.1 Boundary condition errors: . . . 125
4.8.0.2 Numerical errors . . . 125
4.8.0.3 Physical modelling errors . . . 125
4.8.0.4 Flow field analysis . . . 125
4.8.0.5 Contours: lower needle lift . . . 126
4.8.0.6 Contours: nominal needle lift . . . 128

5 Cavitation simulation in a single-hole injector **129**
5.1 Introduction . . . 129
5.2 Test case description: . . . 129
5.3 Numerical errors (Grid sensivity analysis) . . . 133
5.3.0.7 Case setup: . . . 133
5.3.0.8 Results: . . . 135
5.3.0.9 Discussions: . . . 136
5.4 Physical modelling errors . . . 137
5.4.1 Turbulence models comparison . . . 137
5.4.1.1 Case setup: . . . 137
5.4.1.2 Results: . . . 137
5.4.1.3 Discussions . . . 143
5.4.2 Cavitation models evaluation . . . 144
5.4.2.1 Case setup . . . 144
5.4.2.2 Results: . . . 144
5.4.2.3 Discussions . . . 149
5.4.3 Uncertainties of cavitation models and impact of parameters used in these models . . . 149
5.4.3.1 Case setup: . . . 150
5.4.3.2 Results: . . . 150
5.4.3.3 Discussions: . . . 151
5.4.4 Influence of compressibility on cavitation . . . 151
5.4.4.1 Case setup . . . 152
5.4.4.2 Results: . . . 153

5.4.4.3 Discussions: 160
5.5 Summary 161
5.5.1 Numerical errors: 161
5.5.2 Physical modelling errors: 161
5.5.2.1 Turbulence model evaluation 161
5.5.2.2 Cavitation model evaluation 161
5.5.2.3 Uncertainties of cavitation models and impact of parameters used in these models 162
5.5.2.4 Influence of compressibility on cavitation 162

6 Cavitation simulations in an enlarged multi-hole injector 163

6.1 Introduction 163
6.2 Test case decription: 163
6.3 Nominal needle lift 165
6.3.1 Grid sensitivity analysis 165
6.3.1.1 Case setup 165
6.3.1.2 Results 165
6.3.1.3 Discussions 168
6.3.2 Case study 1: Simulation of full-cavitating conditions at CN 1.48 and 4.57. 168
6.3.2.1 Case setup 168
6.3.2.2 Results 170
6.3.2.3 Qualitative comparison with experimental data 182
6.3.2.4 Discussions: 184
6.4 Lower needle lift 185
6.4.1 Case study 2: Simulation of onset conditions at CN 1.48 185
6.4.1.1 Case setup 185
6.4.1.2 Results 185
6.4.1.3 Discussions: 192
6.5 Case study 3: influence of viscosity and density on cavitation 192
6.5.0.4 Case setup 192
6.5.0.5 Results: 193
6.5.0.6 Discussions: 201
6.6 Summary: 202

6.6.1 Nominal needle lift 202
6.6.2 Low needle lift 202
6.6.3 Influence of viscosity and density on cavitation 202

7 Conclusions and recommendations for future works: 203

7.1 Conclusions 203
7.1.1 Single phase simulations in an enlarged multi-hole injector 203
7.1.2 Cavitation simulations in a single hole injector 205
7.1.3 Cavitation simulations in an enlarged multi-hole enlarged injector 207
7.2 Recommendations for future works 209
7.2.1 Experimental studies 209
7.2.2 Computational studies 209

Bibliography 211

List of Figures

1.1 Two photographs showing direct and indirect injection system engines. On the left a typical direct injection system setup with a multi-hole injector and on the right an indirect injection system setup with a single-hole injector. Source: Bosch (2016d) . . . 11

1.2 A typical common rail injection system. Source: Hitachi (2011) . . . 12

1.3 Schematic of a typical common rail injection system. Source: Roth (2004) . . . 13

1.4 Typical injector geometries: valve cover orifice and sac type. Both axisymmetric with 6 hole configuration. Source: Mitroglou et al. (2011) . . . 14

1.5 High speed digital images showing vortex cavitation inside the enlarged fuel injector. (a) Hole-to-hole connecting cavitation (b) Needle string. Source: Arcoumanis et al. (2001) . . . 16

1.6 The distribution of two phases in the computational domain. A) Standard VOF application, b) Homogeneous distribution of the gaseous phase. Source: (Schnerr and Sauer, 2001) . . . 19

2.1 Occurence of the hydraulic flip. (a) Spray like jet at inlet pressure 15 lb/in^2 emerging from the orifice when the nozzle is cavitating. (b) Emergence of a glass-like jet as cavitation reaches the nozzle exit and air downstream with pressure higher than the fuel vapour pressure occupies the volume previously occupied by cavitation at higher CN (at inlet pressure above 15 lb/in^2). . . . 24

2.2 Throttle geometry "U" in 300 μm thick sheet steel. 301 μm inlet width, 284 μm outlet width, 20 μm inlet radius, 1 mm throttle hole length. Source: Winklhofer et al. (2001) . . . 26

2.3 Cavitation distribution in 2D nozzle, nozzle inlet diameter 0.301 mm, nozzle outlet diameter 0.284 mm. The blue colour represent pure vapour state, the red colour represent the pure liquid state. Source: Winklhofer et al. (2001) . . . 26

2.4 Cross section through the x–z-plane for $CN = 1.5$ showing an additional cavitation zone in the centre of the liquid core, source: Bauer et al. (2012) . . . 27

2.5 (a) Time-integrated X-ray images of nozzle inlet, taken with an unfocused X-ray monochromatic X-ray beam at $CN = 11.2$, (b) Raster-scan grid, (c) Interpolated contour plots of time-averaged vapour projection for $CN = 11.2$. Source: Duke et al. (2013a) 28

2.6 Cavitation regimes identified in large-scale sac-type hole nozzle. Source: Arcoumanis et al. (2001) 30

2.7 a) High-speed digital image showing 'hole-to-hole' connecting string cavitation. b) High-speed digital image showing 'needle string' or 'needle cavitation'. Source: Arcoumanis et al. (2001) 31

2.8 Gas/Vapour bubble captured using neutron radiography technique in the nozzle. Source: Takenaka et al. (2005) 32

2.9 Identified cavitation damage sites (marked by square white rectangles in (a) and by black rectangles in (b)) by scanning electron microscopy. Source: Asi (2006) . 33

3.1 u-velocity cell at a boundary 72

4.1 Isometric view of the transparent enlarged conical mini-sac type nozzle and needle at nominal needle lift (6 mm). 76

4.2 Side view (z-y plane) and sectional view of the injector nozzle. All dimension are in mm, the tolerances are not given. 77

4.3 (a) Side view (z-y plane) of the injector needle. All dimension are in mm, the tolerances are not given. (b) Typical model parts of an enlarged injector and needle assembly. 1) Needle 2) injector 3) injector hole 4) sac volume 5) needle seat 6) seat annulus 7) cartridge wall 8) needle wall 9) pressure measuring tap (also outlet boundary conditions for CFD) 10) back flow hole. 77

4.4 Section view of the fuel injector displaying positions where LDV measurements were taken, (a) corresponds to Series 1 experiments, (b) corresponds to Series 2 experiments. All dimensions are in mm. 78

4.5 The locations of LDV measurement planes in one of the injector holes. Source: Roth (2004) 78

4.6 Schematics of the refractive index matching test rig with incorporated large-scale injector. 79

4.7 (A) Isometric view of the enlarged injector and needle at nominal needle-lift (6.00 mm), (B) the complete flow domain (C) one-sixth of flow domain with periodic (cyclic) boundary conditions. The numbers represents the boundaries of flow domains, (1) inlet (2) outlet (3) walls (4) periodic (cyclic) interface. 80

4.8 (A) Mesh of the complete fluid volume, (B) Mesh of the one-sixth of the fluid volume. 81

4.9 Normalized mean axial velocity comparisons for flow domains with the 'complete flow domain' and 'one-sixth of the flow domain' with periodic boundary conditions. 82

4.10 (A) Flow Domain for the lower needle lift. (B) flow domain for the nominal needle lift. The numbers represent boundaries of flow domains, (1) inlet (2) outlet (3) walls (4) periodic 84

4.11 (A) The Lower needle lift grid with uniform element size (B) The lower needle lift flow domain displaying the region of local refinement (red sphere), 'Sphere of influence' method (Guide, 2012) has been used for local grid refinement. 84

4.12 Normalized mean axial velocity and RMS comparisons at x = 9.5 mm from the origin 85

4.13 Normalized mean axial velocity and RMS comparisons at x = 10.5mm, 13.5 mm and 16.5 mm from the origin. 86

4.14 Normalized mean axial velocity and RMS comparisons at x = 9.5 mm. 10.5 mm and 13.5 mm from the origin 88

4.15 Normalized mean axial velocity and RMS comparisons at x = 16.5 mm from the origin 89

4.16 (A) One-sixth of the flow domain at low lift with periodic (cyclic) boundary conditions. The numbers represents boundaries of flow domains, (1) inlet (2) outlet (3) walls (4) periodic (cyclic) interface, (B) Mesh for one-sixth flow domain. . . 90

4.17 Normalized mean axial velocity and RMS comparisons at x = 9.5 mm and 10.5 mm from the origin. 91

4.18 Normalized mean axial velocity and RMS comparisons at x = 13.5 mm and 16.5 mm from the origin. 92

4.19 Mean velocity profiles (vector) at different planes obtained using standard $k-\epsilon$ and realizable $k-\epsilon$ models. 93

4.20 Comparison of turbulent viscosity of standard $k-\epsilon$ and realizable $k-\epsilon$ turbulence models on x-y plane 94

4.21 Normalized mean axial velocity comparisons for near wall modelling approaches . 96

4.22 y^* comparisons 97

4.23 y^+ comparisons 98

4.24 Normalized mean axial velocity and RMS comparisons at x = 9.5 mm and 10.5 mm from the origin 99

4.25 Normalized mean axial velocity and RMS comparisons at x = 9.5 mm and 10.5 mm from the origin 100

4.26 Velocity vectors at nominal needle lift, grid 3. 101

4.27 planes in flow domain for flow field analysis 102

4.28 2D velocity streamlines on plane 1. 103

4.29 Vectors plotted on the x-y plane, indicating that velocity is approaching parabolic profile. 103

4.30 Velocity profile on x-y plane as fluid enters the inclined annulus. 104

4.31 Zoom of vortex at the sharp corner, showing clockwise direction of the vortices . 104

4.32 Zoom of vortices in the sac region and recirculation region on injector hole 105

4.33 pressure field. 105

4.34 Isosurface of vorticity magnitude (0.5% of the magnitude) showing 'hole-to-hole connecting vortex. 106

4.35 Velocity vector projected on the isosurface of vorticity magnitude (0.5% of the magnitude), showing hole to hole connecting vortex in the clockwise direction. . 107

4.36 2D vectors plotted on plane 2 indicating a collision of fluid with injector wall just below the injector hole. 107

4.37 Velocity streamline on plane 2 indicates a 'hook' like fluid trail before entering the hole. The fluid streamline indicates the large volume of fluid going into sac region then going towards injector hole. Additional vortices in the sac volume can also be seen. 108

4.38 Velocity vectors on the cyclic interface indicate the presence of 'hole to hole' connecting vortex. Additional vortices in the sac volume can also be seen. 108

4.39 Velocity streamline on the cyclic interface indicates the presence of 'hole to hole' connecting vortex. Additional vortices in the sac volume can also be seen. 109

4.40 Bottom view of the injector. Isosurface of vorticity (0.5% of the magnitude) showing the prediction of vortices in the injector. 109

4.41 Bottom view of the injector. Isosurface of vorticity (0.5% of the magnitude) showing the prediction of vortices in the injector. Velocity vectors have been plotted on the front periodic interface showing the clockwise direction of rotation of 'hole-to-hole' connecting vortex. Velocity vectors have also been plotted on the back side (bottom of the image) of the periodic interface suggesting the counter-clockwise direction of rotation of 'hole-to-hole' connecting vortex. 110

4.42 Bottom view of the injector. Isosurface of vorticity (0.5% of the magnitude) showing the prediction of vortices in the injector. Streamlines indicating the path of the fluid. 110

4.43 A view of the injector from the bottom (one-sixth of the flow domain). Isosurface of vorticity magnitude (0.5% of the magnitude) with the front faced removed, showing vortices emerging from needle wall and entering the injector hole facing it. 112

4.44 View from the injector the origin (needle centre), view from the injector the origin (needle centre), isosurface of vorticity magnitude (0.5% of the magnitude) showing the presence of 'hole-to-hole' connecting vortex and 'counter-rotating' vortices emerging from the needle wall and entering the injector hole facing it. 113

4.45 Velocity vectors on plane 4 show the merging of fluid at the centre plane of the injector hole due to symmetrical converging geometry. 113

4.46 Velocity streamlines on plane 4 show the merging of fluid at the centre plane of the injector hole due to symmetrical converging geometry. 114

4.47 Lower pressure regions corresponding to the core of ‘counter-rotating’ vortices. . 114

4.48 Velocity streamlines on plane 4 and pressure contours on plane 1 which indicate higher pressure in the sac region. 115

4.49 Normalised vorticity contours projected on the planes perpendicular to the injector hole. The vorticity is normalised by multiplying it by nozzle diameter D and dividing it by injection velocity U_{inj}. Realizable $k-\epsilon$ model. Positive (red) shows anticlockwise rotation and negative (blue) direction shows clockwise direction. . . 115

4.50 Normalised vorticity contours projected on the planes perpendicular to the injector hole. Standard $k-\epsilon$ model. Positive (red) shows anticlockwise rotation and negative (blue) direction shows clockwise direction. 116

4.51 planes in the flow domain for flow field analysis 117

4.52 2D velocity streamlines on plane 1. 118

4.53 Magnified view of the cartridge, showing vortex being generated at the sharp corner of the cartridge. 118

4.54 Magnified view of the sac region, showing 2D vectors. 119

4.55 2D vectors plotted on plane 2. 119

4.56 2D vectors plotted on the cyclic plane. 120

4.57 3D velocity streamlines 120

4.58 Side view of the vorticity. Isosurface of vorticity (0.5% of the magnitude) showing the prediction of vortices in the injector. 121

4.59 Bottom view of the injector. Isosurface of vorticity (0.5% of the magnitude) showing the prediction of vortices in the injector. 122

4.60 Bottom view of the injector. Isosurface of vorticity (0.5% of the magnitude) showing the prediction of vortices in the injector. Velocity vectors have been plotted on the front periodic interface showing the counter-clockwise direction of rotation of ‘hole-to-hole’ connecting vortex. Velocity vectors have also been plotted on the back side (bottom of the image) of the periodic interface suggesting the clockwise direction of rotation of ‘hole-to-hole’ connecting vortex. 122

4.61 Isosurface of vorticity magnitude (0.5% of the magnitude) showing ‘counter-rotating’ vortices emerging from the needle wall and entering the injector hole just opposite to needle wall. Also, vectors plotted on the cyclic interface to show hole to hole connecting vortex. 123

4.62 Vectors plotted on the plane 4 also reveal the direction of rotation of counter-rotating vortices emerging from the needle wall and entering injector hole opposite to it. Pressure contours reveal corresponding low-pressure region at the core of the vortex. 123

4.63 Normalised vorticity contours projected on the planes perpendicular to the injector hole. Realizable $k - \epsilon$ model. Positive (red) shows anticlockwise rotation and negative (blue) direction shows clockwise direction. 124

4.64 Comparison of y^+ for different grids at lower needle lift, +x,+y,+z view. 126

4.65 y^+ contours at grid 7 at the lower needle lift, +x,+y,+z view. 127

4.66 Comparison of y^+ for different grids at the nominal needle lift, +x,+y,+z view. . 128

5.1 Schematic of the cavitating nozzle under study, source: Duke et al. (2013a). . . . 130

5.2 (a) The raster scan grid which shows 100 transverse (y) and 19 streamwise(x) positions where measurements of vapour fraction were taken, (b) Time-averaged X-ray radiography measurement of vapour fraction interpolated onto the contour at $CN = 11.2$, (c) Time-averaged X-ray radiography measurement of vapour fraction interpolated onto the contour at $CN = 10.7$ (d) Time-integrated X-ray images of nozzle inlet, taken with an unfocused X-ray monochromatic X-ray beam at $CN = 11.2$. Source: Duke et al. (2013a) 131

5.3 2D flow domain for the present case: The numbers represent boundaries of flow domains, (1) inlet (2) outlet (3) wall (4) axis. 133

5.4 (a) 2D hexahedral mesh for the flow domain. 10 inflation cells were added to the wall in order to accurately capture near wall flow regime. (b) Grid 5 which has been locally refined successively from the grid 1 within the orifice, circular convergent section of the nozzle and circular expansion section of the nozzle, the mesh concentration near wall was further increased to ensure $y^+ < 1$ using y^+ adaptation, (c) Grid without y^+ adaptation (grid 3) (d) Grid with y^+ adaptation (grid 5). 134

5.5 (a) Grid independence study - vapour volume fraction, (b) Grid independence study - velocity. 135

5.6 Comparison of the predicted total volume fraction of vapour in slices across the nozzle and experimentally measured the total vapour volume fraction of vapour in slices across the nozzle. 137

5.7 Qualitative comparison between the experimental and CFD results. 138

5.8 Vapour volume fraction predicted using different turbulence models. 139

5.9 Predicted mean axial velocity on plane 1 using different turbulence models. . . . 140

5.10 Turbulent viscosity contours obtained using different turbulence models. 141

5.11 Predicted total volume fraction of vapour in slices across the nozzle. 145

5.12 Visual comparison of vapour volume fraction predicted using two cavitation models. 145

5.13 Qualitative comparison between the experimental and CFD predicted results. (a) X-ray radiography measurement at $CN = 11.2$, (Duke et al., 2013a), (b) SS model (c) ZGB model. 146

5.14 Comparison of the evaporation rate of SS and ZGB model. $\rho_l = 777.97 kgm^{-3}$, $\rho_v = 1 kg\ m^{-3}$ . . . 147

5.15 Comparison of the condensation rate of SS and ZGB model. $\rho_l = 777.97 kgm^{-3}$, $\rho_v = 1 kg\ m^{-3}$ . . . 148

5.16 Influence of cavitation models parameter on vapour volume fraction. . . . 150

5.17 Influence of the vapour compressibility on the vapour volume fraction. . . . 153

5.18 Qualitative comparison between the experimental and CFD predicted results to check influences of vapour compressibility. (a) X-ray radiography measurement at $CN = 11.2$, (Duke et al., 2013a), (b) ZGB model, incompressible, $\alpha_{nuc} = 0.0001$, (c) ZGB model, compressible, $\alpha_{nuc} = 0.0001$. . . . 154

5.19 Density comparisons: (a) Incompressible vapour (b) Ideal gas formulation for density. . . . 155

5.20 Qualitative comparison of the predicted vapour volume fraction to check effects of vapour compressibility. (a) ZGB model, incompressible, $\alpha_{nuc} = 0.0001$, (b) ZGB model, compressible, $\alpha_{nuc} = 0.0001$. . . . 155

5.21 The predicted pressure and velocity profile on the nozzle axis. . . . 156

5.22 (a) The predicted speed of sound for vapour, liquid and mixture at nozzle axis, (b) The Mach number of sound for vapour, liquid and mixture at nozzle axis. . . 157

5.23 (a) The predicted pressure along the nozzle wall, (b) the predicted pressure along the nozzle axis (c) Pressure contour obtained using the mixture model (left) and multifluid (eulerian multi-phase) model (right). Source: Battistoni et al. (2014). . 158

5.24 (a) The predicted liquid and vapour density and (b) The predicted liquid and vapour volume fraction on the nozzle axis. . . . 159

5.25 (a) Vapour volume fraction (b) pressure . . . 160

6.1 Locations inside one of the injector hole for the second series of LDV measurements. Source: Roth et al. (2002) . . . 164

6.2 Normalized mean axial velocity and RMS comparisons at x = 9.5 mm, x = 10.5 mm and x = 13.5 mm from the origin. . . . 166

6.3 Normalized mean axial velocity and RMS comparisons at x = 16.5 mm from the origin. . . . 167

6.4 Predicted vapour volume fraction using different grids at different planes. . . . 167

6.5 (A) One-sixth of the flow domain at the full needle lift with periodic (cyclic) boundary conditions. The numbers represent boundaries of flow domains, (1) inlet (2) outlet (3) walls (4) periodic (cyclic) interface, (B) Mesh for the flow domain. . . . 169

6.6 Sketch showing needle and injector assembly and the positions where LDV measurements of mean and RMS velocity were recorded. All dimensions are in mm. . . . 169

6.7 Normalized mean axial velocity and RMS comparisons at x = 9.5 mm and x = 10.5 mm from the origin. 170

6.8 Normalized mean axial velocity and RMS comparisons at x = 13.5 mm and x = 16.5 mm from the origin. 171

6.9 The predicted vapour volume fraction using (a) incompressible gas assumption, (b) ideal gas assumption at $CN = 1.48$ 173

6.10 The predicted vapour volume fraction at $CN = 4.57$, vapour is assumed to be an ideal gas 174

6.11 (a) The pressure contour on the centre plane at $CN = 1.48$. (b) The predicted pressure at the injector hole axis. The direction of flow is from right to left. . . . 175

6.12 (a) The pressure contour on the centre plane at $CN = 4.57$. (b) The predicted pressure at the injector hole axis. The direction of flow is from right to left. . . . 176

6.13 Isosurface of vorticity (0.5% of the magnitude) at $CN = 1.48$ indicate vortices; the hole-to-hole connecting vortex can be easily identified, the isosurface of cavitation also indicate cavitation formation at the upper edge of the entrance of the injector hole. The cavitation then travels with the flow and remains in the vicinity of the wall and end at approx 7/8 of the injector hole length. In the cavitation isosurfaces, the red colour represents the maximum concentration of vapour volume fraction and blue represents the minimum. 177

6.14 Image showing isosurface of cavitation, an isosurface of vorticity magnitude (0.5% of the magnitude), velocity vectors and streamline at $CN = 4.57$. In the cavitation isosurfaces, the red colour represents the maximum concentration of vapour volume fraction and blue represents the minimum. 177

6.15 Zoom of the sac region showing velocity vectors and 3d velocity streamlines at $CN = 4.57$. The velocity vectors and 3d streamlines indicate the presence of the vortex in the sac region. 178

6.16 Image showing isosurface of vorticity magnitude (0.5% of the magnitude) and pressure contours plotted on the periodic boundary face at $CN = 4.57$. The pressure contour indicates lower pressure at the core of 'hole-to-hole' connecting vortex. 178

6.17 Isometric view of the injector. The isosurface of vorticity magnitude (0.5% of the magnitude) showing the probability of occurrence of vortices in the injector hole at $CN = 4.57$ 179

6.18 Bottom view of the injector.The isosurface of vorticity magnitude (0.5% of the magnitude) showing the probability of occurrence of vortices in the injector hole at $CN = 4.57$ 180

6.19 Bottom view of the injector. The isosurface of vorticity magnitude (0.5% of the magnitude) showing the probability of occurrence of vortices in the injector hole at $CN = 4.57$. Velocity vectors have been plotted on the front periodic plane from which 'hole-to-hole' connecting vortex appears in a counter-clockwise direction and velocity vectors have also been plotted on the back side (bottom of the image) of the periodic interface from which 'hole-to-hole' connecting vortex appears in a counter-clockwise direction. 180

6.20 A view of the injector from the centre at $CN = 4.57$. Isosurface of vorticity magnitude (0.5% of the magnitude) indicates vortices emerging from the needle wall and entering the injector hole, isosurface of vorticity magnitude also indicate the presence of 'hole-to-hole' connecting vortex. Vectors plotted on plane 4 indicate opposite direction of rotation. Vectors also plotted on the periodic boundary which also indicate the presence of 'hole-to-hole' connecting vortex. 181

6.21 A view of the injector from the centre. Streamlines plotted at $CN = 4.57$, indicate the presence of counter-rotating vortices originating from the needle wall and entering the injector hole. The low-pressure region can also be seen at the core of the vortices. 181

6.22 Vapour volume fractions and non-dimensionalised vorticity are plotted at different slices in the injector holes. The vorticity is non-dimensionalised by multiplying with the injector hole diameter which is 3.5 mm and divided by average velocity which is 18.5 $m\ s^{-1}$ at $CN = 4.57$ (Roth et al., 2002; Roth, 2004). 182

6.23 (a) Still photograph (side view) of the geometry induced cavitation formed at the upper edge of the entrance of the injector hole and travelling downstream, the image indicates that cavitation stays in the vicinity of the injector wall, source: Afzal et al. (1999). (b) isosurface of cavitation prediction at $CN = 4.57$, nominal needle lift (6.00 mm). 183

6.24 (a) Still photograph of the geometry induced cavitation formed at the upper edge of the entrance of the injector hole and travelling downstream, the image indicates cavitation remains stays in the vicinity of the injector wall, the image also indicates horseshoe appearance of cavitation source: Afzal et al. (1999). (b) isosurface of cavitation prediction at $CN = 4.57$, nominal needle lift (6.00 mm), also indicate horseshoe appearance. 183

6.25 (a) 3D photograph of the geometry induced cavitation formed at the upper edge of the injector hole entrance and travelling downstream, source: Afzal et al. (1999). (b) isosurface of cavitation prediction at $CN = 4.57$, nominal needle lift (6.00 mm). 184

6.26 Normalized mean axial velocity and RMS comparisons at x = 9.5 mm, 13.5 mm and x = 16.5 mm from the origin. 186

6.27 Normalized mean axial velocity and RMS comparisons at x = 9.5 mm, 13.5 mm and x = 16.5 mm from the origin. 187

6.28 The predicted vapour volume fraction and velocity streamline in the injector. . . 188

6.29 Isosurface of vapour pressure 189

6.30 Magnified view of the injector. The predicted vapour volume fraction and velocity streamline can be seen. Velocity streamlines indicate a recirculation region at the upper edge of the injector hole on which 3d velocity vectors have also been plotted. 189

6.31 Bottom view of the injector.The isosurface of vorticity magnitude (0.5% of the magnitude) showing the probability of occurrence of vortices in the injector hole. 190

6.32 Bottom view of the injector. The isosurface of vorticity magnitude (0.5% of the magnitude) showing the probability of occurrence of vortices in the injector hole. Velocity vectors have been plotted on the front periodic interface from which 'hole-to-hole' vortex appears to be in the clockwise direction of rotation. Velocity vectors have also been plotted on the back side (bottom of the image) of the periodic interface from which 'hole-to-hole' connecting vortex appears to be in the counter-clockwise direction of rotation. 190

6.33 Bottom view of the injector. Isosurface of vorticity magnitude (0.5% of the magnitude) with the front face removed indicates the probability of occurrence of 'hole-to-hole' connecting vortex and 'counter-rotating' vortices emerging from the needle wall and entering the injector hole'. 191

6.34 A view of the nozzle from the centre. Vectors plotted on plane 4 as well as on both the periodic faces. Vectors indicate the different direction of vortices which emerging from the needle wall and entering the injector hole. Vectors also indicate a presence of 'hole-to-hole' connecting vortex. 191

6.35 The array of images showing the predicted vapour volume fraction of cases simulated for parametric study. Case 1*: Reference the case (see the case at $CN = 1.48$ in § 6.3.2), Case 1: Viscosity of vapour increased by 20%, Case 2: Viscosity of liquid and vapour increased by 20%, Case 3: Viscosity of liquid and vapour increased by 20% and density of vapour increased by 20%, Case 4: Viscosity and density of both phases are increased by 20%. 195

6.36 The array of images showingthe predicted vapour volume fraction of cases simulated for parametric study on the nozzle wall. Case 1*: Reference case (see the case at $CN = 1.48$ in § 6.3.2), Case 1: Viscosity of vapour increased by 20%, Case 2: Viscosity of liquid and vapour increased by 20%, Case 3: Viscosity of liquid and vapour increased by 20% and density of vapour increased by 20%, Case 4: Viscosity and density of both phases are increased by 20%. 196

6.37 The array of images showing the predicted viscosity of cases simulated for parametric study. Case 1*: Reference case (see the case at $CN = 1.48$ in § 6.3.2), Case 1: Viscosity of vapour increased by 20%, Case 2: Viscosity of liquid and vapour increased by 20%, Case 3: Viscosity of liquid and vapour increased by 20% and density of vapour increased by 20%, Case 4: Viscosity and density of both phases are increased by 20%. 197

6.38 The array of images showing the predicted density of cases simulated for parametric study. Case 1*: Reference case (see the case at $CN = 1.48$ in § 6.3.2), Case 1: Viscosity of vapour increased by 20%, Case 2: Viscosity of liquid and vapour increased by 20%, Case 3: Viscosity of liquid and vapour increased by 20% and density of vapour increased by 20%, Case 4: Viscosity and density of both phases are increased by 20%. 198

6.39 The array of images showing the predicted absolute pressure of cases simulated for parametric study. Case 1*: Reference case (see the case at $CN = 1.48$ in § 6.3.2), Case 1: Viscosity of vapour increased by 20%, Case 2: Viscosity of liquid and vapour increased by 20%, Case 3: Viscosity of liquid and vapour increased by 20% and density of vapour increased by 20%, Case 4: Viscosity and density of both phases are increased by 20%. 199

6.40 The array of images showing the predicted velocity of cases simulated for parametric study. Case 1*: Reference case (see the case at $CN = 1.48$ in § 6.3.2), Case 1: Viscosity of vapour increased by 20%, Case 2: Viscosity of liquid and vapour increased by 20%, Case 3: Viscosity of liquid and vapour increased by 20% and density of vapour increased by 20%, Case 4: Viscosity and density of both phases are increased by 20%. 200

6.41 Zoom of the predicted pressure in sac region for case 1* and case 2. Comparison of pressure field for case 1 and 2 indicate a very small reduction of lower pressure region for case 2 with an increase of viscosity indicated using a red circle. 201

List of Tables

4.1 Flow conditions for the first and second series of LDV measurements at lower needle lift and nominal lift. 76

4.2 working-fluid 78

4.3 Flow conditions of the first and second series of LDV measurements at high lift . 81

4.4 Boundary Conditions 81

4.5 Mesh description, y^+ values are obtained after the simulations. 82

4.6 Boundary Conditions 83

4.7 Grid description, y^+ values are obtained after the simulations (see Figure 4.64 and 4.65) 85

4.8 Grid description, y^+ values are obtained after the simulations (see Figure 4.66) . 87

4.9 Flow conditions for the first and second series of LDV measurements at lower needle lift 90

4.10 Boundary Conditions 90

4.11 Mesh description, y^+ values are obtained after the simulations. 93

4.12 Grid description, y^+ and y^*values are obtained after the simulations (see Figure 4.23 (a) & (b) and 4.22 (a) & (b)). 95

5.1 Operating conditions for cases. 130

5.2 Fluid properties at 25°C 130

5.3 Boundary Conditions 134

5.4 Grid description 136

5.5 Maximum y^+ obtained using different turbulence models. 143

6.1 Operating conditions of the test rig for LDV measurements at cavitating conditions. 164

6.2 working-fluid 164

6.3 Number of Control volumes (cells) in different grids 165

6.4 Boundary Conditions 165

6.5 Physical models used 168

6.6 Boundary Conditions 169

6.7 Boundary Conditions 185

6.8 Case setup for the parametric study to check influence of viscosity and density on cavitation. 193

Chapter 1

Introduction

1.1 Motivation

The worldwide concern over global warming and the quantitative relationship between carbon dioxide emissions and global warming have attracted the attention of government and industries all over the world. According to IPCC (United Nations Intergovernmental Panel on Climate Change) Fifth Assessment Report published in the year 2014 (Stocker, 2014), human activities are predominantly responsible for the increase in the concentration of greenhouse gases in the atmosphere. One of the large contributors of the greenhouse gas is the transport sector (EPA, 2016b; European-Commission, 2011) amongst which road transport is the major contributor (European-Commission, 2011). Hence emission standard is getting stricter by each year. The European Manufacturers Association (ACEA) decided in 1998 that average CO_2 emission for the new car should be reduced to 140 g/km by 2008 (European-Commission, 1998) and have set an even more stringent target of 95g/km for the year 2021 (European-Commission, 2016). The tight legislations combined with the customer's demand for improved performance and fuel efficiency has stimulated further research in IC engines. Also, with the limited fossil reserve and anticipated demand for cars in future with an increase in the global population, there is an urge in the industry to harness power from alternative sources of energy that can be used in the existing setup, e.g., IC engine with little or no modification.

This has prompted governments to come up with stricter emission standards (Eur-Lex, 2015) and also introduce higher carbon taxes (HM-Government, 2016) to mitigate factors which cause the above. The European Automobile Manufacturers' Association's (ACEA) have decided in 1998 that average CO_2 emissions for new cars should be reduced to 140 g/km by 2008 (European-Commission, 1998), implying a reduction in fuel consumption of more than 25% from the 1995 baseline, while a more stringent target of 95g/km to be achieved by 2021 (European-Commission, 2016). The tight legislation combined with the increased customer demand for improved performance has encouraged further research in IC engines. Additionally, there is an urge in the industry to harness alternative (non-fossil) sources of energy which can be used in the existing setup (IC engines) with little or no modifications.

In parallel to above-mentioned the implementation of 'direct injection' technology in IC engines has resulted in significant improvements in fuel economy, emissions, and brake horsepower. Direct injection engines use fuel injectors which operate at very high-pressure over very short time durations, allowing the precise amount of fuel to be injected into the engine combustion chamber. Direct injection technology has been simultaneously developed for both spark ignition and diesel engines to improve efficiency. Direct injection technology in diesel engines was more successful because its implementation resulted in significant improvement in fuel economy and performance characteristics. It did not achieve the same commercial success in spark ignition engines due to relatively high cost, lower than expected gains in fuel economy and full load performance and the requirement for a lean NOx after-treatment systems (Zhao, 2009). Nonetheless, having an ability to meter fuel accurately and continuous improvements in fuel injection technology, gasoline direct injection systems have almost eliminated the use of carburettor in road transport engines (Rewse-Davies, 2015).

The recent buzzing trend in the automotive industry is engine downsizing. Engine downsizing is a use of the smaller engine in the car which can provide the power of a larger engine and without compromising much with the fuel economy. It is achieved by use of boosting device such a turbocharger and fuel injectors. The smaller engine displacement allows higher fuel efficiency and loss of power is compensated using turbochargers. One of such recent examples is a Peugeot 1.6 BlueHDI diesel, it has NEDC (New European Drive Cycle) fuel economy figure of 94 mpg and has combined CO_2 emission of 79g/km and also achieves 120 brake horsepower; the engine powers the car Peugeot 208. (Lilly, 2016). Amongst gasoline engine Ford's 1L Ecoboost is capable of achieving 58 mpg (NEDC figure) and 123 brake horsepower and emits 114 g/ km of CO_2 (Bray, 2012a), the engine is used on the car Ford Fiesta.

However, turbocharged engines suffer turbo lag[1]. One of the ways to compensate turbo lag is scavenging. In the scavenging process, both intake and exhaust valves open simultaneously. This creates a dynamic pressure differential between intake and exhaust sides of the engine. Fresh air flows into the combustion chamber and flushes out the exhaust gases through the exhaust valves to the exhaust manifold. The increased flow of exhaust gas creates 50% more torque at low engine speeds compensating turbo lag (Bosch, 2016c).

Fuel injection technology is also continuously being improved. The major fuel injector manufacturers for IC engine are Bosch, Delphi, and Denso. All companies mentioned above are producing solenoid valve and as well as piezoelectric controlled injectors for precise fuel metering. Recently, Bosch has introduced 'control valve operation' for optimised fuel metering in engines (Bosch, 2016c). In 'control valve operation' the engine control unit and high-pressure injectors operate in a closed loop. During the injection, the control unit measures the activation signal and determines the opening and closing of the valve needle to compute the duration of the opening phase. It allows the electronic control unit to calculate the injection amount at every injection and also allows it to readjust it if necessary. Hence, this process makes it possible to calibrate the fuel quantity with minimal tolerances.

Other technologies that reduce greenhouse gas emissions have also emerged. They include hybrid electric vehicle, plug-in hybrid vehicle, battery electric vehicle and battery electric vehicle with range extender. The hybrid electric vehicle combines a conventional IC engine with the electric propulsion system. One of the examples is Toyota Prius, according to the NEDC (New European Drive Cycle), it can achieve approximately 94 mpg and has combined CO_2 output of approximately 70 g/km (Bray, 2016). Plug-in hybrid vehicles are similar to hybrid vehicles, additionally, they can be charged by plugging them into an external source of electric power. Toyota Prius plug-in hybrid version achieves 135 mpg and has combined CO_2 output of 49 g/km according to NEDC test (Bray, 2012b). The battery electric vehicles use chemical energy stored in rechargeable battery packs. Nissan Leaf is presently the world's largest selling battery electric vehicle, the car has zero tailpipe emission and according to the NEDC can travel up to 155 miles (249 km) with 30 KWh battery pack on full charge (5.5 hours) (Nissan, 2016). Battery electric vehicle with range extender use an internal combustion engine with a generator to charge the battery pack, this allows extending the range of Battery electric vehicles. However, the engine doesn't affect the performance of the vehicle because its sole purpose it to charge the battery pack. One of such example is Chevrolet Volt. The only electric range of the vehicle is approximately 53 miles or 85 km at full charge (120V 15 A US outlet) according to the US Environment Protection Agency. With gasoline engine as a range extender, it can achieve 420 miles (680 km) and its combined electric-mode/gasoline unit achieve approx 42 mpg and has combined CO_2 output of 32 g/km (EPA, 2016a). The same car is known as Opel Ampera in Europe and Vauxhall Ampera in the United Kingdom. According to the NEDC, it can achieve 1.2 L/100 km or 235 mpg and has a total range of approx 310 miles (500 km) (Bray, 2013). The car uses GM indirect injection 1.4L EcoFlex engine, presently the engine uses port fuel injection system but GM is planning to introduce direct injection technology to this engine (GM-Europe, 2008). Another such example is BMW i3; it can achieve 130 to 160 km (80 to 100 mi) range at full charge (Thomas, 2015), and according to the company website 80% of its battery can be charged within three hours (BMW, 2015). With a range extending capability it can achieve a total range of approx 270 km (170 mi) emitting approximately 23 g/km of CO2 (Thomas, 2015).

---

[1] In turbocharged engines at low RPM, the turbocharger does not produce the required boost (the amount by which intake manifold pressure exceeds atmospheric pressure), results in slowed throttle response. Turbo lag is said to be the time required to change power output to throttle change (Enginebasics, 2010).

Hence, dependability on IC engines for road transport is likely to continue and therefore, they require being continuously improved to meet future emission standards, consumer requirement for power and torque and fuel efficiency. As previously mentioned about the improvements made in IC engines by implementing the direct injection technology but the direct injection technology has to be further improved. Direct injection engines use high-pressure injectors to spray fuel into engine combustion chamber. The spray directly affects air/fuel mixture and therefore affects the combustion. The typical operating pressure of (Gasoline direct injection) engine lies in between 180 to 250 bars (Bosch, 2016b) and of direct injection diesel engine lies in between 1800 to 2200 bars (Bosch, 2016a). The operating pressure is higher for diesel injectors because of higher compression ratio. Injection duration of both gasoline and diesel is within the frame of milliseconds. However, direct injection is itself a very complicated process. Injecting fuel at very high pressures in such a short duration of times leads to massive liquid fuel acceleration as it travels in the injector nozzle resulting in the formation of localised low-pressure regions. In such low-pressure zones, when the liquid fuel pressure becomes lower than its saturated vapour pressure then the liquid starts to boil and form vapour pockets/bubbles. This process is called cavitation.

Cavitation has both desirable and undesirable effects. The occurrence of cavitation in fuel injector nozzles directly influences the spray quality. Experimental studies on single hole injectors showed that cavitation enhances spray atomization and causes an increase of the spray angle (Soteriou et al., 1995) which enhances air/fuel mixing, although, undesirable consequences such as hydraulic flip[2] has also been reported (Bergwerk, 1959; Nurick, 1976; Soteriou et al., 1995). Single hole injectors are used in indirect injection engines (Heywood, 1988). In the direct injection engines, multi-hole injectors are preferred. One of the confirmed advantages of multi-hole injectors is spray stability against injection and back pressure (Mitroglou et al., 2006). It also allows flexibility for the number of injection holes and their spatial arrangement allowing even distribution of fuel in the combustion chamber to form homogeneous air/fuel mixture (Nouri et al., 2012). Experimental studies have shown that cavitation also enhances spray atomization in multi-hole injectors (Soteriou et al., 1995; Roth, 2004; Mitroglou et al., 2011). Nevertheless, due to transient nature of cavitation, undesirable consequences such as fluctuations in spray angle (Mitroglou et al., 2011) and partial hydraulic flip also have been reported (Soteriou et al., 1995). Additionally, material damage due to shocks produced because of the rapid (supersonic) implosion of cavitation bubbles (Brennen, 1995) has been reported (Asi, 2006; Gavaises et al., 2007). Therefore, understanding of internal flow in particular cavitation is critical for efficient fuel injector design and consequently more efficient engines.

On the other hand, biofuels have emerged as one of the alternative energy in the last two decades (Kovarik, 2013). Biofuels such as bioethanol, biodiesel and biogas uptake CO_2 during cultivation of their feedstock, therefore, can help in reducing global greenhouse gas emissions (MacLean and Lave, 1998). Bioethanol and biodiesel can be blended with gasoline and diesel and be used in gasoline and diesel engines without many modifications (MacLean and Lave, 1998). Biogas can also be used in IC engines with some modifications, however, biogas as a fuel has very low energy density and itself contains CO_2 hence does not offer desirable power and torque characteristics (Porpatham et al., 2008).

The present study focusses on the analysis of internal flows in direct injection diesel fuel injectors using diesel and biodiesel fuel. The chosen system is the diesel over gasoline because it is more fuel efficient (Zhao, 2009). On the contrary, power and torque characteristics are superior in gasoline engines, but refining engine operations and processes such as fuel injection can help in achieving desirable characteristics it diesel engines.

To analyse internal flow in diesel injectors numerous experimental and numerical techniques are available. An experimental technique such as high-speed video imaging provides qualitative information of cavitation occurrence in the injector holes. High-speed video imaging is used with a refractive index matching test rigs. In such test rigs, transparent replicas of fuel injectors are used with the fluid of same refractive index which allows full optical access to complex liquid-gas interface with no distortion of light (Nouri et al., 1988). High-speed imaging with refractive index matching has been used to visualise cavitation in single-hole (Bergwerk, 1959;

---

[2] In single hole injectors when cavitation annularly occupies the entire nozzle length and reaches the nozzle outlet, air or gas from downstream with having higher local pressure than the vapour pressure of the liquid enters the nozzle from its outlet and replaces the volume occupied by the cavitation. This leads to complete detachment of liquid from the wall forming a smooth glass-like jet. This phenomenon is called 'hydraulic flip' (Soteriou et al., 1995)

Nurick, 1976; Soteriou et al., 1995) and multi-hole injectors (Soteriou et al., 1995; Afzal et al., 1999; Arcoumanis et al., 1999, 2000, 2001; Roth et al., 2002; Roth, 2004; Mitroglou et al., 2011; Hayashi et al., 2012). High-speed video imaging has also been used to study the influence of cavitation on emerging sprays in single-hole (Bergwerk, 1959; Nurick, 1976; Soteriou et al., 1995) and multi-hole injectors (Soteriou et al., 1995; Roth, 2004; Mitroglou et al., 2011; Hayashi et al., 2012). LDV (Laser Doppler Velocimetry) is also used with the refractive index matching test rigs to measure the velocity of fluid in single-hole (Arcoumanis et al., 1992) and multi-hole injectors (Arcoumanis et al., 1998; Roth et al., 2002; Roth, 2004). Recently Bauer et al. (2012) have used computer tomography imaging to obtain quantitative information of cavitation in the injector. Duke et al. (2013a) have used X-Ray Radiography imaging to obtain data of cavitation in fuel injector nozzle.

Numerical techniques such as CFD (computational fluid dynamics) can also be used for predicting and analysing the internal flows of fuel injectors. CFD uses Navier-Stokes equations which can describe the fluid flows. The advantage of CFD over experiments is that it allows analysing the flow in regions of the system which are inaccessible using experimental methods and since simulations are performed using computers hence they can also have a cost advantage over experiments. A validated CFD simulation can assist in the enrichment of the understanding of the flow field and can be used in improving the designs of existing components. Therefore, various numerical treatments for multi-phase flows such as the volume of fluid (VOF) model (Noh and Woodward, 1976; Hirt and Nichols, 1981), the mixture model (Manninen et al., 1996), the eulerian-multi-phase approach (see Drew and Passman, 2006) and the Eulerian-Lagrangian technique (Kubota et al., 1992; Giannadakis et al., 2004) and in conjunction with several cavitation models such as barotropic (Schmidt et al., 1999; Kärrholm et al., 2007), transport equation based models (Merkle et al., 1998; Kunz et al., 1999; Schnerr and Sauer, 2001; Singhal et al., 2002), etc. have been developed for modelling cavitating flows and numerous attempts have been made to quantitatively and qualitatively evaluate them in single-hole (Roth, 2004; Duke et al., 2013b) and multi-hole injectors (Roth, 2004; Giannadakis et al., 2007, 2008; Papoulias, 2013) (please refer chapter 2, ‘Literature review’ for further details). In the present study, after the literature review, relevant experimental studies would be selected for CFD simulations. The Literature review would also be used to determine appropriate CFD modelling approaches that would be used to accurately and computationally ‘cheaply’ predict internal flows in single-hole and multi-hole injectors for diesel and biodiesel fuel applications. If simulation results achieve good agreements with the experimental data, then the identified approaches can be used to improve the existing fuel injector designs.

1.2 Biodiesel

Biodiesel is a non-petroleum-based diesel fuel which is made of ‘mono-alkyl esters’ of long chain fatty acids derived from vegetable oils and animal fats. The term biodiesel refers to pure fuel called B100 which has been designated as an alternative fuel by U.S. Departments of Energy and Transportation. B100 can be used in its pure state but more commonly blended with petrodiesel (ASTM, 2009). The blends are often denoted by acronyms such as B20, which indicates 20% biodiesel with petrodiesel. The most common blend in the United States B20 which is 20% biodiesel with 80% fossil diesel, however in Europe the current regulations allows 5.75% of biodiesel to be blended with fossil diesel (Demirbas, 2007).

Biodiesel can be derived from the variety of sources called feedstock including vegetable oils (e.g. soybean, cottonseed, palm, peanut, rapeseed/canola, sunflower, safflower, coconut), animal fats (e.g. tallow), waste oils (e.g. used frying oil) as well as microalgae. The choice of raw material often depends on its availability at particular geographical location (Knothe et al., 2005).

One of the methods to obtain biodiesel is transesterification, in which the vegetable oil or animal fat is reacted with an alcohol (usually methanol or ethanol) in the presence of a catalyst which is usually a base to give corresponding alkyl esters (biodiesel) (Fukuda et al., 2001; Knothe et al., 2005).

1.3 Why biodiesel?

As abovementioned biofuels emerged as one of the possible sustainable solutions amongst alternative/renewable energy sources in last two decades (Kovarik, 2013). They can be used in existing setup in particular with small or no modifications, especially in power generation and propulsion applications i.e. diesel and petrol engines. Biofuel fuel consumption has continuously increased and it is anticipated that biofuel could account for up to 27 percent of the worldwide transportation fuel by 2050 (Eisentraut et al., 2011). Biofuels are defined as fuels, which are derived from biological carbon fixation; they include any fuel derived from biomass. However primary requirement of any biofuel as mentioned (Johnson et al., 2007; Sivakumar et al., 2010) to be renewable and sustainable are:

(i) It should have potential to replace fossil fuel and should not affect the global food supplies

(ii) It must have net positive energy balance

(iii) It should have minimal negative environment impact

Biofuels are mainly classified into biodiesel, bioethanol and biogas, and each has their own merits and drawbacks. Bioethanol is alcohol-based fuel mainly derived from biomass such as corn, maize, and sugarcane, and yeast, herbaceous and woody biomass (Johnson et al., 2007). Most of the current spark ignition engines can run on blended gasoline and bioethanol. Bio-ethanol assists in obtaining higher octane number ON[3] and reduces the pollutant emission, although problems such as metal corrosion have been reported when a higher concentration of bio-ethanol is used (Joshi et al., 2000). Biogas is obtained by Anaerobic digestion (AD). AD is the breakdown of organic material by microorganisms in the absence of oxygen which produces biogas. However, biogas is methane-rich gas and can be used as a fuel (NNFCC, 2016). As already mentioned

---

[3] Octane number: Octane number is defined as petrol's resistance to knock. The octane number (ON) scale is based on two hydrocarbons which define the end of the scale. By definition, normal heptane ($n - C_7H_{16}$) has a value zero and isooctane ($C_8H_{18} : 2, 2, 4\check{}trimethylpentane$) has octane number of 100. A blend of these two hydrocarbons defines knock resistance of intermediate octane numbers (Heywood, 1988).

Biogas can be used in IC engines, however, engines require conversion. Biogas is a low energy density fuel and contains a large proportion of CO_2, therefore, does not offer desirable torque and power characteristic (Porpatham et al., 2008).

Biodiesel is derived from botanical biomass such as oil producing plant seeds, algae, and tallow and sometimes used vegetable oil (Mittelbach and Remschmidt, 2004; Knothe et al., 2005; Johnson et al., 2007). These oils contain triacylglycerol fatty acids and resemble conventional fossil fuels which can be transesterified into biodiesel (Fukuda et al., 2001; Knothe et al., 2005). Biodiesel is blended with conventional diesel and can be used in conventional diesel engines. Biodiesel has lubricating property and often used as additives to conventional diesel (berkeleybiodiesel.org, 2015). Biodiesel also assists in reducing the pollutant emission to the atmosphere because of zero sulphur content and have higher oxygen content (Mittelbach and Remschmidt, 2004; Knothe et al., 2005; Demirbas, 2005), which also means higher cetane number CN[4] (Demirbas, 2005). However, at higher concentration biodiesel blends requires engine modification because biodiesel blends have solvent properties to degrade rubber equipment (berkeleybiodiesel.org, 2015).

Nevertheless, it has been argued by MacLean et al. (2000) that fuel from food sources i.e. biodiesel or bioethanol can be attractive only if co-products are in high demand and their production does not diminish food supply. The question, 'How good a biofuel is?' is often subjected to the geographical location of its respective feedstock and its combination with respective powertrain! Nonetheless methods such as 'life cycle analyses' (Guinée, 2002; Horne et al., 2009) or 'net energy balance' (Durante and Miltenberger, 2004) are used to assess the sustainability of biofuels. The potential of each fuel and powertrain combination can be assessed only through an economy-wide examination of the material inputs and environment discharges associated with "life cycle" of each combination (MacLean et al., 2000).

Life cycle assessment (LCA) is a systematic evaluation of environmental impacts arising associated with all stages of a product's life. It is referred as a 'cradle to grave' approach or 'well to wheel' approach to analysing energy impact of making products (Guinée, 2002). 'Net Energy Balance' as defined by Durante and Miltenberger (2004) is the net amount of energy consumed in the production of fuel or biofuel and is compared to the amount of energy a fuel can produce.

One of the first comprehensive LCA on biodiesel sourced from soybean oil in the USA was conducted by Sheehan et al. (1998). The parameters used were 'life cycle energy efficiency' and 'fossil energy ratio' (FER). The life cycle energy efficiency is a ratio of fuel product energy to total primary energy used in fuel production. Fossil Energy Ratio' (FER) which is the ratio of 'Renewable Fuel Energy Output/Fossil Energy Output'. Estimated life cycle energy efficiency

---

[4] This cetane number is inverse function of ignition delay; higher cetane number corresponds to lower ignition delay. The cetane number scale is defined by blends of two pure hydrocarbon reference fuels (Heywood, 1988). Cetane (n-hexadecane, $C_{16}H_{34}$), a hydrocarbon with high ignition quantity, represents the top of the scale with a cetane number 100. An isocetane, heptamethylnonane (HMN), which has very low ignition quality, represents the bottom of the scale with cetane number 15. This cetane number CN of a fuel is given by the following equation:

$$\text{CN} = \text{percent n-cetane} + 0.15 \times \text{percent of HMN} \tag{1.1}$$

If a CN is too high, combustion can occur before the fuel and air are properly mixed, resulting in incomplete combustion and smoke. If a CN is too low, engine roughness, misfiring, higher air temperatures, slower engine warm-up, and also incomplete combustion occur. Most engine manufacturers in the United States designate a range of required CN, usually 40–50, for their engines (Knothe et al., 2005). In Europe, the CN has to be minimum 49 (Wauquier, 1995).

of biodiesel was 80.55%. The estimated FER for pure biodiesel fuel was 3.215 indicating pure biodiesel yields three times more fuel energy for every unit fossil energy consumed in its production. The predicted FER for B20 was 0.98 and fossil diesel was 0.83. For CO_2 emissions it was estimated that use of pure biodiesel can reduce CO_2 emissions by 78.45% and B20 can reduce CO_2 emissions by 15.66% from an urban bus. The Sheehan et al. (1998) model was used by Pradhan et al. (2009) to determine significant changes in the original inventory. The estimated FER for pure biodiesel was 4.56. The improvement was attributed to improved soybean yields and more energy-efficient soybean crushing and conversion facilities.

The LCA studies of biodiesel fuel are often specific to the feedstock and its geographical location. The LCA studies by De Nocker et al. (1998) on biodiesel derived from rapeseed and fossil diesel with the geographical score in Belgium showed that total negative environment impact of biodiesel is 5% to 20% lower than fossil diesel. However, it was argued that benefits of biodiesel in terms of greenhouse gas uptake are compensated by other environment impacts such as impacts on water, eutrophication, acidification and photochemical oxidant formation. In the LCA study conducted by Niederl and Narodoslawsky (2004), environment impacts on production of biodiesel sourced from tallow and vegetable oil were analysed and compared with those of fossil diesel. The results indicated biodiesel sourced from tallow and vegetable oil have the lower impact than fossil diesel in most of the examined scenarios. LCA studies conducted in the Philippines by Pascual and Tan (2004) also showed lower negative environment impacts of biodiesel fuel than those of fossil diesel. In an emerging market like India, Jatropha is being viewed as the potential biodiesel feedstock. The LCA results of Achten et al. (2010) suggests that production and use of Jatropha biodiesel could decrease the non-renewable energy requirement by 82%.

Biodiesel from algae has also become an important area of interest. As mentioned by Demirbas and Demirbas (2011), algae can be grown anywhere and does not require fertile land or a food crop. Its processing requires less energy than it provides. It is also one of the fastest growing plants and 50% of weight can be converted into oil. This oil can be used to make biodiesel using transesterification method for cars, truck and aeroplanes. However, it has been argued citedemirbas2011importance, kendall2013comparing that for sustainable production of biodiesel from algae, it is important to identify the strains of algae which produce most lipids which can be transesterified into biodiesel. So far no industrial scale process designed specifically for biodiesel yet exists (Slade and Bauen, 2013), hence in LCA studies for biodiesel from algae, data is often extrapolated from laboratory scale systems or from commercial schemes which are designed to produce high-value products such as health and food supplements. Nevertheless, Slade and Bauen (2013) argued that such LCAs can still serve as a tool to design systems to produce biodiesel from algae. Their study suggested that it may not be possible to produce biodiesel from algae with present techniques, it might be possible in the future as experience with algal cultivation increases.

Though all LCA results have not favoured biofuels: LCA conducted by MacLean et al. (2000) with geographical scope of USA, highly supported fossil fuel over biofuels due to their high energy content, ease of use and lower production cost than biofuels regardless higher greenhouse emissions in fossil fuel lifecycle. The fossil fuels which were considered were reformulated gasoline, reformulated diesel, methanol and compressed natural gas (CNG), the biofuels considered were biodiesel from soybeans and ethanol from corn, woody biomass, and herbaceous biomass. In a similar study by Joshi et al. (2000) in which extraction, production, transportation, storage, and distribution were also included in the life cycle phases of fossil and alternative fuels. The results also highly favoured fossil fuels. Though, it was proposed that if all the fossil energy in biofuel production cycle were replaced with biofuel energy using the sustainable method it could result in zero net carbon dioxide emissions.

However, it can be argued that the number of LCA studies listed is incomplete and may not be enough to assess the sustainability of biodiesel. Since, automotive tailpipe emission data does not provide a complete picture of overall emissions, the LCA study which assesses the environmental impact throughout production and operations (tailpipe emissions) assists in the full assessment. Most of the listed LCA studies suggest the sustainable production of biodiesel fuel. Therefore, it can be cautiously stated that use of biodiesel can help in reducing greenhouse gas emission into the atmosphere, alleviating the demands on limited fossil reserve and meeting the anticipated energy requirements of the future. The above can be further supported by continuously improving IC engine technologies such as direct injection, engine downsizing, etc. As previously mentioned direct injection technology has assisted in reducing the fuel consumption. However, significant improvements have not been achieved for NO_x and soot reductions (Pignon, 2005; Agarwal et al., 2013), therefore, this technology needs to be further improved. In the preceding section, it was recognised that understanding of internal flow in fuel injectors is critical, in particular, the occurrence of cavitation. Hence, this study would focuss on the analysis of internal flow in fuel injectors of diesel engines with diesel and biodiesel fuels.

1.4 Advantages and disadvantages of biodiesel fuel

A summary of advantages and disadvantages of biodiesel are listed below which can help better selection of such fuel for different applications.

1.4.1 Advantages:

- Biodiesel can be produced from various feedstocks; there have been more than 350 identified oil-bearing crops from which biodiesel can be produced (Demirbas, 2007).

- Due to biodiesel's ability to be used directly in existing diesel engines, it has been argued (Sheehan et al., 1998) that biodiesel offers an immediate potential support to reduce demands of fossil diesel as well as to assist in reducing dependencies on foreign petroleum.

- Most of the above-mentioned LCAs indicates biodiesel can help to reduce greenhouse gas emission due to CO_2 uptake during biodiesel crop cultivation.

- Blending biodiesel with fossil diesel can assist in SO_x emissions reduction. Pure biodiesel has no sulphur content (Demirbas, 2007). Use of B100 can 100% eliminate SO_x tailpipe emissions (Sheehan et al., 1998).

- Biodiesel also contains 11% by weight of oxygen while fossil diesel has zero percent oxygen (Demirbas, 2005; Canakci, 2007). Therefore, biodiesel has a better combustion efficiency due to an increase of homogeneity of oxygen with the fuel during combustion. Hence, biodiesel has higher cetane number (or lower ignition delay).

- It has been also reported that the use of biodiesel blend can dramatically reduce particulate matter[5] (PM) reduction (Knothe et al., 2006).

- Biodiesel is a non-toxic fuel and degrades faster than fossil diesel (Knothe et al., 2005; Demirbas, 2007). It's higher oxygen content also assist in biodegradation process (Demirbas, 2007).

- Biodiesel has excellent lubricity and it is steadily gaining the advantage with the advent of low-sulphur fossil diesel fuels, which have less lubricity. Adding 1 to 2% of biodiesel as an additive restores lubricity of low sulphur diesel fuel (Knothe et al., 2005).

1.4.2 Disadvantages:

- Biodiesel has a higher viscosity than fossil diesel (Knothe et al., 2005). The viscosity of biodiesel and conventional diesel increase with a decrease in temperature and vice versa. Fuel with relatively high viscosity will not break into fine particles when sprayed, large particles will burn slowly leading to poor engine performance (Nabi et al., 2009). It has been reported that final spray tip penetration of biodiesel is greater than those of diesel due to higher viscosity (He et al., 2008; Gao et al., 2009). Lower spray angle of biodiesel than fossil diesel has also been attributed to higher viscosity(Gao et al., 2009; Wang et al., 2010). The lower viscosity of biodiesel also influences the flow characteristic in the fuel injector. An attempt will be made to address this issue in the present research work.

- Biodiesel has the higher surface tension (Sheehan et al., 1998) which is strongly related to higher NOx formation. According to Varatharajan and Cheralathan (2012), surface tension results in the increase in droplet size which inhibits the air-fuel mixing and can reduce the fraction of fuel burned in the premixed combustion phase and lead to increase the duration of diffusion flame combustion. Hence, increase in NO_x emissions.

- Biodiesel and diesel, both contains few long chain hydrocarbons called waxes that crystallise (Sheehan et al., 1998; Knothe et al., 2005) at a lower temperature called cloud point. The cloud point is the warmest temperature at which such crystallisation occurs (Knothe and Steidley, 2005). The cloud point of biodiesel, in general, is higher than fossil diesel (Sheehan et al., 1998; Knothe et al., 2005; Demirbas, 2007).

- Biodiesel also has a higher density than conventional diesel (Knothe et al., 2005). Density is believed to be the main property that influences the amount of fuel injected (Boudy and Seers, 2009). Higher density results in higher mass injection into the combustion chamber and also results in poor atomization (Öner and Altun, 2009).

---

[5] Particulate matter is a complex mixture of extremely small particles and liquid droplets. Particle pollution is made up of a number of components i.e. acids (i.e. nitrates and sulphates), organic chemicals, metals, soils and dust particles (Knothe et al., 2005).

- Biodiesel has lower heating value than fossil diesel (Sheehan et al., 1998; Knothe et al., 2005; Atabani et al., 2012) which results in the increase in fuel consumption (Monyem and Van Gerpen, 2001; Canakci, 2007) and lower generation of power and torque (Monyem and Van Gerpen, 2001; Carraretto et al., 2004; Buyukkaya, 2010).

- Biodiesel has higher oxygen content which also correlates to shorter ignition delay and cetane number (Demirbas, 2005; Canakci, 2007), but, the higher oxygen content in biodiesel is also viewed as one of the contributing factors for higher NO_x emissions (Canakci, 2007).

1.5 Diesel injection systems

In diesel engines, fuel is injected mainly using two methods: direct injection and indirect injection.

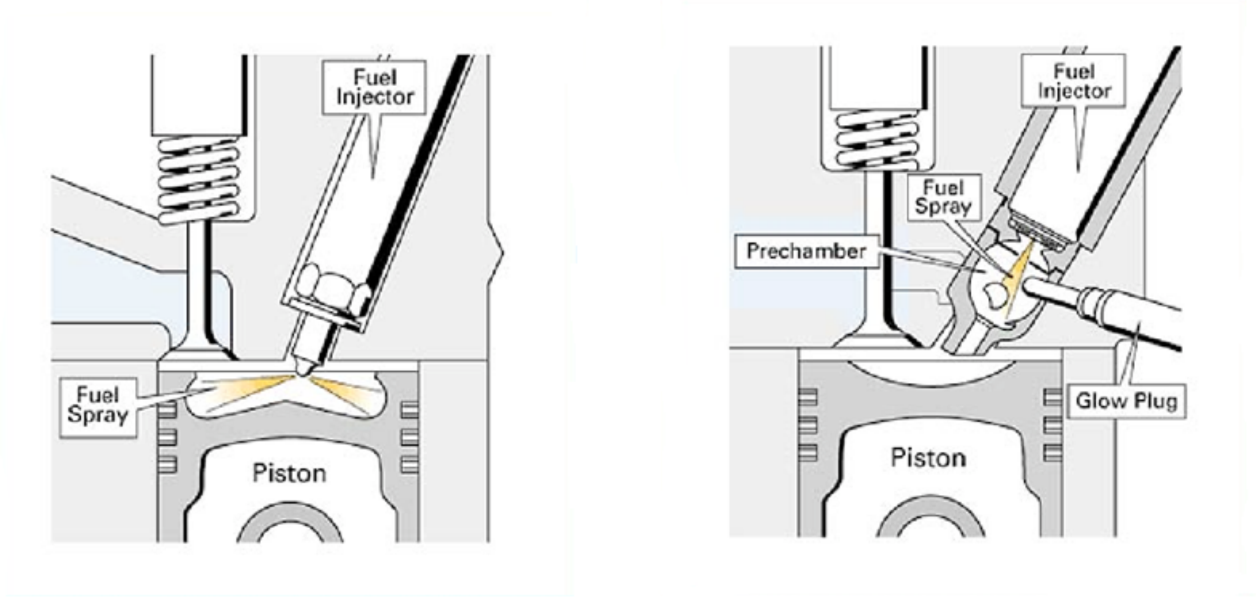

Figure 1.1: Two photographs showing direct and indirect injection system engines. On the left a typical direct injection system setup with a multi-hole injector and on the right an indirect injection system setup with a single-hole injector. Source: Bosch (2016d)

1.5.1 Indirect injection

In indirect injection diesel engine, the fuel is delivered into a volume of the combustion chamber called pre-chamber. During the compression stroke, the air is forced from the main combustion chamber to the pre-chamber through a nozzle or an orifice or set of orifices creating a highly turbulent air motion inside. Towards the end of the compression stroke, diesel fuel is injected into the pre-chamber through a nozzle as a single spray. Combustion starts in the pre-chamber, the increase in pressure with combustion forces fluid back into the main chamber where it further mixes with the main chamber air resulting in the power stroke. The indirect injection engine operates at much lower operating pressure than direct injection engine. A glow plug as a starting aid is often provided in indirect injection engines (Heywood, 1988).

1.5.2 Direct injection

In direct injection systems, fuel is directly injected into the combustion chamber. Direct injection is achieved using a distributor pump or unit injectors or a common rail direct injection system. Distributive pumps supply fuel to injector from fuel tank into cylinders of the engine using separate pressure lines to the injectors. It is timed to provide fuel just before the piston reaches the top dead centre on the compression stroke. The distributive pump has only one fuel pressure mechanism regardless of the number of cylinders. It has a distributor designed to share the pressurised fuel to individual cylinders according to the injector order. Distributive pumps can be mechanically or electronically controlled (Denso, 2015). In a unit injector, the injector and pump are combined into one unit and positioned over each cylinder. The unit injector can also be electronically controlled or mechanically controlled by a camshaft. The unit injectors can operate at considerably higher injection pressure than distributive pumps. Electronically controlled injectors have the advantage over mechanically controlled unit pumps for more precise control over injection timing and fuel quantity (Bosch, 1999).

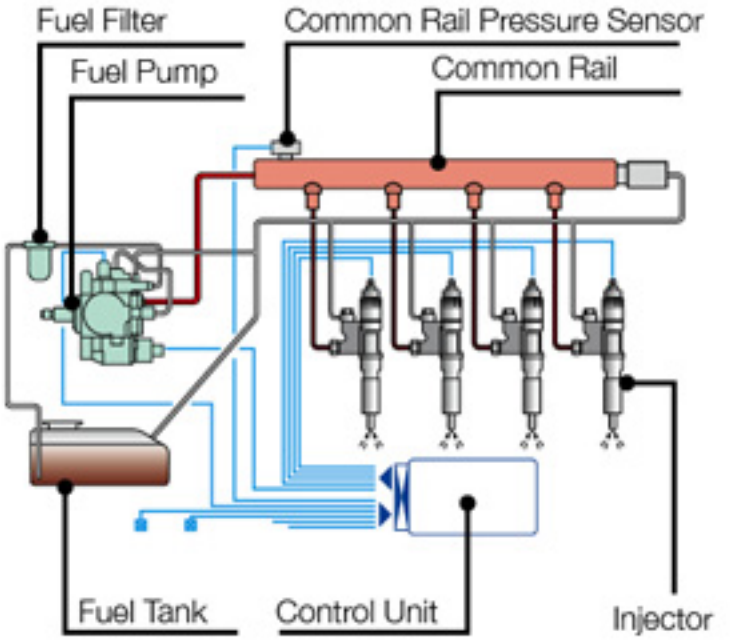

Figure 1.2: A typical common rail injection system. Source: Hitachi (2011)

In common rail systems (see Figure 1.2), a high-pressure pump is used to store a reservoir of fuel at high pressure in a common fuel rail or high-pressure pipe. The common rail is connected to fuel injectors which are connected to individual engine cylinders. The common rail supplies pressurised fuel to injectors. The fuel injectors are controlled by an ECU (electronic control unit). When fuel injectors are electronically activated fuel is sprayed into cylinders at desired pressure. The needle in the fuel injector is opened and closed by the actuator which can be a solenoid valve or a Piezo valve. The main advantage of common rail system over other mentioned systems is that in common rail system fuel pressure is independent of engine speed and load conditions. This feature provides a flexibility in controlling both injection quantity and fuel quantity. Hence, a near constant (square) injection rate can be achieved from start to the end of the injection event (Bosch, 1999). This allows better spray penetration and mixing and consequently assists in achieving an improved combustion and pollution reduction. The highly pressurised spray can be achieved even at low engine speeds (Hannu Jääskeläinen, 2015).

Electronic controls in common rail systems allow 'pilot injection' which also assists in noise reduction. The pilot injection is achieved by injecting a small amount of fuel just before the main injection event. This smoothes the start of combustion eliminating the pressure spikes that produce engine rattling (Baker, 2016). In some sophisticated common rail systems, as many as five injection events are performed per stroke. The pilot injection also assists in NO_x reduction. Hence, the present study is focussed on common rail injectors due to the stated advantages. Details of the functioning of a typical common rail fuel injector are described in next sub-subsection.

1.5.2.1 Fuel injector

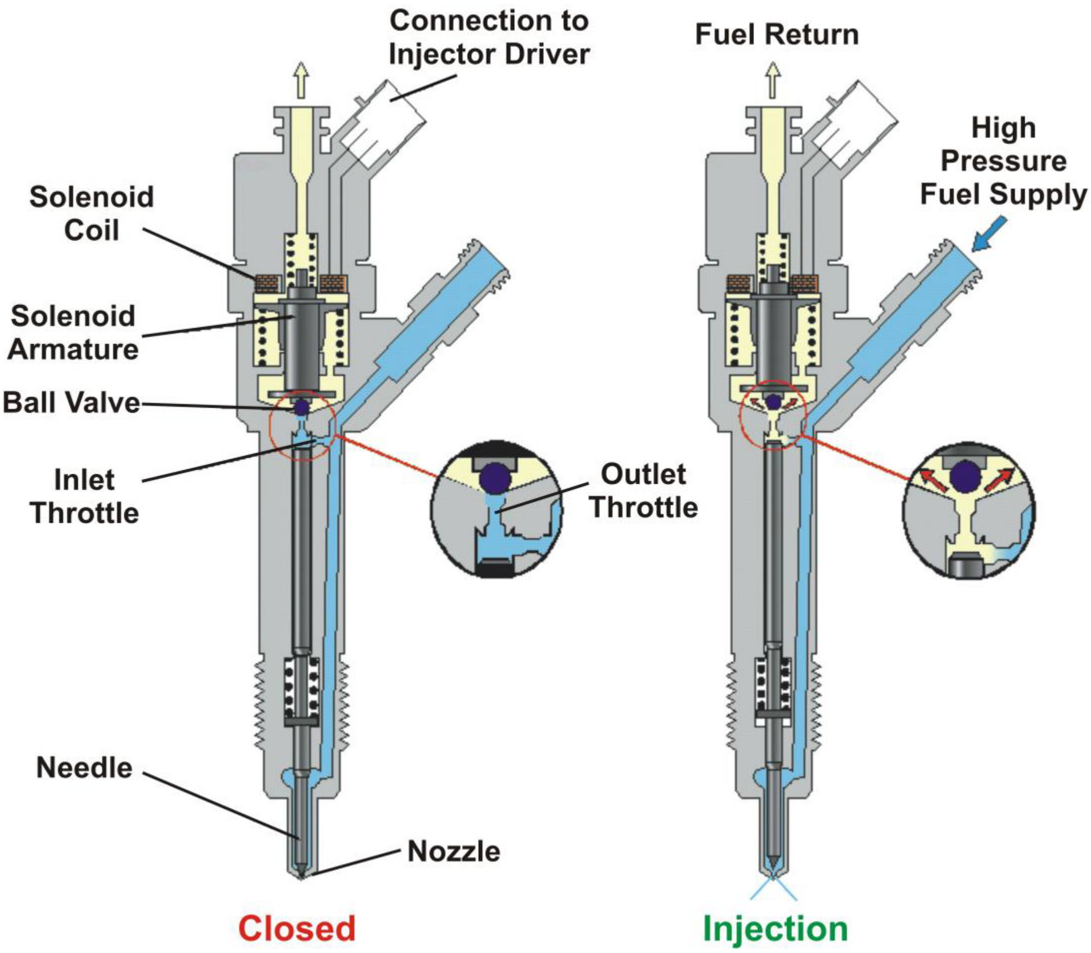
Connection to Injector Driver
Fuel Return
High Pressure Fuel Supply
Solenoid Coil
Solenoid Armature
Ball Valve
Inlet Throttle
Outlet Throttle
Needle
Nozzle
Closed
Injection

Figure 1.3: Schematic of a typical common rail injection system. Source: Roth (2004)

Multi-hole injectors are used in direct injection engines to ensure even distribution of fuel and good penetration of fuel into the rapidly moving dense air stream (Bonnick, 2011). In this sub-subsection, a functioning of typical solenoid activated multi-hole fuel injector is shown. The present description is based on Roth (2004). In Figure 1.3, a typical solenoid valve activated diesel fuel injector is presented in the closed and injecting state.

When the solenoid is not activated the injector spring closes the ball valve. The fuel pressure acts on the upper and lower needle section. Since the upper section is broader than lower section a force imbalance is influenced. This keeps the needle pressed on the seat and no fuel can pass through nozzle holes.

When the solenoid is energised the armature is pulled upward, the ball valve opens up and fuel can pass through the throttle to fuel return lines. This results in a reduction of pressure on the upper section of the needle. At this moment pressure at lower portion of the needle is higher than upper section of the needle. This results in upward movement of the needle and consequently a spray. A typical opening and closing operation can take around 5 milli seconds.

1.5.2.2 Injector geometries

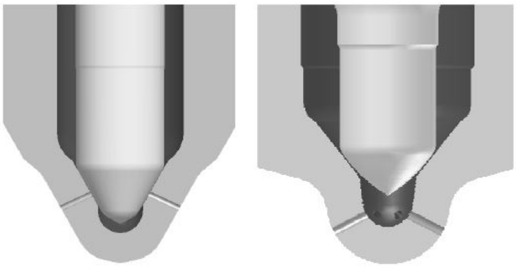

Figure 1.4: Typical injector geometries: valve cover orifice and sac type. Both axisymmetric with 6 hole configuration. Source: Mitroglou et al. (2011)

The popular multi-hole injector geometries are sac type and valve cover orifice (VCO). The sac type nozzles have a cup volume below the injection holes and needle. The cup volume is designed to match the requirement of immediate response at the initial stage of injection where the needle is not yet fully open. Hence, the sac is used for storing a certain amount of fuel at the end of each injection. This fuel is then redistributed at the beginning of the new cycle. This allows balancing the weak start delivery rates (Papoulias, 2013). In the VCO type injectors there is no cup volume below the injection holes and needle. The needle goes all the way down at the end of the injector covering the entire flow passage and blocking the hole entrances (Roth, 2004; Papoulias, 2013). Both designs have their own advantages and disadvantages. These days injector geometries are further being refined to combine beneficial features of both the VCO and sac type nozzles (Papoulias, 2013).

1.6 Cavitation

When a body of liquid is heated at a constant pressure or when its pressure is reduced at a constant temperature by static or dynamics means a state is reached at which vapour or gas or gas filled voids become visible and grow. In the case of heating at constant pressure, the process is called ‘boiling’ and in the case of reduced pressure at constant temperature, the process is called ‘cavitation’ (Knapp, Daily, and Hammitt, 1979). Thus cavitation can be defined as the formation of vapour bubbles in the liquid when the local pressure drops below the vapour pressure threshold.

Nucleation is said to be the initial stage of cavitation, in a typical hydraulic machinery it can usually occur in two forms, homogeneous or heterogeneous form. The thermal motions within the liquid form temporary, microscopic voids which act as nuclei necessary for rupture of the liquid and formation of microscopic bubbles; this is defined as homogenous nucleation. Heterogeneous nucleation occurs due to the presence of nuclei like submerged micro gas or vapour bubbles or impurities in the working liquid. The possibility of heterogeneous nucleation can be further enhanced due to the possible presence of contaminants and dissolved the gas in the micro-crevices of the solid walls surrounding the liquid. Therefore, the quantity of dissolved gas would affect nuclei distribution and would considerably affect cavitation. The inception of cavitation can be either due to homogeneous or heterogeneous nucleation (Brennen, 1995).

1.6.1 Cavitation in fuel injectors

Direct injection is achieved by injecting fuel at very high pressure using injectors over the very short duration of time. A typical opening and closing needle operation can take around five milliseconds. Such operations lead to massive fuel acceleration as it travels in the injector forming low-pressure regions. Cavitation starts to occur in such low-pressure zones when the liquid pressure goes lower than its vapour pressure threshold. Experimental studies on single hole nozzle suggest the occurrence of cavitation at the sharp entrance of the injector (Bergwerk, 1959; Nurick, 1976; Arcoumanis et al., 1992; Soteriou et al., 1995; Desantes et al., 2009; Duke et al., 2013a). It is widely believed that as the fuel enters the injector hole, it separates from the wall at the entrance due to the sudden reduction of the cross-sectional area leading to the formation of recirculation regions where pressure goes lower than vapour pressure threshold; this is defined as geometry induced cavitation. LDV measurements of the mean axial velocity at different axial locations in single-hole injector by Arcoumanis et al. (1992) have shown the presence of recirculation regions near the entrance of the injector.

One of the ways to assess cavitation intensity in nozzles and orifice is cavitation number or CN. It is a non-dimensional parameter indicating cavitation intensity and it is independent of Reynolds number (Bergwerk, 1959).

$$CN = \frac{p_{inj} - p_{back}}{p_{back} - p_v} \tag{1.2}$$

where, p_{inj} is injection pressure, p_{back} is the back pressure, p_v is the vapour pressure.

Studies in single-hole injectors have shown that cavitation influences the emerging spray. A significant increase in spray angle with an increase in cavitation number has been observed (Nurick, 1976; Soteriou et al., 1995; Desantes et al., 2009). An enhancement in atomization which assists in air-fuel mixing has also been observed with an increase in cavitation number (Soteriou et al., 1995). However, experimental studies (Bergwerk, 1959; Nurick, 1976; Soteriou et al., 1995) suggest that in single-hole injectors when cavitation reaches the hole exit it suddenly disappears, and emerging spray takes a form of the smooth glass-like jet (see Figure 2.1). This phenomenon occurs because air or gas from the downstream chamber having the local pressure higher than the cavitation vapour enters the injector from the outlet and occupies the volume previously filled by cavitation which results in complete detachment of liquid from the wall forming a smooth glass-like jet. This phenomenon is called 'hydraulic flip'.

Experimental studies on multi-hole injectors have shown the appearance of cavitation at the upper edge of the entrance of the injector hole (Soteriou et al., 1995; Arcoumanis et al., 1999, 2001; Afzal et al., 1999; Arcoumanis et al., 2001; Roth et al., 2002; Roth, 2004). Likewise, single-hole injectors, LDV measurements have of mean velocity in multi-hole injectors also confirm recirculation region at the upper edge of the entrance of the injector holes (Arcoumanis et al., 1998; Roth et al., 2002; Roth, 2004). However, In many cases at lower needle lift due to constricted fluid path, the cavitation has been observed appearing at the bottom edge of the injector hole entrance (Mitroglou et al., 2011; Hayashi et al., 2012).

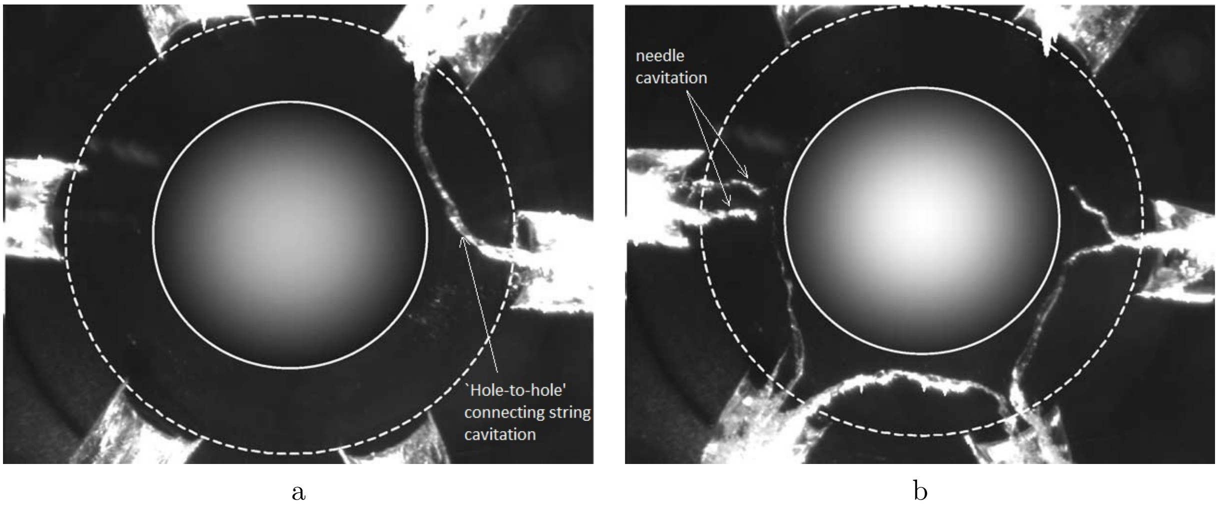

Figure 1.5: High speed digital images showing vortex cavitation inside the enlarged fuel injector. (a) Hole-to-hole connecting cavitation (b) Needle string. Source: Arcoumanis et al. (2001)

In multi-hole injectors vortex type cavitation or cavitating strings have been observed (Arcoumanis et al., 1999, 2001; Roth et al., 2002; Roth, 2004; Mitroglou et al., 2011; Hayashi et al., 2012; Nouri et al., 2012). Experimentalists have mostly seen two types of string cavitation: 'hole-to-hole' cavitation and 'needle strings' (see Figure 1.5). The formation o 'hole-to-hole' vortex is attributed due to vortex flow in the space between the needle, needle seat and two adjacent holes. 'Needle strings' are believed due to intense vortex flow around the injector hole axis, leading to the low-pressure region in the vortex core to initiate cavitation (Roth et al., 2002; Roth, 2004).

Investigations on the influence of cavitation on spray have shown an increment in spray angle with an increase in cavitation number in multi-hole injectors. It has been observed that the jet diverges and atomises instantly when cavitation appears upstream of the injector hole (Soteriou et al., 1995; Roth, 2004; Mitroglou et al., 2011). Additional instabilities in spray angle due to the presence of 'string cavitation' have also been reported (Mitroglou et al., 2011). Partial hydraulic flip has been observed in the VCO type injectors (Soteriou et al., 1995). In partial hydraulic flip, air at the downstream chamber having higher pressure than fuel vapour pressure enters the injector hole from the exit and occupies the upper part of the injector hole previously occupied by the cavitation. Hence, the emerging spray forms the glass-like body at the side and remains fuzzy at the bottom side. More details of such can be found in chapter 2 ‘literature review.’

Cavitation bubble collapse also causes surface erosion in hydraulic equipment. The implosion of cavitation bubble over a sufficient time can cause severe damage to the hydrodynamic surface. The surface erosion is believed to be due to frequent strain resulting from intense pressure waves created by microjet and local shockwave during supersonic bubble collapse (Brennen, 1995). Many researchers have observed damage on the injector surface due to the cavitation bubble collapse. Asi (2006) observed cavitation damage in the vicinity of needle seat of the injector. Gavaises et al. (2007) also noticed cavitation erosion sites in VCO and mini sac type diesel injectors. In VCO type nozzle two locations of surface erosion were observed. The first one was at the top part of the hole close to the entrance. They recognised other cavitation damage sites sidewise (0 degrees or 3o’ clock and 180 degrees or 9o’ clock position) of the injector hole entry. In the mini-sac type diesel injector, the cavitation sites were observed on the needle as well as inside the sac.

As we know, biodiesel has emerged as one of the alternative fuel for the future; its behaviour has been extensively compared with conventional diesel. Comparative studies in single hole injectors (Park et al., 2007; Suh et al., 2008) and multi-hole injectors (Nouri et al., 2012) have suggested that inception of cavitation occurs at higher cavitation number in biodiesel than fossil diesel which is due to the higher viscosity of biodiesel. Experimental studies indicate that biodiesel has a slightly higher spray length and smaller spray cone angle which is due to biodiesel’s higher viscosity and higher density (He et al., 2008; Wang et al., 2010). Additionally, experimental studies (Park et al., 2007, 2009) have reported larger droplet sizes of biodiesel than fossil diesel which is due to higher viscosity and surface tension in biodiesel.

1.7 Role of CFD on cavitation Modelling

Computational Fluid Dynamics or CFD is an interdisciplinary topic. It provides a qualitative and quantitative prediction of flow field using fluid mechanics, numerical analysis, and computer science. It uses numerical methods to solve fundamental non-linear differential equations which describe the fluid flow i.e. Navier-Stokes and associated equations for predefined geometries and boundary conditions. However, CFD has complexities; it is difficult to obtain analytical solutions of these equations and therefore, require significant computing resources. Hence, the development of computational fluid dynamics is closely related to the advancement of the high-speed computers.

The aerospace industry was the first to use CFD techniques into the design, R & D and manufacture of aircraft and jet engines. The science is being recently applied to the design of internal combustion engines, the combustion chamber of gas turbines, furnace. It is also being used in automotive aerodynamics, heating, ventilation and air conditioning, building design and even swimsuit design.

The main advantages of CFD are:

1. Component design in short turnover time. The CFD simulation can help an engineer assess the performance of the component before its manufacturing; this helps in the reduction in time spent in design and numbers of prototypes.
2. Ability to analyse flow physics in some parts of the system which are inaccessible using experimental methods.
3. CFD allows engineers to explore operational parameters under hazardous conditions previously considered "impossible" using normal testing procedure i.e. safety studies and accidental scenarios.

Navier-stokes and associated equations can be used to describe the internal flows of IC engine fuel injectors, and therefore numerous attempts have been made in CFD model development for this purpose. The most popular approaches for simulating multi-phase flows are:

(i) The VOF (Volume of Fluid) model: The VOF model (Noh and Woodward, 1976; Hirt and Nichols, 1981) is a numerical technique for tracking interface between two immiscible fluids in a fixed mesh. In VOF method, a single continuity and momentum equation is shared by the fluids, and volume fraction of each of the fluids in each computational cell is tracked everywhere in the domain by using an additional transport equation of volume fraction. The sum of volume fractions of all fluids must be equal to unity in each computational cell, which automatically satisfies the continuity. The VOF model can be used for cavitating flows and for which it determines the cavitation volume using large scale interface; however, phases are separated by an interface and not interpenetrating[6] or polydispersed as perceived in bubbly flows (see Figure 1.6).

(ii) Homogeneous equilibrium model (HEM): This model assumes velocity, pressure and temperature are equal between phases. The phases move in proximity to each other. Therefore, mass, momentum and energy transfer between them occur rapidly, so equilibrium is instantly achieved. In the model, the fluid resembles a homogeneous mixture of n-phases. The model equation resembles for a pseudo-fluid with mixture properties and an equation of state which links the phases to obtain these mixture thermodynamic properties. The sum of volume fractions α_l (liquid) and α_v in the control volume can be equal to any value between 0 and 1, depending on the volume occupied by liquid or gas phase (Brennen, 1995; Corradini, 1997; Lagumbay et al., 2007). The model also solves transport equation of volume fraction of phases to track them. The model is suitable for cavitating flows because it allows phases to be interpenetrating.

(iii) The mixture model: The mixture model (Manninen et al., 1996) is similar to homogeneous equilibrium model; only It also allows slip between phases.

---

[6] Interpenetrating: The individual phase properties are no longer identifiable, and liquid gas phases coexist everywhere in the domain (Read and Piccioli, 2015).

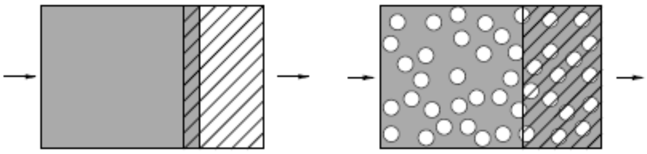

Figure 1.6: The distribution of two phases in the computational domain. A) Standard VOF application, b) Homogeneous distribution of the gaseous phase. Source: (Schnerr and Sauer, 2001)

(iv) Eulerian multi-fluid model: The Eulerian multi-fluid model assumes that fluid consists of n different phases, treated as interpenetrating continue. The model solves mass, momentum and energy conservation equations for each component however pressure is equal in all phases. The phases interact each other using mass, momentum and energy exchange source terms contained in conservation equations which also allows slip velocity between phases. However, these additional source terms require further modelling which adds more empiricism into calculations (see Drew and Passman, 2006).

(v) Eulerian-Lagrangian model: The Eulerian-Lagrangian model treats one phase as continuous in the Eulerian frame and another phase as discrete in the Lagrangian frame. The Navier-Stokes equations provide a solution of continuous phase taking into account the effect of dispersed phase volume fraction and contains mass, momentum and energy exchange source terms which provide coupling between phases. The model tracks discrete particles or bubbles/droplets throughout the flow field using based on force balance (Newton's second law) on each entity (Giannadakis et al., 2004). The model requires additional equations for discrete phase.

In parallel with multi-phase modelling approaches, numbers of cavitation models have been developed and evaluated. Most cavitation models work within the framework of above-mentioned approaches. The popular cavitation modelling approaches are briefly reviewed below:

(i) Barotropic Model: In barotropic models, the change in the fluid density is only dependent on local pressure variation which implies in the case of two-phase bubbly flow for an instantaneous change in pressure the bubble will undergo an instant change in volume. The phase transfer from liquid to vapour is instant when the local fluid pressure goes lower than the vapour pressure threshold and vice-versa (Schmidt et al., 1999; Kärrholm et al., 2007).

(ii) Transport equation based models: In such models, the vapour fraction is governed by a conservation equation; the vapour production (cavitation) and destruction (condensation) depend on the rate term which lies on the right-hand side of the equation. In many models (Alajbegovic et al., 1999; Alajbegovic, 1999; Schnerr and Sauer, 2001; Yuan et al., 2001; Singhal et al., 2002; Alajbegovic et al., 2002; Zwart et al., 2004; Martynov, 2005), the rate term is based on 'Linear-Rayleigh' which is first order solution of the 'Rayleigh-Plesset' equation and in many models (Merkle et al., 1998; Kunz et al., 1999, 2000) rate term is simply based on empirical assumptions.

(iii) Eulerian-Lagrangian models: In such models, the liquid is treated as a continuous phase in the Eulerian frame, and the vapour is treated as a disperse phase in the Lagrangian frame. The coupling between both phases is obtained using a source term in the momentum conservation equation of the liquid phase (Giannadakis et al., 2004, 2008).

The popular multi-phase and cavitation modelling approaches are briefly discussed. Nonetheless, it can always be argued that listed models, as well as their description, is incomplete. More elaborate descriptions are available in the chapter 'literature review'. Through the literature review, we would also try to identify suitable CFD models for the purpose of simulating internal flow in fuel injectors of IC engine which is the goal of this study. The literature review would also help in identifying suitable test cases which can be used to assess CFD simulations.

1.8 Aims and objectives of this study

Cavitation is one of the critical phenomena occurring in fuel injectors of IC engines. It directly influences the emerging spray, and hence it affects air-fuel mixing and subsequently combustion and fuel emissions. On the other hand, Biodiesel has emerged as one of those alternative fuels which can help in mitigating the climate change, alleviate the pressure on fossil fuel reserves and can support to meet future energy demands. Therefore, the present study would be focussed on the analysis of the internal flow of diesel and biodiesel fuel in IC engine fuels injectors using CFD. Therefore, this study aims for:

1. Single-phase simulations: Identify appropriate test case for simulation using the literature review. Identify appropriate grid by grid independence study. Identify suitable turbulence model for the multi-hole injector. Validate simulations by comparing simulations results with experimental results.

2. Cavitation model assessment: Identify appropriate test case from the literature review. Quantitative and qualitative evaluation of cavitation models. Evaluate cavitation and turbulence models by quantitative and qualitative comparison of prediction results with the experimental data. Identify best-behaved cavitation and turbulence models for the application.

3. Cavitation simulation in multi-hole injectors: Use the identified turbulence model from single-phase simulations and the identified cavitation model from cavitation model assessment to simulate cavitating in the multi-hole injector. Validate simulations by comparing the simulations results with the existing experimental results. After obtaining quantitative and qualitative agreements with the experimental results, use the same approach to model biodiesel fuel properties i.e. higher viscosity and density.

1.9 Thesis outline

Chapter 1: In chapter 1 the motivation for research, brief description of biodiesel, its advantages and disadvantages, IC engines and fuel injectors are given.

Chapter 2: In chapter 2, ‘literature review’ relevant experimental and theoretical studies are reviewed. The review of experimental studies has assisted in identifying suitable data sets for CFD model validation. The theoretical studies are also reviewed to identify suitable CFD modelling approaches to model flows in automotive injectors.

Chapter 3: In this chapter, theoretical models are described which are used for modelling internal flow in fuel injectors in the study.

Chapter 4: In this chapter, ‘Single-phase simulations in an enlarged multi-hole injector’ simulation results at non-cavitating operating conditions in an enlarged mini-sac type multihole(6) injector are presented. Results include assessment of boundary conditions errors, numerical errors and physical modelling errors which include assessment of some two-equation turbulence models and near wall modelling approaches.

Chapter 5: In this chapter ‘Cavitation simulation in a single-hole injector’, results of cavitation simulations in a single-hole injector are presented. Turbulence and cavitation modelling approaches in single-hole injectors are evaluated and presented. Cavitation models are quantitatively evaluated.

Chapter 6: In this chapter, ‘Cavitation simulations in an enlarged multi-hole Injector’ the results of cavitation simulations in an ‘multi-hole’ injector are presented. The identified most suitable approaches for turbulence modelling, and cavitation modelling from chapters four and five are used. Results of the simulations with biodiesel fuel properties are also presented.

Chapter 7: Conclusions of the present study and recommendation for future works are presented.

Chapter 2

Literature Review

2.1 Introduction

In this chapter, to gain the thorough understanding of the internal flow of fuel injectors, several experimental and theoretical studies are analysed. At the end of the chapter, a summary of the review is provided in which the areas that need to be further investigated are identified.

2.2 Experimental fluid dynamics

2.2.1 Single-hole injectors

Bergwerk (1959) performed experimental investigations on transparent injector holes of 0.2 to 2.5 mm diameter using refractive index matching technique. During the experimental studies, the fluid was sprayed directly into the atmosphere. Many important observations were made including the formation of cavitation at the sharp entrance of the injector hole and occasion occurrence of 'hydraulic flip'[1] (Figure 2.1 (b)). However, it was noticed that hydraulic flip could only be formed in axisymmetrical injector holes. The influence of cavitation on the discharge coefficient was also investigated, it was observed that discharge coefficient decreased with an increase of cavitation number and is more sensitive to change in cavitation number than Reynolds number in turbulent flow regime.

Influence of cavitation, Reynolds number and cavitation number on discharge coefficient[2] has also been investigated by Spikes and Pennington (1959). The experiments were performed using

---

[1] In single hole injectors when cavitation annularly occupies the entire nozzle length and reaches the nozzle outlet, air or gas from downstream with having higher local pressure than the cavitation vapour enters the nozzle from its outlet and replaces the volume occupied by the cavitation. This leads to complete detachment of liquid from the wall forming a smooth glass-like jet. This phenomenon is called 'hydraulic flip' (Soteriou et al., 1995).

[2] Discharge coefficient is used to measure losses in nozzles. It is ratio of actual discharge to theoretical discharge or ratio of mass flow rate at exit to that of an ideal nozzle.

$$C_d = \frac{\dot{m}_{actual}}{\dot{m}_{Bernoulli}} = \frac{\dot{m}}{A\sqrt{2\rho\Delta p}} \tag{2.1}$$

where $\dot{m}$ is mass flow rate of fluid through constriction (unit mass of fluid per unit time), A is cross sectional area, ρ is density of fluid, Δp is pressure drop across constriction.

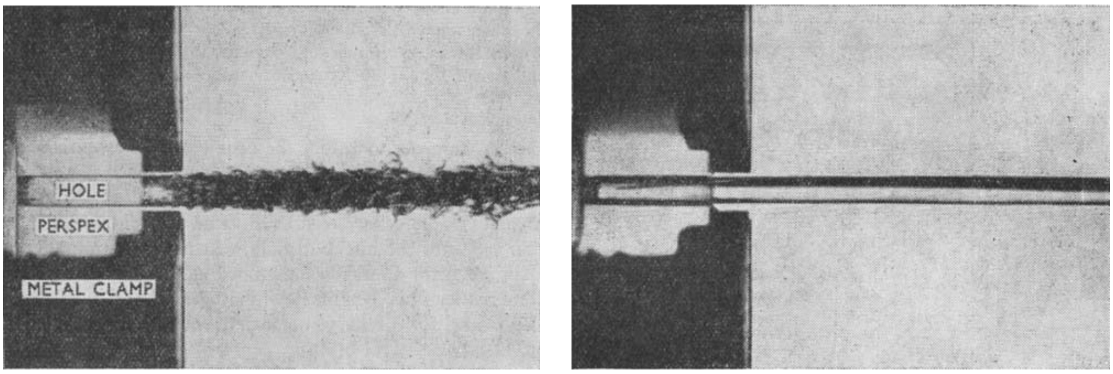

(a) (b)

Figure 2.1: Occurence of the hydraulic flip. (a) Spray like jet at inlet pressure 15 lb/in^2 emerging from the orifice when the nozzle is cavitating. (b) Emergence of a glass-like jet as cavitation reaches the nozzle exit and air downstream with pressure higher than the fuel vapour pressure occupies the volume previously occupied by cavitation at higher CN (at inlet pressure above 15 lb/in^2).

submerged orifices (square-edged and chamfered). While performing experiments on square-edged orifice, it was observed that change in cavitation number resulted in an increase in discharge coefficient; however, Reynolds number effects were marginal. Tests on chamfered orifice were performed to determine the optimum angle and depth of chamfer to maintain a constant discharge coefficient over the greatest possible range of operating conditions. Experiment results suggested the optimum nozzle which has a chamfer angle of 50° and diameter at the entrance of $1/\sqrt{0.61}$ times the orifice diameter. Nonetheless, Reynold number effects were evident. An increase in the discharge coefficient was observed with an increase in Reynolds number up to $Re = 40,000$ after which discharge coefficient did not significantly increase.

Experimental studies on square-edged orifices were performed by Nurick (1976). The fluid was injected into a gas chamber with a fixed outlet pressure. The occurrence of cavitation was observed at the entrance of the orifice. At the cavitating conditions, the jet had a 'ruffled' appearance (similar to Fig 2.1 (a)). With increasing the cavitation number, the cavitation region lengthened to almost four orifice diameter before it reached the exit leading to the emergence of 'hydraulic flip' and disappearance of cavitation.

Arcoumanis et al. (1992) performed Laser Doppler Velocimetry (LDV) at different positions of single hole enlarged diesel nozzle at $Re = 18800$ to obtain mean and fluctuating velocity profile. The LDV measurements for mean velocity indicated strong recirculation region at the entrance of the injector nozzle. Greater values of RMS velocity were also measured at the recirculation region.

Chaves et al. (1995) studied internal flow of real size (0.2 mm in diameter and 1 mm in length) single hole diesel nozzle with considerably high injection pressure (100 $MPa \approx 1000$ bar) on steady-state test rig. Modified laser-two-focus-velocimeter was used for discharge measurement and measurement of flow velocity in the nozzle hole. The occurrence of cavitation was observed at the entrance of the nozzle. The cavitation was seen reaching the nozzle exit with an increase of injection pressure. At this condition, the discharge coefficient and the spray angle were steady and were not affected by a further increase in injection pressure.

Experimental investigations of cavitation in single hole square-edged orifices have also been performed by Soteriou et al. (1995). In first series of experiments, the injector was submerged in the oil reservoir. The onset of cavitation occurred at the entrance of the injector. With an increase in the cavitation number, the cavitation was observed spreading throughout the length of the injector hole, after which cavitation occupied the entire cross-sectional area and the orifice was choked. At this condition, any further decrease in the downstream pressure does not cause a change in the mass flow rate, provided the upstream pressure is fixed. Choking occurs in bubbly flows because in bubbly flows even a small proportion of gas/vapour reduce sonic speed in liquid-vapour mixture substantially, in many cases even lower than mixture constituents (liquid and gas) and therefore, the bubbly flow becomes locally supersonic. Hence, at the position where the cavitation structure ends due to higher local pressure, the fluid reattains the sonic speed of liquid, and the mean flow becomes subsonic, producing a shock. Due to this shock, no signal is propagated upstream from the downstream, causing the orifice to choke. In the same set of experiments, the influence of cavitation on the coefficient of discharge was also investigated which also suggested that at a low value of cavitation number, the coefficient of discharge remained constant. The coefficient of discharge decreased with an increase of the cavitation number unless a choked flow condition occurs at which coefficient of discharge becomes constant.

In the second series of experiments (Soteriou et al., 1995), the fluid was injected into a gas container. During the investigation, a ruffling jet was first observed at the cavitation onset. The cavitation region and spray cone angle increased with an increase of cavitation number until the cavitation reached the hole exit. A further increase of cavitation number the cavitation disappeared and the flow emerged as a smooth column of liquid of a smaller diameter than the injector nozzle or, in other terms, 'hydraulic flip' occurred as previously observed by Bergwerk (1959) and Nurick (1976). The 'hydraulic flip' in single-hole injector was referred by Soteriou et al. (1995) as 'Total hydraulic flip' or 'THF' because the liquid column was almost symmetric about the orifice axis. At 'THF' a further increase in the cavitation number did not produce any change in the appearance of the jet. Likewise, in the case of submerged orifice the coefficient of discharge decreased with an increase in cavitation number, however, after achieving a certain value (0.56) where the THF occurred, the coefficient of discharge did not decrease with the increase of the cavitation number.

Winklhofer et al. (2001) used a 2D model nozzle (Figure 2.2) to perform the investigative study of cavitation occurring in the injector and its influence on the mass flow rate. In the experiment the exit of the nozzle was connected to the fluid circuit. The outlet pressure was varied in order to obtain desired cavitation numbers. The start of cavitation was observed at 60 bar pressure drop (Figure 2.3 (a)). The incipient cavitation regimes were seen just at the downstream of flow separation of the nozzle entrance. With an increase of the pressure, full cavitation regime was obtained (Figure 2.3 (b)) after which choked flow was observed (Figure 2.3 (c)). Their velocity measurement showed that presence of the cavitation in the throttle entrance allows considerably high flow velocities at the liquid – gas interface. Nonetheless, the throttle geometry had imperfections (Figure 2.2) leading to more cavitation than the ideal condition.

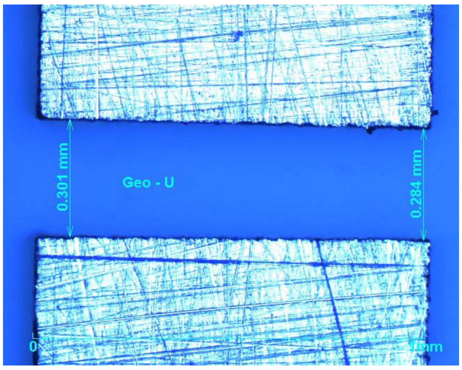

Figure 2.2: Throttle geometry ”U” in 300 μm thick sheet steel. 301 μm inlet width, 284 μm outlet width, 20 μm inlet radius, 1 mm throttle hole length. Source: Winklhofer et al. (2001)

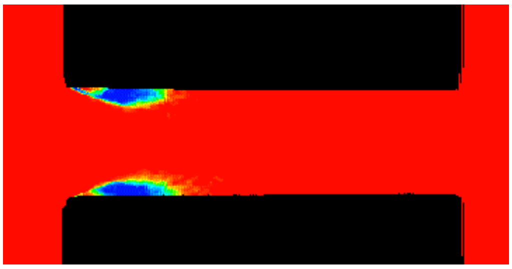

(a) Inception cavitation, $\Delta p \approx 60 bar$

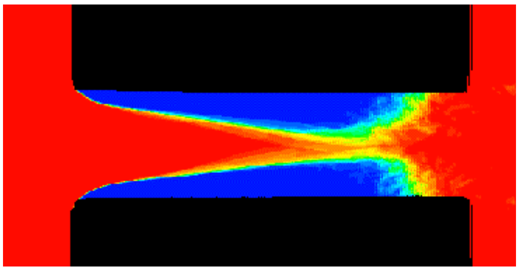

(b) Full cavitation, $\Delta p \approx 70 bar$

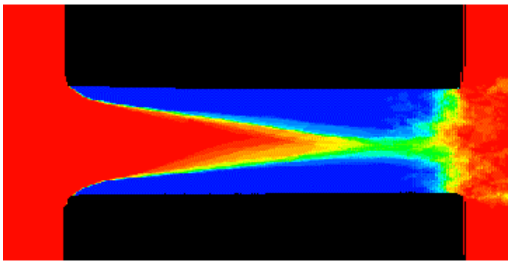

(c) Choked flow. $\Delta p \approx 77 bar$

Figure 2.3: Cavitation distribution in 2D nozzle, nozzle inlet diameter 0.301 mm, nozzle outlet diameter 0.284 mm. The blue colour represent pure vapour state, the red colour represent the pure liquid state. Source: Winklhofer et al. (2001)

Desantes et al. (2009) performed experiments on single-hole real size axisymmetrical injector in order to investigate the influence of cavitation on the emerging spray. Two series of experiments were performed. In the first series the fuel was sprayed into a pressurised chamber filled with diesel fuel. In the second series the fuel was sprayed into a nitrogen-pressurized chamber. The near nozzle spray was visualised using high-speed imaging and backlight illumination. The experimental results revealed an increment in the spray cone angle with an increase in cavitation for both cases.

Bauer et al. (2012) used the X-ray computer tomography to measure vapour volume fraction in an enlarged single-hole nozzle. The nozzle design and flow rate enabled quasi-steady flow. The computer tomography image were taken at close to the entrance of the nozzle, it showed that cavitation is concentrated at the annulus suggesting the production of cavitation vapour at the sharp entrance of the injector hole. The computer tomography images showed that concentration of vapour at the annulus increased as flow travelled downstream to almost one-third of the length of an injector. The results also showed additional cavitation at the centre of the liquid core near the nozzle exit (Figure 2.4) for which it was suggested that possible isolated nucleation events at the core of the liquid at almost half of the nozzle length. The possible isolated nucleation events were thought to be due to the possible swirl motion causing the local pressure at the liquid core to decrease below its vapour pressure.

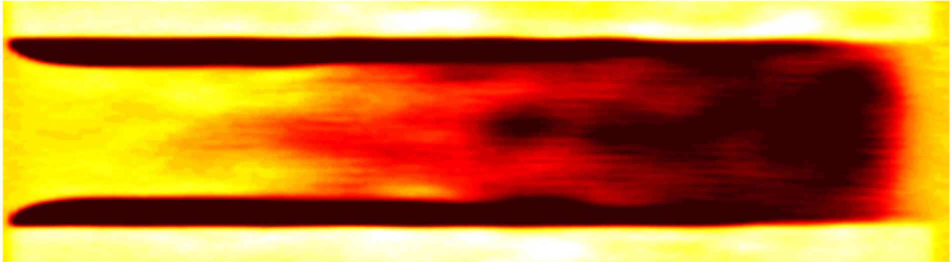

Figure 2.4: Cross section through the x–z-plane for $CN = 1.5$ showing an additional cavitation zone in the centre of the liquid core, source: Bauer et al. (2012)

The X-ray radiography measurement performed on single hole nozzle by Duke et al. (2013a) which enabled them to obtain qualitative and quantitative data of cavitation. Qualitative results indicate that (Figure 2.5 (a) and (c)) vapour is generated at the sharp entrance of the nozzle orifice, as flow travels downstream vapour travels along the wall, shortly thereafter vapour separates from the walls and mixes with the fluid at the centre line as it travels further downstream. However, this is in contrast with same research group's next experiment (Duke et al., 2014) in which it was observed that cavitation remained close to the wall as fluid travelled downstream. Except, the length of the nozzle of the orifice in the following experiment was 3.05 mm compare to 2.5 mm for the present case. It was inferred that vapour along the centre line is due to the detachment of vapour from the wall and its transport to the liquid core due to the radially inward negative pressure gradients. Non-uniform distribution of vapour was attributed to machining defects (Figure 2.5 (a) and (c)). The quantitative results showed the highest concentration of vapour near the injector entrance to one-third of its length indicating that most phase change occurred due to the lower local pressure at the entrance of the nozzle orifice.

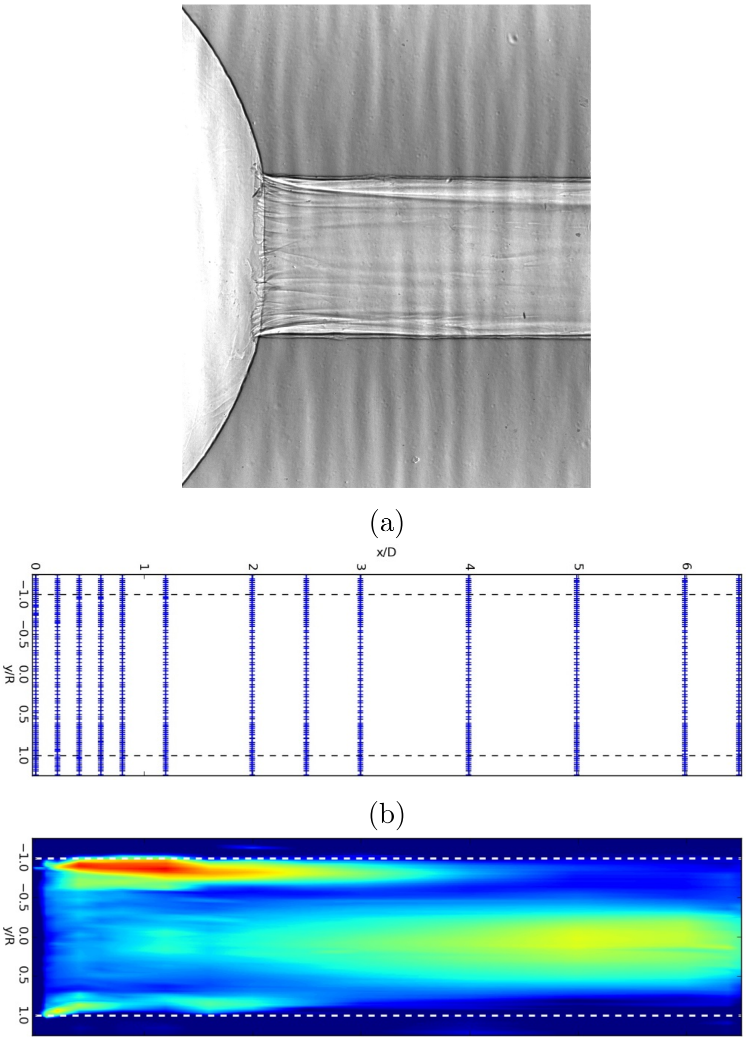

(a)

(b)

(c)

Figure 2.5: (a) Time-integrated X-ray images of nozzle inlet, taken with an unfocused X-ray monochromatic X-ray beam at $CN = 11.2$, (b) Raster-scan grid, (c) Interpolated contour plots of time-averaged vapour projection for $CN = 11.2$. Source: Duke et al. (2013a)

2.2.2 Multi-hole injectors

Soteriou et al. (1995) also performed experimental investigation on enlarged and real size sac type and VCO (valve covered orifice) type multi-hole injectors. In sac type nozzles, the flow characteristics were similar in real size and enlarged injectors. At cavitation onset, the cavitation bubbles appeared on the upper edge of the injector hole entrance. With an increase of cavitation number the cavitation foam was seen spreading down and across filling the hole. At the cavitation onset, the jet from each hole diverged and atomised immediately after the exit. An increase in spray angle was observed with an increase of the cavitation number. With further increase in the cavitation number, the cavitation was extended across and down to the of the hole, the flow comprised of an opaque white foam. At this point, the hole was choked and the further increase of cavitation number did not alter the spray angle. Results in VCO type injectors showed similar flow and spray characteristics in real size and enlarged VCO type injectors. However, in the real size nozzles at needle lift around 0.05 mm, the partial hydraulic flip was observed. Unlike total hydraulic flip (THF) in a single-hole injector, in partial hydraulic flip the cavitation occupies only the upper part of the injector hole due to the injector geometry so when the cavitation reaches the injector hole exit, the gas downstream of the chamber is drawn up to the side of the orifice into a region of recirculation due to the local pressure being lower than the downstream pressure. This leads to the disappearance of cavitation at the upper portion of the injector hole and the formation of asymmetric spray.

Arcoumanis et al. (1998) used Laser Doppler Velocimetry (LDV) and high-speed imaging in a mini-sac type enlarged (20 times) vertical multi-hole diesel injector nozzle at the nominal lift and lower lift. LDV results revealed the presence of recirculation region at the upper edge of the entrance of injector holes. Higher values of RMS velocity were measured at the lower needle lift than at higher needle lift. High-speed video results showed higher cavitation number for the onset of cavitation at the lower needle lift.

Afzal et al. (1999) performed the experimental investigations on enlarged mini-sac and VCO type injectors. High-speed imaging was used to visualise cavitation. A similar formation of geometrical cavitation was observed in both type of injectors, however, the cavitation structures in the VCO injector type injector were slightly different. In the VCO type injector at the nominal lift larger area was occupied by the vapour film and the cavitation structure never reached the steady state. While in the case of mini-sac type injector at the nominal needle lift, the area occupied by vapour was slightly smaller but achieved a stable film structure. The string type cavitation was also observed for both cases. The difference was attributed to enhanced flow turbulence in the VCO injector.

Arcoumanis et al. (2001) used high-speed video and still imaging method to investigate cavitation in real size and enlarged transparent mini-sac type multi-hole injectors. Using the still imaging different cavitation regimes of geometrically induced cavitation in the injector hole of enlarged multi-hole injector were identified. At the onset, a bubbly structure was observed (Figure 2.6 (a)). With the increase in the cavitation number, a pre-film stage occurred which consisted of dense bubble cloud (Figure 2.6 (b)). After a further increase of the cavitation number, a film stage occurred (Figure 2.6 (c)). In the enlarged injector string type, cavitation structures were also observed to form inside the sac volume which appeared to develop transiently and recurrently between the adjacent injector holes. Images were also taken from the bottom of the injector which showed string type cavitation structures (Figure 2.7 (a) and (b)). Two type of string cavitation structures were observed. The first type was seen in the volume between the needle, needle seat and two adjacent injector holes. This was later called as 'hole-to-hole' connecting vortex (see Figure 2.7 (a)). The second type was seen emerging from the needle wall facing the injector hole and then facing the injector hole. This type of string cavitation was later called ‘needle string’ or ‘string cavitation’ by Roth et al. (2002); Roth (2004) (see Figure Figure 2.7 (b)). As aforementioned experimental studies were also performed in the real size mini-sac type injector. In the real size injector, it was realised that higher cavitation number is required to initiate cavitation. Once cavitation forms, the sequence of cavitation regime were similar to the enlarged model. It was also observed that the cavitation does not scale with the hole size, therefore, a relatively larger vapour volume was observed.

Roth et al. (2002); Roth (2004) used high-speed video and still imaging process to visualise cavit-

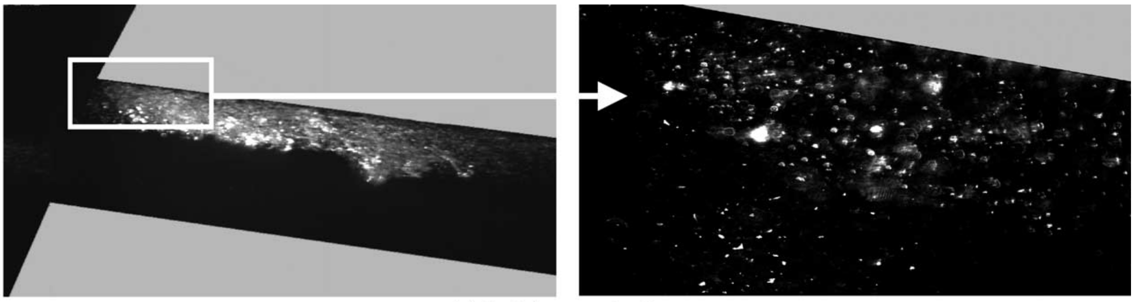

(a) Incipient cavitation

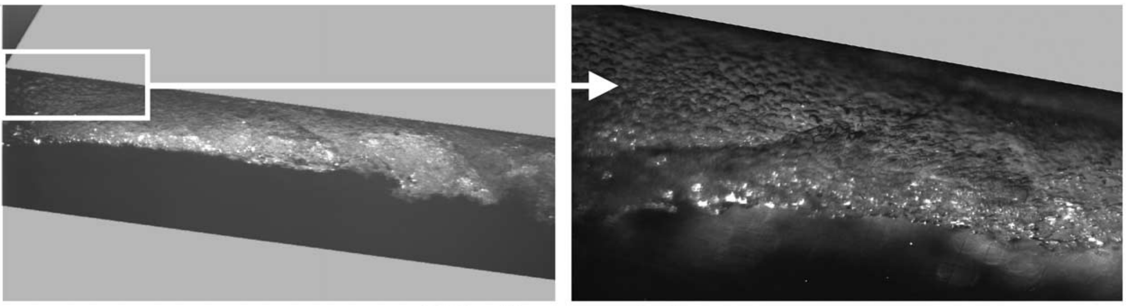

(b) Pre-film stage cavitation

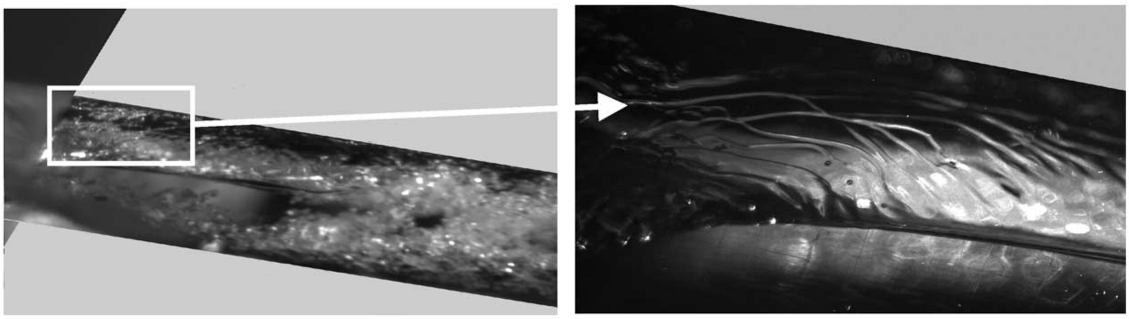

(c) Film stage cavitation

Figure 2.6: Cavitation regimes identified in large-scale sac-type hole nozzle. Source: Arcoumanis et al. (2001)

ation in mini-sac and VCO type multi-hole fuel injectors. Laser Doppler Velocimetry technique was also used to measure the mean axial velocity and RMS velocity at different axial locations in the injector hole. Results from still imaging of the enlarged mini-sac type injector hole showed the formation of different cavitation regimes at different cavitation numbers as previously observed by Arcoumanis et al. (2001). In addition to the geometric cavitation, string type cavitation structures were observed to form in the injector hole and well inside the sac volume. Two type of string type cavitation structures were observed: ‘Hole-to-hole’ connecting cavitation strings as previously observed by Arcoumanis et al. (2001) were seen at higher needle lift positions in both the min-sac and the VCO type nozzles and ‘needle strings’ which were observed originating from needle wall facing the injector hole and entering the injector hole. Needle strings were more frequently observed inside the VCO type injector than mini-sac type injector at low needle lift but were less frequently observed at higher needle lifts. Formation of ‘hole-to-hole’ connecting cavitation strings was attributed to vortex flow in the sac volume between the needle, needle seat and two adjacent holes. Formation of ‘needle strings’ was attributed to strong vortex flow around the hole axis, leading to low pressure region in the vortex core to initiate cavitation.

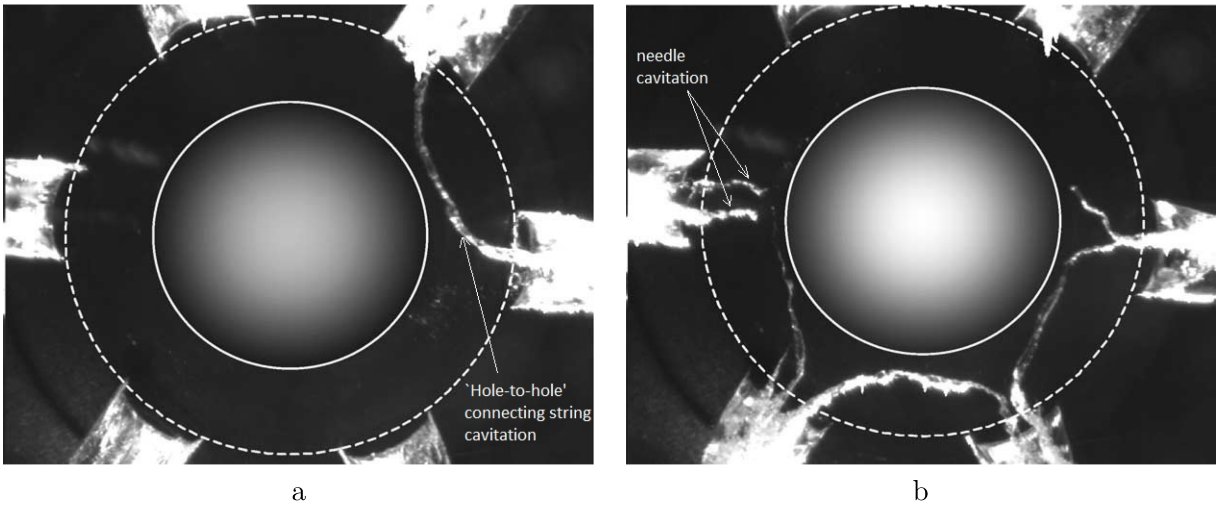

Figure 2.7: a) High-speed digital image showing 'hole-to-hole' connecting string cavitation. b) High-speed digital image showing 'needle string' or 'needle cavitation'. Source: Arcoumanis et al. (2001)

Two series of LDV experiments were performed (Roth et al., 2002; Roth, 2004). In the first series, the Reynolds number were kept constant while the cavitation number were varied. In the second series, both the Reynolds number and the cavitation number were varied. LDV results at non-cavitation conditions showed a recirculation region at the upper part of the entrance of the injector hole at both lower and nominal needle lifts in the mini-sac type injector. Higher values of RMS velocity were measured at the lower needle lift. LDV measurement could not be taken at the cavitation region because the cavitation vapour could distort the laser beam, hence, LDV measurements were taken only at the locations where cavitation was not occurring. LDV measurement at cavitating conditions showed an increase in the RMS velocity at the lower part of the injector hole with an increase in cavitation number. However, differences have been noticed by the author in LDV results of the mean axial velocity and RMS velocity between the first and second series of experiments at non-cavitating conditions (Roth, 2004, pg.175-178) which were not noticed by experimentalists (Roth et al., 2002; Roth, 2004).

Takenaka et al. (2005) used neutron radiography to investigate cavitation phenomenon in the metallic real size multi-hole diesel fuel injector. Results showed the presence of gas/vapour bubbles in the sac and the nozzle hole as well as in the recess between needle and nozzle wall (see Figure 2.8).

Gavaises et al. (2009) used high-speed digital imaging to visualise cavitation in an enlarged VCO injector at the fixed needle lift and flow rate conditions. To suppress the geometric cavitation, the injector holes were tapered and their sharp edges at the entrance were filleted. Observation showed that the filleted tapered holes suppressed the formation of geometric cavitation. Nonetheless, the string type cavitation was still observed at low lift. The string type cavitation was observed inside the injector holes and was observed linking successive injector holes. It was stated that cavitation strings in this particular geometry (VCO injector) appear in areas where large-scale vortices develop and arise either from preexisting geometric cavitation sites or could be from the trapped air at the downstream of the hole exit.

Mitroglou et al. (2011) examined the effects of the string cavitation on the near nozzle spray

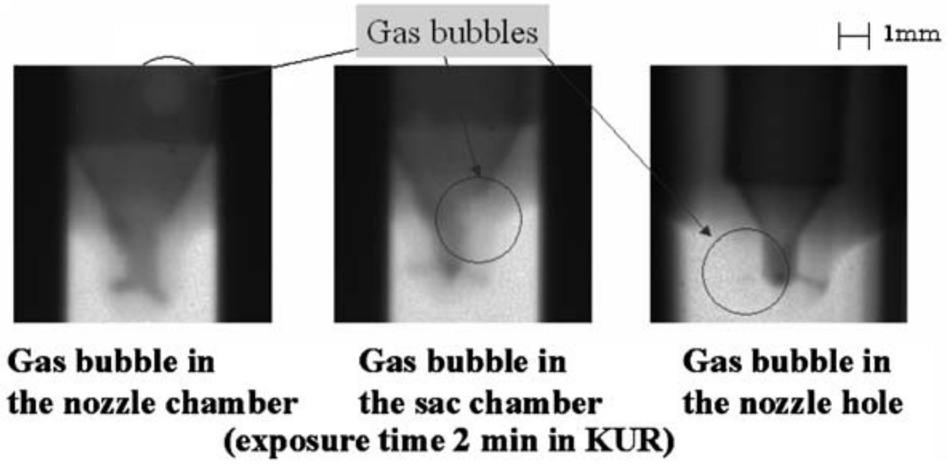
Gas bubbles
1mm
Gas bubble in the nozzle chamber
Gas bubble in the sac chamber
Gas bubble in the nozzle hole
(exposure time 2 min in KUR)

Figure 2.8: Gas/Vapour bubble captured using neutron radiography technique in the nozzle. Source: Takenaka et al. (2005)

angle. The investigated nozzle geometry was VCO (valve cover orifice). The scaling factor for the enlarged nozzles was 10. High-speed imaging technique was utilised to investigate flow characteristics in the large scale injector. During high-speed imaging of the enlarged VCO model at a low cavitation number $CN = 3$ and the Reynolds number around 12000 at low needle lift (0.02mm), occasional string type cavitation structures were observed which influenced the emerging spray. When no string was present, the observed spray angle was 18° - 20° while when the string was present, the observed spray angle was 50°. At a higher cavitation number $CN = 6.3$ and the Reynolds number 18000 the geometric cavitation regime became larger and occupied more of the cross-sectional area and extended inside the hole. However, spray angle was not much affected due to the intense interaction between geometric and string cavitation. Still, it was observed when the string cavitation lies on the part which is not occupied by geometric cavitation (bottom part of the injector hole), the increase in spray angle was pronounced. At the full needle lift (0.25 mm), an intense geometric induced cavitation was observed reaching the exit of the injector hole. So at this conditions, the string cavitation was affecting the lower boundary of the spray. But, the spray angle at the lower boundary was observed to be reduced by 50% than the lower lift case. For which it was mentioned that at the higher needle lift the upper part of the injector hole is strongly occupied by the geometric cavitation structure so influences of string cavitation were less pronounced. It was also stated that in the VCO type nozzles where even though the sac volume is absent, the clearance between the needle wall and the injector entrance promote the swirling motion at injector hole entry. This swirling motion gives rise to 'string cavitation' which interacts with the geometric cavitation.

Hayashi et al. (2012) used high-speed imaging and micro-PIV (particle image velocimetry) to visualise cavitation in a real size diesel multi-hole injector. Hayashi et al. also attempted to investigate a relation between cavitation in the injector and the subsequent spray. A transient analysis was performed. As the needle was lifted the cavitation initially appeared at the lower edge of the injector hole entrance. As gradually the needle was lifted cavitation appeared from the upper edge of the injector hole. The increment in spray angle with the needle lift was observed. Visualisation also showed a presence of the string cavitation in the sac volume which was also seen entering the injector hole and subsequently increasing the spray angle. Velocity vectors obtained from PIV showed vortices in the sac volume of the injector.

Mirshahi et al. (2013) performed experimental studies on 15x enlarged multi-hole (6) GDi injector. Tests were performed on a open loop test rig where the nozzle was spraying liquid (water) into the atmosphere. The occurrence of cavitation in the injector hole was recorded using CCD camera. The main observations were: a) Cavitation inception at a higher cavitation number at the lower needle lift. b) The decrease of spray cone angle and almost becoming constant with an increase of the cavitation number. c) An increase in spray cone angle with an increase in the needle lift. d) String cavitation affected the spray cone angle. Spray cone angle increased when needle string was present in the injector hole. When the cavitation string was observed tilted downward the spray cone axis also tilted downward. When the cavitation string was observed tilted upward the spray cone axis was also tilted upwards.Mirshahi et al. (2013) also observed two 'counter-rotating' string cavitation structures in the injector nozzle which were seen intermingling with each other as the flow traversed downstream. However, Mirshahi et al. (2013) could not locate the origin of such 'counter-rotating' string cavitation because the open loop test rig did not allow them to place the camera at the bottom of it.

2.2.3 Cavitation damage

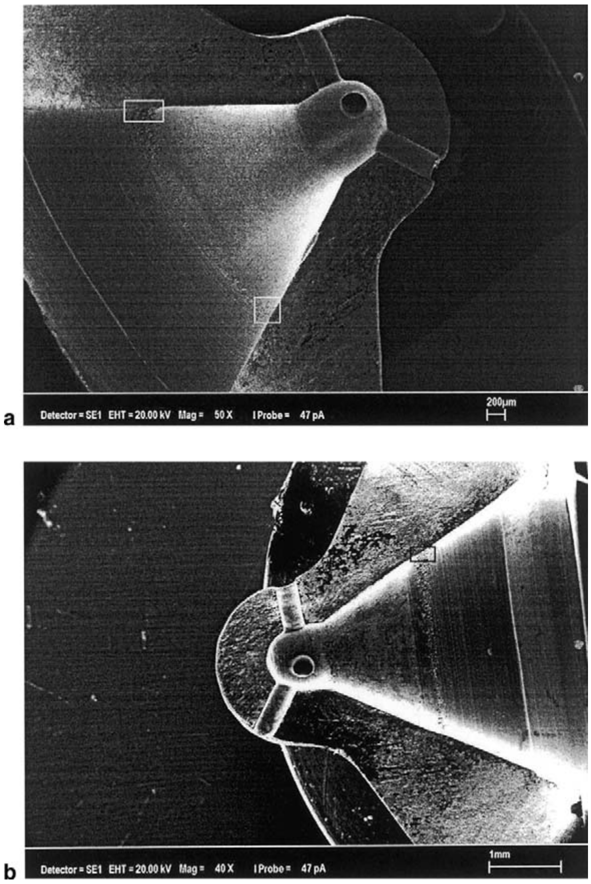
a
Detector = SE1 EHT = 20.00 kV Mag = 50 X I Probe = 47 pA
200µm
b
Detector = SE1 EHT = 20.00 kV Mag = 40 X I Probe = 47 pA
1mm

Figure 2.9: Identified cavitation damage sites (marked by square white rectangles in (a) and by black rectangles in (b)) by scanning electron microscopy. Source: Asi (2006)

Surface erosion of hydraulic equipment is attributed to cavitation bubble collapse. One of the dominant features of the cavitating bubble collapse is a re-entrant microjet, due to asymmetry i.e. presence of a nearby solid boundary. Such asymmetry causes one side of the bubble to accelerate more inward than opposite side and this results in the development of high-speed re-entrant jets, which penetrate the bubble. Additionally, highly accelerated bubble collapse causes localised shock wave. When the cavitation collapse occurs close to the solid surface, these intense disturbances cause highly localised and transient surface stresses, repetition of this causes local surface fatigue and subsequent detachment and flaking of material surfaces (Brennen, 1995).

Asi (2006) conducted failure investigation on the mini sac type diesel fuel injector used in a truck. Scanning electron microscope examination of the failed nozzle surface revealed roughness, microscopic craters, localised plastic deformation and pits in the surface damaged region in the vicinity of needle seat (see Figure 2.9). The damaged surface showed characteristic of cavitation damage. It was shown that cracks originated from the cavitation damage propagated subsurface as fatigue crack.

Gavaises et al. (2007) also examined cavitation erosion sites in diesel injectors. VCO and mini-sac type diesel multi-hole injectors were examined. In a VCO type nozzle with a nominal hole diameter of 0.2 mm, two sites of surface erosion were identified. The first one was found at the top part of the hole close to the entry. The second and third erosion sites were observed at the 3o' clock and 9o' clock positions (sidewise entrance) of the nozzle. In the mini sac type diesel injector nozzle with a nominal hole diameter of 0.3 mm, the cavitation sites were observed on the needle and inside the sac.

2.2.4 Biodiesel cavitation

Park et al. (2007) investigated the occurrence of cavitation and its influence on the emerging spray in an enlarged single-hole fuel injector for biodiesel and diesel fuel. The study showed that the onset of cavitation occurs at a higher cavitation number using biodiesel fuel than diesel fuel, which was supposedly affected by the larger viscosity and density of the biodiesel fuel. Park et al. (2007) also measured the droplet size of biodiesel and fossil diesel. Smaller droplet size was observed when fuel was cavitating. On comparison of the droplet size of diesel and biodiesel fuel, larger droplet size was recorded for the biodiesel fuel, which was attributed to its higher viscosity and surface tension of the biodiesel.

Suh et al. (2008) performed experiments on cylinder cross-section orifice (enlarged single hole nozzle) with diesel and biodiesel fuels. CCD camera was used to acquire high-resolution images of the diesel and biodiesel. Results showed the onset of cavitation using the biodiesel fuel would occur at higher cavitation number than the diesel fuel, possibly due to the higher viscosity and density of biodiesel fuel.

Nouri et al. (2012) performed experiments on two 15x enlarged model of multi-hole (6) axisymmetric GDi injector. Experiments were first performed with 100% water; later glycerine was added at different concentration ratio to increase the viscosity and the density of the fluid to mimic a bio-diesel blend. High-speed imaging was performed to visualise the cavitation. Delay of the onset of the cavitation was observed with an increase in a concentration of glycerine.

2.2.5 Experimental studies for non-ICE application

Constricted flow geometries are common in devices such as valves, flow controllers, pipes, heat exchangers, fuel supply of aircraft, cars and trucks. Cavitation is one of the problems in these internal flow devices as it affects their performances and also causes significant component surface damage due to the bubble collapse. Cavitation at the gas phase can behave like a compressible fluid and cause the flow to choke at the area of constriction. At this condition, such devices fail to reach their designed mass flow rates.

Davis (2008) analysed cavitating flow in a converging-diverging nozzle. They performed experiments using water and aviation fuels. The occurrence of cavitation in the nozzle was recorded using high-speed imaging. The pressure at the centre-line was also measured. At the full cavitating condition the nozzle was choked since flow rate at the outlet was constant even though the downstream pressure was varied since the upstream pressure was kept constant. Hence it was inferred that a supersonic condition was present at the nozzle throat. High-speed imaging results of water showed that the bubble formation initiated at the nozzle throat due to a lower local pressure. These bubbles grew rapidly and distorted into slug-like voids. However, further downstream, due to a higher local pressure, the bubble structure collapsed over a small region. This bubble collapse was referred as a bubbly shock and was stated that this exhibits many characteristics of shock waves of gas dynamics. The pressure curve of water at the nozzle centre-line showed a sharp increase in pressure just downstream of the cavitation region indicating a shock. Nonetheless, the bubbly shock was not so pronounced for aviation fuel cases which were attributed to multi-component compositions of such fuels.

2.3 Numerical modelling

2.3.1 Single bubble dynamics

Lord Rayleigh (1917) derived a relation for a time-varying spherical bubble radius R_B in an infinite body of liquid. The relation was derived from Navier-Stokes equation on the assumptions that bubble is spherical and has a homogeneous distribution of gas/vapour. The model assumes constant liquid density. The closure requires specifying the pressure at the bubble boundary $p_{(R_B)}$ and far-field pressure p_∞.

$$\frac{p_{(R_B)} - p_\infty}{\rho_l} = R_B \frac{d^2 R_B}{dt^2} + \frac{3}{2}\left(\frac{dR_B}{dt}\right)^2 \tag{2.2}$$

Plesset (1949) expanded the Rayleigh model and included the effect of surface tension S, viscosity μ_l and vapour pressure p_B of the liquid.

$$p_{(R_B)} = p_B - \frac{4\mu_l}{R_B}\frac{dR_B}{dt} - \frac{2S}{R_B} \tag{2.3}$$

By inserting the equation (2.3) in the equation (2.2), he obtained the following relation which is known to solve the time varying bubble radius $R_B(t)$ in the infinite body of the incompressible liquid.

$$\frac{p_B - p_\infty}{\rho_l} = R_B \frac{d^2 R_B}{dt^2} + \frac{3}{2}\left(\frac{dR_B}{dt}\right)^2 + \frac{4\nu_l}{R_B}\frac{dR_B}{dt} + \frac{2S}{\rho_l R_B} \tag{2.4}$$

Knapp et al. (1979) further expanded the Rayleigh Model model and assumed the gas in the spherical cavity to be ideal gas.

$$p_{(R_B)} = p_B - \frac{4\mu_l}{R_B}\frac{dR_B}{dt} - \frac{2S}{R_B} + \frac{NT_B}{R_B^3} \tag{2.5}$$

In the equation (2.5), N has been defined as a constant for fixed mass of gas, T_B has been defined as a gas temperature. They used the model for predicting cavitation inception. They suggested that the presence of dissolved gas would serve as an additional nucleation site and would enhance cavitation.

Moss (1997) modified the Rayleigh-Plesset equation; he assumed liquid to be compressible and the liquid body to be 25 times the bubble radius instead of infinite in Rayleigh-Plesset equation. He assessed his model by comparing with experiment measurement in which he measured the driving pressure. He found that his model performed better than Rayleigh-Plesset equation.

2.3.2 Cavitation Models

2.3.3 Rayleigh relation based cavitation models:

One of the popular approaches to model cavitation is to use Rayleigh relation. In this approach, first order solution of Rayleigh-Plesset equation (2.4) is used which governs the rate of evaporation (vapour production) and condensation. The surface tension and viscosity terms are neglected.

$$\dot{R_B} = \sqrt{\frac{|p_B - p_\infty|}{\rho_l}} \tag{2.6}$$

In many cavitation models, the far-field pressure p_∞ is taken as cell pressure p_{cell} and the bubble pressure p_B is taken as the vapour pressure p_v (Singhal et al., 2002).

Hence, for cavitation $p_v \geq p_{cell}$

$$\dot{R_B} = \sqrt{\frac{p_v - p_{cell}}{\rho_l}} \tag{2.7}$$

The same relation is used for modelling condensation, $p_{cell} \geq p_v$:

$$\dot{R_B} = \sqrt{\frac{p_{cell} - p_v}{\rho_l}} \tag{2.8}$$

In the cavitation model presented by Schnerr and Sauer (2001); Yuan et al. (2001), the bubble liquid flow is treated as a homogeneous vapour-liquid mixture, the vapour is assumed to be consists of mini spherical bubbles, and the vapour fraction is defined as:

$$\alpha_v = \frac{V_{vapour}}{V_{mixture}} = \frac{n_B V_l \cdot \frac{4}{3}\pi R_B^3}{V_v + V_l} = \frac{n_B V_l \cdot \frac{4}{3}\pi R_B^3}{n_B V_l \cdot \frac{4}{3}\pi R_B^3 + V_l} = \frac{n_B \cdot \frac{4}{3}\pi R_B^3}{n_B \cdot \frac{4}{3}\pi R_B^3 + 1} \tag{2.9}$$

where R_B is the radius of the bubble, n_B is defined as the bubble number density per unit volume of pure liquid. Using equation (2.9), the following expression can be derived for bubble radii:

$$R_B = \left(\frac{\alpha_v}{(1-\alpha_v)} \frac{3}{4\pi} \frac{1}{n_B}\right)^{\frac{1}{3}} \tag{2.10}$$

The following equation accounts for the transport of vapour fraction, α:

$$\frac{\partial \alpha_v \rho_v}{\partial t} + \nabla \cdot (\alpha \rho_v \overrightarrow{U}_{mixture}) = R \tag{2.11}$$

where R is net phase change rate. For the net phase change rate R, the model uses linear Rayleigh relationship for evaporation (2.7) and condensation (2.8). The following equations are used for phase change rate.

when $p_v \geq p_{cell}$, cavitation:

$$R_e = \frac{\rho_v \rho_l}{\rho_{mixture}} \alpha_v (1-\alpha_v) \frac{3}{R_B} \sqrt{\frac{2}{3} \frac{|p_v - p_{cell}|}{\rho_l}} \tag{2.12}$$

when $p_v \leq p_{cell}$, condensation:

$$R_c = -\frac{\rho_v \rho_l}{\rho_{mixture}} \alpha_v (1-\alpha_v) \frac{3}{R_B} \sqrt{\frac{2}{3} \frac{|p_v - p_{cell}|}{\rho_l}} \tag{2.13}$$

In this model, the net phase rate change in the equation is taken to be proportional to $\alpha(1-\alpha)$. It has an unusual property; it approaches zero when $\alpha = 0$ and $\alpha = 1$ and reaches the maximum reaches the maximum in between. The vapour fraction, α, per unit volume of the mixture is dependent on the bubble concentration per unit volume of liquid, n_B, is kept constant assuming constant nucleation site per volume (m^3) of pure liquid. The model was evaluated by Yuan et al. (2001) for a single-hole fuel injector. The bubble concentration per unit volume n_B of pure liquid was varied to match the experimental observations. Reasonable qualitative agreements with experimental observations was obtained at $n_B = 1.5 \times 10^{14}\ m^{-3}$.

The model was also used by Mohan et al. (2014) to simulate diesel and biodiesel flow in a single-hole injector. Initially, steady state simulations were performed using diesel fuel. The simulations were validated by comparing simulation results with the experimental results of Winklhofer et al. (2001) for the mass flow rate, pressure and velocity distribution. After which biodiesel flow was simulated. Comparison of prediction results of diesel and biodiesel showed that the cavitation phenomenon was more pronounced in the diesel case which is observed in many experimental studies (Park et al., 2007; Suh et al., 2008; Nouri et al., 2012)

Singhal et al. (2002) proposed a model based on a homogeneous equilibrium mixture approach. The fluid density $\rho_{mixture}$ is assumed to be a function of vapour mass fraction f, which is computed with continuity and momentum equation. The relation between $\rho_{mixture}$ and f is given by:

$$\frac{1}{\rho_{mixture}} = \frac{f}{\rho_v} + \frac{1-f}{\rho_l} \tag{2.14}$$

The vapour volume fraction is deduced from f as:

$$\alpha_v \equiv f\frac{\rho_{mixture}}{\rho_v} \tag{2.15}$$

or

$$\frac{V_v}{V_l + V_v} \equiv \frac{m_v}{m_l + m_v}\frac{\rho_{mixture}}{\rho_v} \tag{2.16}$$

Therefore, equation (2.14) can be written as:

$$1 = f\frac{\rho_{mixture}}{\rho_v} + (1-f)\frac{\rho_{mixture}}{\rho_l} \tag{2.17}$$

Hence

$$1 = \alpha_v + \alpha_l \tag{2.18}$$

The vapour mass fraction, f is governed by the following equation:

$$\frac{\partial}{\partial t}(\rho f) + \nabla \cdot (\rho \overrightarrow{U} f) = \nabla \cdot (\Gamma \nabla f) + R_e - R_c \tag{2.19}$$

where R_e and R_c denote vapour generation and condensation rates, Γ is the diffusion coefficient. The equation (2.19) allows both liquid and vapour phases to expand and compress if phases are assumed to be compressible. The vapour is assumed to be consisted of mini spherical bubbles and the vapour volume fraction is defined as:

$$\alpha_v = \frac{V_{vapour}}{V_{mixture}} = \frac{N_B \frac{4}{3}\pi R_B^3 \cdot V_{mixture}}{V_{mixture}} = N_B \frac{4}{3}\pi R_B^3 \tag{2.20}$$

where N_B is defined as the bubble concentration per unit volume of the liquid/vapour mixture.

The vapour production and destruction are determined by the following expressions: when $p_v \geq p_{cell}$, evaporation:

$$R_e = C_e \frac{\sqrt{k}}{\sigma} \rho_l \rho_v \left[\frac{2}{3} \frac{p_v - p_{cell}}{\rho_l} \right]^{\frac{1}{2}} (1 - f) \tag{2.21}$$

when $p_v \leq p_{cell}$, condensation:

$$R_e = C_e \frac{\sqrt{k}}{\sigma} \rho_l \rho_v \left[\frac{2}{3} \frac{p_{cell} - p_v}{\rho_l} \right]^{\frac{1}{2}} f \tag{2.22}$$

where C_e and C_v are two empirical constants. To include influence of turbulence, the phase change threshold has been changed to:

$$p_v = (p_{sat} + p'_{turb}/2) \tag{2.23}$$

where p'_{turb} is determined by:

$$p'_{turb} = 0.39 \rho k \tag{2.24}$$

$$\frac{1}{\rho_{mixture}} = \frac{f_v}{\rho_v} + \frac{f_g}{\rho_g} + \frac{1 - f_v - f_g}{\rho_l} \tag{2.25}$$

For non-condensable gas, density is calculated using ideal gas formulation, the volume fraction of non-condensable gas density ρ_g is modified as:

$$\alpha_g = f_g \frac{\rho}{\rho_g} \tag{2.26}$$

$$\alpha_l = 1 - \alpha_v - \alpha_g \tag{2.27}$$

Hence the final form of vapour production and condensation rate can be written as: when $p_v \geq p_{cell}$, evaporation:

$$R_e = C_e \frac{\sqrt{k}}{\sigma} \rho_l \rho_v \left[\frac{2}{3} \frac{p_v - p_{cell}}{\rho_l} \right]^{\frac{1}{2}} (1 - f_v - f_g) \tag{2.28}$$

when $p_v \leq p_{cell}$, condensation:

$$R_c = C_e \frac{\sqrt{k}}{\sigma} \rho_l \rho_v \left[\frac{2}{3} \frac{p_{cell} - p_v}{\rho_l} \right]^{\frac{1}{2}} f_v \tag{2.29}$$

In the model f_g is prescribed as a part of the model input. The most satisfactory values of C_e and C_c determined by authors (Singhal et al., 2002) were $C_e = 0.02$ and $C_c = 0.01$. The model was evaluated for the high-speed flow over hydrofoil and submerged cylindrical bodies, in both cases the prediction results were in good agreements with the experimental data. The model was also assessed for flow inside the square-edged orifice, the computed data compared well with the experimental data.

A cavitation model proposed by Zwart et al. (2004) is also based on the similar assumption (Schnerr and Sauer, 2001; Yuan et al., 2001; Singhal et al., 2002) the fluid is a homogeneous vapour-liquid mixture, the vapour is assumed to be consisted of mini spherical bubbles, the vapour volume fraction is defined as:

$$\alpha_v = \frac{V_{vapour}}{V_{mixture}} = \frac{N_B \frac{4}{3}\pi R_B^3 \cdot V_{mixture}}{V_{mixture}} = N_B \frac{4}{3}\pi R_B^3 \tag{2.30}$$

where N_B is the concentration of bubbles per unit volume of liquid/vapour mixture. The vapour fraction is governed by the following equation:

$$\frac{\partial \alpha_v \rho_v}{\partial t} + \nabla \cdot (\alpha_v \rho_v \overrightarrow{U}_{mixture}) = R \tag{2.31}$$

where R is the net phase change rate and is defined by the following equation:

$$R = N_B \times \left(4\pi R_B^2 \rho_v \frac{dR_B}{dt} \right) \tag{2.32}$$

The equation (2.32) is also used to model condensation process.

Therefore,
when $p_v \geq p_{cell}$, evaporation:

$$R_e = \frac{3\alpha_v \rho_v}{R_B} \sqrt{\frac{2}{3} \frac{p_v - p_{cell}}{\rho_l}} \tag{2.33}$$

when $p_v \leq p_{cell}$, condensation:

$$R_c = \frac{3\alpha_v \rho_v}{R_B} \sqrt{\frac{2}{3} \frac{p_{cell} - p_v}{\rho_l}} \tag{2.34}$$

The model is said to work well for condensation but was reported to be physically incorrect and numerically unstable for cavitation (Zwart et al., 2004). The model is based on the assumption that cavitation bubbles do not interact with each other, however, it was argued that this only occurs at the earliest stages of cavitation, when cavitation bubbles grow from nucleation site. Zwart, Gerber, and Belamri (2004) further argued that when vapour fraction increases, the nucleation site density must decrease accordingly. Hence, Zwart et al. (2004) replaced α with $\alpha_{nuc}\ (1-\alpha)$ for vaporisation. R_B is interpreted as the radius of a nucleation site. Hence, the final form of the cavitation model is:

if $P_{cell} \leq P_v$, evaporation:

$$R_e = F_{vap} \frac{3\alpha_{nuc}(1-\alpha_v)\rho_v}{R_B} \sqrt{\frac{2}{3} \frac{P_v - P_{cell}}{\rho_l}} \tag{2.35}$$

if $P_{cell} \geq P_v$, condensation:

$$R_c = F_{cond} \frac{3\alpha_v \rho_v}{R_B} \sqrt{\frac{2}{3} \frac{P_v - P_{cell}}{\rho_l}} \tag{2.36}$$

where

$$\begin{aligned} R_B &= \text{bubble radius} = 1 \times 10^{-6} \\ \alpha_{nuc} &= \text{nucleation site volume fraction} = 5 \times 10^{-4} \\ F_{vap} &= \text{evaporation co-efficient} = 50 \\ F_{cond} &= \text{condensation co-efficient} = 0.01 \end{aligned} \tag{2.37}$$

The model was evaluated for flow over a hydrofoil (Zwart et al., 2004). Reasonable quantitative agreements with experimental data were achieved.

The cavitation models presented by Schnerr and Sauer (2001); Yuan et al. (2001); Singhal et al. (2002); Zwart et al. (2004) allows parameters to be adjusted which account for liquid quality[3]. One of the parameters which account for liquid quality is the bubble nuclei concentration, a quantity that can be measured. (Billet, 1985). However, the in above-stated models, the bubble nuclei concentration is constant. Martynov (2005); Martynov et al. (2006) argued that the bubble nuclei concentration increases in the low-pressure region and the above stated models fail to reproduce this effect. Hence based on Yuan et al. (2001) cavitation model, Martynov (2005); Martynov et al. (2006) an algebraic cavitation model for the bubble nuclei concentration n_B that increases with the liquid tension:

$$n_B = n_* \left(\frac{p_v - p_{min}}{p_v} \right)^{\frac{3}{2}} \tag{2.38}$$

where n_* is the number density of cavitation sites when $p_{min} = 0$, p_{min} is the minimum absolute pressure in the cavitation region.

Alajbegovic (1999); Alajbegovic et al. (1999, 2002) presented an empirical approach for variation of bubble number density N_B per total volume of fluid with respect to variation in the vapour volume fraction α. The relationship is expressed by:

$$N_B = \begin{cases} N_{B0} \text{ for } \alpha \leq 0.5 \\ 2(N_{B0} - 1)(1 - \alpha) + 1 \text{ for } \alpha > 0.5 \end{cases} \tag{2.39}$$

The initial value of bubble number density N_{BO} was assumed to be 10^{12}. Equation (2.39) suggests that the bubble number density achieves the value of unity when α reaches unity. The model implementation uses a two-fluid (Eulerian-Eulerian multi-fluid) model in which mass, momentum, energy conservation and turbulence equations are solved for each phase. The mass transfer terms for liquid to vapour and vice versa is approximated using Rayleigh equation (2.6):

---

[3] The liquid quality effects are associated with the concentration of cavitation bubble nuclei in the liquid (Martynov, 2005)

$$R_e = \rho_{vap} N_B 4\pi R_B^2 \dot{R_B} = -R_c \tag{2.40}$$

R is the mean bubble radius. The bubble diameter is uniquely defined if the volume fraction α and bubble number density N_B is known:

$$R_B = \frac{1}{2}\left(\frac{6\alpha_v}{\pi N_B}\right)^{\frac{1}{3}} \tag{2.41}$$

The model was used to simulate the cavitation in high-pressure swirl injectors (Alajbegovic et al., 2002). The model has been implemented in the commercial code AVL FIRE.

2.3.4 Empirical and semi-empirical models

These cavitation models are based on empirical assumptions. In such models, the phase change depends on the difference between the local pressure and the vapour pressure of the liquid. These models contain many empirical parameters which are required to be adjusted for respective cases.

Merkle et al. (1998) proposed a semi-empirical model for cavitation. The model uses the following equation for vapour transport

$$\frac{\partial \alpha_v \rho_v}{\partial t} + \nabla \cdot (\alpha_v \rho_v \overrightarrow{U}_{mixture}) = R \tag{2.42}$$

In the transport equation (2.42), the phase transformation from liquid to vapour is modelled being proportional to the liquid volume fraction and the amount of which by which the local cell pressure is below the vapour pressure.

So when $p_v \geq p_{cell}$, evaporation:

$$R_e = \frac{C_{dest} \cdot \rho_l \alpha_l MIN[0, p_{cell} - p_v]}{\rho_v (0.5 \rho_l U_\infty^2) t_\infty} \tag{2.43}$$

where C_{dest} is a dimensionless empirical parameter and is required to be tuned according to individual cases to obtain the optimum solution, U_∞ is the free stream velocity (≈ velocity at inlet), t_∞ is the mean flow time scale and is defined as the ratio between the characteristic length (inlet diameter) to the relative velocity (inlet velocity) scale ($t_\infty = \frac{l}{U_\infty}$) and is dimensionless for both the production and destruction rates.and α_l is the liquid volume fraction:

$$\alpha_l = \frac{\text{total liquid volume}}{\text{total volume}} \tag{2.44}$$

Similar equation is used for the transformation of vapour to liquid R_c:

when $p_v \leq p_{cell}$, evaporation:

$$R_c = \frac{C_{prod} \cdot \rho_l \alpha_l MAX[0, p_{cell} - p_v]}{(0.5\rho_l U_\infty^2)t_\infty} \tag{2.45}$$

where C_{prod} is another empirical constant.

Kunz et al. (1999) proposed a cavitation model similar to that of Merkle et al. (1998). Unlike Merkle et al. (1998), two separate equations are used to model evaporation (cavitation) and condensation. For transformation of liquid to vapour, R_e is proportional to the liquid volume fraction and the amount of which the pressure is below the vapour pressure.

when $p_v \geq p_{cell}$, evaporation:

$$R_e = \frac{C_{dest} \cdot \rho_v \alpha_l MIN[0, p_{cell} - p_v]}{(\frac{1}{2}\rho_l U_\infty^2)t\ _\infty} \tag{2.46}$$

where C_{dest} is a dimensionless empirical constant, U_∞ is the free stream velocity, α_l is the liquid volume fraction:

$$\alpha_l = \frac{\text{total liquid volume}}{\text{total volume}} \tag{2.47}$$

The transformation of vapour to liquid R_c is modelled using the third order polynomial function of the vapour volume fraction α.

$$R_c = \frac{C_{prod} \cdot \rho_v (\alpha_l)^2 (1 - \alpha_l)}{t_\infty} \tag{2.48}$$

where C_{prod} is again a dimensionless empirical constant.

Kunz et al. (1999) evaluated their model for flow over axisymmetric submerged bodies. The empirical constants were $C_{dest} = 0.2$ and $C_{prod} = 0.2$. The model was evaluated for a similar geometry by Ha et al. (2009), the empirical constants were kept $C_{dest} = 1000$ and $C_{prod} = 10$ to obtain a correct flow field and reasonable agreement with the experimental data. Roohi et al. (2013) used the model to model flow around two-dimensional hydrofoil, the empirical constants were kept $C_{dest} = 2 \times 10^4$ and $C_{prod} = 1.0 \times 10^3$.

The model was further developed by Kunz et al. (2000). The fluid was assumed to be a mixture of pure liquid, vapour and non-condensable gas.

$$\rho_{mixture} = \rho_l \alpha_l + \rho_v \alpha_v + \rho_g \alpha_g \tag{2.49}$$

The vapour production terms remained the same as equation (2.46), but the condensation term was changed to:

$$R_c = \frac{C_{prod} \cdot \rho_v (\alpha_l - \alpha_g)^2 (1 - \alpha_l - \alpha_g)}{t_\infty} \tag{2.50}$$

The model was evaluated for flow over axisymmetric submerged bodies (Kunz et al., 2000). To obtain optimum agreements with the experimental data empirical constants were set to 100 for C_{dest} and 100 for C_{prod}.

2.3.5 Barotropic cavitation models

Barotropic models: In the barotropic assumption, the local variation of density is a function of the local change of pressure only. Hence, in models based on the barotropic assumption, if the local pressure is greater than the vapour pressure then the fluid is liquid, else vapour.

Schmidt et al. (1999) presented a two-dimension model that treats liquid and vapour as a continuum and was developed for predicting the small-scale high-speed cavitating nozzle flows. The model assumed fluid to be Eulerian compressible liquid–vapour mixture based on the homogeneous equilibrium model (HEM). The phase transfer from liquid to vapour is instant when the local fluid pressure goes lower than the vapour pressure threshold and vice-versa. For each phase, the change in local density was directly related to change in the local pressure and the square of sonic speed. The sonic speed in the liquid-vapour mixture was computed using the Wallis (1969) model. However, the model did not account for the turbulence effects and also did not consider liquid quality effects on cavitation.

Kärrholm et al. (2007) used a similar approach to Schmidt et al. (1999) in their cavitation model. But, their model can be used in three-dimensional geometries. Additionally, Kärrholm et al. (2007) model has three options to calculate speed of sound in liquid-vapour mixture which are linear model (see Kärrholm, 2008), Wallis (1969) model and Chung et al. (2004) model. The Kärrholm et al. (2007) model is implemented as cavitatingFoam in OpenFOAM CFD suite with turbulence models. Kärrholm et al. (2007) model also does not account for the liquid quality effects on the cavitating flow.

The model (Kärrholm et al., 2007) was used for modelling internal flow for the real size single hole nozzle (Kärrholm et al., 2007; Salvador et al., 2010) and multi-hole nozzle for diesel fuel (Salvador et al., 2010, 2011). The simulations result achieved reasonably good agreements with experimental data for mass flow rate, momentum flux and mean velocity. Salvador et al. (2011) also performed a comparative computational study of biodiesel and diesel fuel to investigate the influence of biodiesel fuel properties on cavitation. Results showed higher mass flow, momentum flux and lower exit velocity for biodiesel fuel. However, the model is reported to be diverging (Kärrholm et al., 2007; Kärrholm, 2008) when more realistic models (Wallis, 1969; Chung et al., 2004) were used to calculate the speed of sound in the liquid-vapour mixture, hence a simpler but inaccurate linear model was used (Kärrholm et al., 2007; Kärrholm, 2008; Salvador et al., 2010, 2011).

One of the drawbacks of the barotropic models which is self-acknowledged by its authors (Schmidt, Rutland, and Corradini, 1999) is an allowance of gradual density changes when gradual pressure gradient exists. Hence, they cannot be easily applied to the large-scale lower speed cavitating flows where there are very small pressure differences but quite steep density gradients (Giannadakis et al., 2008).

2.3.6 Eulerian-Langrangian models

The Eulerian-Lagrangian approach is one of the most comprehensive methods available for cavitation modelling. In the Eulerian-Lagrangian approach, the liquid is modelled as a continuous phase in the Eulerian frame, and cavitating bubbles are tracked in a Lagrangian fashion. In this subsection, we cover the Eulerian-Lagrangian approach.

One of the early models in this category was proposed Kubota et al. (1992). The model combines both macroscopic and microscopic views. In the macroscopic view, the fluid is considered as a mixture composed of two incompressible media, liquid and vapour. The two phases are treated as a continuum. The change in the local vapour volume fraction causes the density of the continuum to change from liquid to vapour and vice versa. In the microscopic view, the model treats cavity as a cloud of small bubbles of uniform size homogeneously distributed in the cavitating cell. In order to model bubble growth and collapse Rayleigh equation was modified for a cluster of bubbles in a sub-grid-scale. The bubble number density and initial bubble radii are assumed to be constant. The model was tested for the hydrofoil for the onset of cavitation: the computed results were in qualitative agreements with the experimental data. However, Kubota et al. (1992) stated that the model cannot be used for vapour film type cavitation because it requires different assumptions.

Giannadakis et al. (2004) presented a cavitation model based on Eulerian-Lagrangian approach. The model consisted continuous phase and dispersed phase equations. The continuous phase was described in the Eulerian frame of reference by conservation equations which also included the effects of dispersed phase volume fraction and momentum exchange terms between two phases. The dispersed phase model consists of many sub-models and incorporates many features which are assumed to take place in cavitating flow such as bubble formation through nucleation, momentum exchange between bubbly flows, bubble growth and collapse due to non-linear dynamics, bubble turbulent dispersion and bubble growth and collapse through the dynamic break up. The model also incorporated a novel approach accounting to bubble motion in Eulerian grids with a size comparable to that of the grid. The model was evaluated by authors for a single-hole diesel injector with 0% hydro grinding and 9.5% hydro grinding. The simulations results were in reasonable agreement for the case of the nozzle with zero hydro grinding. The model showed transient nature.

Gavaises and Giannadakis (2004) used Giannadakis et al. (2004) model to simulate cavitating flow in an enlarged mini-sac type multi-hole diesel injector. The simulation results were assessed by comparison with CCD images of Afzal et al. (1999) and LDV measurement for the mean axial velocity and RMS of Roth et al. (2002); Roth (2004). Qualitative comparison of the prediction results with CCD images suggested reasonable agreements. Due to the transient nature of the model, the mean axial velocity and RMS velocity at different time intervals were compared with the experimental data, the comparison showed that the predicted mean axial velocity and RMS velocity were in the same trend as those of the experiments.

Giannadakis et al. (2008) further implemented bubble break-up and coalescence submodels to their existing model (Giannadakis et al., 2004). The model was evaluated for four cases. 1) Single-hole injectors with 0% and 9% hydro grinding. 2) A large-scale single-hole nozzle used for CT measurements. 3) Enlarged multi-hole model with LDV measurement for the mean axial velocity and RMS. 4) Real-size multi-hole injector with optical access. The single-hole real size injector predictions were initially compared against CCD images of the single-hole injector of the same size and with the same profile (0 % and 9% hydro grinding). The predicted results showed visual similarities with CCD images however due to unavailability of quantitative data of vapour volume, the cavitation model could not be quantitatively assessed for the cavitation in this case. However, the CT measurements of the cavitation vapour allowed Giannadakis et al. (2008) to quantitatively assess their cavitation model. The model was quantitatively evaluated by comparing the predicted spatially averaged liquid volume fraction across cross-section along the injector hole with CT measurements. Comparisons showed reasonable quantitative agreements with experimental data at low CN. For high CN case discrepancies were realised near the exit of the injector hole. The reasons given for discrepancies were non-resolved fluctuations of the local pressure which was attributed to the turbulence model used (standard $k-\epsilon$).

The simulations in a multi-hole axisymmetric mini-sac type enlarged injector were performed at nominal (6.00 mm) needle lift at $CN = 0.45$, 1.08 and 1.49 and at lower (1.60 mm) needle lifts at $CN = 1.48$ and 2.39. The simulations were evaluated by the comparison of predicted mean axial velocity and vapour volume fraction with the experimental LDV and CCD results from Roth et al. (2002); Roth (2004) at different cavitation regimes (inception and full cavitation). Due to the aforementioned transient nature of the model, the mean axial velocity at different positions was averaged at different time instances and then was compared with the LDV results. The predicted mean axial velocity at nominal needle lift was reasonably consistent with the experimental data at all axial positions in the injector hole. However, at lower needle lift there were discrepancies in the shape of the predicted velocity axial profile with the experimental data at the axial locations in the middle and near the end of the injector hole. These discrepancies were attributed to possible needle eccentricity and to the turbulence modelling approach (RNG $k-\epsilon$ model) which was used. Similar to Giannadakis et al. (2007), two methods were again used to compute RMS velocities i.e. RMS velocities computed from turbulence models and from the standard deviations of mean axial velocity at each measured planes. Likewise, Giannadakis et al. (2007) higher magnitudes of RMS velocity were computed using turbulent model than from standard deviations of mean velocity and RMS velocity values obtained from turbulence model were again in better agreements with the experimental data. Reasonable qualitative agreements were achieved when the prediction results were compared with the CCD images for the both enlarged and real size multi-hole injector.

Papoulias (2013) also used Giannadakis et al. (2008) model to simulate cavitating flow in a enlarged multi-hole mini-sac injector at $CN = 1.07$ and at needle lift $= 4.0$ mm. Simulations were also performed using eulerian linear Rayleigh cavitation models (Schnerr and Sauer, 2001; Singhal et al., 2002; Zwart et al., 2004). The computational grid used contained approx 500,000 cells. The results were again assessed by comparing the mean axial velocity and RMS velocity with the LDV data of Roth (2004). In a Lagrangian model, a similar method was used to compute the mean velocity and the RMS velocity as Giannadakis et al. (2007), however the quantitative comparison did not show significant advantages of the Lagrangian model over the Eulerian models.

The cavitation modelling approach adopted by Giannadakis et al. (2004, 2008) is possibly one of the most detailed approaches and incorporates many features which are assumed to take place in cavitating flows. However, models have some disadvantages. The models assume both liquid and vapour phase to be incompressible. The incompressible assumption inhibits these models to describe the compressible flow dynamics in the two-phase region. In addition, these models contain many submodels which contain many parameters, as an example (Giannadakis et al. (2008) model contain 24 input parameters (see Papoulias, 2013, pg. 286)) that are required to be adjusted to obtain the optimum result.

2.3.7 Homogeneous Relaxation Model

The 'homogeneous relaxation model' (HRM) was originally developed for modelling flash boiling[4] by Schmidt et al. (2010) but was adapted for cavitating flows by (Neroorkar et al., 2012). In HRM version for cavitating flows, the phase transfer from liquid to vapour is governed by the pressure difference between local pressure and liquid vapour pressure. The model is based on the assumption that as the phase transfer is occurring in the cell volume from one phase to another, the fluid may not be in the thermodynamic equilibrium. Therefore, the instantaneous vapour mass fraction relaxes towards equilibrium conditions over the empirical time scale. The model has been implemented for cavitation in OpenFOAM as HRMFoam and has also been implemented for cavitation in the CFD suite CONVERGE. However, the model has been calibrated to operate at pressure over 1 Mpa or over 10 bars (Neroorkar et al., 2012). Hence, it cannot be used to model quasi-steady cases such as enlarged model test rigs which operate at much lesser inlet-outlet pressure ratios. The HRM also does not account for liquid quality effects.

2.4 CFD simulations

2.4.1 Single-phase simulations

Arcoumanis et al. (1998) performed single-phase simulations of non-cavitating flows in an enlarged multi-hole nozzle at full lift and nominal lift using in-house RANS code (Theodorakakos, 1997). They used standard $k - \epsilon$ model for turbulence. Due to manufacturing tolerances in the geometry, two sets of simulations were performed, one with geometry identical to a nominal geometric characteristic of fuel injector nozzle, other with geometry with actual hole diameter. The recirculation area at the entrance of the hole was not very well simulated. Nevertheless, the predictions from the second set of simulations were in better agreement with experimental result and were in better agreements with the experiment values of full needle lift than the nominal lift. The discrepancies between the computational and experimental results were attributed to a very coarse mesh (50052 cells) and the turbulence model.

Papoutsakis et al. (2009) performed a comparative study to assess the predictive capability of an LES model and RANS model for internal flow in the multi-hole nozzle at non-cavitating conditions and nominal needle lift (6.00 mm). The simulation results were compared with available LDV results (Roth et al., 2002; Roth, 2004). The standard $k-\epsilon$ model was used for the RANS simulations and Smagorinsky (1963) model was used for the LES simulations. The same computational grid was used for both the RANS and LES simulations. The grid contained 850,000 cells per 60° sector. The comparisons showed that similar results were obtained for the mean axial velocity and RMS velocity and both were in good agreements with the experimental data. No clear advantage of the LES model over RANS model was identified.

---

[4] In a flash boiling process, a phase change occurs in a high-temperature liquid that is depressurized below its vapour pressure. The elevation in vapour pressure makes liquid further susceptible to evaporate (Neroorkar, 2011).

Papoulias (2013) also performed single-phase simulations in an enlarged mini-sac type multi-hole injector at nominal needle lift = 4.00 mm. The simulations were assessed by comparing the predicted mean and RMS velocity with the LDV measurements (Roth et al., 2002; Roth, 2004). Simulations were performed using RANS and LES models. The RANS models used were standard $k-\epsilon$, RNG $k-\epsilon$, realizable $k-\epsilon$ and RSM (Reynolds Stress Model). For the LES simulations Smagorinsky (1963) model was used. The RANS grid comprised of approximate 500,000 computational cells and the LES grid comprised of approximate 1.5 million computational cells. Comparing with the experimental results showed reasonable agreements of the mean axial velocity were achieved using RSM, SST $k-\omega$ and RNG $k-\epsilon$ turbulence models. The mean axial velocity was underpredicted using standard $k-\epsilon$ and realizable $k-\epsilon$ models and was overestimated using LES for which he stated that the time step size and the cell size used were not balanced to accomplish the accuracy of LES.

2.4.2 Cavitation simulations

Battistoni et al. (2014) used two different modelling approaches to simulate cavitation conditions in a single-hole injector. The operating condition at $CN = 11.2$ and $Re = 1.58 \times 10^4$ and volumetric flow rate $\approx 26.8\ lh^{-1}$ or $0.008\ ls^{-1}$ on the steady state test rig (Duke et al., 2013a) was simulated. The first numerical approach used a homogeneous mixture model with the volume of fluid (VOF) method, in which the phase change is modelled via the homogeneous relaxation model (HRM) (Neroorkar et al., 2012). The second approach is based on the multifluid (Eulerian multiphase model) multi-phase model and used Rayleigh-Plesset bubble dynamics based cavitation model for predicting the cavitation (Battistoni et al., 2012). Both models included undissolved gas as additional phase apart from liquid and vapour. The compressibility of vapour was taken into consideration for which the ideal gas model was used. The standard $k-\epsilon$ model was used for turbulence. The results were evaluated by quantitatively comparing the predicted vapour volume fraction with the experimentally measured total volume fraction of vapour in slices across the nozzle. The results obtained using the multifluid model was in better agreement with experiment, the results obtained using homogeneous model over predicted the void fraction, however, mesh resolution was different for both cases. Both models predicted a shock just downstream of the cavitation region inside the nozzle. The location of the shock was slightly different in the two approaches.

2.4.3 Cavitation damage simulations

Gavaises et al. (2007) adapted the Eulerian-Lagrangian cavitation model (Giannadakis et al., 2004) for modelling cavitation and cavitation erosion. The model additionally calculated the acoustic pressure on the wall surface; the computed magnitude of the acoustic pressure on wall surfaces was correlated to the probable locations of cavitation erosion.

Koukouvinis et al. (2013) proposed a post-processing procedure utilising results of the flow field solution to correlate cavitation with cavitation erosion. The authors stated that the presented methodology would be valid in both Eulerian and Lagrangian framework. Erosion indexes were proposed and were based on the vapour volume fraction, pressure, the rate of bubble collapse and the acoustic pressure. It was stated that the predicted erosion areas on the surface were similar to those found in the experiments.

2.5 Summary

An extensive collection of literature has been reviewed in this chapter to provide an understanding of internal flow in the fuel injectors of IC engines. From experimental studies on single-hole nozzles, it has been learnt that cavitation originates at the sharp entrance of the injector hole where the local pressure goes lower than the vapour pressure threshold. However, confusion persists for the pattern of two-phase flows for the occurrence of void observed at the nozzle centre line; there are two opinions. The first one is that the voids seen around the nozzle centre line are due to isolated nucleation events (Bauer et al., 2012), the other opinion is that such voids are caused by the convection of the vapour from the nozzle wall to the centre line due to negative radially inward pressure gradients (Duke et al., 2013a). It has also been realised that local sonic speed in a bubbly flow becomes substantially low, on many occasions, it becomes even lower than mixture constituents, this can lead to the formation of shocks that can choke the orifice.

Since the multi-hole injectors are geometrically different from the single-hole injector; experimental studies on multi-hole injectors show that geometrically induced cavitation initiates at the upper edge of the entrance of the injector hole at most needle lift positions. However, at some cases (Mitroglou et al., 2011; Hayashi et al., 2012), it has been observed that cavitation originated at the lower edge of the entrance of the injector hole due to constricted flow passage. Additionally, in multi-hole injectors, the occurrence of cavitating vortex have been observed due to vortices in the injector.

From the literature review, it has also been realised that cavitation directly influences the emerging spray; experimental studies indicate that increase in the cavitation number causes an increase in spray angle and fuel atomization and hence evaporation in both single and multi-hole injectors. Experimental studies on axis-symmetrical single-hole injectors have also recorded occurrences hydraulic flip at high cavitation number. In multi-hole injectors, fluctuations in the spray angle have been observed due to vortex type cavitation.

Most of the experimental studies on cavitation in injector/nozzle do not provide quantitative information of cavitation vapour inside the injector hole. However, recent attempts have been made to quantify the cavitation vapour volume fraction using computer tomography (Bauer et al., 2012) and X-ray radiography (Duke et al., 2013a). Nevertheless, experimental methods are yet to be developed which can provide vital information such as flow field velocity, void fraction, together with local pressure and temperature in bubbly flows.

Nonetheless, good qualitative and quantitative information from the experimental studies provides a benchmark for assessment of CFD models. Data from experimental studies of Roth et al. (2002); Roth (2004) satisfy most of the requirements for multi-hole injectors except it does not provide quantitative information of cavitation in the injectors. Though, X-ray radiography measurements of vapour fraction by Duke et al. (2013a) can be used to assess cavitation models quantitatively.

There are four multi-phase approaches used for cavitation modelling by researchers: 1) The VOF model 2) Eulerian Mixture model 3) Eulerian-Eulerian or Eulerian multi-fluid model and 4) Eulerian-Lagrangian model. The VOF (Volume of Fluid) is a Eulerian interface tracking technique between two immiscible fluid in a fixed mesh. It is a single fluid approach and shares a single continuity, and momentum equations between phases and volume fraction of each of the fluids in each computational cell are tracked everywhere in the domain by using an additional transport equation of volume fraction. The main disadvantage of VOF method is it doesn't allow phases to be polydispersed and hence it is not suitable for cavitating flows. A Eulerian mixture model is a single-fluid approach; the fluid resembles a homogeneous mixture of n-phases. The model equation resembles for a pseudo-fluid with mixture properties and an equation of state which links the phases to obtain these mixture thermodynamic properties. The model also solves transport equation of volume fraction of phases to track them. The main advantage of the Eulerian Mixture model is it allows phases to be polydispersed as expected in cavitating flows. The model is also computationally cheap as it solves equations for a single-fluid. In the Eulerian-Eulerian or Eulerian multi-fluid approach, the mass, momentum and energy conservation equations are solved for each phase which makes this approach computationally more expensive than Eulerian-Mixture approach. The phases interact with each other using mass, momentum and energy exchange source terms which require modelling. The slip (relative velocity between phases) is allowed, and phases are allowed to be polydispersed. However, the literature review doesn't tell significant advantage over of Eulerian-multi-fluid approach over Eulerian-mixture approach. Also, the modified Eulerian-mixture model of Manninen et al. (1996) allows slip between the phases. Nevertheless, it is still not clear from the experimental data in the literature review about the relative velocity between phases in bubbly flows. The Eulerian-Lagrangian approach has also been used for the cavitation modelling. Its solves liquid phase in the Eulerian frame and the vapour phase to be in the Lagrangian frame. The Eulerian-Lagrangian model of Giannadakis et al. (2004) is the most detailed cavitation model as it considers many features which are assumed to take place in the cavitating flows. However, it requires many sub-models (which have their limitations) to mimic those characteristics and therefore, requires many empirical constants, which also makes such models very computationally expensive and time-consuming. Hence, in this study, mixture model would be used for cavitation simulations.

Several cavitation models have been reviewed: each has their strength and weaknesses. One of the popular cavitation approaches is barotropic. These models work with Eulerian-Mixture model. Both phases are assumed to be compressible; the phase transfer is instant and occurs when the local pressure goes lower than the vapour pressure threshold. One of the weaknesses of such models is the allowance of gradual density changes when gradual pressure gradient exist.Hence these models cannot be easily applicable to large-scale low-speed cavitating flows i.e. steady-state enlarged-model fuel injector test rigs where there are small pressure differences but steep density gradients (Giannadakis et al., 2008).

One of the popular approaches in cavitation modelling is linear Rayleigh or simplified Rayleigh. It has become an attractive choice due to simplicity in its numerical implementation. This method used the first order solution of Rayleigh equation which governs bubble growth and collapse. One of the weaknesses of this approach is that it shows the linear behaviour of bubble growth and collapse; however, comparisons have demonstrated that it gives results similar to full Rayleigh equation which shows parabolic bubble growth and collapse, at larger time steps and steady state assumptions in the Eulerian framework (Sauer, 2000; Martynov, 2005). The equation has been implemented in a similar way in most models; it is used in the cavitation and condensation rate terms. Most models do not include the diffusion term for which the principal argument is that diffusion rate is very low in the cavitation process (Martynov, 2005). Nevertheless, literature review suggests that these models have described cavitation flow with reasonable accuracy, therefore, in the present work, two linear Rayleigh based cavitation models, Schnerr and Sauer (2001) and Zwart et al. (2004) models would be used.

The Reynolds number in the test studies ranged from 15800 to 39500, and the flow regime is quasi-steady, and the present study requires some parametric studies. Hence, steady-state RANS approach appeared to be most desirable due to its ability to predict quasi-steady flow efficiently with sufficient accuracy. The main criticism of RANS is that turbulence eddies are not resolved but modelled (DNS resolves the complete turbulence spectrum, and LES can solve 80% of the turbulence energy (Pope, 2001)) which leads to the loss of many details. Also, RANS require turbulence models and as well as wall functions which add further empiricism to the solution. Nevertheless, this method is quite suitable for design and development which requires many parameters to be evaluated and hence requires numerous predictions. The literature review also indicates that RANS predicts similar flow regime that needs to be simulated as in this study with satisfactory accuracy.

As the bubbly flow behaves like a compressible fluid, in this study, the influence of compressible vapour assumption on cavitation would also be assessed. For this study, the chosen solver is ANSYS Fluent to simulate internal flow in single-hole and multi-hole injectors; the solver is widely used and has been validated for several cases. It also allows phases to be compressible in cavitating flow simulations.

Hence, this study would be comprised of:

1. Single phase simulation in multi-hole injector:
    (a) Grid sensitivity analysis in order to see the influence of the numbers of mesh on results at lower (1.6 mm) and nominal (6.0 mm) needle lift.
    (b) Check the influence of turbulence model, validate results by comparing it with experimental data. Select the best turbulence model in RANS category for cavitating flow analysis.

    (c) Flow field analysis and interpretation of physical results.

2. Cavitation simulations in single-hole injector
    (a) Grid sensitivity analysis
    (b) Turbulence model analysis, identify the most suitable turbulence model for the test case.
    (c) Cavitation model analysis
        i. comparative analysis of cavitation models
        ii. assessment of adjustable parameters which account for liquid quality on cavitation results.
        iii. assessment of liquid and vapour compressibility.
3. Cavitation simulations in multi-hole injector
    (a) Cavitation simulations in an enlarged multi-hole injector at both lower (1.6 mm) and nominal (6.0 mm) needle lift. Use the most suitable grid and best-behaved turbulence model from single-phase simulations. Furthermore, check the influence of grid density at the cavitating conditions. Use the identified most suitable cavitation model from single hole cavitation simulations.
    (b) Flow field analysis and interpretation of physical results at cavitating conditions.
    (c) After achieving quantitative and qualitative agreements with experimental data, the simulations would be performed with biodiesel fuel properties.

Chapter 3

Governing equations

3.1 Favre-averaged Navier-Stokes

Turbulent flow regime contains many eddies of different length scale and time scales. These eddies are responsible for enhancing the transport, including that of turbulent kinetic energy. The larger eddies contain most of the turbulent energy which cascades down to smaller and smaller eddies to Kolmogorov scale until dissipated to heat by viscous forces. The Navier-Stokes equations can describe the full-spectrum of turbulent flow from Large-eddies to up to Kolmogorov's scale (Tennekes and Lumley, 1972).

Direct Numerical Simulations can simulate the full spectrum of turbulent flow. However, it requires an enormous amount of computing power to resolve all scales, because the difference between the scales of flow geometry and the smallest turbulent scale which is Kolmogorov's scale is of many orders of magnitude. The computational domain must be significantly larger than the large scale L while the grid size must be of the order of Kolmogorov's scale η. Hence, the number of grid points required is proportional to $L/\eta \approx Re^{3/4}$, therefore, the number of grid points needed to perform a three-dimensional DNS scales like the 9/4 power of Reynolds number. The time scale of smallest eddies also governs time-step size in DNS. The ratio of the integral time scale of the flow to the Kolmogorov's time scale is proportional to $Re^{1/2}$, the number of time step required to advance the solution by fixed time has the same dependence as Re. If the CPU time required by a numerical algorithm is proportional to the total number of grid points, then the cost of calculation will depend on the product of the number of grid points by the number of time steps and hence would be of the order of $Re^{11/4} \approx Re^3$ (Piomelli, 1997, 1999; Pope, 2001). Hence, by increasing Reynolds number by the factor of 10 requires an increase of computing requirement by 1000 which makes DNS implausible for many practical applications.

Most of the computational effort in DNS is consumed on the smallest eddies while the energy and anisotropy are contained in the larger eddies. Therefore, to reduce computational cost, many techniques are developed. One of them is LES or Large Eddy Simulations. The large scale eddies are explicitly solved in LES whereas small scale eddies are modelled using sub-grid scale models (Pope, 2001), this greatly reduces the computational cost compared to DNS. The LES uses low-pass filtering process which decomposes the velocity into the sum of filtered (or resolved) and residual (or sub-grid scale) components. The filtered velocity field - which is three-dimensional and time dependent represents the motion of large eddies. The filter in LES is applied to the inertial region of the spectrum and hence the mesh resolution is nearly independent of the Reynolds number. However, the cost of LES depends on the Reynolds number if a solid object is present because in this case, the largest scales of motion are dependent on the Reynolds number. It was estimated by Chapman (1979) that the mesh resolution required to resolve the outer layer of the boundary layer is proportional to $Re^{0.4}$ while for the viscous sublayer, the resolution required is proportional to $Re^{1.8}$. Hence, LES can be extended to flows at Reynolds number at least an order of magnitude higher than DNS, its application for engineering flows remain expensive unless a wall model is used to resolve near wall turbulence but it introduces further empiricism (Piomelli, 1997, 1999). Nonetheless, LES still requires substantially finer meshes than ones used in RANS simulations. The accuracy of LES simulations also depends on the time step size since time step size is required to be smaller than the time scale of the smallest resolved scale of motion (Piomelli, 1997, 1999). The LES simulation has to run for a sufficiently long flow-time to obtain stable statistic of the flow being modelled, which also increases the computing requirement.

Therefore, time-averaging techniques are applied to Navier-Stokes equations to lessen computing cost and time. These are RANS (Reynolds-Averaged Navier-Stokes) for incompressible flow and FANS (Favre-Averaged Navier-Stokes or density-weighted RANS equations) for compressible flows. In these approaches, any instantaneous quantity is decomposed into ensemble average (mean) and fluctuating components and introduced into governing equations (Wilcox et al., 1998). The main advantage of RANS and FANS is that it allows for coarser mesh and larger time step than DNS and LES because turbulent scales no longer have to be resolved, which leads to the less expensive solution (Hanjalic, 2005). However, it leads to the loss of details of the flow since turbulent eddies are not resolved but modelled. A turbulence model must be used to approximate the unknown Reynolds stresses and other correlations; it introduces errors and limitations. Nonetheless, both RANS and FANS predict mean flow with decent accuracy in considerably smaller computing cost and time (Wilcox et al., 1998) which is the primary requirement for an engineer for product design and development and hence widely used in industry. In particular, for the flow field of this study, which is quasi-steady, Favre averaging assuming flow to be stationary is computationally very efficient and provides a good compromise with experimental measurements.

3.2 Mixture model

In the mixture model, one set of governing equations is used for mass, momentum, energy with the volume fraction equation for the secondary phases and turbulence closure model. One assumes that the velocity, temperature and pressure between the phases are equal in the mixture model. This assumption is based on the notion that the difference in these variable potentials will promote momentum, energy and mass transfer rapidly enough so that equilibrium is reached. The resulting equations would resemble of a pseudo-fluid with mixture properties and an equation of state which links the phases to obtain mixture thermodynamics properties (Brennen, 1995; Manninen et al., 1996; Corradini, 1997; Lagumbay et al., 2007).

The mixture density is calculated using:

$$\rho_m = \sum_{k=1}^{n} \alpha_k \rho_k \tag{3.1}$$

where, α_k is the volume fraction of the phase k.

In the present study, the multiphase system is comprised of two phases: liquid phase and vapour phase. Therefore, the mixture density is computed using the following equation.

$$\rho_m = \alpha_l \rho_l + \alpha_v \rho_v \tag{3.2}$$

Since,

$$\alpha_l + \alpha_v = 1 \tag{3.3}$$

Hence, the equation (3.2) becomes,

$$\rho_m = (1 - \alpha_v)\rho_l + \alpha_v \rho_v \tag{3.4}$$

Similarly, the mixture viscosity is defined using the following relation:

$$\mu_m = (1 - \alpha_v)\mu_l + \alpha_v \mu_v \tag{3.5}$$

The mixture specific enthalpy is defined using the following relationship.

$$s_m = (1 - \alpha_v)s_l + \alpha_v s_v \tag{3.6}$$

The thermal conductivity of the two-phase mixture is described by the following relationship.

$$\lambda_m = (1 - \alpha_v)\lambda_l + \alpha_v \lambda_v \tag{3.7}$$

3.3 Conservations equations

3.3.1 Continuity equation:

The conservation of mass in an infinitesimal single-fluid element can be expressed using the following equation

$$\frac{\partial \rho}{\partial t} + \frac{\partial}{\partial x_i}(\rho u_i) = 0 \tag{3.8}$$

where ρ is the density of the fluid, however, when the mixture model is used, $\rho = \rho_m$ as described in the equation (3.2) and u_i is the fluid velocity in i^{th} direction.

3.3.2 Momentum equation:

The conservation of momentum in an infinitesimal single-fluid element can be expressed using the following equation

$$\frac{\partial}{\partial t}(\rho u_i) + \frac{\partial}{\partial x_j}(\rho u_j u_i) = -\frac{\partial p}{\partial x_i} + \frac{\partial t_{ij}}{\partial x_j} + F_i \tag{3.9}$$

where t_{ij} is viscous stress tensor, the term F_i in equation (3.9) may contain body forces in the ith coordinate. For present application e.g. modelling of fluid flow inside the IC engine fuel injectors, the fluid is assumed to be Newtonian and therefore, the viscous stress is:

$$t_{ij} = 2\mu s_{ij} - \frac{2}{3}\mu \frac{\partial u_k}{\partial x_k}\delta_{ij} \tag{3.10}$$

where μ is the molecular viscosity of the fluid, but, when the mixture model is used, $\mu = \mu_m$ as described in the equation (3.5). The s_{ij} is the instantaneous strain rate tensor

$$s_{ij} = \frac{1}{2}\left(\frac{\partial u_i}{\partial x_j} + \frac{\partial u_j}{\partial x_i}\right) \tag{3.11}$$

3.3.3 Energy equation:

The conservation of energy in an infinitesimal fluid element can be expressed by the following equation using specific enthalpy (Poinsot and Veynante, 2005):

$$\frac{\partial}{\partial t}(\rho h_s) + \frac{\partial}{\partial x_j}(\rho u_j u_i) = \frac{Dp}{Dt} + \frac{\partial}{\partial x_i}\left(\lambda \frac{\partial T}{\partial x_i}\right) + t_{ij}\frac{\partial u_i}{\partial x_i} + S_E \tag{3.12}$$

When λ is the thermal conductivity of the fluid when the mixture model is used, the thermal conductivity is λ_m and is defined by the equation (3.7). S_E contains any other volumetric heat sources.

3.4 Favre-averaged equations

After applying Favre-averaging to the conservation equations, (see Poinsot and Veynante, 2005), the mean conservation equations are arrived and can be written as:

3.4.1 Favre-averaged continuity equation

$$\frac{\partial \overline{\rho}}{\partial t} + \frac{\partial}{\partial x_i}(\overline{\rho}\tilde{u}_i) = 0 \tag{3.13}$$

where $\overline{\rho}$ is the fluid density and when the mixture model is used, $\overline{\rho} = \overline{\rho_m} = \widetilde{\alpha_v}\overline{\rho_v} + (1 - \widetilde{\alpha_l})\overline{\rho_l}$, $\widetilde{u_i}$ is the Favre-averaged velocity.

3.4.2 Favre-averaged momentum equation

$$\frac{\partial}{\partial t}(\overline{\rho}\widetilde{u_i}) + \frac{\partial}{\partial x_j}(\overline{\rho}\widetilde{u_j}\widetilde{u_i}) = -\frac{\partial \overline{p}}{\partial x_i} + \frac{\partial}{\partial x_j}[\overline{t_{ij}} - \overline{\rho}\widetilde{u_j'' u_i''}] + F_i \tag{3.14}$$

3.4.3 Favre-averaged energy equation

$$\frac{\partial}{\partial x_i}(\overline{\rho}\widetilde{h_s}) + \frac{\partial}{\partial x_j}(\overline{\rho}\widetilde{h_s}\widetilde{u_i}) = \overline{\frac{Dp}{Dt}} + \frac{\partial}{\partial x_i}\left(\overline{\lambda_{eff}\frac{\partial T}{\partial x_j}} - \overline{\rho}\widetilde{u_j'' h_s''}\right) + \overline{\tau_{ij}\frac{\partial u_i}{\partial x_j}} \tag{3.15}$$

where

$$\overline{\frac{Dp}{Dt}} = \frac{\partial p}{\partial t} + \overline{u_i\frac{\partial p}{\partial x_i}} = \frac{\partial \overline{p}}{\partial t} + \widetilde{u_i}\frac{\partial \overline{p}}{\partial x_i} + \overline{u''\frac{\partial p}{\partial x_i}} \tag{3.16}$$

$\widetilde{h_s}$ is the specific enthalpy of the fluid when the mixture model is used, the specific enthalpy is described using

$$\widetilde{h_s} = \widetilde{\alpha_v}\widetilde{h_v} + (1 - \widetilde{\alpha_v})\widetilde{h_l} \tag{3.17}$$

The effective thermal conductivity λ_{eff} is defined by the following equation:

$$\lambda_{eff} = \lambda + \lambda_t \tag{3.18}$$

where λ is the thermal conductivity of the fluid, when the mixture model is used, λ becomes λ_m and is defined using the following equation

$$\lambda_m = \widetilde{\alpha_v}\lambda_v + (1 - \widetilde{\alpha_v})\lambda_l \tag{3.19}$$

where $\widetilde{\alpha_v}$ and $\widetilde{\alpha_l}$ are density weighted (Favre-averaged) volume fractions of vapour and liquid, λ_v and λ_l are thermal conductivities of vapour and liquid and λ_t is the turbulent thermal conductivity, defined according to the turbulent model used (Fluent, 2012). T is the local temperature.

3.5 Compressible flow closure approximations

For the second-order closure models, closure approximations must be proposed for the mass averaged Reynolds stress tensor and heat flux vector. Also, depending on the turbulence model used, additional closure approximations may be needed to close the system of equations defining the model. In this section, most commonly used correlations for compressible flows are briefly discussed.

3.5.1 Reynolds stress tensor:

Most of zero, one, and two equation models use the Boussinesq approximation with the suitable generalisation for compressible flows.

$$\tau_{ij} = \bar{\rho}\widetilde{u_i'' u_j''} = 2\mu_t \left(\frac{1}{2} \left(\frac{\partial \widetilde{u_i}}{\partial x_j} + \frac{\partial \widetilde{u_j}}{\partial x_i} \right) - \frac{1}{3} \frac{\partial \widetilde{}_k}{\partial x_k} \delta_{ij} \right) - \frac{2}{3} \rho k \delta_{ij} \tag{3.20}$$

where μ_t is the turbulent viscosity and is computed using turbulence model.

3.5.2 Turbulent heat flux vector

The turbulent heat flux vector $q_T = \bar{\rho}\widetilde{u''_j h''_s}$ is assumed to be proportional to the mean enthalpy equation.

$$q_T = \bar{\rho}\widetilde{u''_i h''_s} = -\frac{\mu_t}{Pr_t}\frac{\partial \widetilde{h}}{\partial x_j} \tag{3.21}$$

where Pr_t is the turbulent Prandtl number. A constant value of 0.9 is generally used for Pr_t (Wilcox et al., 1998).

3.5.3 Heat diffusion flux

The heat diffusion flux can be rewritten as:

$$\overline{\lambda_{eff}\frac{\partial T}{\partial x_i}} = \lambda_{eff}\frac{\partial \widetilde{T}}{\partial x_i} \tag{3.22}$$

3.5.4 Pressure-velocity correlation

The term $\overline{u''\partial p/\partial x_i}$, in equation (3.16) is simply neglected in most RANS codes (Poinsot and Veynante, 2005).

3.6 Cavitation models

The cavitation models which are used in this project are described in this section.

3.6.1 Schnerr and Sauer model

Schnerr and Sauer (SS) model: In the cavitation model proposed by Schnerr and Sauer (Schnerr and Sauer, 2001), the bubble liquid flow is treated as a homogeneous vapour-liquid mixture. The vapour is assumed to consist of mini spherical bubbles. The first order solution of

Rayleigh-Plesset equation or "linear Rayleigh" is used for vapour production and condensation. The vapour volume fraction is defined by the following equation:

$$\alpha_v = \frac{V_{vapour}}{V_{mixture}} = \frac{n_B V_l \cdot \frac{4}{3}\pi R_B^3}{V_v + V_l} = \frac{n_B V_l \cdot \frac{4}{3}\pi R_B^3}{n_B V_l \cdot \frac{4}{3}\pi R_B^3 + V_l} = \frac{n_B \cdot \frac{4}{3}\pi R_B^3}{n_B \cdot \frac{4}{3}\pi R_B^3 + 1} \tag{3.23}$$

where R_B is the radius of the bubble, n_B is defined as the bubble number density per unit volume of pure liquid. Using equation (3.23), the following expression can be derived for bubble radius:

$$R_B = \left(\frac{\alpha_v}{(1-\alpha_v)} \frac{3}{4\pi} \frac{1}{n_B} \right)^{\frac{1}{3}} \tag{3.24}$$

The transport equation of the vapour fraction is

$$\frac{\partial \alpha_v \rho_v}{\partial t} + \frac{\partial}{\partial x_i}(\alpha_v \rho_v u_j) = R \tag{3.25}$$

where R is the net phase change rate.

Using "linear Rayleigh" equation under which the vapour production and condensation depend on the square root of the difference between the far-field pressure and vapour pressure of the liquid. However, in the CFD codes, the local cell pressure is used instead of the far-field pressure. The model uses the following equations for phase change.

when $p_v \geq p_{cell}$, cavitation:

$$R_e = \frac{\rho_v \rho_l}{\rho_{mixture}} \alpha_v (1-\alpha_v) \frac{3}{R_B} \sqrt{\frac{2}{3} \frac{|p_v - p_{cell}|}{\rho_l}} \tag{3.26}$$

when $p_v \leq p_{cell}$, condensation:

$$R_c = -\frac{\rho_v \rho_l}{\rho_{mixture}} \alpha_v (1-\alpha_v) \frac{3}{R_B} \sqrt{\frac{2}{3} \frac{|p_v - p_{cell}|}{\rho_l}} \tag{3.27}$$

The net mass transfer rate, equation (3.26) in the existing model is proportional to $\alpha(1-\alpha)$, and has an interesting property, it approaches zero when $\alpha = 0$ and $\alpha = 1$ and reaches the maximum in between. The vapour volume fraction per unit volume of mixture α is dependent on the parameter n_B which is kept constant assuming constant nucleation site per unit volume m^3 of pure liquid.In the model the bubble concentration per unit volume of pure liquid, n_B often needs to be calibrated to match the experimental data (Yuan et al., 2001).

The transport equation of vapour fraction will take the following form.

When $p_v \geq p_{cell}$, cavitation:

$$\frac{\partial \alpha_v \rho_v}{\partial t} + \frac{\partial}{\partial x_i}(\alpha_v \rho_v u_j) = \frac{\rho_v \rho_l}{\rho_{mixture}} \alpha_v (1-\alpha_v) \frac{3}{R_B} \sqrt{\frac{2}{3} \frac{|p_v - p_{cell}|}{\rho_l}} \tag{3.28}$$

When $p_v \leq p_{cell}$, condensation:

$$\frac{\partial \alpha_v \rho_v}{\partial t} + \frac{\partial}{\partial x_i}(\alpha_v \rho_v u_j) = -\frac{\rho_v \rho_l}{\rho_{mixture}} \alpha_v (1 - \alpha_v) \frac{3}{R_B} \sqrt{\frac{2}{3} \frac{|p_v - p_{cell}|}{\rho_l}} \tag{3.29}$$

3.6.1.1 Favre-averaged transport equation of vapour fraction

Applying Favre-averaging to transport equations, we obtain the following form.

when $\overline{p_v} \geq \overline{p_{cell}}$, cavitation:

$$\frac{\partial}{\partial t}(\widetilde{\alpha_v}\overline{\rho_v}) + \frac{\partial}{\partial x_i}(\widetilde{\alpha_v}\overline{\rho_v}\tilde{u}_j) = \frac{\overline{\rho_v \rho_l}}{\overline{\rho_{mixture}}} \widetilde{\alpha_v}(1 - \widetilde{\alpha_v}) \frac{3}{R_B} \sqrt{\frac{2}{3} \frac{|\overline{p_v} - \overline{p_{cell}}|}{\overline{\rho_l}}} - \frac{\partial}{\partial x_i}(\overline{\rho}\widetilde{\alpha_v'' u_j''}) \tag{3.30}$$

For the closure of Reynolds flux term $\overline{\rho}\widetilde{\alpha_v'' u_j''}$, gradient transport assumption is employed (Pope, 2001)

$$-\overline{\rho}\widetilde{\alpha_v'' u_j''} = \frac{\mu_t}{Sc_t} \frac{\partial \widetilde{\alpha_v}}{\partial x_j} \tag{3.31}$$

where Sc_t is a turbulent Schmidt number. Most CFD procedures assume it to be equal to 1 (Pope, 2001; Versteeg and Malalasekera, 2007).

therefore, we obtain:

$$\frac{\partial}{\partial t}(\widetilde{\alpha_v}\overline{\rho_v}) + \frac{\partial}{\partial x_i}(\widetilde{\alpha_v}\overline{\rho_v}\tilde{u}_j) = \frac{\overline{\rho_v \rho_l}}{\overline{\rho_{mixture}}} \widetilde{\alpha_v}(1 - \widetilde{\alpha_v}) \frac{3}{R_B} \sqrt{\frac{2}{3} \frac{|\overline{p_v} - \overline{p_{cell}}|}{\overline{\rho_l}}} + \frac{\partial}{\partial x_i}\left(\frac{\mu_t}{Sc_t} \frac{\partial \widetilde{\alpha_v}}{\partial x_j}\right) \tag{3.32}$$

when $\overline{p_v} \leq \overline{p_{cell}}$, condensation:

$$\frac{\partial}{\partial t}(\widetilde{\alpha_v}\overline{\rho_v}) + \frac{\partial}{\partial x_i}(\widetilde{\alpha_v}\overline{\rho_v}\tilde{u}_j) = -\frac{\overline{\rho_v \rho_l}}{\overline{\rho_{mixture}}} \widetilde{\alpha_v}(1 - \widetilde{\alpha_v}) \frac{3}{R_B} \sqrt{\frac{2}{3} \frac{|\overline{p_v} - \overline{p_{cell}}|}{\overline{\rho_l}}} + \frac{\partial}{\partial x_i}\left(\frac{\mu_t}{Sc_t} \frac{\partial \widetilde{\alpha_v}}{\partial x_j}\right) \tag{3.33}$$

3.6.2 Zwart-Gerber-Belamri model

Zwart, Gerber and Belamri (ZGB) model: Similar to Schnerr and Sauer model, the model also assumes fluid to be homogeneous vapour-liquid mixture and vapour is assumed to be consist of mini spherical bubbles (Zwart et al., 2004). Again, the first order solution of Rayleigh-Plesset equation or “linear Rayleigh” is used for vapour production and condensation. Vapour volume fraction is defined by the following equation:

$$\alpha_v = \frac{V_{vapour}}{V_{mixture}} = \frac{N_B \frac{4}{3}\pi R_B^3 \cdot V_{mixture}}{V_{mixture}} = N_B \frac{4}{3}\pi R_B^3 \tag{3.34}$$

where R_B is the radius of the bubble, N_B is defined as the bubble concentration per unit volume of the fluid mixture. The transport equation of the vapour fraction is

$$\frac{\partial \alpha_v \rho_v}{\partial t} + \frac{\partial}{\partial x_i}(\alpha_v \rho_v u_j) = R \tag{3.35}$$

where R is net phase change rate and is defined by the following equation:

$$R = N_B \times \left(4\pi R_B^2 \rho_v \frac{dR_B}{dt}\right) \tag{3.36}$$

The equation (3.36) is also used to model condensation process.

Therefore,

when $p_v \geq p_{cell}$, cavitation:

$$R_e = \frac{3\alpha_v \rho_v}{R_B}\sqrt{\frac{2}{3}\frac{|p_v - p_{cell}|}{\rho_l}} \tag{3.37}$$

when $p_v \leq p_{cell}$, condensation:

$$R_c = -\frac{3\alpha_v \rho_v}{R_B}\sqrt{\frac{2}{3}\frac{|p_v - p_{cell}|}{\rho_l}} \tag{3.38}$$

The model is said to work well for condensation but it has been reported to be physically incorrect and numerically unstable for cavitation. The model is based on the assumption that cavitation bubbles do not interact with each other, however, it has been argued Zwart et al. (2004) that this only occurs at the earliest stages of cavitation, when cavitation bubbles grow from nucleation site. Hence, Zwart, Gerber and Belamri further argued that when vapour fraction increases, nucleation site density must decrease accordingly, hence, replaced α with $\alpha_{nuc}\ (1-\alpha)$ for vaporisation. R_B is interpreted as the radius of a nucleation site. Hence the final form of cavitation model is:

if $p_{cell} \leq p_v$, evaporation:

$$R_e = F_{vap}\frac{3\alpha_{nuc}(1-\alpha_v)\rho_v}{R_B}\sqrt{\frac{2}{3}\frac{|p_v - p_{cell}|}{\rho_l}} \tag{3.39}$$

if $p_{cell} \geq p_v$, condensation:

$$R_c = -F_{cond}\frac{3\alpha_v \rho_v}{R_B}\sqrt{\frac{2}{3}\frac{|p_v - p_{cell}|}{\rho_l}} \tag{3.40}$$

The default values of model constants are:

$$\begin{aligned} R_B &= \text{bubble radius} = 1 \times 10^{-6} m \\ \alpha_{nuc} &= \text{nucleation site volume fraction} = 5 \times 10^{-4} \\ F_{vap} &= \text{evaporation co-efficient} = 50 \\ F_{cond} &= \text{condensation co-efficient} = 0.01 \end{aligned} \tag{3.41}$$

The model constants may need to be calibrated to match the experimental data.

The transport equation of vapour fraction will take the following form.

When $p_v \geq p_{cell}$, cavitation:

$$\frac{\partial \alpha_v \rho_v}{\partial t} + \frac{\partial}{\partial x_i}(\alpha_v \rho_v u_j) = F_{vap} \frac{3\alpha_{nuc}(1-\alpha_v)\rho_v}{R_B} \sqrt{\frac{2}{3}\frac{|p_v - p_{cell}|}{\rho_l}} \tag{3.42}$$

When $p_v \leq p_{cell}$, condensation:

$$\frac{\partial \alpha_v \rho_v}{\partial t} + \frac{\partial}{\partial x_i}(\alpha_v \rho_v u_j) = -F_{cond} \frac{3\alpha_v \rho_v}{R_B} \sqrt{\frac{2}{3}\frac{|p_v - p_{cell}|}{\rho_l}} \tag{3.43}$$

3.6.2.1 Favre-averaged transport equation of vapour fraction

Applying Favre-averaging to transport equations, we obtain the following form.

when $\overline{p_v} \geq \overline{p_{cell}}$, cavitation:

$$\frac{\partial}{\partial t}(\widetilde{\alpha_v}\overline{\rho_v}) + \frac{\partial}{\partial x_i}(\widetilde{\alpha_v}\overline{\rho_v}\tilde{u_j}) = F_{vap} \frac{3\alpha_{nuc}(1-\widetilde{\alpha_v})\overline{\rho_v}}{R_B} \sqrt{\frac{2}{3}\frac{|\overline{p_v} - \overline{p_{cell}}|}{\overline{\rho_l}}} + \frac{\partial}{\partial x_i}\left(\frac{\mu_t}{Sc_t}\frac{\partial \widetilde{\alpha_v}}{\partial x_j}\right) \tag{3.44}$$

if $\overline{p_{cell}} \geq \overline{p_v}$, condensation:

$$\frac{\partial}{\partial t}(\widetilde{\alpha_v}\overline{\rho_v}) + \frac{\partial}{\partial x_i}(\widetilde{\alpha_v}\overline{\rho_v}\tilde{u_j}) = -F_{cond} \frac{3\widetilde{\alpha_v}\overline{\rho_v}}{R_B} \sqrt{\frac{2}{3}\frac{|\overline{p_v} - \overline{p_{cell}}|}{\overline{\rho_l}}} + \frac{\partial}{\partial x_i}\left(\frac{\mu_t}{Sc_t}\frac{\partial \widetilde{\alpha_v}}{\partial x_j}\right) \tag{3.45}$$

3.7 Turbulence models

In this section, RANS-based two-equation turbulence models which are used in this study are outlined. In such two equation models, Boussinesq approximation, equation (3.20) is used to compute Reynolds stresses.

3.7.1 Standard $k - \epsilon$ model

The Standard standard $k - \epsilon$ model (Launder and Spalding, 1972) is based modelled transport equations for turbulent kinetic energy k and turbulence dissipation rate ϵ. The transport equation for k is modelled from the exact equation of turbulent kinetic energy (see Davidson et al., 2003). However, the transport equation of ϵ is derived using intuitive reasoning. In the derivation of the standard $k - \epsilon$ model, the flow is assumed to be fully turbulent and effects of molecular viscosity are negligible. Hence, the model is valid only for fully turbulent flows.

$$\frac{\partial(\overline{\rho}k)}{\partial t} + \frac{\partial}{\partial x_j}(\rho k \widetilde{u_j}) = \frac{\partial}{\partial x_j}\left[\left(\mu + \frac{\mu_t}{\sigma_k}\right)\frac{\partial k}{\partial x_j}\right] + 2\mu_t \overline{s_{ij}} \cdot \overline{s_{ij}} - \rho\epsilon \tag{3.46}$$

$$\frac{\partial(\overline{\rho}\epsilon)}{\partial t} + \frac{\partial}{\partial x_j}(\rho \epsilon \widetilde{u_j}) = \frac{\partial}{\partial x_j}\left[\left(\mu + \frac{\mu_t}{\sigma_\epsilon}\right)\frac{\partial \epsilon}{\partial x_j}\right] + C_{1\epsilon}\frac{\epsilon}{k}2\mu_t \overline{s_{ij}} \cdot \overline{s_{ij}} - C_{2\epsilon}\rho\frac{\epsilon^2}{k} \tag{3.47}$$

The above equations contain five adjustable constants $C_\mu = 0.09$, $\sigma_k = 1.00$, $\sigma_\epsilon = 1.30$, $C_{1\epsilon} = 1.44$ and $C_{2\epsilon} = 1.92$. These default values have been determined from experiments for fundamental turbulent flows including frequently encountered shear flows like boundary layers, mixing layers and jets as well as for decaying isotropic grid turbulence. They have been found to work fairly well for a wide range of wall-bounded and free shear flows (Launder and Spalding, 1972).

$\overline{s_{ij}}$ is the mean strain rate tensor.

$$\overline{s_{ij}} = \frac{1}{2}\left(\frac{\partial \widetilde{u_i}}{\partial x_j} + \frac{\partial \widetilde{u_j}}{\partial x_i}\right) \tag{3.48}$$

The shear stress is related to the mean strain rate via eddy viscosity eq. (3.20). The eddy viscosity is isotropic in this model and is determined uniquely by local values of density, ρ, turbulent kinetic energy, k and a turbulent length scale.

$$\mu_t = C_\mu \overline{\rho} k^{\frac{1}{2}} l \tag{3.49}$$

where C_μ is dimensionless constant (0.09). In this model the transport equation of k is solved and the length scale l is determined by the solution of transport equation for the rate of dissipation ϵ.

$$l = \frac{k^{\frac{3}{2}}}{\epsilon} \tag{3.50}$$

Hence, equation (3.49) can be re-written as:

$$\mu_t = C_\mu \bar{\rho} \frac{k^2}{\epsilon} \tag{3.51}$$

3.7.2 Realizable $k - \epsilon$ model

The realizable k-ϵ turbulence model proposed by Shih et al. (1994) shares the same transport equation (3.46) for k as the standard $k - \epsilon$ model but has different transport equation for the rate of turbulent dissipation ϵ. Transport Equation for ϵ has been derived from the exact equation for the transport equation of the mean square of vorticity fluctuations (see Tennekes and Lumley, 1972)

$$\frac{\partial \bar{\rho} \epsilon}{\partial t} + \frac{\partial}{\partial x_j}(\bar{\rho} \epsilon \widetilde{u_j}) = \frac{\partial}{\partial x_j}\left[\left(\mu + \frac{\mu_t}{\sigma_\epsilon}\right)\frac{\partial \epsilon}{\partial x_j}\right] + \rho C_1 S \epsilon - \rho C_2 \frac{\epsilon^2}{k + \sqrt{\nu \epsilon}} \tag{3.52}$$

where

$$C_1 = max\left[0.43, \frac{\eta}{\eta + 5}\right], \; \eta = S\frac{k}{\epsilon}, \; S = \sqrt{2\overline{s_{ij}} \cdot \overline{s_{ij}}} \tag{3.53}$$

The constants are as follows:
$C_{1\epsilon} = 1.44$, $C_2 = 1.9$, $\sigma_k = 1.0$ and $\sigma_\epsilon = 1.2$.

To be realizable the model requires maintaining the non-negativity of normal stress $\overline{u_i''^2} \geq 0$ and 'Schwarz inequality' (Schumann, 1977; Lumley, 1979). The 'Schwarz inequality' is defined by the following term:

$$\frac{(\overline{u_i'' u_j''})^2}{\overline{u_i''^2}\;\overline{u_j''^2}} \leq 1 \tag{3.54}$$

The 'realizability' is achieved by modified formulation of C_μ, which is no longer a constant as in the standard $k - \epsilon$ model.

The $C\mu$ is computed from:

$$C_\mu = \frac{1}{A_0 + A_S \frac{kU^*}{\epsilon}} \tag{3.55}$$

where

$$U^* \equiv \sqrt{\overline{s_{ij}}\;\overline{s_{ij}} + \widetilde{\Omega_{ij}}\widetilde{\Omega_{ij}}} \tag{3.56}$$

and

$$\widetilde{\Omega_{ij}} = \overline{\Omega_{ij}} - \nabla \times \omega_k \tag{3.57}$$

where $\overline{\Omega_{ij}}$ is the mean rate of rotation tensor $= \frac{1}{2}\left(\frac{\partial \widetilde{u_i}}{\partial x_j} - \frac{\partial \widetilde{u_j}}{\partial x_i}\right)$, viewed in a moving reference frame with angular velocity ω_k. The model constants A_o and A_s are given by:
$A_o = 4.04,\ A_s = \sqrt{6}cos(\phi)$
where $\phi = \frac{1}{3}cos^{-1}(\sqrt{6}W)$, $W = \frac{\overline{s_{ij}}\ \overline{s_{jk}}\ \overline{s_{ki}}}{\tilde{s}^3}$, $\tilde{s} = \sqrt{\overline{s_{ij}}\ \overline{s_{ij}}}$ and $\overline{s_{ij}} = \frac{1}{2}\left(\frac{\partial \widetilde{u_i}}{\partial x_j} + \frac{\partial \widetilde{u_j}}{\partial x_i}\right)$

The eddy viscosity is again assumed to be isotropic and is calculated from:

$$\mu_t = C_\mu \overline{\rho} \frac{k^2}{\epsilon} \tag{3.58}$$

3.7.3 Launder and Sharma $k - \epsilon$ model

The transport equation for k and ϵ as follows:

$$\frac{\partial(\overline{\rho}k)}{\partial t} + \frac{\partial}{\partial x_j}(\overline{\rho}k\widetilde{u_j}) = \frac{\partial}{\partial x_j}\left[\left(\mu + \frac{\mu_t}{\sigma_k}\right)\frac{\partial k}{\partial x_j}\right] + 2\mu_t\overline{s_{ij}}\cdot\overline{s_{ij}} - \overline{\rho}\epsilon - 2\mu_t\left(\frac{\partial\sqrt{k}}{\partial x_j}\right) \tag{3.59}$$

$$\begin{aligned}\frac{\partial(\overline{\rho}\epsilon)}{\partial t} + \frac{\partial}{\partial x_j}(\overline{\rho}\epsilon\widetilde{u_j}) = \frac{\partial}{\partial x_j}\left[\left(\mu + \frac{\mu_t}{\sigma_\epsilon}\right)\frac{\partial \epsilon}{\partial x_j}\right] + C_{1\epsilon}\frac{\epsilon}{k}2\mu_t f_1\overline{s_{ij}}\cdot\overline{s_{ij}} - C_{2\epsilon}f_2\rho\frac{\epsilon^2}{k} \\ +2\frac{\mu\mu_t}{\rho}\left[\frac{\partial\widetilde{u_i}^2}{\partial x_j^2}\right]^2\end{aligned} \tag{3.60}$$

The constant $\sigma_k = 1,\ \sigma_\epsilon = 1.3,\ C_{1\epsilon} = 1.44,\ C_{2\epsilon} = 1.92,\ f_1 = 1$ and $f_2 = 1 - 0.03\exp(-Re_t^2)$ where, $Re_t \equiv \frac{k^2}{\nu\epsilon}$

The isotropic eddy viscosity is computed by:

$$\mu_t = C_\mu f_\mu \overline{\rho}\frac{k^2}{\epsilon} \tag{3.61}$$

where $C_\mu = 0.09$, $f_\mu = \exp\left[\frac{-3.4}{(1+R_t/50)^2}\right]$

The model has been proposed by Launder and Sharma (1974) to predict low-Reynolds number phenomenon in the boundary layer and duct flows. On comparing transport equation of k (3.59) and ϵ (3.60) with transport equations (3.46) and (3.47) of standard $k - \epsilon$ model, the transport equations k and ϵ in Launder and Sharma $k - \epsilon$ model contains two additional source terms $-2\mu_t\left(\frac{\partial\sqrt{k}}{\partial x_j}\right)$ and $2\frac{\mu\mu_t}{\rho}\left[\frac{\partial\widetilde{u_i}^2}{\partial x_j^2}\right]^2$. Apart from additional source terms, the model also contains damping functions, f_1, f_2 and f_μ (in equation (3.61)). These terms are only active close to walls and enables model to predict k and ϵ down to the viscous sublayers. However these terms won't be active in turbulence dominant region, hence, it can be argued that Launder and Sharma $k - \epsilon$ model would produce similar results to the standard $k - \epsilon$ model in the turbulent region.

3.7.4 Standard $k - \omega$ model

The standard $k - \omega$ model was proposed by Wilcox et al. (1998). The model also incorporates modifications for low-Reynolds-number effects, compressibility and shear flow spreading. The model is an empirical model based on transport equation for k and specific dissipation rate ω, which is the ratio of ϵ to k. In this subsection, we present the version of $k-\omega$ model implemented in ANSYS Fluent. The transport equation for k and ω are as follows:

$$\frac{\partial(\overline{\rho}k)}{\partial t}+\frac{\partial}{\partial x_j}(\overline{\rho}k\widetilde{u_j})=\frac{\partial}{\partial x_j}\left[\left(\mu+\frac{\mu_t}{\sigma_k}\right)\frac{\partial k}{\partial x_j}\right]+2\mu_t\overline{s_{ij}}\cdot\overline{s_{ij}}-\overline{\rho}\beta^* f_{\beta^*}k\omega \tag{3.62}$$

$$\frac{\partial(\overline{\rho}\omega)}{\partial t}+\frac{\partial}{\partial x_j}(\overline{\rho}\omega\widetilde{u_j})=\frac{\partial}{\partial x_j}\left[\left(\mu+\frac{\mu_t}{\sigma_\omega}\right)\frac{\partial \omega}{\partial x_j}\right]+\alpha\frac{\omega}{k}2\mu_t\overline{s_{ij}}\cdot\overline{s_{ij}}-\overline{\rho}\beta f_{\beta}\omega^2 \tag{3.63}$$

The isotropic eddy viscosity is computed from:

$$\mu_t=\alpha^*\frac{\overline{\rho}k}{\omega} \tag{3.64}$$

3.7.4.1 Low-Reynolds-Number correction

The coefficient α^* damps the turbulent viscosity causing a low-Reynolds number correction. It is given by:

$$\alpha^*=\alpha^*_\infty\left(\frac{\alpha^*_0+Re_t/R_k}{1+Re_t/R_k}\right) \tag{3.65}$$

where

$$Re_t=\frac{\overline{\rho}k}{\mu\omega} \tag{3.66}$$

$$R_k=6 \tag{3.67}$$

$$\alpha^*_0=\frac{\beta_i}{3} \tag{3.68}$$

$$\beta_i=0.072 \tag{3.69}$$

In high-Reynolds number for of $k-\omega$ model, $\alpha^*=\alpha^*_\infty=1$.

3.7.4.2 Modelling turbulence production

In the production term $\alpha\frac{\omega}{k}2\mu_t\overline{s_{ij}}\cdot\overline{s_{ij}}$ of transport equation (3.63) of ω:

$$\alpha = \frac{\alpha_\infty}{\alpha^*}\left(\frac{\alpha_0 + Re_t/R_\omega}{1 + Re_t\Re_\omega}\right) \tag{3.70}$$

where $R_w = 2.95$, α^* and Re_t are given by equation (3.65) and (3.66).

3.7.4.3 Modelling turbulence dissipation

In the dissipation term $\overline{\rho}\beta^* f_{\beta^*}\omega$ of transport equation for k (3.62):

$$f_{\beta^*} = \begin{cases} 1, & \text{if } \chi_k \le 0 \\ \frac{1+680\chi_k^2}{1+400\chi_k^2} & \text{if } \chi_k > 0 \end{cases} \tag{3.71}$$

where

$$\chi_k \equiv \frac{1}{\omega^3}\frac{\partial k}{\partial x_j}\frac{\partial \omega}{\partial x_j} \tag{3.72}$$

and

$$\beta^* = \beta_i^*[1 + \zeta^* F(M_t)] \tag{3.73}$$

$$\beta_i^* = \beta_\infty^*\left(\frac{4/15 + (Re_t/Re_\beta)^4}{1 + (Re_t/Re_\beta)^4}\right) \tag{3.74}$$

where $\zeta^* = 1.5$, $Re_\beta = 8$ and $\beta_\infty^* = 0.09$

In the dissipation term $\overline{\rho}\beta f_\beta\omega^2$ of transport equation (3.63) of ω:

$$f_\beta = \frac{1 + 70\chi_\beta}{1 + 80\chi_\beta} \tag{3.75}$$

$$\chi_\beta = \left|\frac{\overline{\Omega_{ij}}\cdot\overline{\Omega_{jk}}\cdot\overline{E_{ki}}}{(\beta_\infty^*\omega)^3}\right| \tag{3.76}$$

$$\overline{\Omega_{ij}} = \frac{1}{2}\left(\frac{\partial\widetilde{u}_i}{\partial x_j} - \frac{\partial\widetilde{u}_j}{\partial x_k}\right) \tag{3.77}$$

$$\beta = \beta_i\left[1 - \frac{\beta_i^*}{\beta_i}\zeta^* F(M_t)\right] \tag{3.78}$$

3.7.4.4 Compressibility correction

$F(M_t)$ is a compressibility function:

$$F(M_t) = \begin{cases} 0, & \text{if } M_t \leq M_{t0} \\ M_t^2 - M_{t0}^2 & \text{if } M_t > M_{t0} \end{cases} \tag{3.79}$$

where

$$M_t^2 \equiv \frac{2k}{a^2} \tag{3.80}$$

and

$$M_{t0} = 0.25 \tag{3.81}$$

$$a = \sqrt{\gamma R \widetilde{T}} \tag{3.82}$$

In the high-Reynolds number form of the $k-\omega$ model, $\beta_i^* = \beta_\infty^*$, in incompressible form, $\beta^* = \beta_i^*$. The compressibility correction has been calibrated for a very limited number of free shear flows and is generally not recommended.

3.7.4.5 Model constants

$\alpha_\infty^* = 1,\ \alpha_\infty = 0.52,\ \alpha_0 = \frac{1}{9},\ \beta_\infty^* = 0.09,\ \beta_i = 0.072,\ R_\beta = 8$

$R_k = 6,\ R_\omega = 2.95,\ \zeta^* = 1.5,\ M_{t0} = 0.25,\ \sigma_k = 2.0,\ \sigma_\omega = 2.0$

3.7.5 SST $k-\omega$ model

Shear stress transport $k-\omega$ model was proposed by Menter (1994). The model effectively blends formulation of the $k-\omega$ model of Wilcox et al. (1998) in near wall region with the standard $k-\epsilon$ model (Launder and Spalding, 1972) in the far field. In order to achieve this, the standard $k-\epsilon$ model is transformed into the $k-\omega$ model but includes the following refinements.

- The standard $k-\omega$ model and the transformed standard $k-\epsilon$ model are both multiplied with blending function and added together.
- The blending function is designed in such a way that in near wall region, it would activate the $k-\omega$ model and away from the surface it would activate the transformed $k-\epsilon$ model.
- The SST model incorporates a damped cross-diffusion term in the ω equation.
- The definition of turbulent viscosity is modified for the turbulent shear stress.
- The empirical constants are different.

The transport equation for the SST $k-\omega$ model are as follows:

$$\frac{\partial(\overline{\rho}k)}{\partial t}+\frac{\partial}{\partial x_j}(\overline{\rho}k\widetilde{u_j})=\frac{\partial}{\partial x_j}\left[\left(\mu+\frac{\mu_t}{\sigma_k}\right)\frac{\partial k}{\partial x_j}\right]+\widetilde{G_k}-Y_k \tag{3.83}$$

$$\frac{\partial(\overline{\rho}\omega)}{\partial t}+\frac{\partial}{\partial x_j}(\rho\omega\widetilde{u_j})=\frac{\partial}{\partial x_j}\left[\left(\mu+\frac{\mu_t}{\sigma_\omega}\right)\frac{\partial \omega}{\partial x_j}\right]+G_\omega-Y_\omega+D_\omega \tag{3.84}$$

The turbulent viscosity is computed from:

$$\mu_t=\frac{\overline{\rho}k}{\omega}\frac{1}{max\left[\frac{1}{\alpha^*},\frac{E_{ij}F_2}{a_1\omega}\right]} \tag{3.85}$$

$$\sigma_k=\frac{1}{F_1/\sigma_{k,1}+(1-F_1)/\sigma_{k,2}} \tag{3.86}$$

$$\sigma_\omega=\frac{1}{F_1/\sigma_{\omega,1}+(1-F_1)/\sigma_{\omega,2}} \tag{3.87}$$

α^* has been defined in equation (3.65). F_1 and F_2 are blending functions given by:

$$F_1=tanh(\Phi_1^4) \tag{3.88}$$

$$\Phi_1=min\left[max\left(\frac{\sqrt{k}}{0.09\omega y},\frac{500\mu}{\overline{\rho}y^2\omega}\right),\frac{4\rho k}{\sigma_{\omega,2}D_\omega^+y^2}\right] \tag{3.89}$$

$$D_\omega^+=max\left[2\overline{\rho}\frac{1}{\sigma_{\omega,2}}\frac{1}{\omega}\frac{\partial k}{\partial x_j}\frac{\partial \omega}{\partial x_j},10^{-10}\right] \tag{3.90}$$

$$F_2=tanh(\Phi_2^2) \tag{3.91}$$

$$\Phi_2=max\left[2\frac{\sqrt{k}}{0.09\omega y},\frac{500\mu}{\overline{\rho}y^2\omega}\right] \tag{3.92}$$

where y is the distance to the next surface and D_ω^+ is the positive portion of the cross diffusion term (3.100).

3.7.5.1 Modelling the turbulence production

The $\widetilde{G_k}$ represents the production term in turbulence kinetic energy equation (3.83), and is given by:

$$\widetilde{G_k} = min(2\mu_t \overline{s_{ij}} \cdot \overline{s_{ij}}, 10\overline{\rho}\beta\omega) \tag{3.93}$$

The term G_ω represents the production term of ω in transport equation (3.84) of specific dissipation rate and is given by:

$$G_\omega = \frac{\alpha_\infty}{\nu_t}\widetilde{G_k} \tag{3.94}$$

In Wilcox et al. (1998)'s $k-\omega$ model, α_∞ is constant (0.52) while in the SST $k-\omega$ model α_∞ is given by

$$\alpha_\infty = F_1\alpha_{\infty,1} + (1-F_2)\alpha_{\infty,2} \tag{3.95}$$

where

$$\alpha_{\infty,1} = \frac{\beta_{i,1}}{\beta^*_{\infty,1}} - \frac{\kappa^2}{\sigma_{\omega,1}\sqrt{\beta^*_\infty}} \tag{3.96}$$

$$\alpha_{\infty,2} = \frac{\beta_{i,2}}{\beta^*_{\infty,2}} - \frac{\kappa^2}{\sigma_{\omega,2}\sqrt{\beta^*_\infty}} \tag{3.97}$$

where κ is 0.41.

3.7.5.2 Modelling the turbulence dissipation

The term Y_k represents the dissipation of turbulence kinetic energy in equation (3.83) and is defined in a similar manner as in the standard $k-\omega$ model, § 3.7.4.3. However in the SST $k-\omega$ model, F_{β^*} is constant and equal to 1.

The term Y_ω represents dissipation of ω in equation (3.84) and is defined in the similar way as in the standard $k-\omega$ model. However, the difference in models is in the way the terms β_i and f_β are modelled. In the standard $k-\omega$ model (see § 3.7.4.3), β_i is constant (0.072) and f_β is defined by equation (3.75). In SST $k-\omega$ model f_β is constant and is equal to 1 and β_i is not constant. Hence:

$$Y_k = \overline{\rho}\beta_i\omega^2 \tag{3.98}$$

β_i is given by

$$\beta_i = F_1\beta_{i,1} + (1-F_1)\beta_{i,2} \tag{3.99}$$

where F_1 is obtained by equation (3.88).

3.7.5.3 Cross diffusion modification

The SST $k-\omega$ is a model based on both the standard $k-\omega$ model and the standard $k-\epsilon$ model. To blend these two models together, the standard $k-\epsilon$ model has been transformed into equations based on k and ω. This is achieved by the introduction of cross-diffusion term D_ω:

$$D_\omega = 2(1-F_1)\overline{\rho}\frac{1}{\omega\sigma_{\omega,2}}\frac{\partial k}{\partial x_j}\frac{\partial \omega}{\partial x_j} \tag{3.100}$$

3.7.5.4 Model constants

$\sigma_{k,1} = 1.176$, $\sigma_{\omega,1} = 2.0$, $\sigma_{k,2} = 1.0$, $\sigma_{\omega,2} = 1.168$

$a_1 = 0.31$, $\beta_{i,1} = 0.075$, $\beta_{i,2} = 0.0828$

Other models constants i.e. $\alpha^*_\infty, \alpha_\infty$, α_0, β^*_∞, R_β, R_k, R_ω, ζ^* and $M_{t,0}$ have same values as standard $k-\omega$ model.

3.8 Wall functions

In this section, the near wall modelling approaches which are used in this study are outlined.

3.8.1 Standard Wall Function

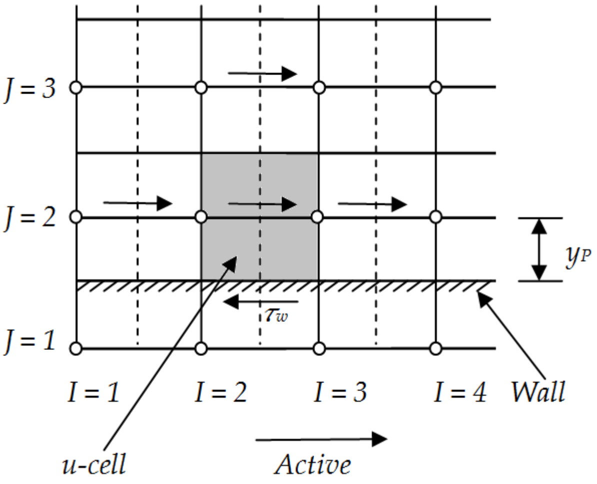

Figure 3.1: u-velocity cell at a boundary

Standard Wall Functions are based on the logarithmic law-of-wall which was first published by Von Karman (1931). The log-law of the wall are directly applied to the first interior node. Let y be a coordinate normal to the solid wall, and y_p (see Figure 3.1) be the first interior node, the mean velocity at this point y_p with $30 < y^+ < 500$ would satisfy the log-law of the wall. The law-of-the-wall for mean velocity yields:

$$u^+ = \frac{\widetilde{u}}{u_\tau} = \frac{1}{k} ln(y^+) + B = \frac{1}{k} ln(Ey^+) \tag{3.101}$$

where u^+ is the dimensionless velocity: $\widetilde{u}$ is the mean velocity parallel to the wall at the near-wall node, divided by friction velocity u_τ. and y^+ is the dimensionless distance from the wall: the y_p normal distance from the wall to the first near-wall node, made dimensionless with friction velocity u_τ and kinematic viscosity ν:

$$y^+ \equiv \frac{y_p u_\tau}{\nu} \tag{3.102}$$

u_τ is the friction velocity, defined by:

$$u_\tau = \sqrt{\frac{\tau_w}{\overline{\rho}}} \tag{3.103}$$

τ_w is wall shear stress, defined by:

$$\tau_w \cong \tau(y) = \mu \frac{\partial \widetilde{u}_i}{\partial x_j} \tag{3.104}$$

$k =$ Von Karman constant ($= 0.4187$) and $B = 5.5$, E is the integration constant which depends on the roughness of the wall, for the smooth wall with constant shear stress E has a value of 9.793. In many CFD codes, at 'wall' boundary conditions, the log-law (3.101) is employed when $y^+ \geq 11.63$. When $y^+ \leq 11.63$, flow is assumed to be laminar ($u^+ = y^+$), (Versteeg and Malalasekera, 2007). However when usind standard wall function it is highly recommended to place first grid normal to the wall at $y+ \approx 30$ below which results would be compromised (Knopp, 2006).

3.8.2 Launder-Spalding Wall function

The standard wall function has its limitations, especially for recirculating flows. Launder and Spalding (1974) proposed modification to the standard wall function:

The law-of-the-wall for mean velocity:

$$U^* = \frac{1}{k} ln(Ey^*) \tag{3.105}$$

where U^* is the dimensionless velocity defined by:

$$U^* \equiv \frac{\widetilde{u} C_\mu^{\frac{1}{4}} k_p^{\frac{1}{2}}}{\tau_w / \overline{\rho}} \tag{3.106}$$

y^* is the dimensionless distance from the wall, defined by:

$$y^* = \frac{\overline{\rho} C_\mu^{\frac{1}{4}} k_p^{\frac{1}{2}} y_p}{\mu} \tag{3.107}$$

where k, E has the same values as standard wall functions, C_μ is related to eddy viscosity, varies with turbulence models, k_p is turbulence kinetic energy at the near-wall node, y_p is the distance normal from the wall to the near wall node. The modified log-law (3.105) is employed when $y^* > 11.225$. When the mesh is such that $y^* < 11.225$, laminar stress-strain relation is applied or $U^* = y^*$. However, the Launder and Spalding wall function require first grid normal to the wall to be placed at $y^* \geq 11.225$ and would typically fail under grid refinement below $y^* \leq 11.225$ (Bredberg, 2000; Fluent, 2012).

3.8.3 Enhanced Wall Treatment method

Enhanced wall treatment method is a near wall modelling approach implemented in ANSYS Fluent (Fluent, 2012), which combines a 'two-layer model' with the 'enhanced wall functions'. In the region where the mesh is fine enough ($y^+ \approx 1$), the model acts like a two-layer model. The model uses the single law-of-the-wall of the so-called 'enhanced wall functions' formulated for the entire wall region.

- In the 'two-layer model', the domain is divided into viscosity affected region and turbulence dominated region. In this approach at the turbulence dominated region, full turbulence models are used while in viscosity affected region, one equation model by Wolfshtein (1969) is used. The turbulent viscosity in the laminar region is smoothly blended with High Reynolds Number turbulent viscosity with a blending function proposed by Jongen (1998).
- In the 'enhanced wall function', the 'law-of-the-wall' is formulated as a single law of wall for entire wall region. This is achieved by blending linear and logarithmic 'law-of-the-wall' using function suggested by Kader (1981).

Chapter 4

Single-phase simulations in an enlarged multi-hole injector

4.1 Introduction

The objective of this chapter is to achieve sound simulations of non-cavitating flow in symmetric multi-hole (6) enlarged (20X) diesel fuel injector. In this chapter, single-phase simulations were performed using commercial CFD suite ANSYS-FLUENT at different needle positions and simulations were assessed by comparing simulation results with experimental measurements. Impacts of errors on simulation results were assessed which are mainly boundary condition errors, numerical errors and physical modelling errors.

4.2 Description of test cases:

In the present study, LDV measurements (Roth et al., 2002; Roth, 2004) of the mean axial velocity and RMS velocity at different planes (Figure 4.4 and 4.5) of the hole of the enlarged multi-hole (6) injector have been used to evaluate the CFD simulations. The transparent nozzle was manufactured of an acrylic material with refractive index of 1.49 of whose dimensions corresponded to 20 times magnification of Bosch conical mini-sac type six hole axisymmetric vertical diesel fuel injector (Figure 4.1, 4.2, 4.3). The diameter of the enlarged injector hole was 3.5 mm, which corresponded to the hole diameter of 0.175 mm (20 times magnification) of a real size injector. The nozzle operated on the steady state test rig at lower (1.60 mm) and the nominal (6.00 mm) needle lifts which corresponded to maximum needle lift of the first stage and second stage of real size diesel injection process.

The working fluid was a mixture of 32% by volume of tetralin (1,2,3,4 – Tetrahydronaphthalene) and 68% by volume of oil of turpentine. The rig operated at the temperature 25±0.5 °C to ensure refractive index of fluid to be 1.49. The refractive index matching technique enabled full optical access to the complex liquid-vapour interface with no distortion of laser beam (Nouri et al., 1988). Experiments performed two sets of velocity measurements using LDV at non-cavitating quasi-steady flow regime (Roth et al., 2002; Roth, 2004).

In the first set of the experiment the Reynolds number Re[1] was kept constant and the cavitation number CN[2] was varied, in the second set both the Reynolds number and cavitation number were varied.

lower needle-lift 1.6 mm

Series	CN	Re	p_{inj}	p_{back}	U_{inj}	*Flow Rate*
1	0.44	18000	2.55 bar	1.80 bar^*	$8.43ms^{-1}$	N/A
2	0.44	18000	2.55 bar	1.80 bar^*	$8.43ms^{-1}$	$0.487ls^{-1}$

nominal needle-lift 6 mm

Series	CN	Re	p_{inj}	p_{back}	U_{inj}	*Flow Rate*
1	0.45	21000	1.80 bar	1.25 bar^*	$9.84ms^{-1}$	N/A
2	0.45	21000	1.80 bar	1.25 bar^*	$9.84ms^{-1}$	$0.568ls^{-1}$

* The pressure values are in absolute pressure. 1 bar = 10^5 Nm^{-2}

Table 4.1: Flow conditions for the first and second series of LDV measurements at lower needle lift and nominal lift.

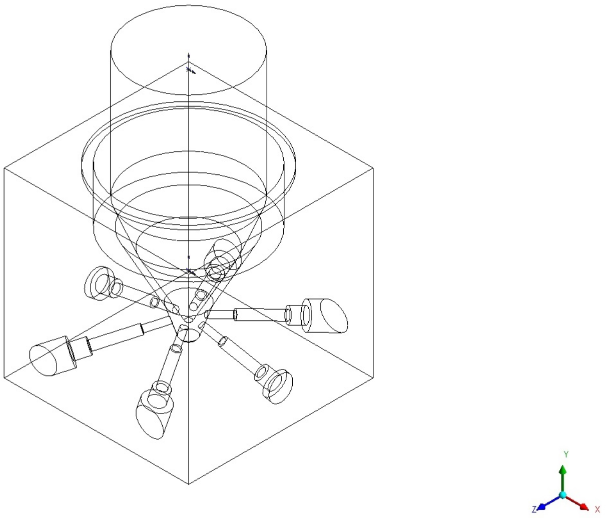

Figure 4.1: Isometric view of the transparent enlarged conical mini-sac type nozzle and needle at nominal needle lift (6 mm).

---

[1] The Reynolds number was based on the diameter of the injector hole:

$$Re = \frac{D \cdot U_{inj}}{\nu} = \frac{D}{\nu}\left(\frac{Q_t}{nA_h}\right) = \frac{4Q_t}{\pi \nu n D} \tag{4.1}$$

where D is the diameter of the injector hole, u_{inj} is the injection velocity, ν is the kinematic viscosity of the fluid, Q_t is the total flow rate of the injector, A_h is the cross section area of the individual injector hole and n is the numbers of injector hole in the fuel injector nozzle (6 in the present case).

[2] CN or cavitation number is a non-dimensional parameter indicating cavitation intensity and it is independent of Reynolds number (Bergwerk, 1959):

$$CN = \frac{p_{inj} - p_{back}}{p_{back} - p_v} \tag{4.2}$$

where, p_{inj} is injection pressure, p_{back} is the back pressure, p_v is saturated vapour pressure.

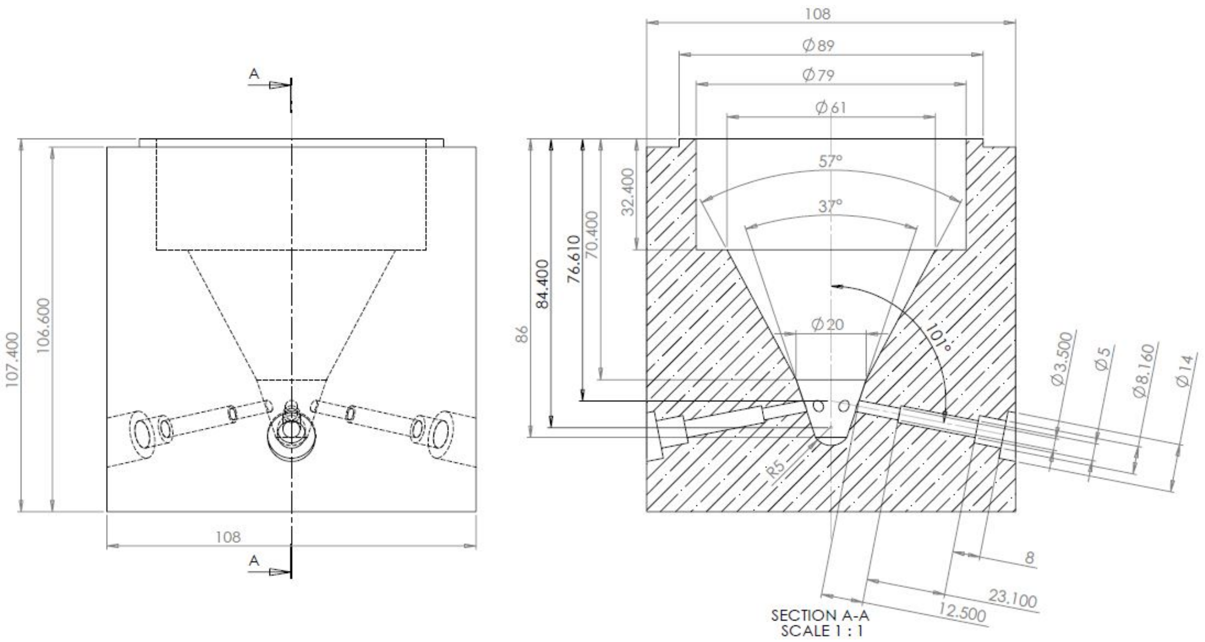
A
107.400
106.600
108
A
108
Ø89
Ø79
Ø61
57°
37°
32.400
70.400
76.610
84.400
86
Ø20
101°
R5
Ø3.500
Ø5
Ø8.160
Ø14
8
23.100
12.500
SECTION A-A
SCALE 1 : 1

Figure 4.2: Side view (z-y plane) and sectional view of the injector nozzle. All dimension are in mm, the tolerances are not given.

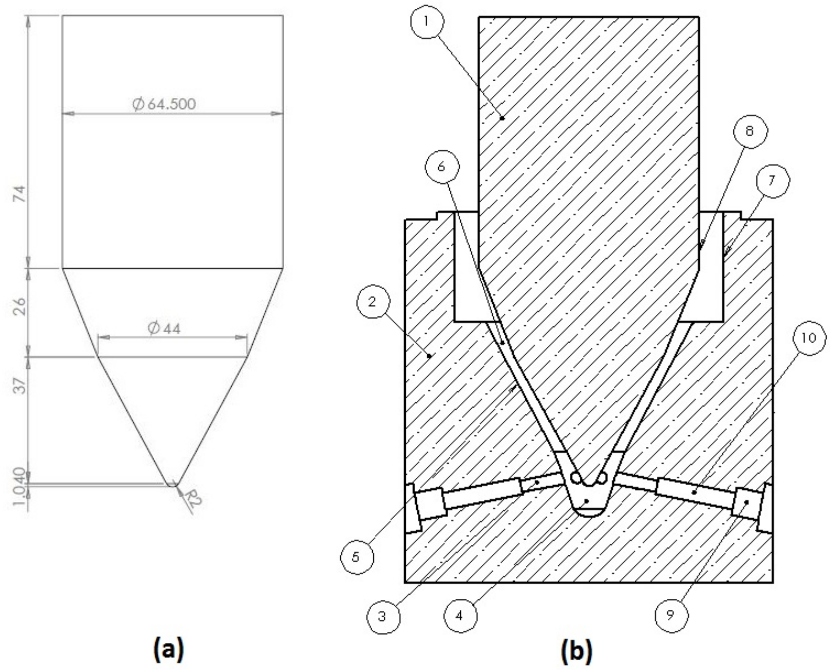
Ø64.500
74
26
Ø44
37
1.040
R2
1
2
3
4
5
6
7
8
9
10
(a)
(b)

Figure 4.3: (a) Side view (z-y plane) of the injector needle. All dimension are in mm, the tolerances are not given. (b) Typical model parts of an enlarged injector and needle assembly. 1) Needle 2) injector 3) injector hole 4) sac volume 5) needle seat 6) seat annulus 7) cartridge wall 8) needle wall 9) pressure measuring tap (also outlet boundary conditions for CFD) 10) back flow hole.

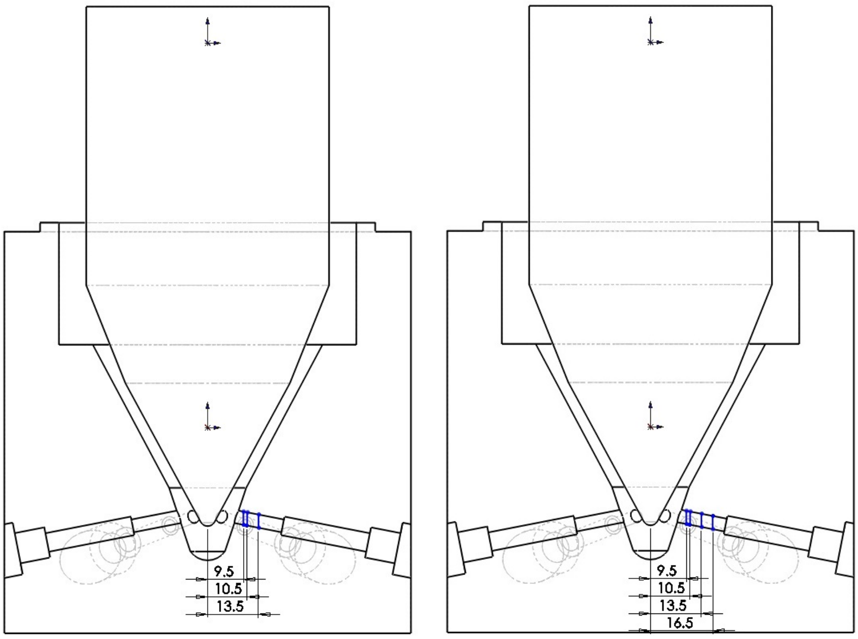
9.5
10.5
13.5
9.5
10.5
13.5
16.5

(a) (b)

Figure 4.4: Section view of the fuel injector displaying positions where LDV measurements were taken, (a) corresponds to Series 1 experiments, (b) corresponds to Series 2 experiments. All dimensions are in mm.

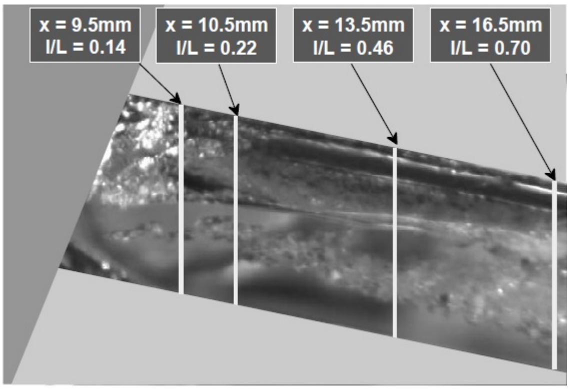
x = 9.5mm
l/L = 0.14
x = 10.5mm
l/L = 0.22
x = 13.5mm
l/L = 0.46
x = 16.5mm
l/L = 0.70

Figure 4.5: The locations of LDV measurement planes in one of the injector holes. Source: Roth (2004)

Working Fluids Properties	
Density	895 $kg\ m^{-3}$
Kinematic viscosity	$1.64 \times 10^{-6}\ m^2 s^{-1}$
Vapour pressure	1000 Nm^{-2}
Surface Tension	0.03 Nm^{-1}
Refractive Index	1.49

Table 4.2: working-fluid

4.2.0.1 Description of the test rig

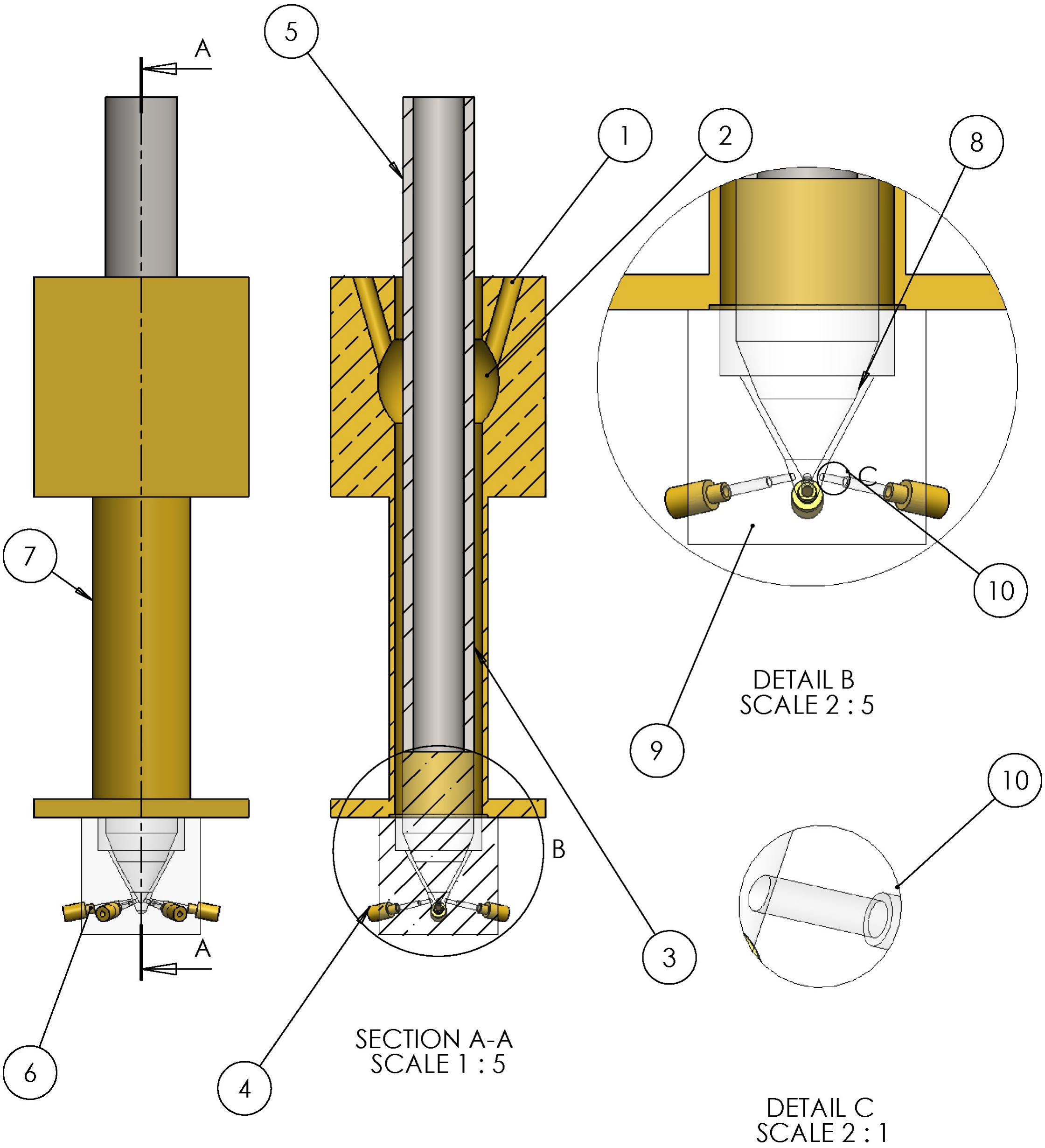
A
5
1
2
8
7
10
DETAIL B
SCALE 2 : 5
9
10
B
3
A
6
4
SECTION A-A
SCALE 1 : 5
DETAIL C
SCALE 2 : 1
C

Figure 4.6: Schematics of the refractive index matching test rig with incorporated large-scale injector.

Figure 4.5 offers a schematic view of test rig with an incorporated large-scale injector used for experiments (see Roth, 2004, pg. 98).

1. Fluid entering the system.
2. Fluid mixing region.
3. Annulus which allows flow to fully develop at the time it reaches the injector.
4. Outlet, fluid goes to temperature control reservoir and re-enters the system.

5. Tube to control needle lift.
6. Outlet pressure measuring position.
7. Inlet pressure measuring position (does not represent the actual position, because is not very precisely described in literature (Roth, 2004, pg. 98)).
8. Needle, at nominal lift (6 mm).
9. Detail view of the nozzle.
10. Zoom of the injector hole where LDV/CCD measurements were taken.

4.3 Boundary condition error analysis

This objective of this study is to assess the impacts on simulation results when a periodic type boundary condition or a periodic interface is used for the enlarged symmetric multi-hole fuel injector nozzle. The periodic boundary conditions are used when the physical geometry of interest (flow-domain) and expected pattern of the solution have periodically repeating nature (Versteeg and Malalasekera, 2007). The Figure 4.7 (B), represents the 'complete flow-domain' and the Figure 4.7 (C), represent 'one sixth of the flow domain with periodic (cyclic) boundary condition'.

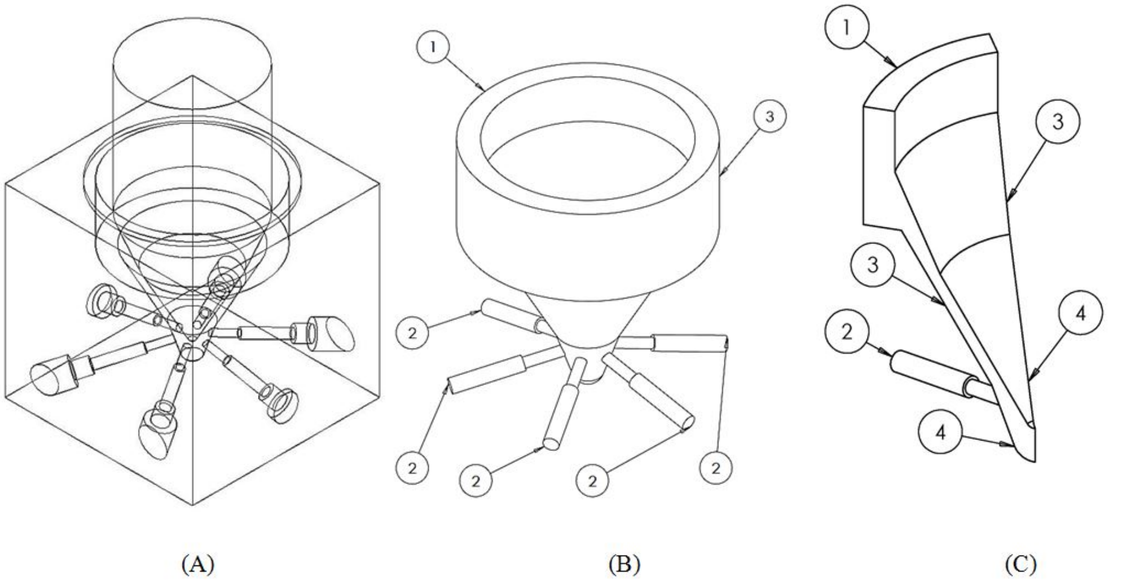

Figure 4.7: (A) Isometric view of the enlarged injector and needle at nominal needle-lift (6.00 mm), (B) the complete flow domain (C) one-sixth of flow domain with periodic (cyclic) boundary conditions. The numbers represents the boundaries of flow domains, (1) inlet (2) outlet (3) walls (4) periodic (cyclic) interface.

4.3.0.1 Case setup

The complete flow domain as shown in Figure 4.7 (B) and one-sixth of the flow domain as shown in Figure 4.7 (C) have been used. The flow domains are discretized into semi-structured (tetrahedral and prism layers) grids, (see Table 4.5, Figure 4.8) which have been generated using automatic grid generation method (Guide, 2012) with similar sizing of control volumes. Non-cavitating operating condition at nominal needle-lift (6.0 mm) (see Table 4.3) is simulated. Steady-state simulations were performed. Turbulence effects are introduced using the realizable $k - \epsilon$ model (Shih et al., 1994) and near-wall turbulence region flow is modelled using the 'enhanced wall treatment' method (see § 3.8.3). The liquid is considered as incompressible, its properties can be found in the table 4.2. Boundary conditions are listed in the table 4.4.

Series	*CN*	*Re*	p_{inj}	p_{back}	U_{inj}	*Flow Rate*
1	0.45	21000	1.80 *bar* (absolute)	1.27 *bar* (absolute)	$9.84ms^{-1}$	N/A*
2	0.45	21000	1.80 *bar* (absolute)	1.27 *bar* (absolute)	$9.84ms^{-1}$	0.568 ls^{-1}

* Flow rate for the first series of experiment is not found in the literature (Roth et al., 2002; Roth, 2004) but is assumed to be the same as that of the second series of experiment (0.586 ls^{-1}).

Table 4.3: Flow conditions of the first and second series of LDV measurements at high lift

Case	Flow volume	Inlet	Outlet	Interface	Walls
1	complete flow volume	mass-flow rate 0.5082 $kg\ s^{-1}$	constant pressure 127000 Nm^{-2}	not required	enhanced wall treatment method
2	one-sixth of fluid volume	mass-flow rate 0.0847 $kg\ s^{-1}$	constant pressure 127000 Nm^{-2}	cyclic	enhanced wall treatment method

Table 4.4: Boundary Conditions

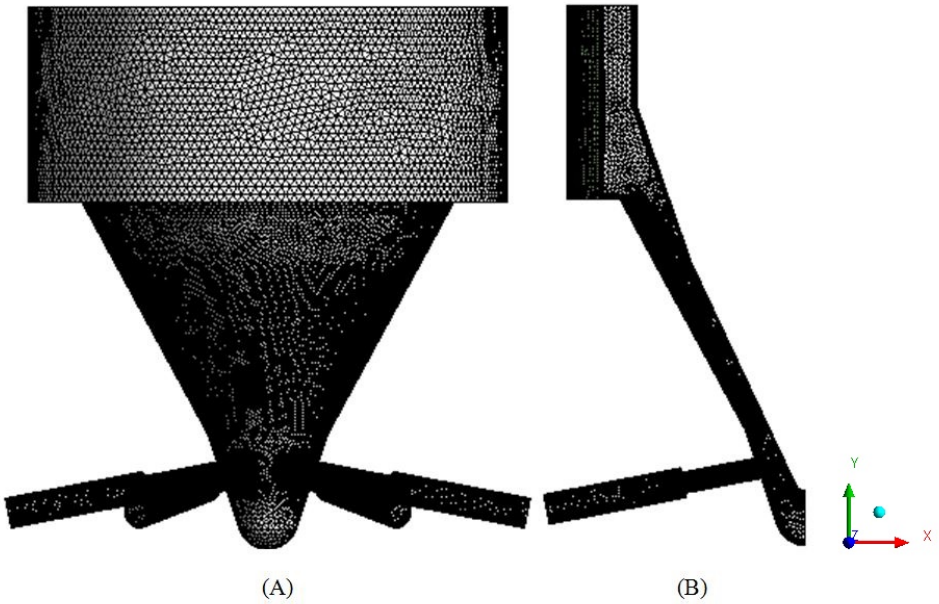

(A) (B)

Figure 4.8: (A) Mesh of the complete fluid volume, (B) Mesh of the one-sixth of the fluid volume.

Case	Flow domain	Control volumes (CV)	Maximum y^+
1	complete flow domain	1,792,278	18.2
2	one-sixth of flow domain	348,476	17.9

Table 4.5: Mesh description, y^+ values are obtained after the simulations.

4.3.0.2 Results

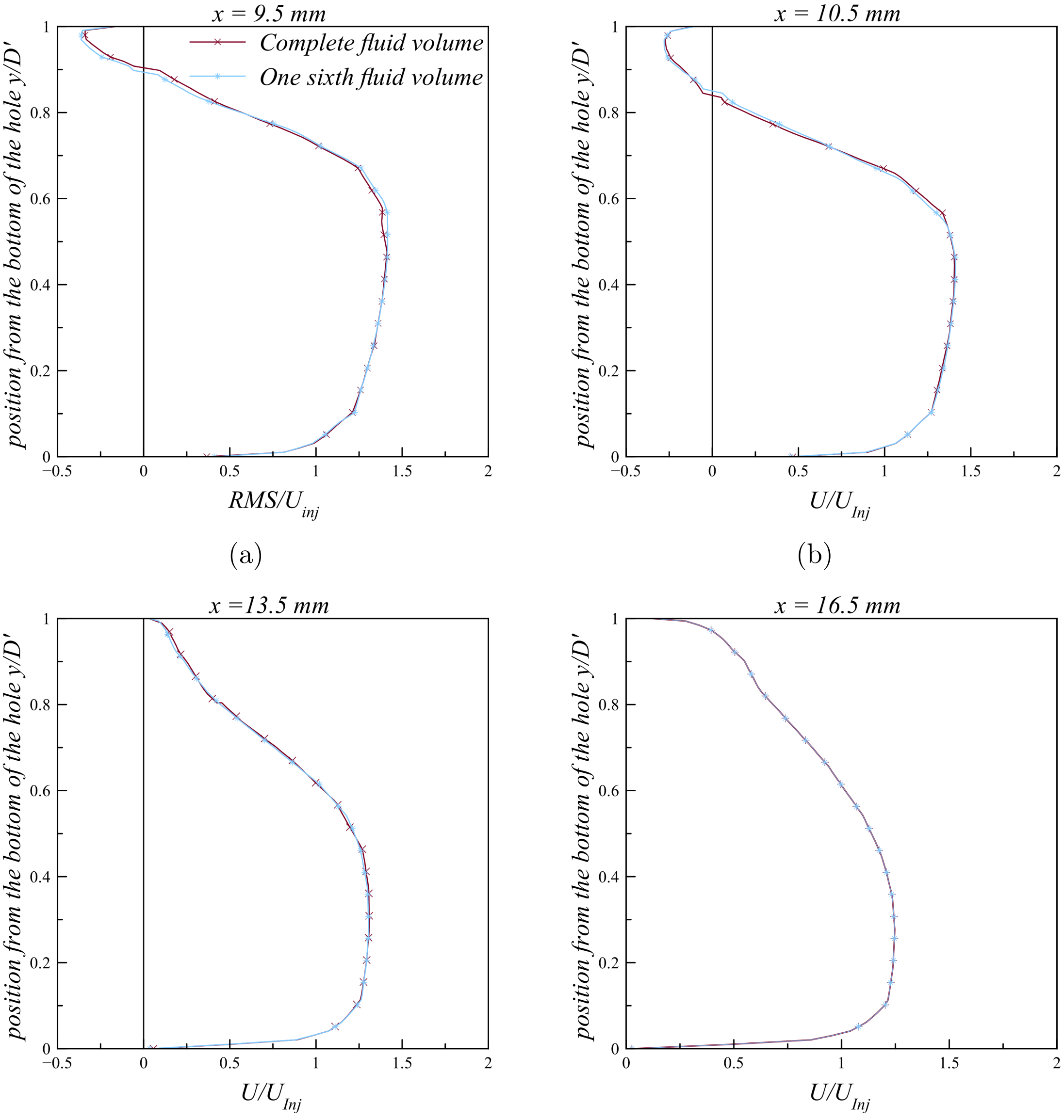

(a) (b) (c) (d)

Figure 4.9: Normalized mean axial velocity comparisons for flow domains with the 'complete flow domain' and 'one-sixth of the flow domain' with periodic boundary conditions.

The predicted mean axial velocities at different planes of the injector hole (see Figure 4.4 and 4.5) were compared for the 'complete flow domain' and 'one-sixth of the flow domain'. The comparison revealed similar results (see Figure 4.9 (a) (b) (c) (d)) for both flow domain with minor variations. These minor variations in the mean axial velocity profiles can be attributed to the difference in locations of grid points in different domains.

4.3.0.3 Discussions:

- Almost similar results are obtained in both cases, hence from the present results, it can be inferred that 'the flow domain with periodic boundary conditions' if correctly applied would produce similar results as 'the complete fluid domain' and therefore would be used in later studies.

4.4 Grid sensitivity analysis

The object of this study is to assess the influence of the grid density in the fluid domain on CFD simulation results. The simulations were performed for both lower (1.60 mm) and nominal lift (6.00 mm) cases at non-cavitating conditions (see Table 4.1).

4.4.1 Case setup

Operating conditions as listed in Table 4.1 for both lower (1.60 mm) and the nominal (6.00 mm) needle lifts are simulated. The simulations were first performed using relatively coarse mesh at both needle lifts; the mesh density was then successively increased until a further increase did not influence the simulation results. The flow domain is one-sixth of the fluid volume with the periodic interface. The grid type is semi-structured consist of primarily tetrahedral elements. Also, prism type cells were added to the wall to resolve the near wall turbulence accurately. At first, the grid was uniformly refined, later, the grid density around the injector hole and the sac volume were refined after successive simulations (see Figure 4.11 and Table 4.7). Considering the flow regime was quasi-steady at non-cavitating conditions at $Re = 18000$ for lower needle lift and $Re = 21000$ for nominal needle lift, steady state simulations were performed using realizable $k-\epsilon$ model (Shih et al., 1994); the near wall turbulence was resolved using 'Enhanced wall treatment' method (see § 3.8.3). The fluid (liquid) was assumed to be incompressible; the fluid properties are listed in the Table 4.2. The boundary conditions used are listed in the Table 4.6 for both the lower and nominal needle lifts.

Case	Inlet	Outlet	interface	Walls
lower (1.6 mm) needle-lift	mass-flow rate 0.0726 $kg\ s^{-1}$	constant pressure 180000 Nm^{-2}	cyclic	enhanced wall treatment method
nominal (6.0 mm) needle-lift	mass-flow rate 0.0847 $kg\ s^{-1}$	constant pressure 127000 Nm^{-2}	cyclic	enhanced wall treatment method

Table 4.6: Boundary Conditions

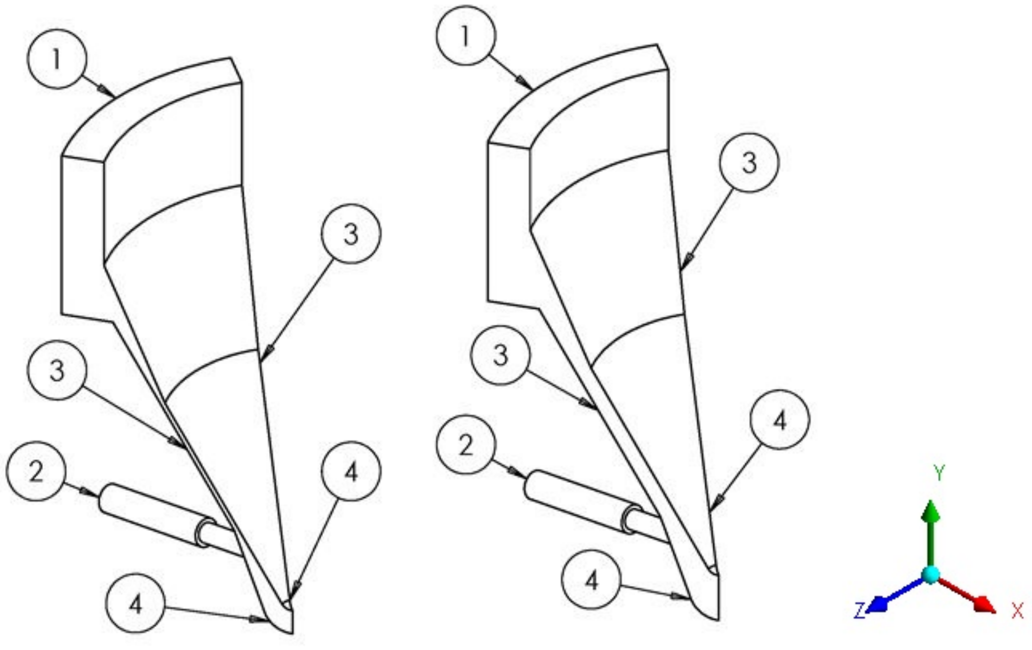

(A) (B)

Figure 4.10: (A) Flow Domain for the lower needle lift. (B) flow domain for the nominal needle lift. The numbers represent boundaries of flow domains, (1) inlet (2) outlet (3) walls (4) periodic

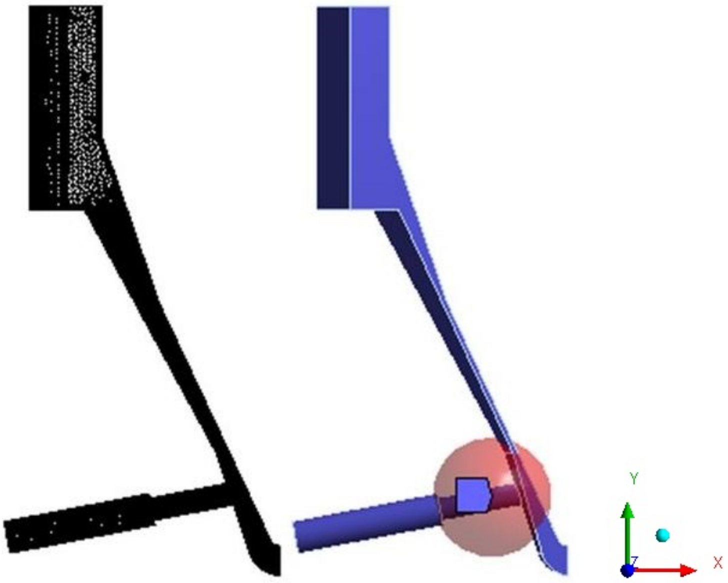

(A) (B)

Figure 4.11: (A) The Lower needle lift grid with uniform element size (B) The lower needle lift flow domain displaying the region of local refinement (red sphere), 'Sphere of influence' method (Guide, 2012) has been used for local grid refinement.

4.4.2 Results: lower needle lift (1.6 mm)

Grid	(CV)*	Refinement method	Refinement factor (global)**	Refinement factor (local)†	Maximum y^+
1	1,792,278	global sizing	1	0	17.7
2	6,892,758	global sizing	3.84	0	10.44
3	11,049,454	global sizing	6.16	0	9.54
4	19,023,384	global sizing	10.61	0	7.5
5	16,410,517	locally refined from Grid 3‡	9.15	≈3	7.21
6	24,038,653	locally refined from Grid 3‡	11.83	≈4	7.14
7	33,446,472	locally refined from Grid 3‡	18.66	≈5	7.16

* Control Volumes

** The global mesh refinement factor is defined as the ratio between numbers of control volumes in the first mesh to numbers of control volumes in the compared mesh.

† The local mesh refinement is defined as the ratio of the overall size of the control volume (cell) to the size of the locally refined control volume.

‡ 'Sphere of influence' method (Guide, 2012) has been used for local grid refinement, the part (volume) of the flow domain locally refined can be seen in figure 4.11.

Table 4.7: Grid description, y^+ values are obtained after the simulations (see Figure 4.64 and 4.65)

It can be seen that similar profiles of the mean axial velocity are achieved in all planes (see Figure 4.4 and 4.5) in grids 5,6 and 7 (Figure 4.12 (a), Figure 4.13 (a), Figure 4.13 (c) and Figure 4.13 (e)). Hence, it can be inferred that the grid independence is being approached.

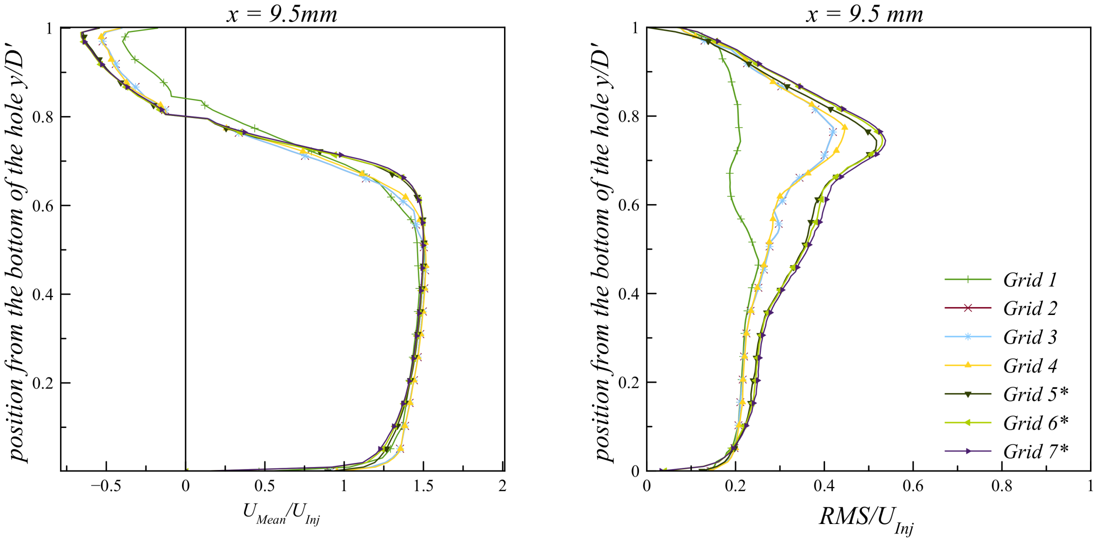

(a) (b)

Figure 4.12: Normalized mean axial velocity and RMS comparisons at x = 9.5 mm from the origin

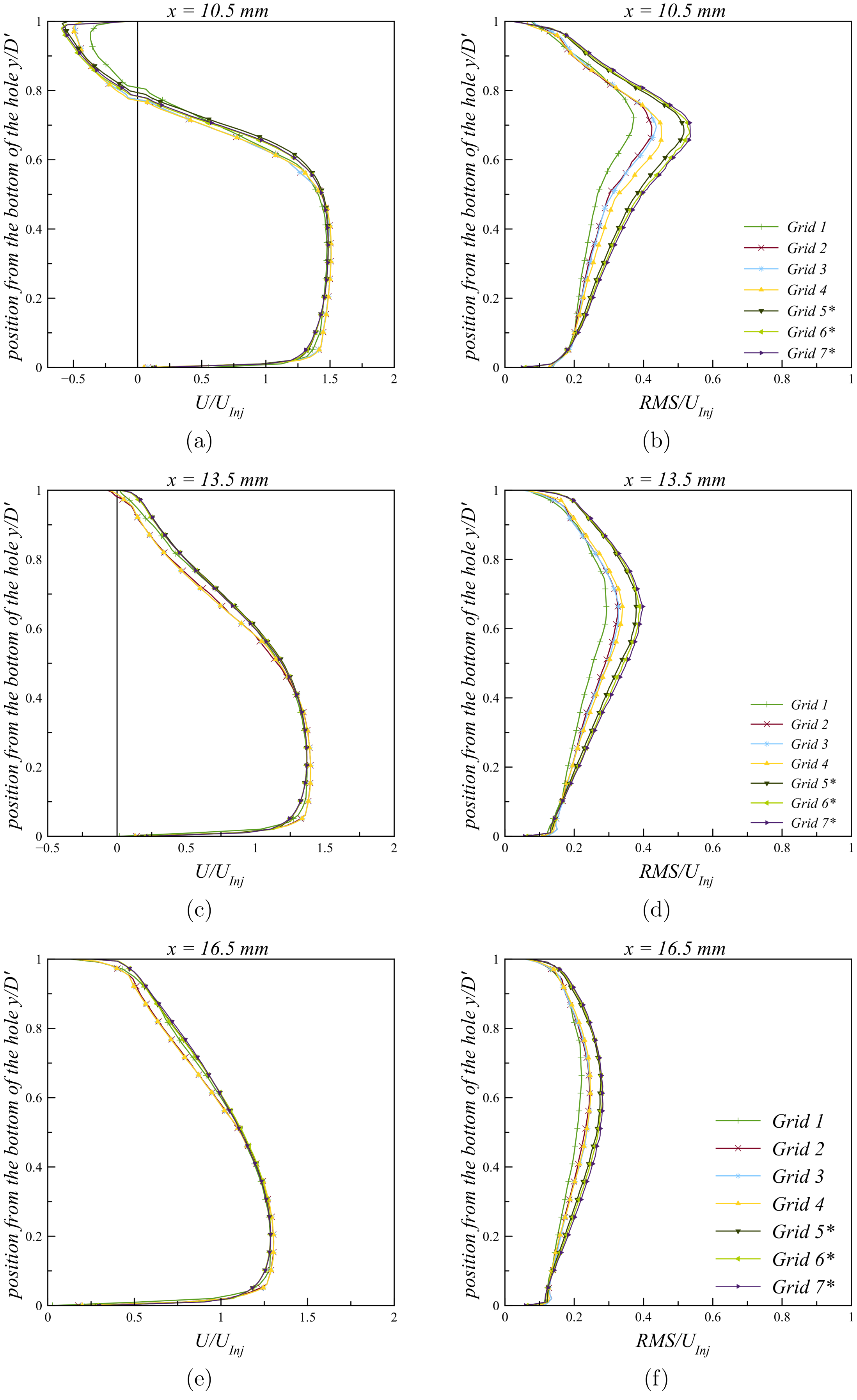

Figure 4.13: Normalized mean axial velocity and RMS comparisons at x = 10.5mm, 13.5 mm and 16.5 mm from the origin.

The RMS velocity is computed using Boussinesq formula (see Equation 3.20) increased with successive grid refinements (Figure 4.12 (b), Figure 4.13 (b), Figure 4.13 (d) and Figure 4.13 (f)); this is because when Boussinesq formula is used to compute the magnitude, the magnitude of RMS velocity depends on the magnitude of mean velocity gradients which increased with successive grid refinements.

4.4.3 Discussion: lower needle lift

- Similar results are achieved for the mean axial velocity from grids 5,6 and 7 therefore, it can be stated that grid independence is being approached for mean axial velocity.
- The RMS velocity magnitude increased with successive grid refinements. This is because the RMS velocity magnitude computed using the Boussinesq formula is dependent on the magnitude of the mean velocity gradients which increased with an increase of grid density.
- As aforementioned, the RMS velocity magnitude increased with successive grid refinements, however, change in the mean axial velocity was not as apparent as the RMS velocity. Hence, it can be stated that the RMS velocity magnitude is more sensitive to grid density than the mean axial velocity.

4.4.4 Results: nominal needle lift (6.0 mm)

Grid	(CV)*	Refinement method	Refinement factor (global)**	Maximum y^+
1	8,067,135	global sizing	1	10.70
2	13,016,832	global sizing	1.61	9.81
3	17,970,861	global sizing	2.22	8.6

* Control Volumes

** The global mesh refinement factor is defined as the ratio between numbers of control volumes in the first mesh to numbers of control volumes in the compared mesh.

Table 4.8: Grid description, y^+ values are obtained after the simulations (see Figure 4.66)

Similar results have been obtained for the mean axial velocity with all grids 1, 2 and 3 at all planes (Figure 4.14 (a), Figure 4.14 (c), Figure 4.14 (e), Figure 4.15 (a)). However improved profile of the mean axial velocity in grid 3 has been obtained particularly at the middle section of the plane x = 9.5 mm possibly due to a higher concentration of control volumes. Nonetheless, the results are very similar for the mean axial velocity; hence it can be argued that grid independence is being approached. Increase in the RMS velocity magnitude with successive grid refinement is seen (Figure 4.14 (b), Figure 4.14 (d), Figure 4.14 (e), Figure 4.15 (b)).

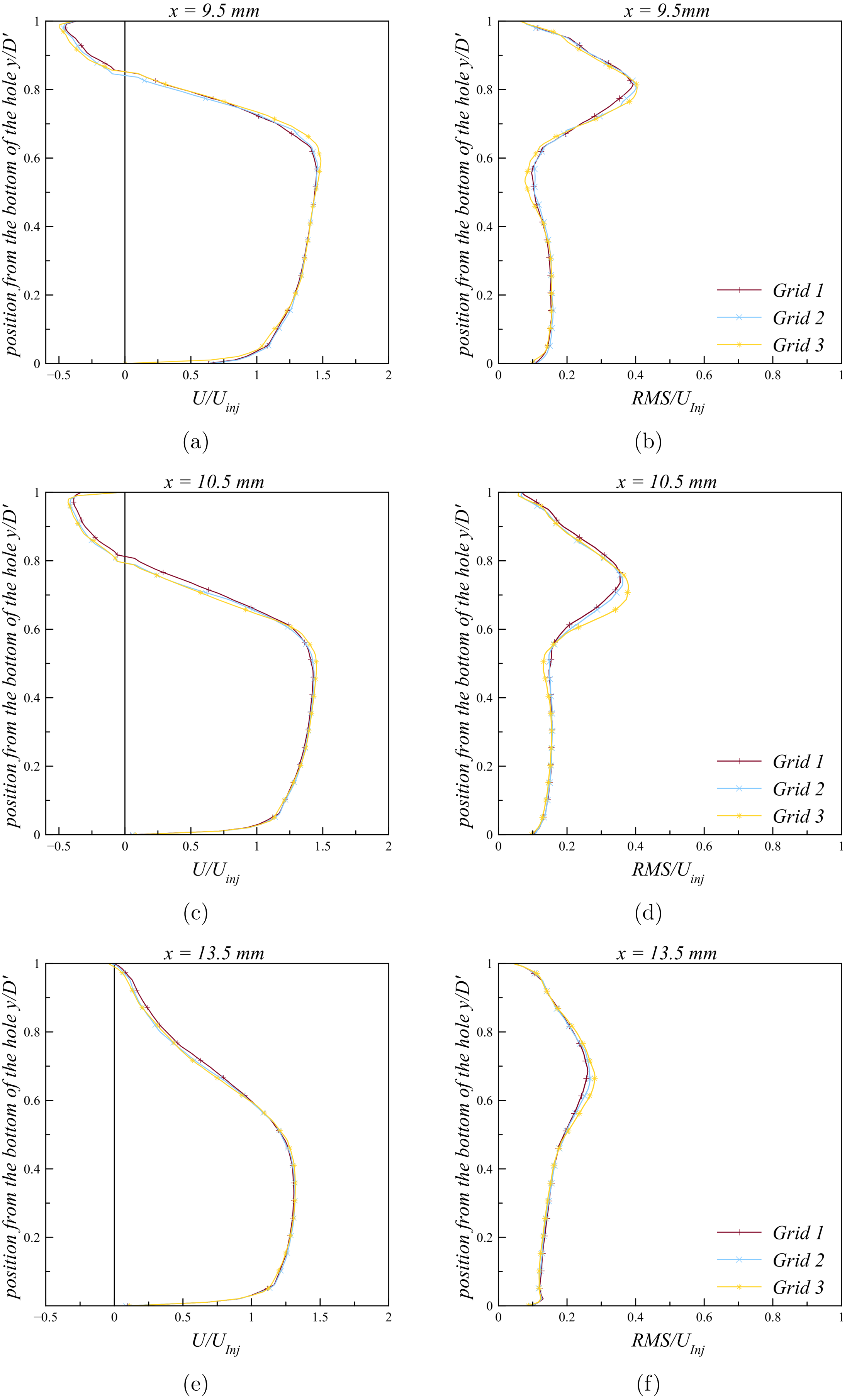

(a) (b) (c) (d) (e) (f)

Figure 4.14: Normalized mean axial velocity and RMS comparisons at x = 9.5 mm. 10.5 mm and 13.5 mm from the origin

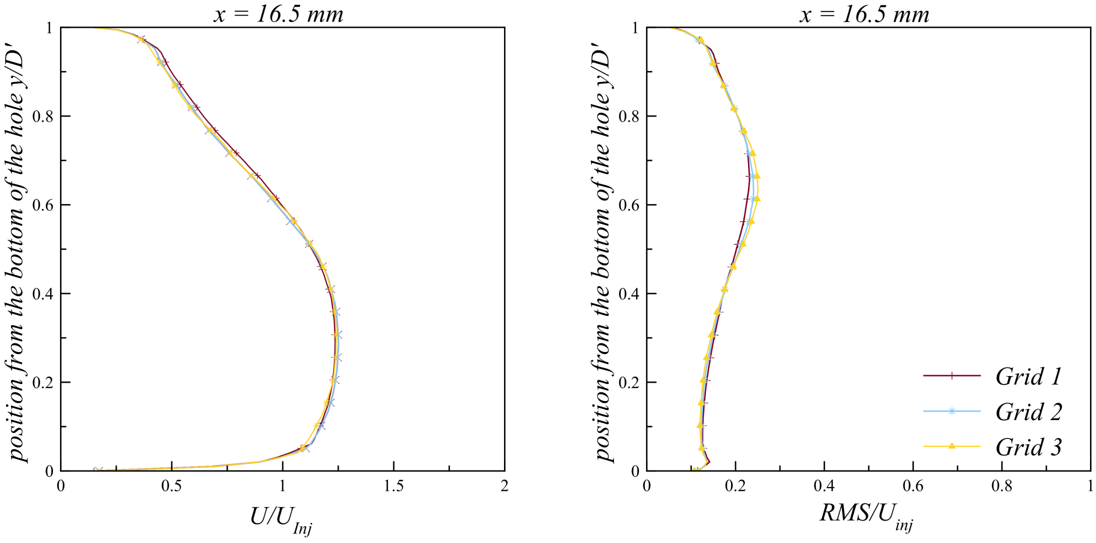

(a) (b)

Figure 4.15: Normalized mean axial velocity and RMS comparisons at x = 16.5 mm from the origin

4.4.5 Discussion: nominal needle lift

- Similar profiles for the mean axial velocity have been achieved with grids 1, 2, 3; hence it can be stated that grid independence is being approached for mean axial velocity.
- Increase in the RMS magnitude was observed with successive grid refinement, reason stated in § 4.4.2.

4.5 Physical modelling errors

4.5.1 Turbulence models comparison

Considering the Reynolds number, based on the diameter of the injector hole (see Equation (4.1)) is around 18000, we assess two high Reynolds number turbulence models for the accurate simulation of internal flow in the enlarged multi-hole (6) injector.

4.5.1.1 Case setup

Non-cavitating condition at low needle lift as described in Table 4.9 is simulated. Since the flow regime is quasi-steady (Roth et al., 2002; Roth, 2004), steady state simulations are performed using Reynolds-Averaged Navier-Stokes equations. From the previous study § 4.4.2, grid 6 has been used (Table 4.12). Simulations have been performed using the standard $k - \epsilon$ and the realizable $k - \epsilon$ model and the 'Enhanced Wall Treatment' method (see § 3.8.3) has been used to resolve near wall turbulence. The liquid phase is assumed to be incompressible. Boundary conditions are listed in Table 4.10.

$Series$	CN	Re	p_{inj}	p_{back}	U_{inj}	$Flow\ Rate$
1	0.44	18000	2.55 bar (absolute)	1.80 bar (absolute)	8.43 ms^{-1}	N/A*
2	0.44	18000	2.55 bar (absolute)	1.80 bar (absolute)	8.43 ms^{-1}	0.487 ls^{-1}

* Flow rate for the first series of experiments are not found in literature (Roth et al., 2002; Roth, 2004), but assumed to have same the value as given for the second series (0.487 ls^{-1}).

Table 4.9: Flow conditions for the first and second series of LDV measurements at lower needle lift

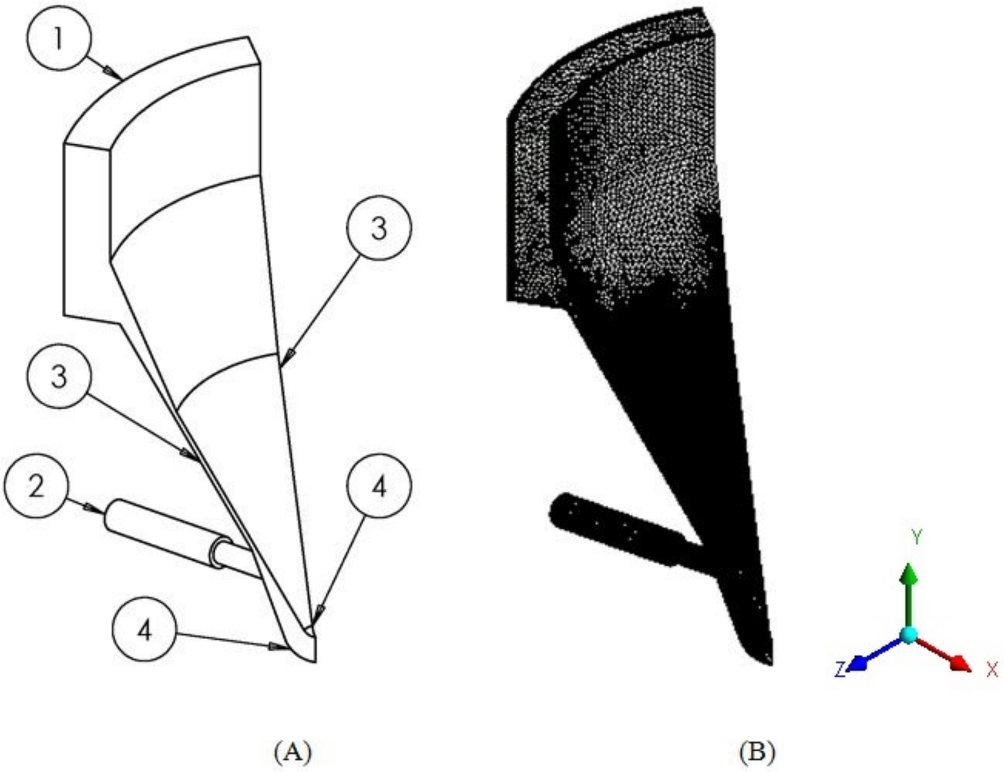

Figure 4.16: (A) One-sixth of the flow domain at low lift with periodic (cyclic) boundary conditions. The numbers represents boundaries of flow domains, (1) inlet (2) outlet (3) walls (4) periodic (cyclic) interface, (B) Mesh for one-sixth flow domain.

Inlet	Outlet	interface	Walls
mass-flow rate 0.0726 $kg\ s^{-1}$	constant pressure 180000 Nm^{-2}	cyclic	enhanced wall treatment method

Table 4.10: Boundary Conditions

4.5.1.2 Results

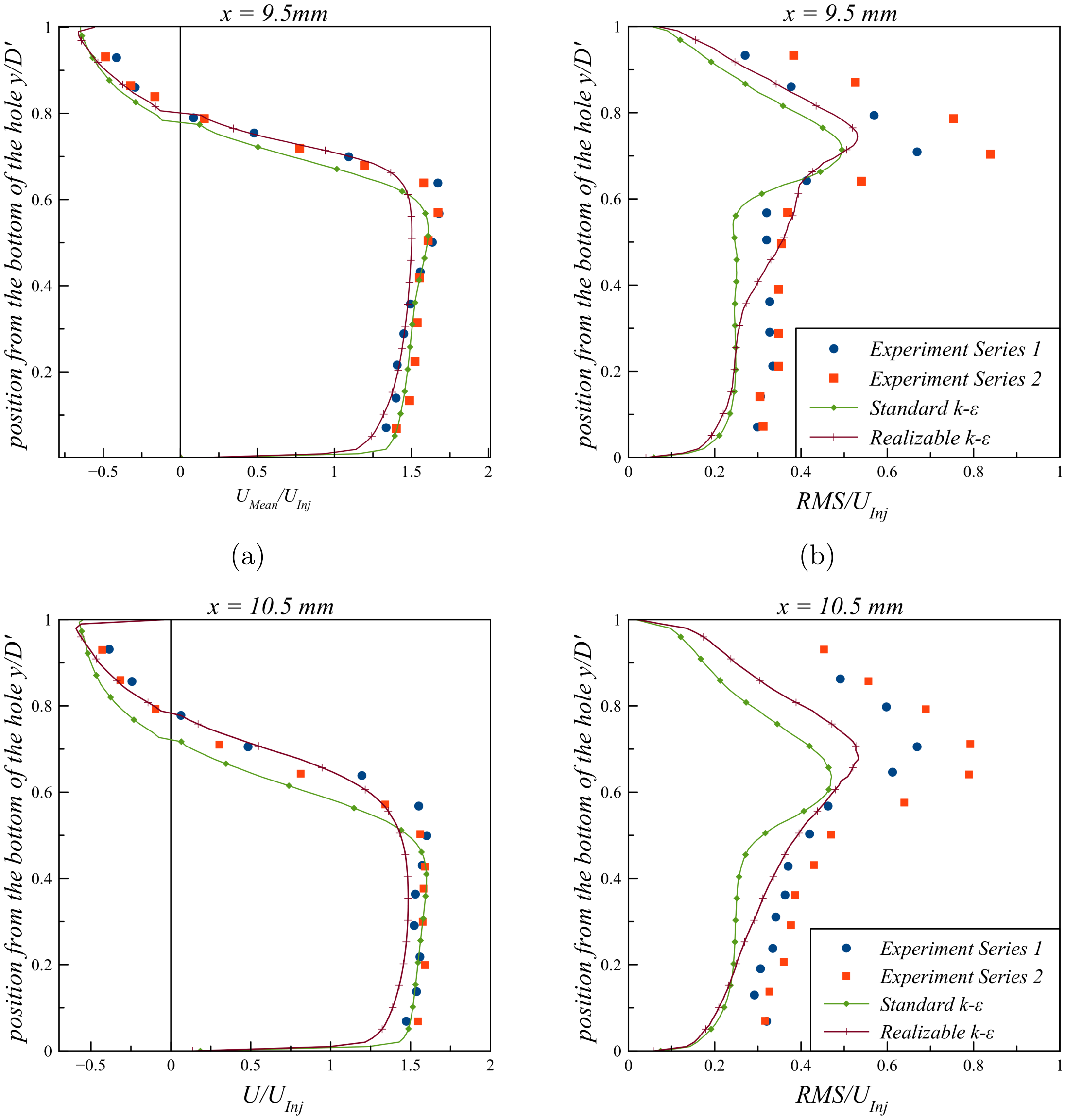

(a) (b)

(c) (d)

Figure 4.17: Normalized mean axial velocity and RMS comparisons at x = 9.5 mm and 10.5 mm from the origin.

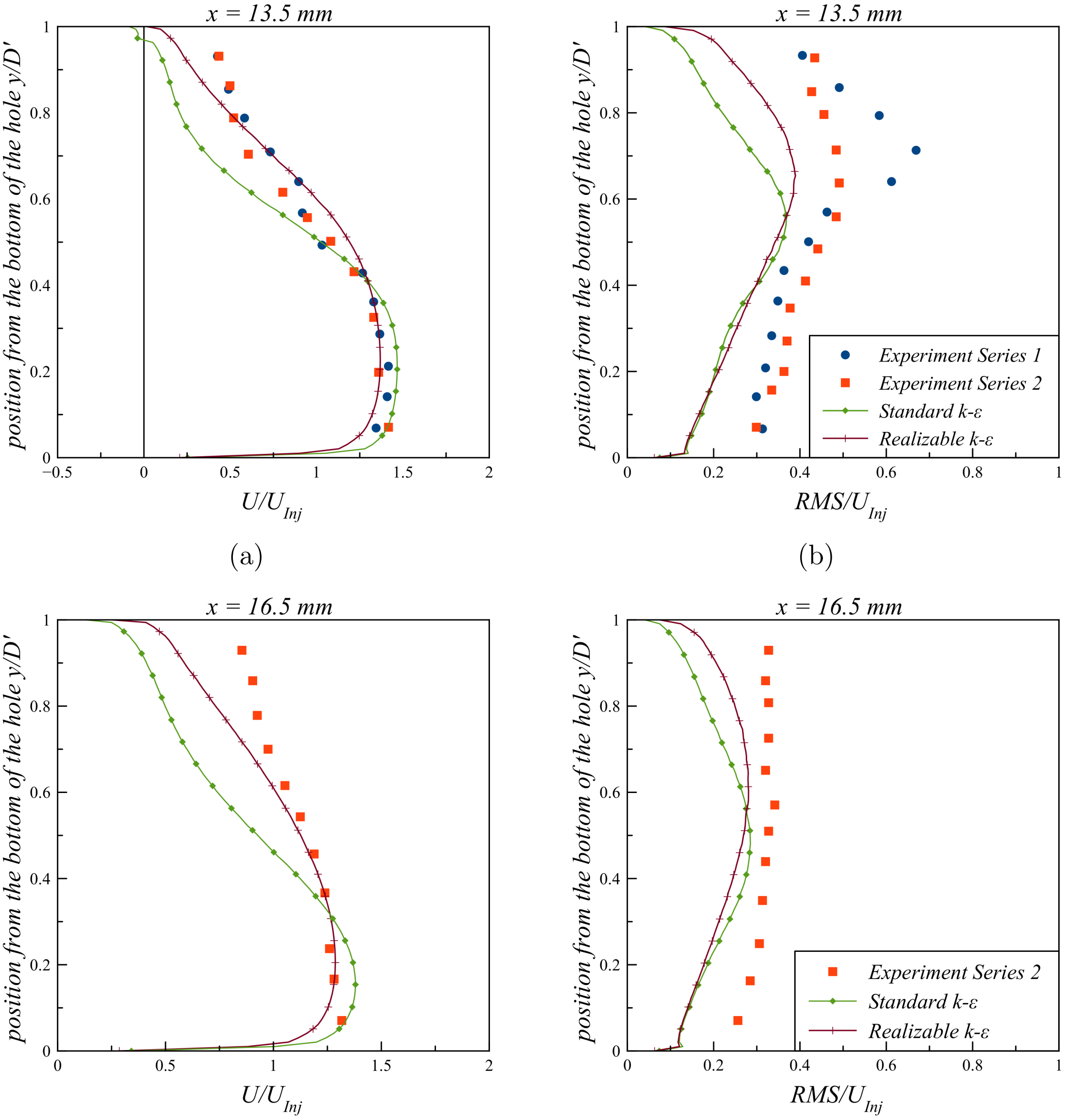

(a) (b)

(c) (d)

Figure 4.18: Normalized mean axial velocity and RMS comparisons at x = 13.5 mm and 16.5 mm from the origin.

Discrepancies in the experimental data, possibly due to needle eccentricity (Giannadakis et al., 2008) can be observed for both the mean axial velocity and RMS velocity for series 1 and 2 experimental data (Figure 4.17 (a), (b), (c), (d) and Figure 4.18 (a) and (b)). At the axial location close to the entrance of the injector hole (x = 9.5 mm), (Figure 4.17 (a)), ($0.8 < y/D' < 1$) experimental data indicates a recirculation region at the upper portion of the plane. It can be seen from Figure 4.17 (a) that recirculation region is more accurately predicted using the realizable $k - \epsilon$ model. The mean axial velocity from the bottom of the injector hole plane to the middle portion ($0.0 < y/D' < 0.6$) are slightly better predicted with the standard $k - \epsilon$ model, however, simulation results improve for the realizable $k - \epsilon$ model in the injector hole from $0.0 < y/D' < 0.6$ (Figure 4.17 (a)). Higher values of RMS velocity (Figure 4.17 (b)) have been predicted using the realizable $k - \epsilon$ model which are also in better agreement with the experimental data despite discrepancies in the experimental data between first and second series of the experiment.

Case	Turbulence models	Control volumes (CV)	Maximum y^+
1	Standard $k-\epsilon$	24,038,653	7.144
2	Realizable $k-\epsilon$	24,038,653	7.144

Table 4.11: Mesh description, y^+ values are obtained after the simulations.

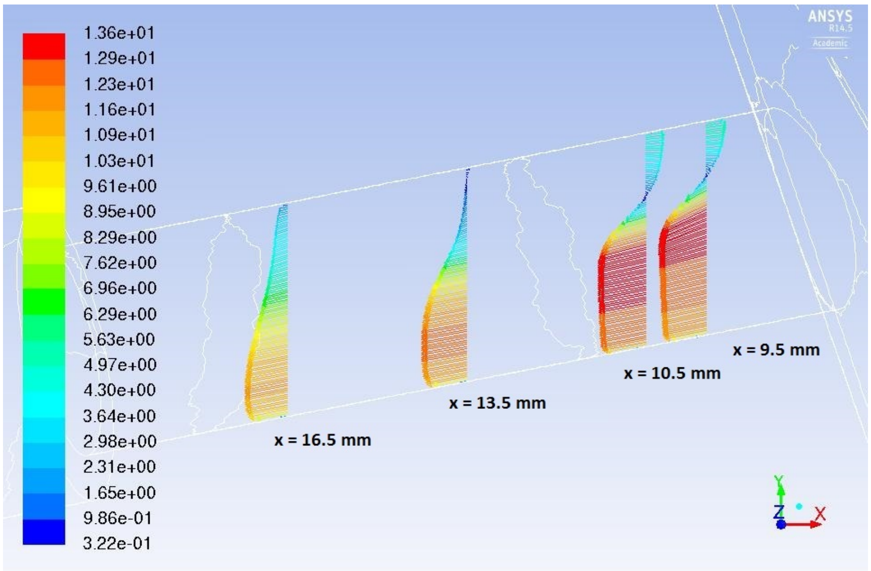

(a) standard $k-\epsilon$ model

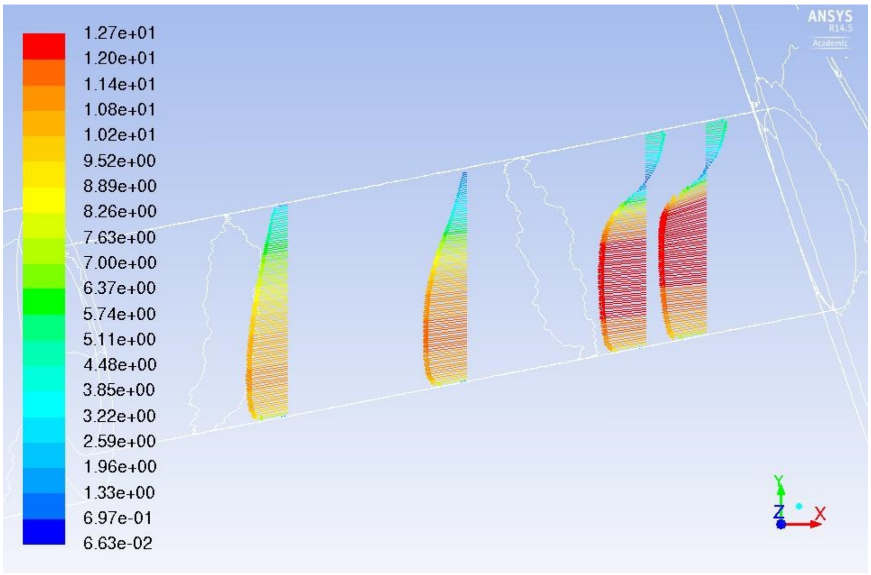

(b) realizable $k-\epsilon$ model

Figure 4.19: Mean velocity profiles (vector) at different planes obtained using standard $k-\epsilon$ and realizable $k-\epsilon$ models.

Similarly on the plane x = 10.5 mm, it can be seen that a recirculation region is more accurately predicted using the realizable $k-\epsilon$ model, however, it can be stated that a slightly better agreement has been achieved for the mean axial velocity using the standard $k-\epsilon$ from the bottom of the plane to the mid of the plane ($0 \leq y/D' \leq 0.5$). The RMS velocity is in better agreement with the experimental data.

On the plane x = 13.5 mm, experimental data for the mean axial velocity (Figure 4.18 (a)) indicates that the flow has reattached. The mean axial velocity prediction using the realizable $k-\epsilon$ shows reattachment and is in better agreement with the experimental data while predictions using the standard $k-\epsilon$ model suggest recirculation. The predicted RMS velocity (Figure 4.18 (b)) using the realizable $k-\epsilon$ model is also in better agreement with the experimental data. On the plane x = 16.5 mm (Figure 4.17 (c)), the experimental data suggest a flow recovery however it is not yet fully recovered. Again better agreement with the experimental data is achieved using the realizable $k-\epsilon$ model. The RMS result is also in better agreement with the experimental data using the realizable $k-\epsilon$ model (Figure 4.18 (d)). The difference in the velocity profiles at different planes using two the turbulence models can also be seen in velocity vectors at all planes in Figure 4.19 (a) and Figure 4.19 (b).

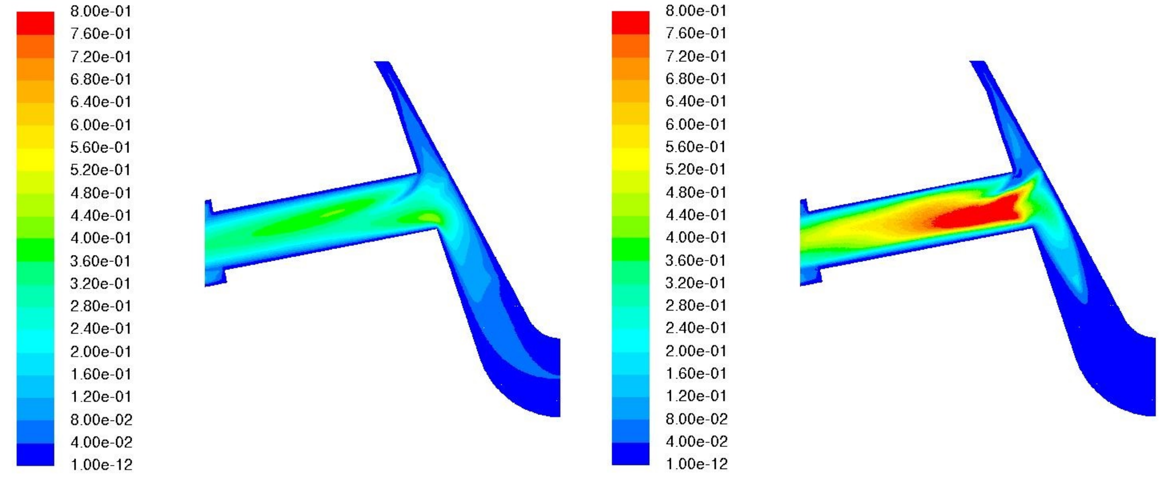

(a) μ_t standard $k-\epsilon$ (b) μ_t realizable $k-\epsilon$

Figure 4.20: Comparison of turbulent viscosity of standard $k-\epsilon$ and realizable $k-\epsilon$ turbulence models on x-y plane

4.5.1.3 Discussion: models comparison

- The recirculation region, flow reattachment and flow recovery are more accurately predicted using the realizable $k-\epsilon$ model than the standard $k-\epsilon$ model for the present application.
- The standard $k-\epsilon$ has a constant C_μ while the realizable $k-\epsilon$ model has a variable C_μ. The C_μ directly influences the turbulent viscosity μ_t and therefore the flow field.
- The variable C_μ in the realizable $k-\epsilon$ model is there to ensure the realizability or to ensure that normal stresses $\overline{u_i'^2}$ do not become negative (Schumann, 1977; Lumley, 1979). Shih et al. (1994) also mentioned that many modellers i.e. Reynolds (1987) have suggested different values for C_μ for different types of flows which have been supported by experimental data (Reynolds, 1987; Shih et al., 1994) i.e. appropriate value for C_μ is found to be

around 0.09 in the logarithmic layer of equilibrium boundary layers, and 0.05 in a strong homogeneous shear flow.

- Nevertheless, the differences in the flow field due to the different formulation of turbulent viscosity, μ_t (Figure 4.20 (a) and (b)) which is due to the different formulations of C_μ in the two models are evident. Therefore, from the present results, it can be inferred that due to the different formulation of μ_t, the realizable $k-\epsilon$ model has captured the recirculation region, flow reattachment and flow recovery or the overall flow field more accurately than the standard $k-\epsilon$ model for the present application.

4.5.2 Near wall modelling

In this section, near wall modelling approaches are evaluated for internal flow predictions of an enlarged symmetric multi-hole (6) diesel fuel injector. The modelling approaches which have been evaluated are: 1) Launder and Spalding approach and 2) Enhanced Wall Treatment method.

4.5.2.1 Case setup

Non-cavitating condition at low needle lift as described in Table 4.9 is simulated. Steady-state simulations have been performed. Turbulence effects are introduced using the realizable $k-\epsilon$ model (Shih et al., 1994) (see § 3.7.2). In the first simulation 'Launder and Spalding (1974) wall functions' are used to resolve near wall turbulence. In the subsequent simulation, 'Enhanced Wall Treatment' method has been used to resolve near wall turbulence. From the previous study § 4.4.2, grid 6 has been used (Table 4.12). The liquid phase is assumed to be incompressible. Boundary conditions are listed in Table 4.10

4.5.2.2 Results

Case	Near-wall modelling	Control volumes (CV)	Maximum y^+	Maximum y^*
1	Launder and Spalding approach	24,038,653	7.06	6.90
2	Enhanced Wall Treatment	24,038,653	7.14	8.95

Table 4.12: Grid description, y^+ and y^*values are obtained after the simulations (see Figure 4.23 (a) & (b) and 4.22 (a) & (b)).

While comparing the predicted mean axial velocity on the plane x = 9.5 mm (Figure 4.21 (a)), it can be seen that good agreements are achieved with the experimental data using both approaches. On the plane x = 10.5 mm (Figure 4.21 (b)) it can be seen that a slightly better agreement with the experimental data for the mean axial velocity is achieved using the Enhanced wall treatment' method. Furthermore, on observing predicted the mean velocity profiles on planes x = 9.5 (Figure 4.21 (a)) and x = 10.5 (Figure 4.21 (b)), it can be seen that a recirculation region at the upper edge of the injector hole entrance is more accurately predicted using the 'Enhanced wall treatment' method. Besides, from the predicted mean axial velocity at each plane (Figure 4.21 (a), (b), (c) and (d)), it can be seen that transition of velocity from laminar to turbulence region is more gradual using the 'Enhanced wall treatment' method than using the 'Launder and Spalding wall functions'. Nonetheless, on the planes x = 13.5 mm (Figure 4.21 (c)) and 16.5 mm (Figure 4.21 (d)), overall mean axial velocity predictions are similar using both approaches.

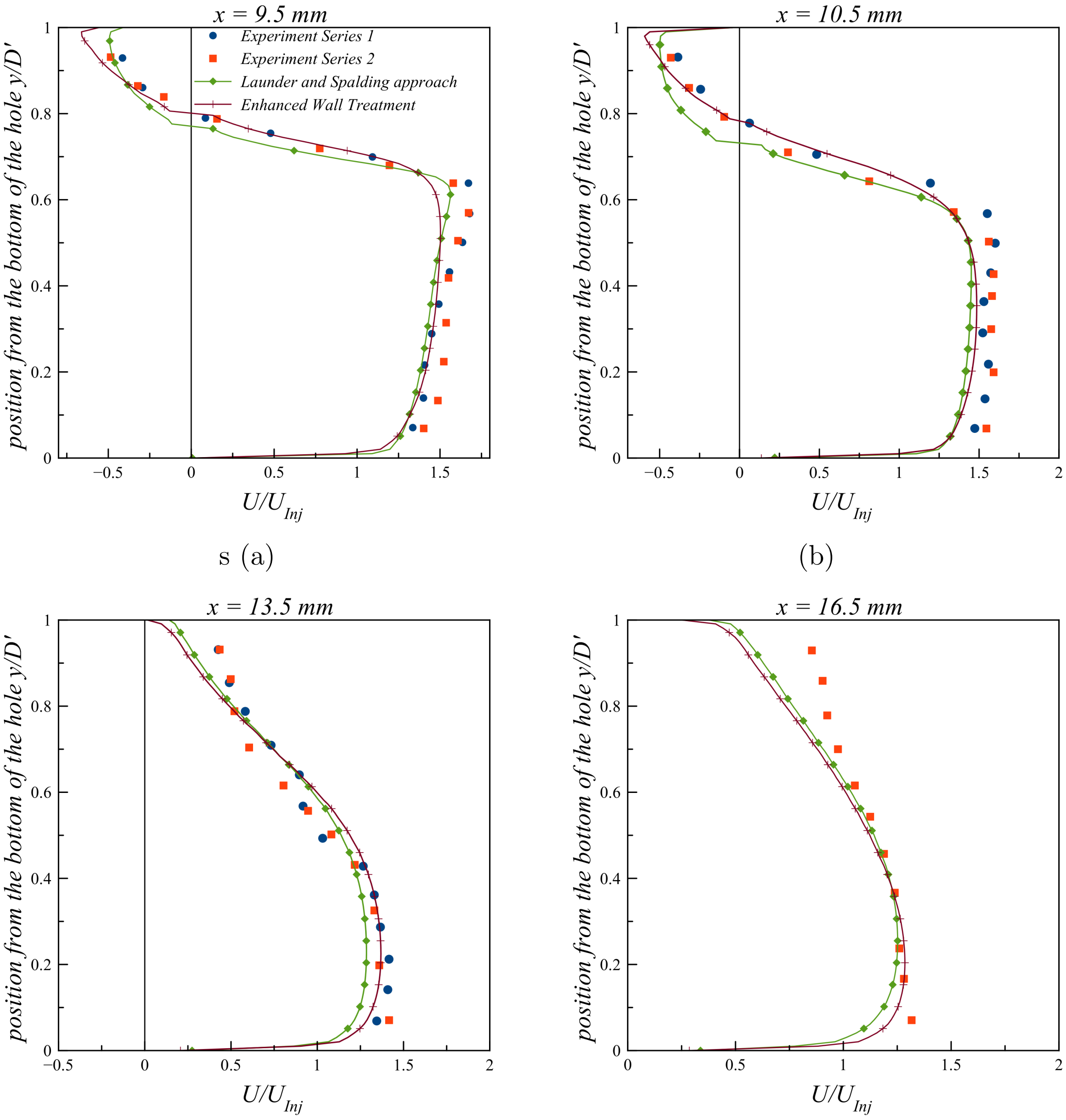

s (a)

(b)

(c)

(d)

Figure 4.21: Normalized mean axial velocity comparisons for near wall modelling approaches

4.5.2.3 Discussion: near wall modelling

- The predicted mean axial velocity profiles clearly indicate a recirculation region at the upper edge of the injector hole entrance, which is more accurately predicted using the 'Enhanced wall treatment' method.
- The 'Launder and Spalding wall functions' are based on the modified logarithmic law, which is said to be valid from $30 < y^* < 300$ and is applied when $y^* > 11.225$, when the $y^* < 11.225$, the model applies laminar stress-strain relationship ($U^* = y^*$).

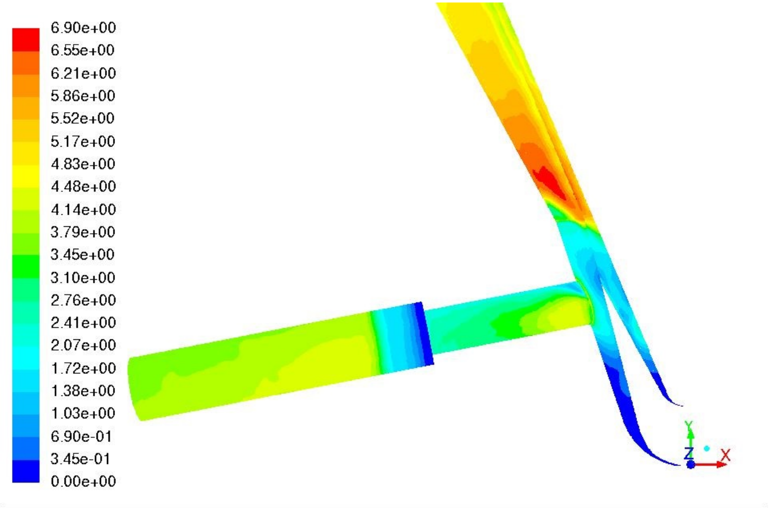

(a) y^* Launder and Spalding approach

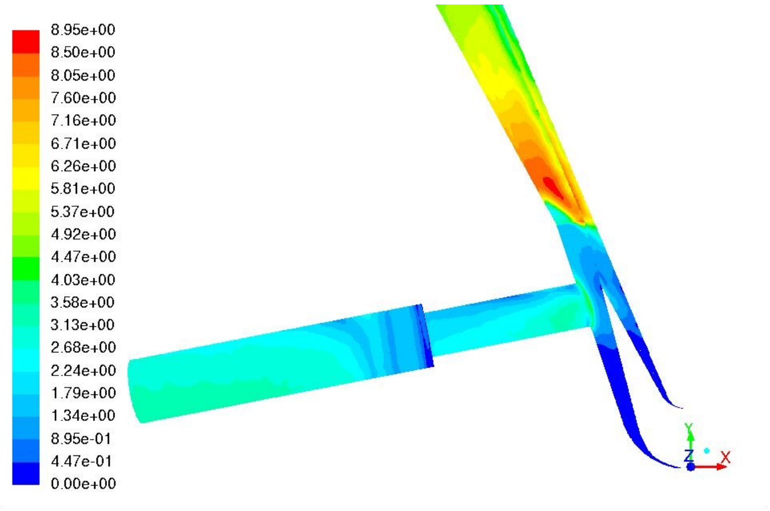

(b) y^* Enhanced wall treatment method

Figure 4.22: y^* comparisons

- The ‘Launder and Spalding wall functions’ have a lower limit of $y^* \approx 15$. The ‘Launder and Spalding wall functions’ would typically deteriorate below this limit and the solution accuracy would be compromised (Launder and Spalding, 1974). It can be seen that y^* in the Figure 4.22 (a), values lower than 15 have been obtained around the injector hole and could have been a reason for the larger recirculation region predicted at the upper edge entrance of injector hole.

- The ‘Enhanced wall treatment’ method is a near wall modelling approach implemented in ANSYS Fluent, it combines ‘two-layer model’ and‘enhanced wall functions’. In the region where the mesh is fine enough ($y^+ \approx 1$), the model acts like a two-layer model. In the ‘two-layer model’ viscosity of the laminar region is smoothly blended with turbulence viscosity using a blending function proposed by Jongen (1998). In the so-called ‘enhanced wall functions’ , the law-of-the-wall is formulated for the entire wall region. This is achieved by blending the linear and logarithmic law-of-the-wall using a function suggested by Kader

(1981). Therefore, it can be seen that in the present case, the 'enhanced wall treatment' method predicted overall better velocity profiles.

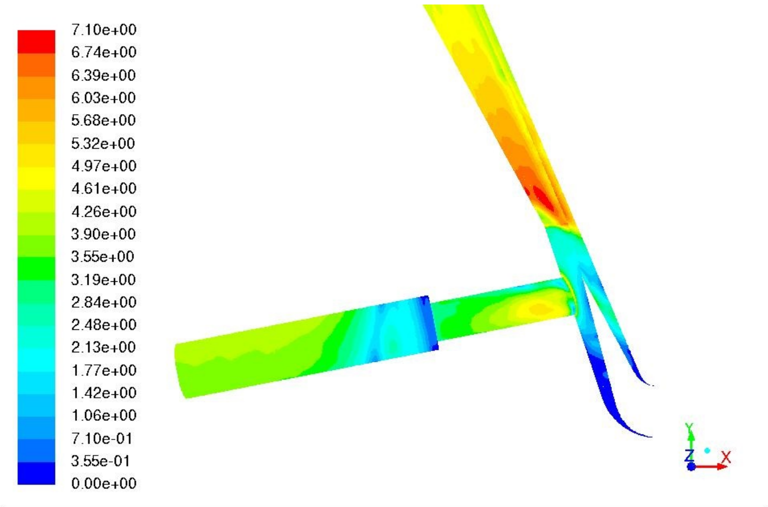

(a) y^+ Launder and Spalding approach

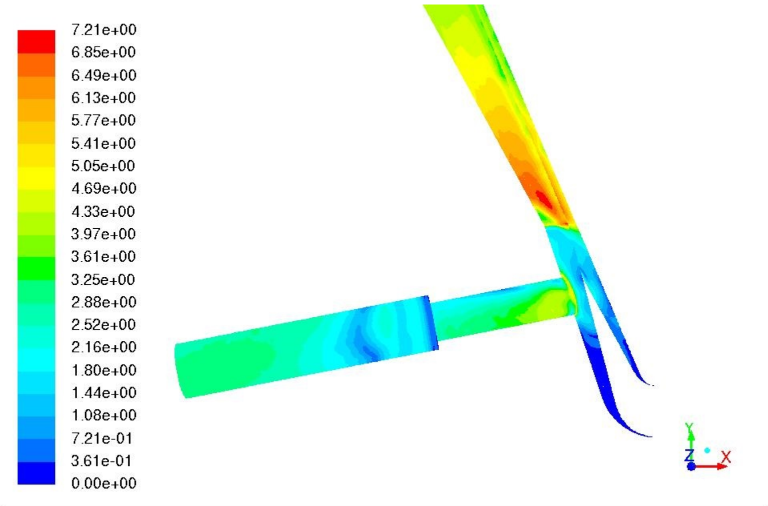

(b) y^+ Enhanced wall treatment method

Figure 4.23: y^+ comparisons

4.6 Validation at the nominal needle-lift

In the previous section § 4.5, we analysed turbulence model behaviour at the lower needle lift (1.6 mm offset from the needle seat) which represents the 1st stage of the fuel injection process in the real size injector. The nominal needle lift (6.00 mm offset from the needle seat) in the enlarged multi-hole injector represents the second stage of the fuel injection process in the real size injector at which maximum flow occurs. As the needle translate upward, the clearance between the needle wall and the injector body increases which changes the flow. Hence, in this section, flow simulation and comparisons with experimental measurement are also required at the nominal needle lift condition. In section the 'grid sensitivity analysis' § 4.4.4, the mean axial velocity results suggested grid independence is being approached. We use the results obtained from grid 3 and compare them with experimental data for the mean axial velocity and RMS velocity. Turbulence model (realizable k-ϵ, see § 4.5.1) and near wall turbulence modelling approach (Enhanced wall treatment, see § 4.5.2) have not been changed.

4.6.0.1 Results:

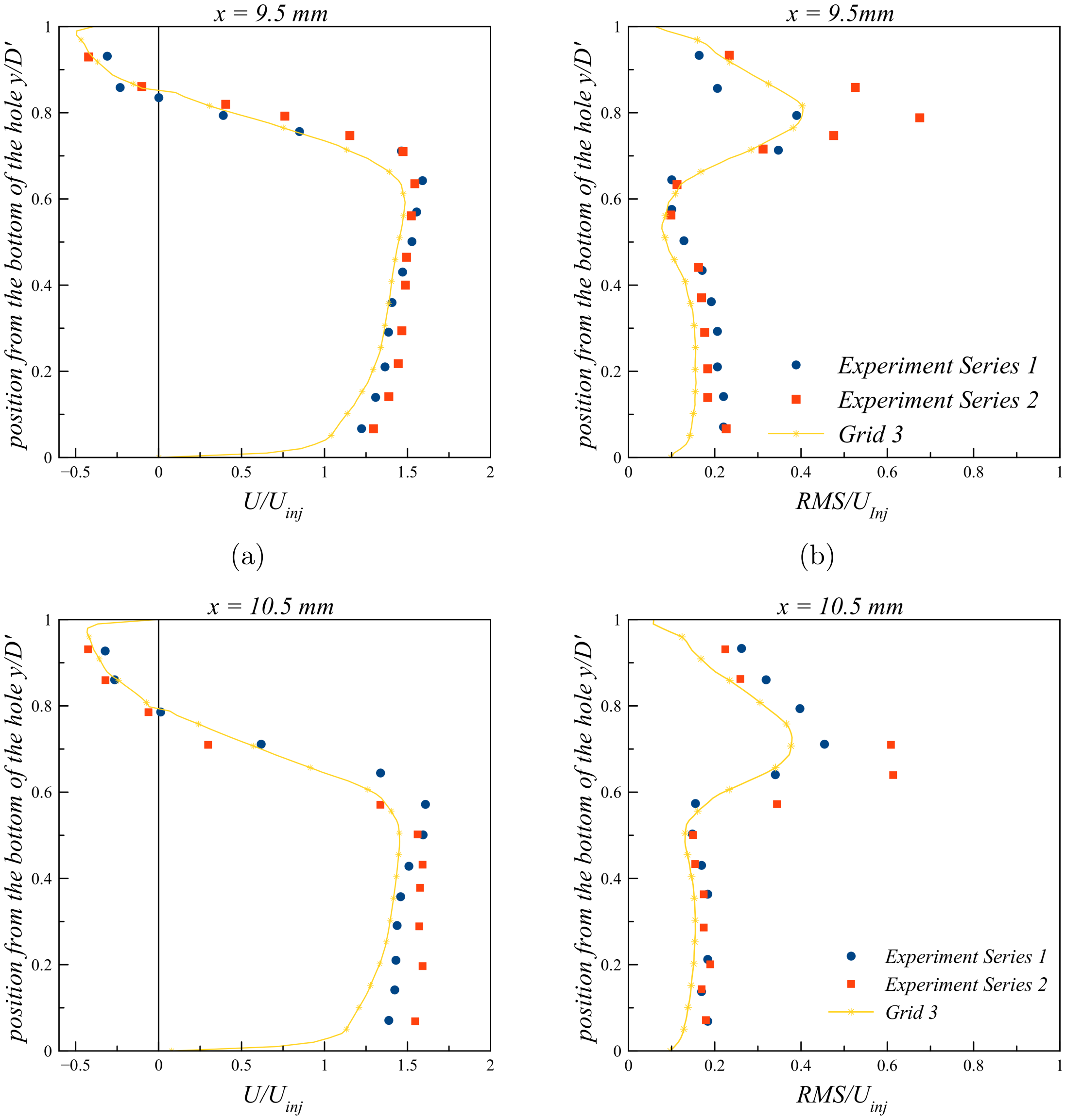

(a) (b)

(c) (d)

Figure 4.24: Normalized mean axial velocity and RMS comparisons at x = 9.5 mm and 10.5 mm from the origin

Differences in the experimental data between series 1 and series 2 experiments can be seen for both the mean axial velocity and RMS velocity (possible reasons mentioned in the previous section § 4.5.1). On the plane x = 9.5 mm (Figure 4.24 (a)), the mean axial velocity results from the experimental data suggest a recirculation region at the upper region of the plane in injector hole. Simulation results showed that a good agreement has been achieved for the mean axial velocity and RMS velocity (Figure 4.24 (b)) throughout the plane.

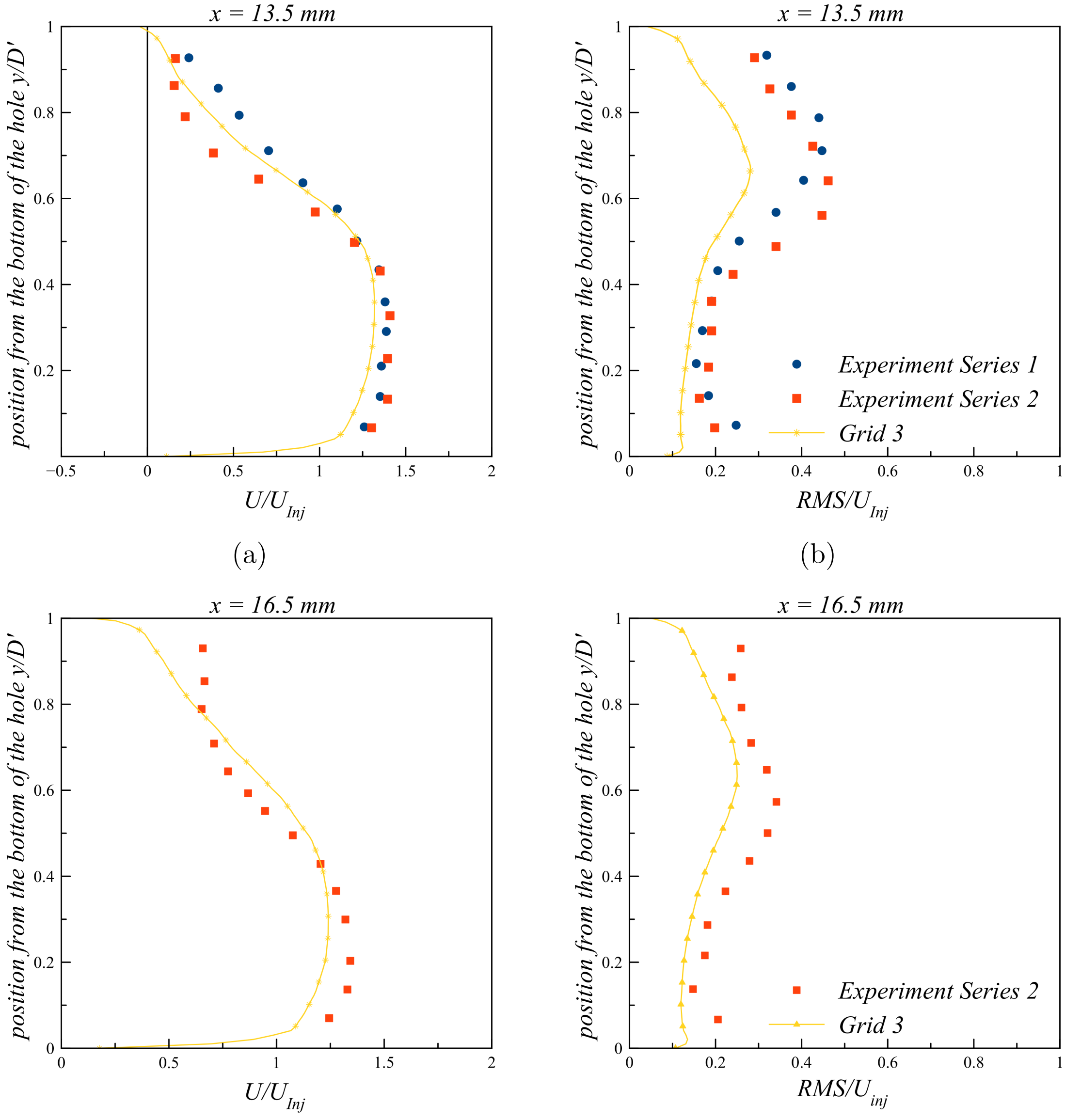

(a) (b)

(c) (d)

Figure 4.25: Normalized mean axial velocity and RMS comparisons at x = 9.5 mm and 10.5 mm from the origin

On the plane x = 10.5 mm (Figure 4.24 (c)), the experimental data again suggest a recirculation at the upper region of the plane in the injector hole. Simulation results for the mean axial velocity again show a good agreement with the experimental data in the recirculation region,and fairly good agreement in the remaining section of the plane. Simulation results for the RMS velocity (Figure 4.24 (d)) also show a good agreement with the experimental data.

On the plane x = 13.5 mm (Figure 4.25 (a) and (b)), large differences in the experimental data for the mean axial velocity and RMS velocity between series 1 and 2 experiment can be found. Nevertheless, on observation of the experimental data, it can be argued that the experimental data for the mean axial velocity suggest a possible reattachment near the plane x = 13.5 mm.

Simulation results for the mean axial velocity do not show a reattachment at the plane x = 13.5 mm, but show the recirculating flow on the top of the plane, Nevertheless simulation results for the mean axial velocity are in fair agreement with the experimental data. The RMS velocity (Figure 4.25 (b)) is under predicted but shows the same shape as the experimental data do.

On the plane x = 16.5 mm (Figure 4.25 (c)), the experimental data for the mean axial velocity indicate that flow has started to recover after reattachment; fairly good agreement for the mean axial velocity has been achieved. The RMS velocity (Figure 4.25 (d)) is under-predicted, but shows the same shape as that of the experimental data. The predicted velocity profile can also be seen at each plane in Figure 4.26.

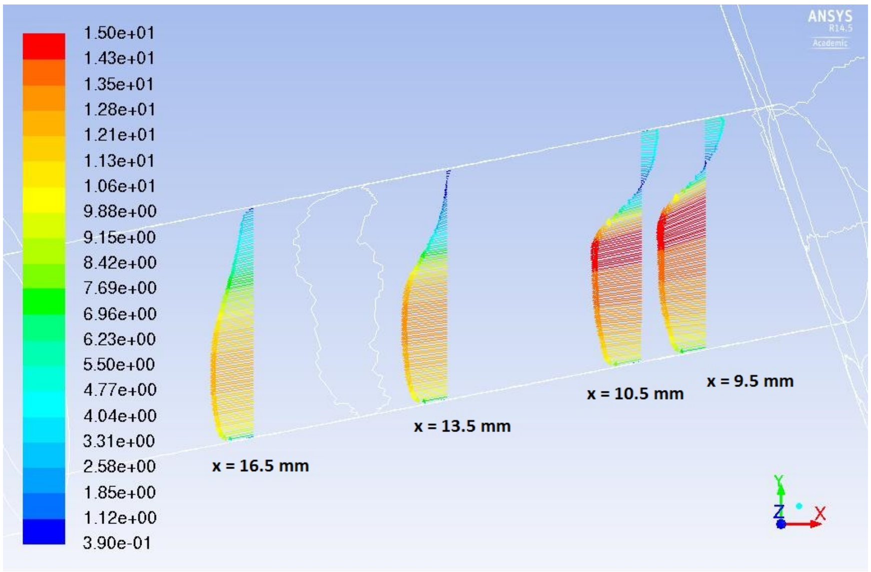

Figure 4.26: Velocity vectors at nominal needle lift, grid 3.

4.6.0.2 Discussion: nominal needle lift

- Variation in the experimental data for the mean axial velocity and RMS velocity between the first and second series of experiments can be seen, which could be speculated due to the possibility of eccentricity of needle as mentioned by Giannadakis et al. (2008).
- Simulation results shows that fairly good agreement with experimental data for the mean velocity and RMS velocity has been achieved.

4.7 Flow field analysis:

Experimental studies on multi-hole injectors revealed the occurrence of cavitation at the upper edge of the entrance of the injector hole (Soteriou et al., 1995; Arcoumanis et al., 2001; Roth et al., 2002; Roth, 2004; Andriotis, 2009). As the fluid enters the injector hole, the sudden reduction of the cross-sectional area enhances the fluid acceleration, in addition, the abrupt change of fluid path causes the fluid to separate from the wall. So, when the fluid re-attaches to the wall it starts to form a recirculation region at the upper edge of the entrance of the injector hole. When the pressure in such recirculation zone goes below the vapour pressure of the liquid then the liquid starts to boils and forms vapour pockets/bubbles. This process is called 'geometrically induced cavitation'.

In multi-hole injectors, cavitation structures due to vortex formation between the sac volume and the injector holes have been observed. Mainly two types of such cavitation structures have been observed: 1) 'hole-to-hole' connecting string cavitation (Figure 2.7 (a)) and 2) 'needle string' or needle cavitation (Figure 2.7 (b)). The 'hole-to-hole' connecting cavitation has been attributed to the formation of a vortex in the volume between the needle, needle seat and two adjacent holes (Afzal et al., 1999; Arcoumanis et al., 2001; Roth et al., 2002; Roth, 2004). 'Needle strings' were attributed to the strong vortex flow around the injector hole axis, leading to the low-pressure region in the vortex core to initiate cavitation (Roth et al., 2002; Roth, 2004). These vortices are stated as prerequisites of vortex type cavitating structure. Therefore, the present section is focussed on detection of such complex vortices and identifying reasons of their formations at the non-cavitating conditions. The outcome of this study can help in identifying the potential cavitation sites and understanding of the formation of such complex vortex structures at cavitating conditions in diesel multi-hole injectors.

4.7.1 Lower needle lift (1.6 mm) flow field:

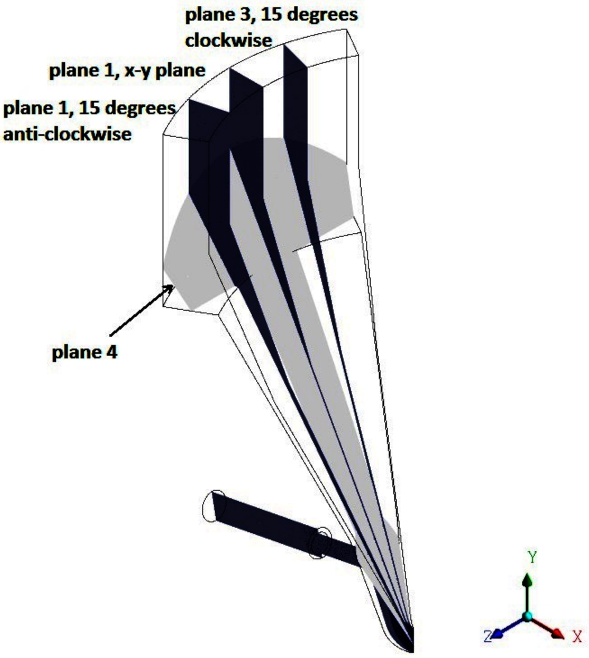
plane 3, 15 degrees clockwise
plane 1, x-y plane
plane 1, 15 degrees anti-clockwise
plane 4
Y
Z
X

Figure 4.27: planes in flow domain for flow field analysis

Therefore, to gain the understanding of the flow field, planes have been set up in the flow domain. The plane 1 is located on the x-y axis, The plane 2 is 15° anti-clockwise and plane 3 is 15° clockwise from an x-y plane. plane 4 is generated parallel to the annulus as shown in Figure 4.27. Results from grid 6 have been used for post processing (see § 4.4.2).

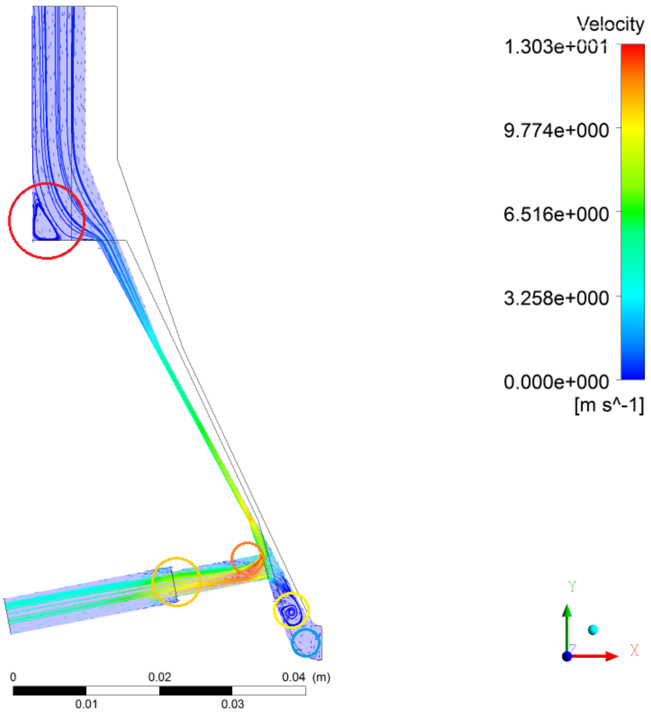

Figure 4.28: 2D velocity streamlines on plane 1.

2D streamlines on plane 1 indicate the presence of vortices in the injector (Figure 4.28). The vortical structure can be seen at the sharp corner (red circle) of the cartridge before the fluid enters the needle a seat annulus. Vortices can also be seen in the sac region as highlighted using yellow and blue circles. Recirculation zone at the entrance of the nozzle hole due to sharp inlet can be seen (highlighted using an orange circle). Vectors have been plotted on the x-y plane which suggests that velocity is approaching the parabolic profile in Figure 4.29.

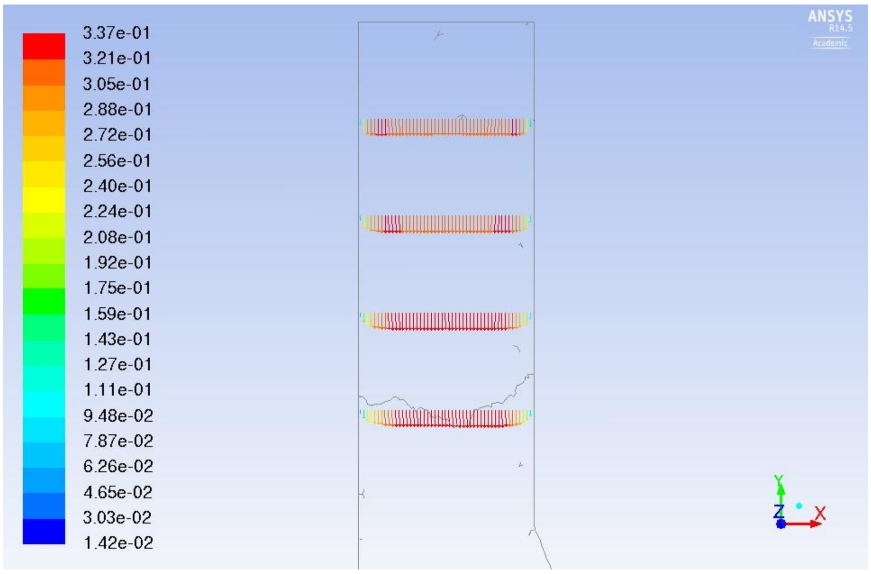

Figure 4.29: Vectors plotted on the x-y plane, indicating that velocity is approaching parabolic profile.

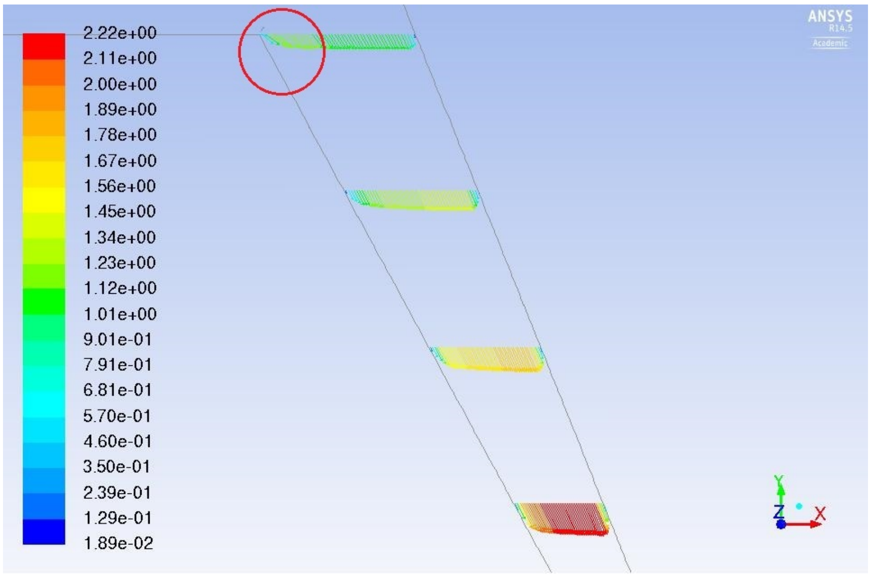

Figure 4.30: Velocity profile on x-y plane as fluid enters the inclined annulus.

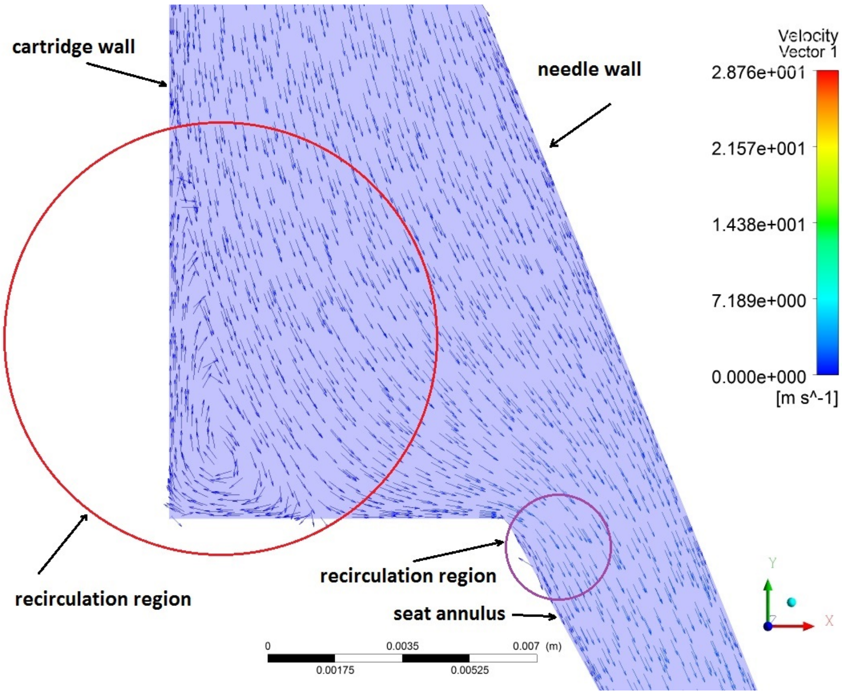

Figure 4.31: Zoom of vortex at the sharp corner, showing clockwise direction of the vortices

The vortical structure can be seen at the sharp edge wall (red circle, Figure 4.31) of the cartridge before the fluid enters the needle seat annulus. From the Figure 4.30 it can also be seen that fluid separates from the wall as it enters the seat annulus due to the sharp-edged wall between the cartridge and needle as shown using red circle.

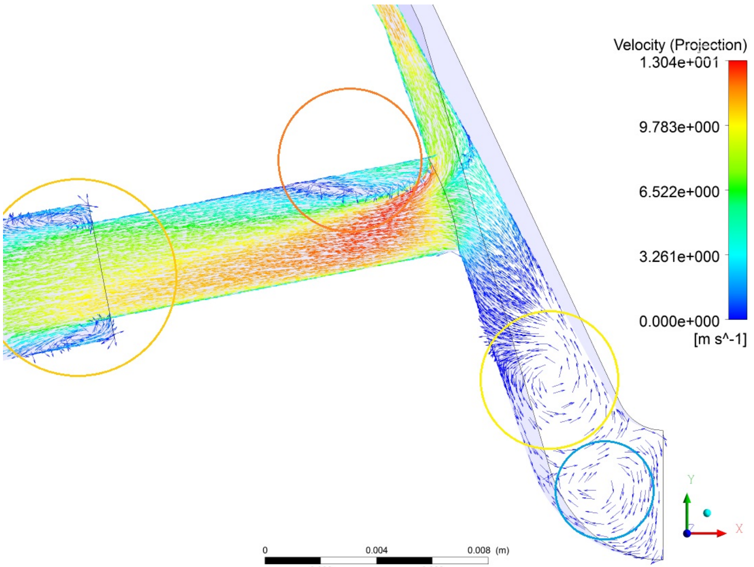

Figure 4.32: Zoom of vortices in the sac region and recirculation region on injector hole

The magnified view of sac region (Figure 4.32) on plane 1, reveals the presence of vortices. The vortex in the sac in the anti-clockwise direction ($+x$, $+y$, $+z$ view) is highlighted using the yellow circle and a vortex in a clockwise direction in a sac volume is highlighted using a blue circle. The recirculation region at the upper edge of the entrance of the injector hole is highlighted using the orange circle. Corresponding to the velocity vectors, the pressure contour (Figure 4.33) suggests a lower pressure at the upper edge of injector hole which corresponds to the expected lower pressure at the recirculation region. In Figure 4.32, it can also be seen that as the fluid exits the nozzle injector hole and enters the back flow hole, it again separates from the wall and hence a ring-shaped vortex is formed at the entrance of the back flow hole (highlighted using the dark yellow circle).

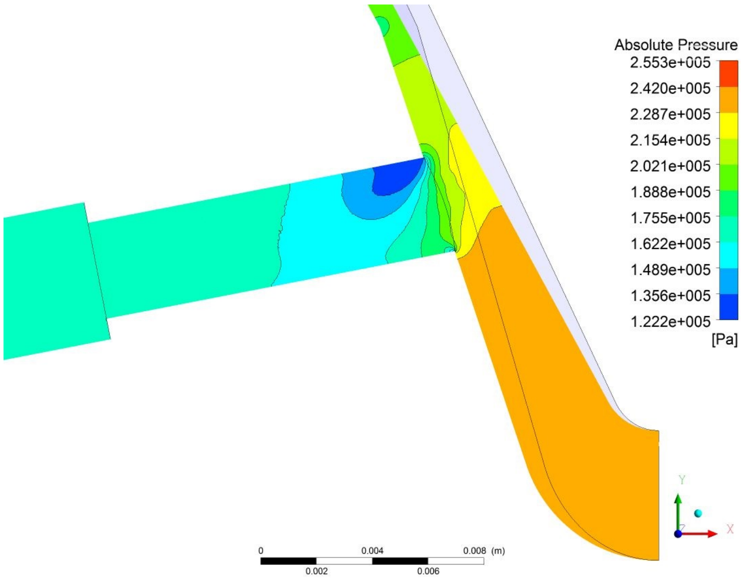

Figure 4.33: pressure field.

4.7.1.1 ‘Hole-to-hole’ connecting vortex

To detect vortices in the injector, the isosurface of vorticity magnitude (0.5% of magnitude)[3] were generated which revealed a presence of the vortex in the space between needle, needle seat and adjacent injector holes or ‘hole-to-hole’ connecting vortex (Figure 4.34, 4.35, 4.40, 4.41 and 4.42). Velocity vector plotted on the periodic plane (Figure 4.35) also indicate the formation of ‘hole-to-hole’ connecting vortex. Vortices were also be detected entering the injector hole, as further illustrated in § 4.7.1.2.

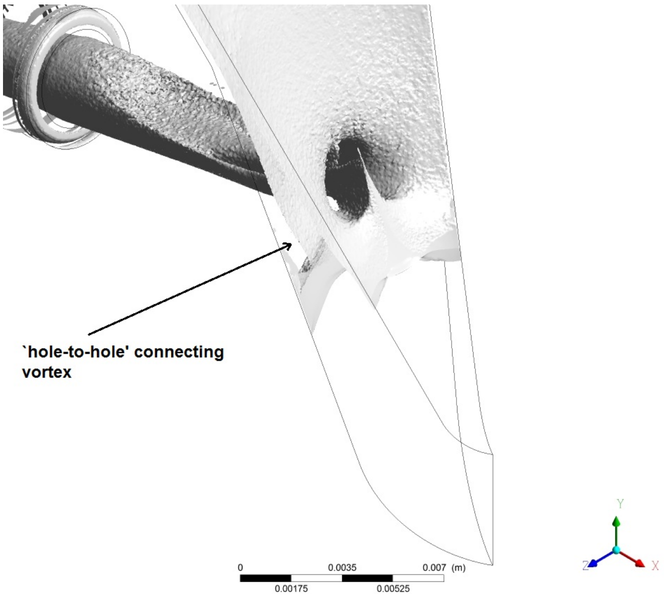

Figure 4.34: Isosurface of vorticity magnitude (0.5% of the magnitude) showing ‘hole-to-hole connecting vortex.

---

[3] A vorticity vector is defined mathematically a curl of the velocity vector:

$$\vec{\zeta} = \nabla \times \vec{U} \tag{4.3}$$

Rate of rotation vector:

$$\vec{\omega} = \frac{1}{2}\nabla \times \vec{U} = \frac{1}{2}curl(\vec{U}) = \frac{\vec{\zeta}}{2} \tag{4.4}$$

Thus, vorticity is defined a rate of rotation of a fluid particle and is twice the angular velocity of the fluid particle.

Vorticity vector in the Cartesian co-ordinates:

$$\vec{\zeta} = \left(\frac{\partial U_z}{\partial y} - \frac{\partial U_y}{\partial z}\right)\hat{i} + \left(\frac{\partial U_x}{\partial z} - \frac{\partial U_z}{\partial x}\right)\hat{j} + \left(\frac{\partial U_y}{\partial x} - \frac{\partial U_x}{\partial y}\right)\hat{k} \tag{4.5}$$

Vorticity vector has direction, the vorticity is positive when it is anti-clockwise and negative when clockwise.

Magnitude of vorticity:

$$|\zeta| = \sqrt{\left(\frac{\partial U_z}{\partial y} - \frac{\partial U_y}{\partial z}\right)^2 + \left(\frac{\partial U_x}{\partial z} - \frac{\partial U_z}{\partial x}\right)^2 + \left(\frac{\partial U_y}{\partial x} - \frac{\partial U_x}{\partial y}\right)^2} \tag{4.6}$$

The vorticity magnitude is a scalar, therefore, the isosurface of vorticity magnitude is a scalar.

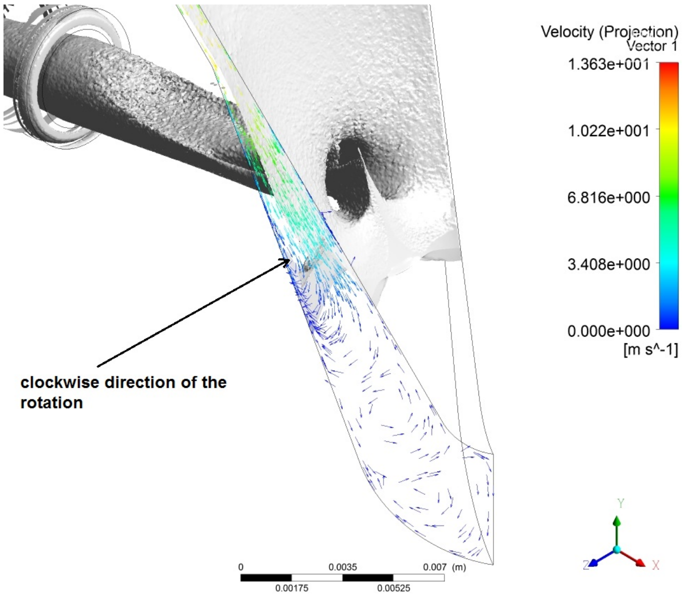

Figure 4.35: Velocity vector projected on the isosurface of vorticity magnitude (0.5% of the magnitude), showing hole to hole connecting vortex in the clockwise direction.

To further analyse 'hole-to-hole' vortex, 2D velocity vectors (Figure 4.36) and streamlines (Figure 4.37) are plotted on plane 2 (see Figure 4.27). From the 2D vectors and streamlines on plane 2 (Figure 4.36 and 4.37), it can be inferred that large volume of fluid which fails to enter the injector hole enters the sac volume after which fluid tends to enter again into the injector hole due to suction caused by lower pressure in the injector hole.

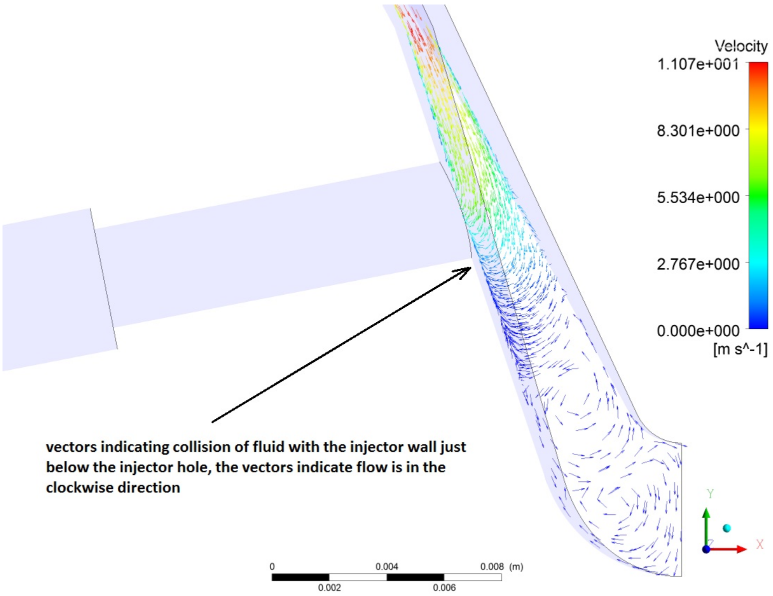

Figure 4.36: 2D vectors plotted on plane 2 indicating a collision of fluid with injector wall just below the injector hole.

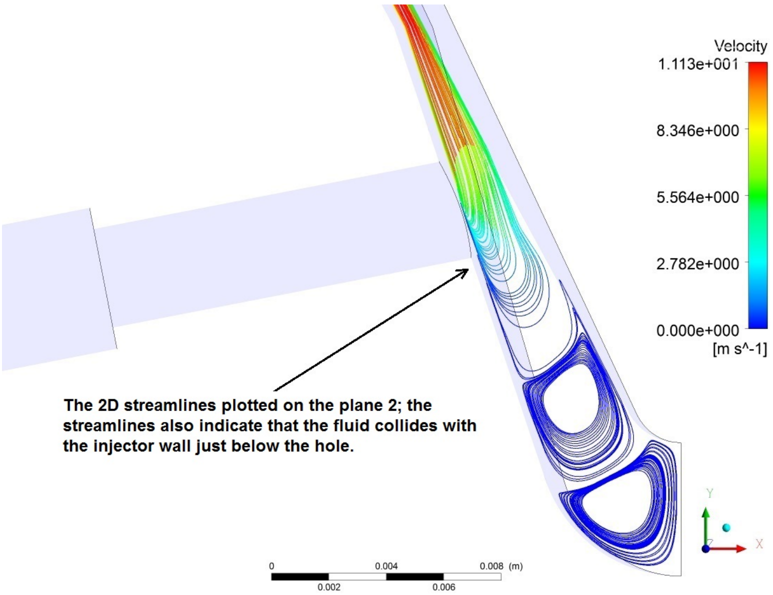

Figure 4.37: Velocity streamline on plane 2 indicates a 'hook' like fluid trail before entering the hole. The fluid streamline indicates the large volume of fluid going into sac region then going towards injector hole. Additional vortices in the sac volume can also be seen.

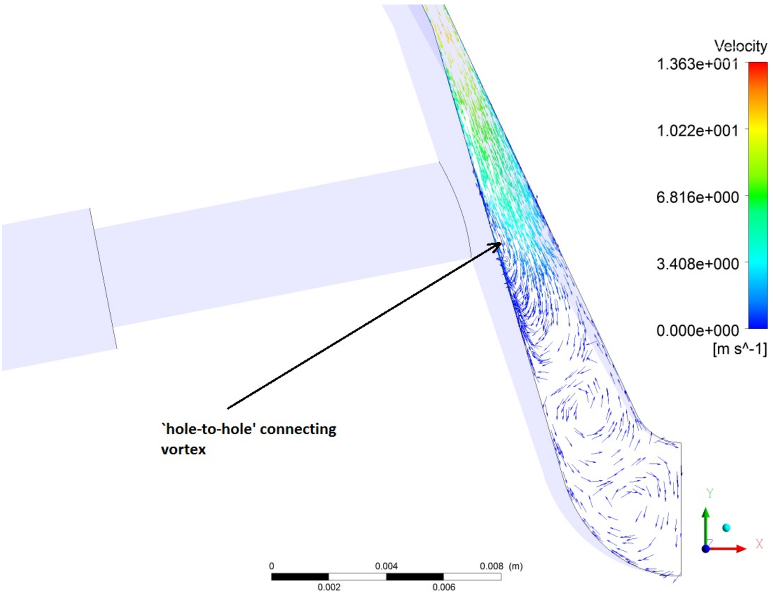

Figure 4.38: Velocity vectors on the cyclic interface indicate the presence of 'hole to hole' connecting vortex. Additional vortices in the sac volume can also be seen.

Hence, it can be seen in the Figures 4.36 and 4.37 that as fluid attempts to enter the injector hole, it follows a hook-shaped trajectory. The lower pressure in the injector hole would continue to draw fluid into it. Therefore, it can be seen from the Figures 4.36 and 4.37 that fluid is entering the injector hole from the bottom and also from sideways (Figure 4.42). The portion of the fluid which still fails to enter the injector hole collides with the wall just below the injector hole leading to the formation of the vortex which spreads annularly in the sac volume (Figure 4.35 ,4.36, 4.37, 4.38 and 4.39). Nonetheless, due to the lower pressure region in the injector hole which continues to draw fluid towards it and would also draw fluid from formed vortex and therefore would affect the shape of it leading to the formation of 'hole-to-hole' connecting vortex.

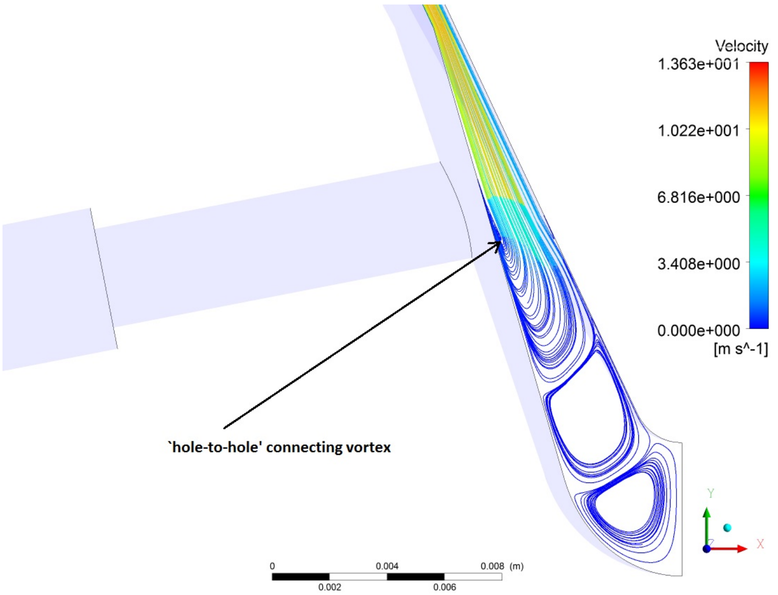

Figure 4.39: Velocity streamline on the cyclic interface indicates the presence of 'hole to hole' connecting vortex. Additional vortices in the sac volume can also be seen.

Vortices in the sac volume of the injector can also be seen from the bottom view of the injector as shown in Figure 4.40, 4.41 and 4.42. From isosurface of vorticity magnitude in Figure 4.40 and 4.41. Vectors plotted on both periodic face also indicate the direction of rotation. Vectors on the front face indicate the clockwise direction of rotation (top left of the Figure 4.41) and vectors plotted on the back face suggest a counter-clockwise direction of rotation.

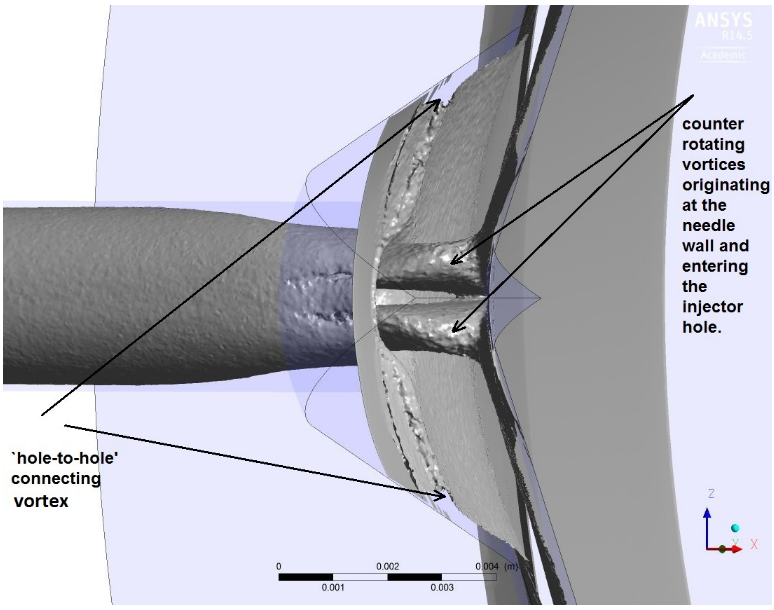
ANSYS
R14.5
Academic
counter rotating vortices originating at the needle wall and entering the injector hole.
`hole-to-hole' connecting vortex
0
0.002
0.004 (m)
0.001
0.003
Z
X

Figure 4.40: Bottom view of the injector. Isosurface of vorticity (0.5% of the magnitude) showing the prediction of vortices in the injector.

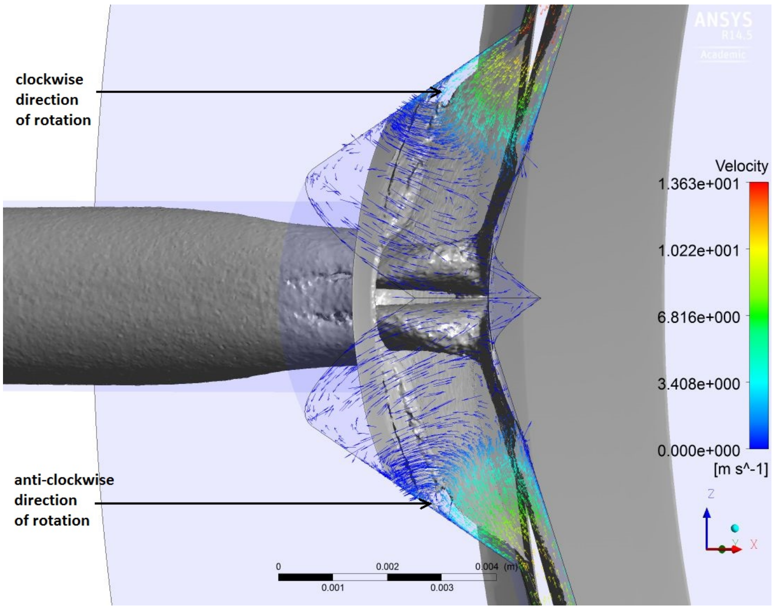
clockwise direction of rotation
anti-clockwise direction of rotation
ANSYS
R14.5
Academic
Velocity
1.363e+001
1.022e+001
6.816e+000
3.408e+000
0.000e+000
[m s^-1]
Z
X
0
0.001
0.002
0.003
0.004 (m)

Figure 4.41: Bottom view of the injector. Isosurface of vorticity (0.5% of the magnitude) showing the prediction of vortices in the injector. Velocity vectors have been plotted on the front periodic interface showing the clockwise direction of rotation of 'hole-to-hole' connecting vortex. Velocity vectors have also been plotted on the back side (bottom of the image) of the periodic interface suggesting the counter-clockwise direction of rotation of 'hole-to-hole' connecting vortex.

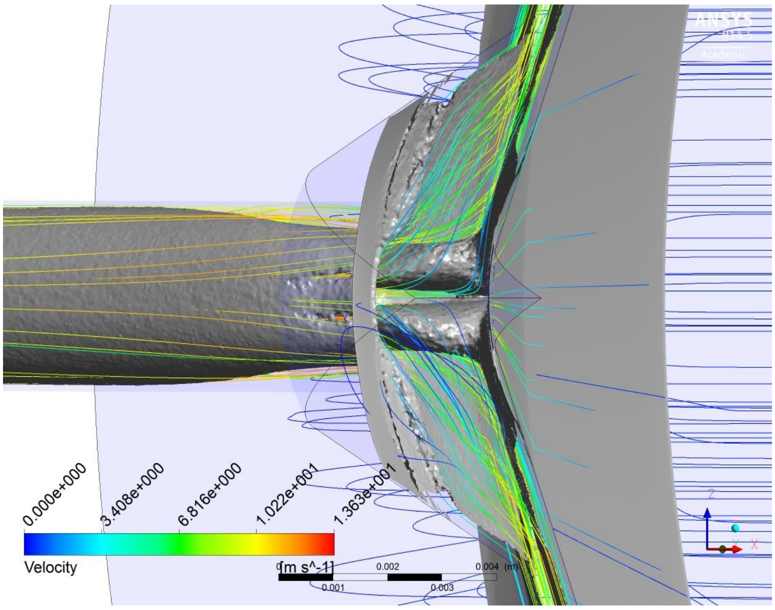
0.000e+000
3.408e+000
6.816e+000
1.022e+001
1.363e+001
Velocity
[m s^-1]
Z
X
0.001
0.002
0.003
0.004 (m)

Figure 4.42: Bottom view of the injector. Isosurface of vorticity (0.5% of the magnitude) showing the prediction of vortices in the injector. Streamlines indicating the path of the fluid.

The identified reasons for the formation of 'hole-to-hole' connecting vortex are described:

- The fluid travels downstream in the injector through the converging path as seen in Figure 4.28.
- The symmetrical 6 injector holes are the outlets for the fluid. The lower pressure in the injector hole would continue to draw fluid into it.
- But at the lower needle lift the annulus space is very narrow, this induces higher acceleration. The volume of fluid which lies on the axis of the injector hole would enter the injector hole straight away (Figure 4.32). However, the fluid which does not lie on the axis of the injector hole would travel into the sac volume annularly (Figure 4.37 and 4.36).
- However, the lower pressure region in te injector would continue to draw fluid into it. Hence, some volume of fluid would enter the injector hole sideways (Figure 4.42) as well as from the bottom of the injector hole (Figure 4.32).
- Nevertheless, some volume of the fluid would still fail to enter the injector hole and would collide with the injector wall just below the injector hole annularly (Figure 4.37).
- The annular collision of the fluid with the wall just below the injector hole would result in the formation of the vortex structure.
- However, the lower pressure in the injector hole would continue to draw fluid towards it and therefore, would draw the fluid from this formed vortex. This would influence the shape of the vortex, leading to the formation of 'hole-to-hole' connecting vortex (Figure 4.38, 4.39, 4.35, 4.40, 4.41 and 4.42).

4.7.1.2 'Counter-rotating' vortices originating from the needle wall and entering the injector hole facing it

Vortex type cavitating structures originating from the needle surface facing the injector hole inlet and extending downstream into the injector hole were observed by Arcoumanis et al. (2001); Roth et al. (2002); Roth (2004) (see Figure 2.7) and were referred as 'needle strings'. As in the previous subsection § 4.7.1.1, the isosurface of vorticity magnitude (0.5% of the magnitude) also detected such vortices emerging from the needle wall and entering the injector hole facing it, therefore, the present section is focussed on their analysis.

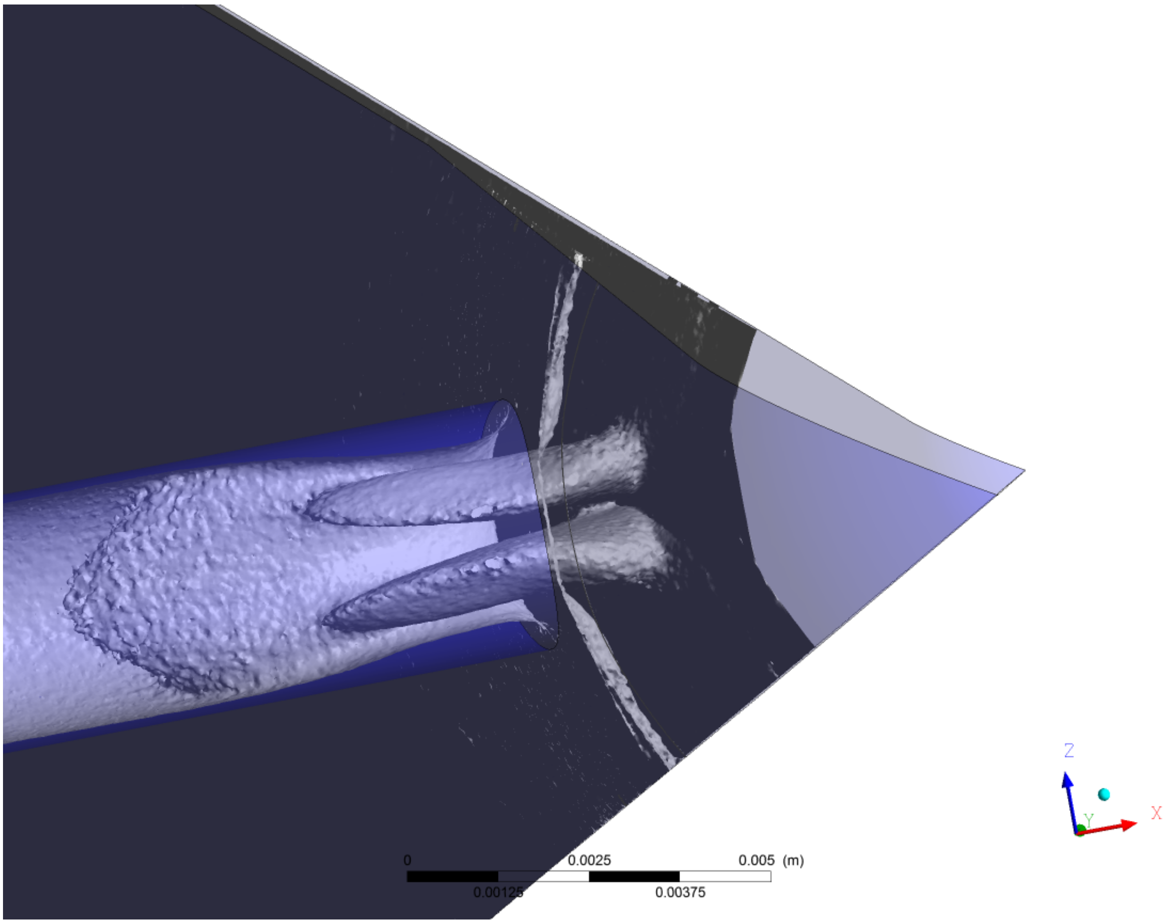

Figure 4.43: A view of the injector from the bottom (one-sixth of the flow domain). Isosurface of vorticity magnitude (0.5% of the magnitude) with the front faced removed, showing vortices emerging from needle wall and entering the injector hole facing it.

On further investigations, it was realised that there are two vortices are originating from the needle wall and entering the injector hole (Figure 4.40, 4.43 and 4.44). To identify the direction of vortices, vectors (Figure 4.45) plotted on the vortex core and plane 4 (Figure 4.27), indicate one vortex has a counter-clockwise direction of rotation and another vortex has a clockwise direction of rotation. Pressure contours plotted on plane 4 (see Figure 4.27) also indicate the low-pressure region on the core of vortices emerging from the needle wall (Figure 4.47). To further strengthen the argument for the presence of vortices in the injector hole emerging from the injector wall vorticity contours have been plotted as shown in Figure 4.49. Since vorticity is a vector and has a direction, the vorticity magnitude and directions are shown in the vorticity contour (Figure 4.49). In which, the red colour represents a positive vorticity or counter-clockwise direction of rotation and blue represents a negative vorticity and a clockwise direction of rotation. Vorticity contours have also been plotted for the results obtained using the standard $k - \epsilon$ model (Figure 4.50) which also indicates the presence of 'counter-rotating' vortices emerging from the needle wall and entering the injector hole. The detected vortices emerging from the needle wall and entering the injector hole can be recognized as a prerequisite of 'needle string' or string type cavitation emerging from the needle wall and entering the injector hole as observed by Arcoumanis et al. (2001) (Figure 2.7).

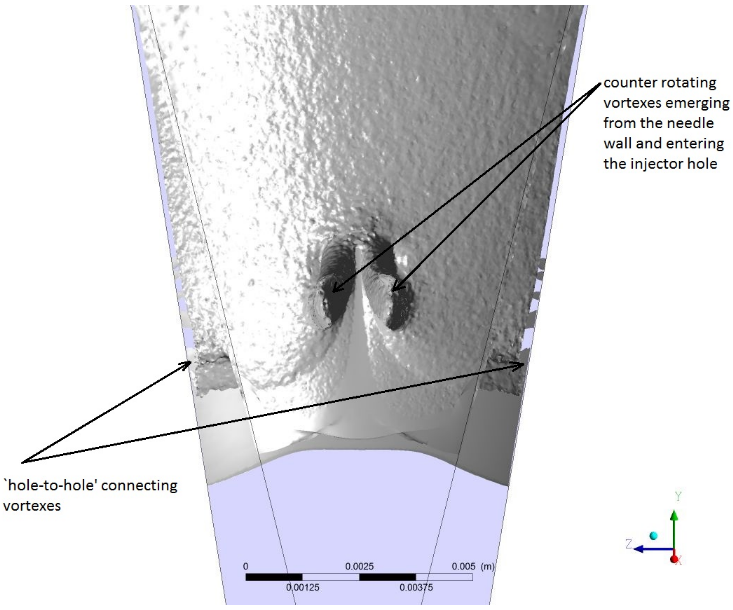
counter rotating vortexes emerging from the needle wall and entering the injector hole
`hole-to-hole' connecting vortexes
0
0.0025
0.005 (m)
0.00125
0.00375
Y
Z
X

Figure 4.44: View from the injector the origin (needle centre), view from the injector the origin (needle centre), isosurface of vorticity magnitude (0.5% of the magnitude) showing the presence of 'hole-to-hole' connecting vortex and 'counter-rotating' vortices emerging from the needle wall and entering the injector hole facing it.

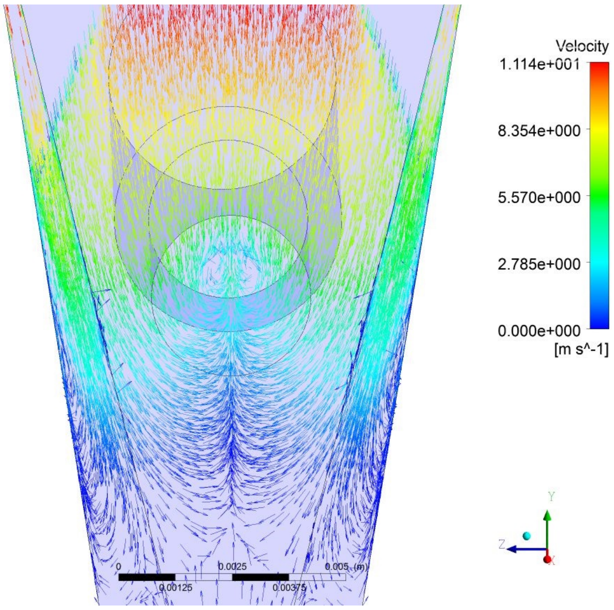

Figure 4.45: Velocity vectors on plane 4 show the merging of fluid at the centre plane of the injector hole due to symmetrical converging geometry.

From the velocity vectors (Figure 4.45) and streamlines (Figure 4.46) which have been plotted on plane 4, it can be seen that as fluid travels downstream in the injector through converging geometry, henceforth the fluid streamlines starts to merge. A large portion of fluid would enter the injector hole, the portion of the fluid which fails to enter the injector hole would tend to travel further downstream into the sac. However, the higher pressure in the sac (Figure 4.48) would resist the fluid entering further into the sac and hence fluid would start to form vortices rotating in the opposite direction just where it start to merge as seen in Figure 4.45 and 4.46.

The lower pressure in the injector hole would continue to draw the fluid towards it resulting in the formation of ‘counter-rotating’ vortices emerging from the needle wall and entering the injector hole facing it.

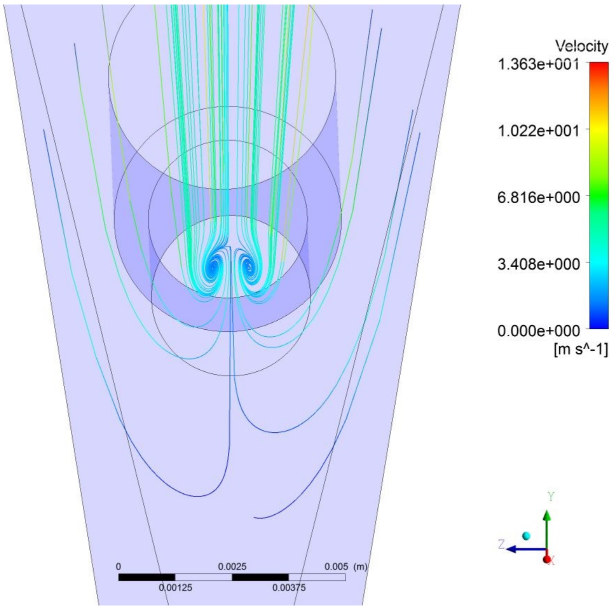

Figure 4.46: Velocity streamlines on plane 4 show the merging of fluid at the centre plane of the injector hole due to symmetrical converging geometry.

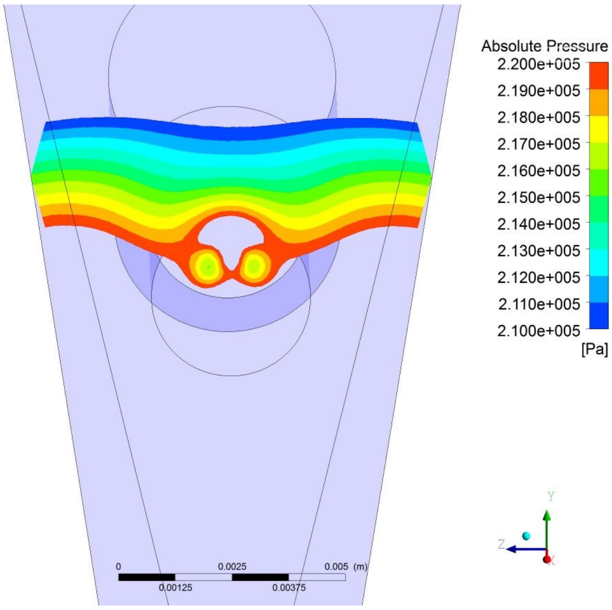

Figure 4.47: Lower pressure regions corresponding to the core of ‘counter-rotating’ vortices.

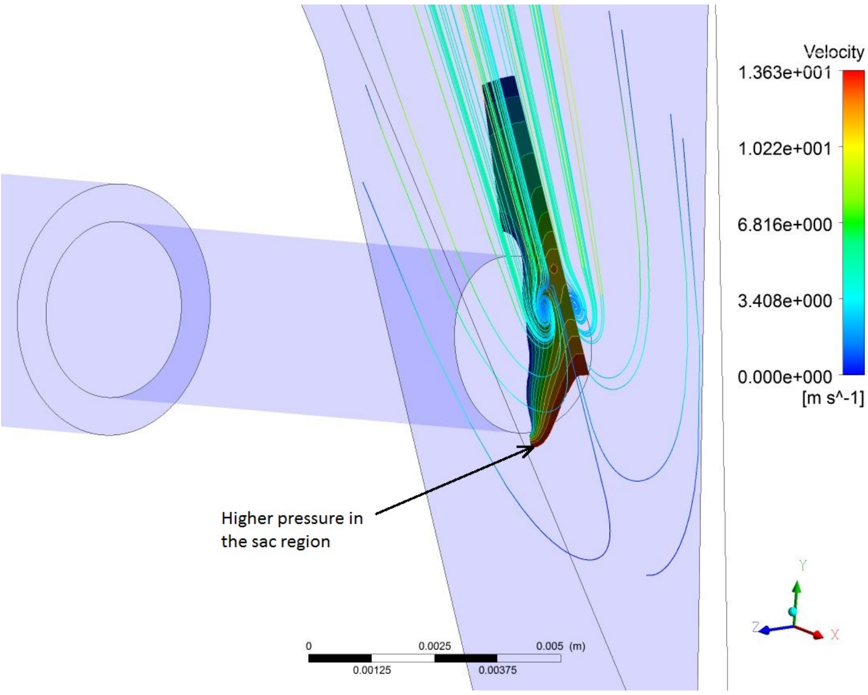
Velocity
1.363e+001
1.022e+001
6.816e+000
3.408e+000
0.000e+000
[m s^-1]
Higher pressure in the sac region
0
0.0025
0.005 (m)
0.00125
0.00375
Y
Z
X

Figure 4.48: Velocity streamlines on plane 4 and pressure contours on plane 1 which indicate higher pressure in the sac region.

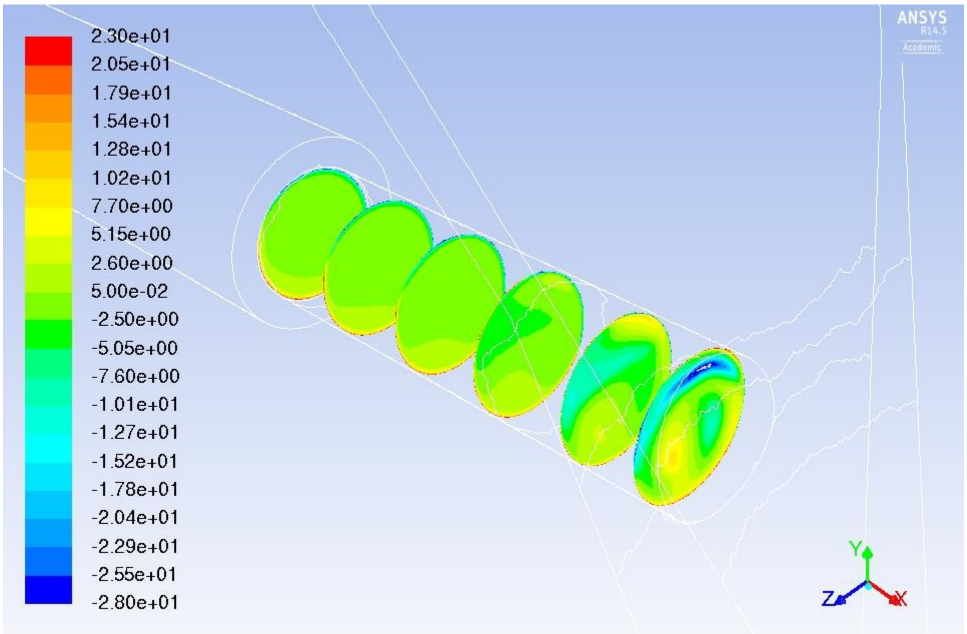
2.30e+01
2.05e+01
1.79e+01
1.54e+01
1.28e+01
1.02e+01
7.70e+00
5.15e+00
2.60e+00
5.00e-02
-2.50e+00
-5.05e+00
-7.60e+00
-1.01e+01
-1.27e+01
-1.52e+01
-1.78e+01
-2.04e+01
-2.29e+01
-2.55e+01
-2.80e+01
ANSYS
R14.5
Academic
Y
Z
X

Figure 4.49: Normalised vorticity contours projected on the planes perpendicular to the injector hole. The vorticity is normalised by multiplying it by nozzle diameter D and dividing it by injection velocity U_{inj}. Realizable $k - \epsilon$ model. Positive (red) shows anticlockwise rotation and negative (blue) direction shows clockwise direction.

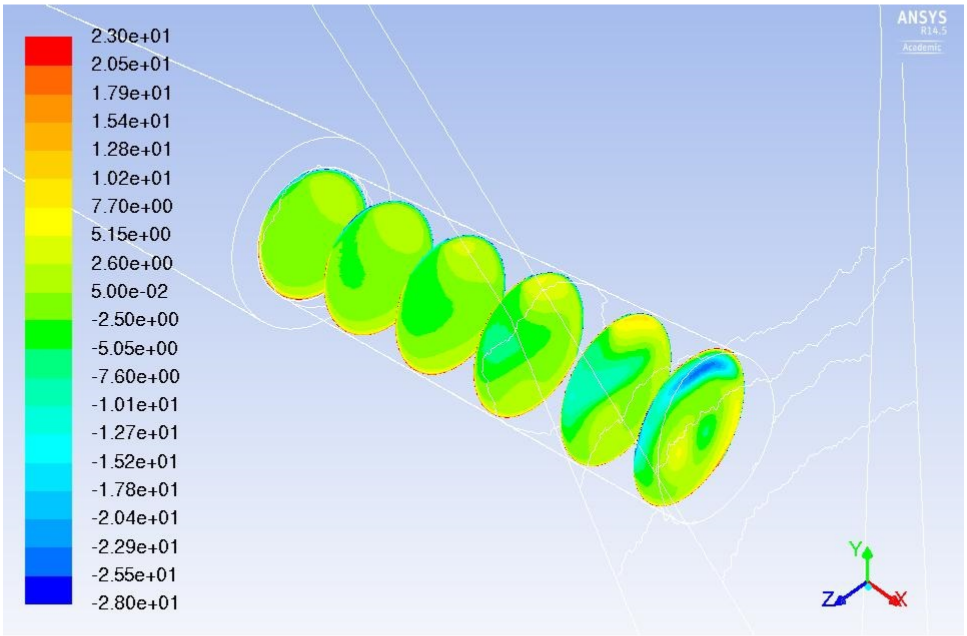

Figure 4.50: Normalised vorticity contours projected on the planes perpendicular to the injector hole. Standard $k - \epsilon$ model. Positive (red) shows anticlockwise rotation and negative (blue) direction shows clockwise direction.

The identified reasons for the formation of ‘counter-rotating’ vortices emerging from needle wall and entering the injector hole facing it are:

- The converging geometry would cause the fluid to accelerate as it travels downstream in the injector. The converging geometry would also cause fluid streamline to merge (Figure 4.46).
- A large portion of fluid that lies along the axis of the injector hole will enter the injector hole straight away.
- The portion of fluid that fails to enter the injector hole would tend to travel further downstream into the sac.
- However, higher pressure in the sac would resist fluid entering further into the sac volume, hence fluid would start to form vortices at the position where fluid streamlines merge (Figure 4.48).
- The lower pressure in the injector hole would continue to draw the fluid towards it hence would result in the formation of ‘counter-rotating vortices’ emerging from the needle wall and entering the injector hole facing it.

4.7.2 Nominal needle lift (6.0 mm) flow field

To analyse the flow field in the injector nozzle, planes have been set up in the flow domain. Like, previous subsection § 4.7.1 plane 1 is the located on the x-y axis, plane 2 is 15° anti-clockwise and plane 3 is 15° clockwise from an x-y plane. Plane 4 is generated parallel to the annulus as shown in Figure 4.51. Results from grid 3 are used for post processing (see § 4.4.4).

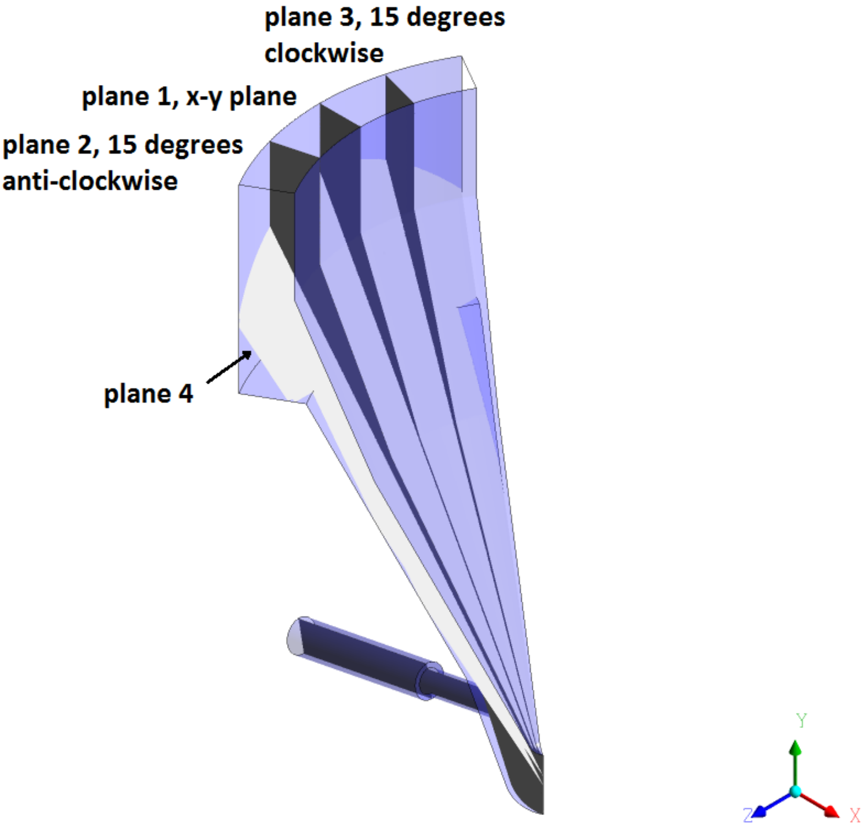
plane 3, 15 degrees clockwise
plane 1, x-y plane
plane 2, 15 degrees anti-clockwise
plane 4
Y
Z
X

Figure 4.51: planes in the flow domain for flow field analysis

On plane 1 (Figure 4.52) 2D streamlines indicate the presence of vortices in the injector hole. From the velocity vectors and streamlines plotted in Figure 4.52 and vectors plotted in Figure 4.53 it can be seen the formation of a recirculation region at the sharp corner of the injector cartridge due to flow separation. The flow further separates from the wall as the fluid enters the seat annulus as highlighted in the Figure 4.53 but it can be seen in the same Figure 4.53 that the fluid re-attaches to the wall as it travels further downstream. In Figures 4.52 and 4.54, the red circle indicates a recirculation region formed at the sharp edge of the cartridge. The yellow circle in the same Figures 4.52 and 4.54 indicates a 'hole-to-hole' connecting vortex in the sac region and the orange circle indicates a recirculation region in the injector hole. In the same Figures 4.52 and 4.54, predicted vortex in the bottom of the sac has been shown using a blue circle and dark yellow circle indicating a possible 'ring-shaped step vortex' as the fluid leaves the injector hole and enters the backflow hole .

Vectors have also been plotted on plane 2 (Figure 4.55) and the cyclic plane (Figure 4.56) which also indicate the presence of 'hole-to-hole' connecting vortex. Since at the nominal needle lift the annular space between needle wall and the injector wall is larger than for the lower lift case (see § 4.7.1), hence the fluid would behave slightly differently for the nominal needle lift case (see the next paragraph). The fluid would travel downstream and the converging geometry would cause the fluid to accelerate. The fluid along the axis of the injector hole would enter the injector hole straight away. The portion of the fluid which fails to enter the injector hole would collide with the injector wall just below the injector hole annularly and would start to form an annular vortex. However, the lower pressure at the injector hole would continue to draw the fluid towards it and would draw the fluid from this formed annular vortex leading to the formation of 'hole-to-hole' connecting vortex. 3d streamlines in Figure 4.57 also indicate the presence of 'hole-to-hole' connecting vortex in the sac region of the injector.

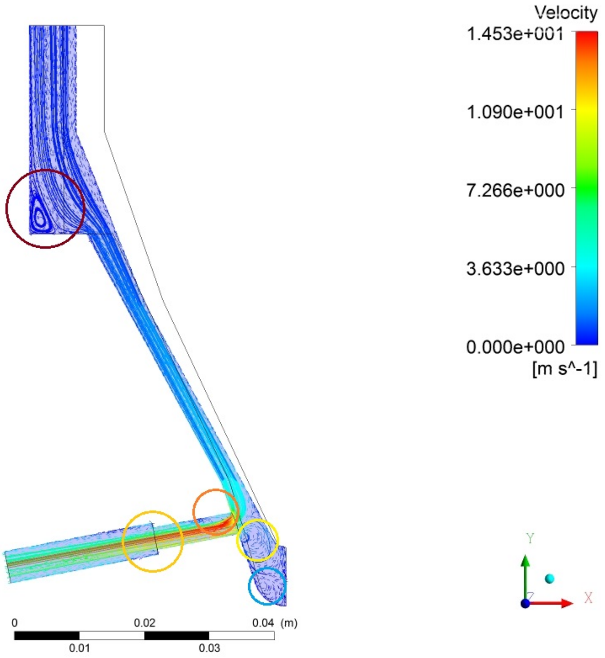

Figure 4.52: 2D velocity streamlines on plane 1.

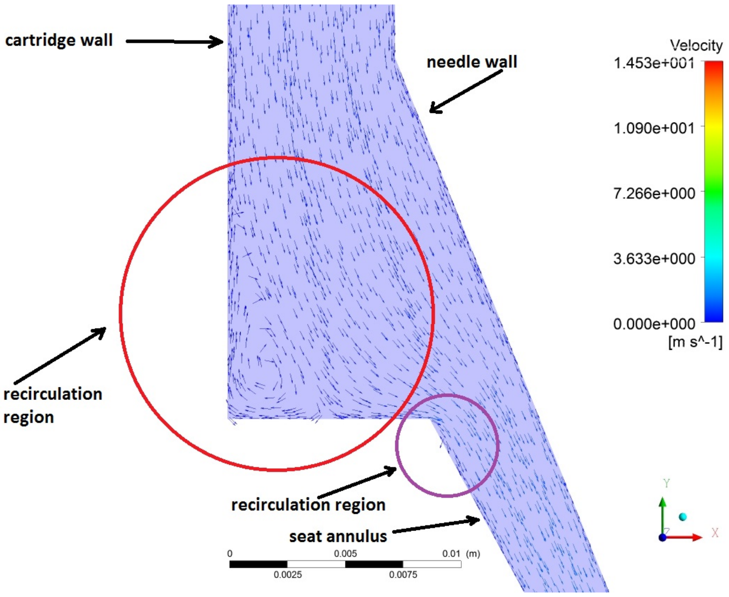

Figure 4.53: Magnified view of the cartridge, showing vortex being generated at the sharp corner of the cartridge.

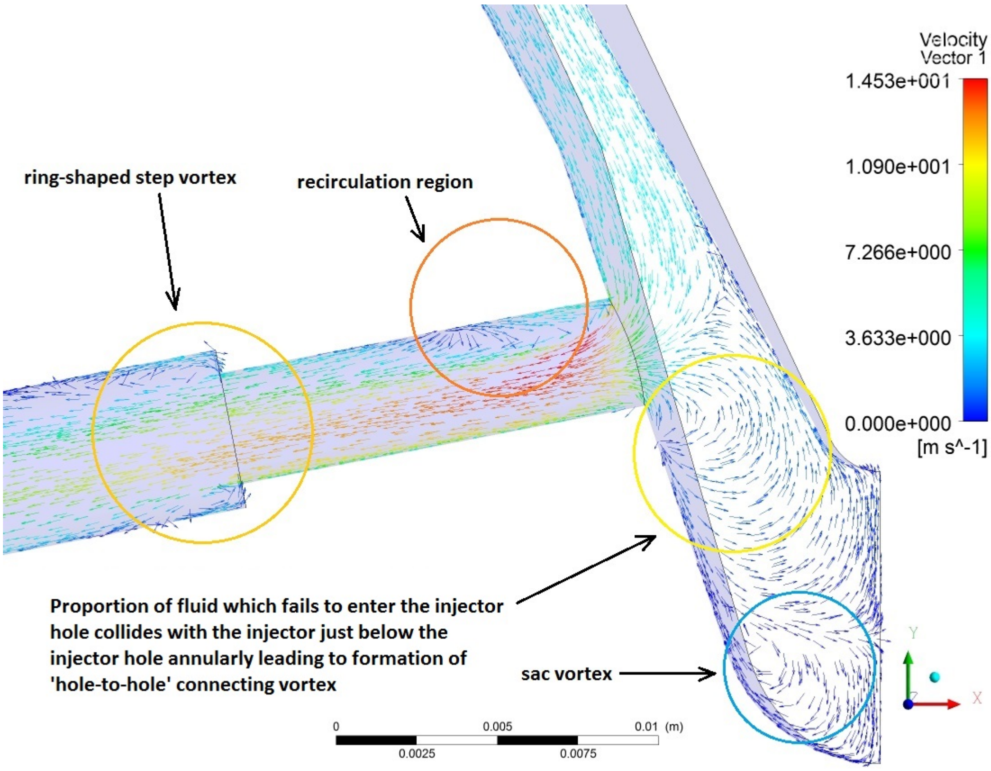

ring-shaped step vortex

recirculation region

Proportion of fluid which fails to enter the injector hole collides with the injector just below the injector hole annularly leading to formation of 'hole-to-hole' connecting vortex

sac vortex

Figure 4.54: Magnified view of the sac region, showing 2D vectors.

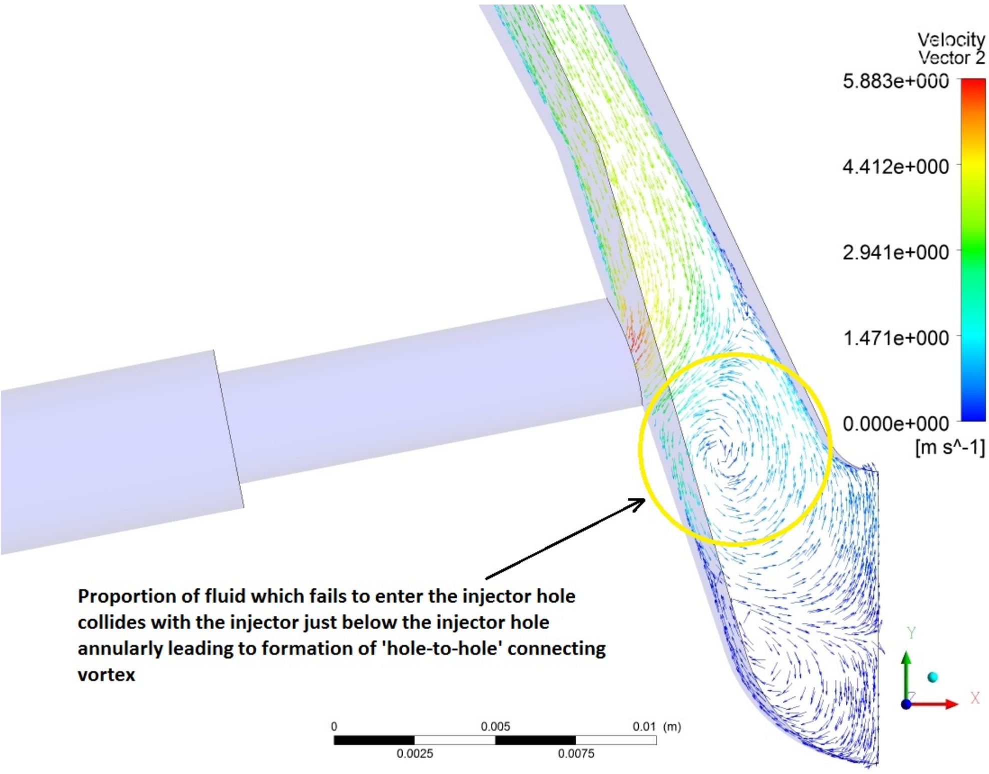

Proportion of fluid which fails to enter the injector hole collides with the injector just below the injector hole annularly leading to formation of 'hole-to-hole' connecting vortex

Figure 4.55: 2D vectors plotted on plane 2.

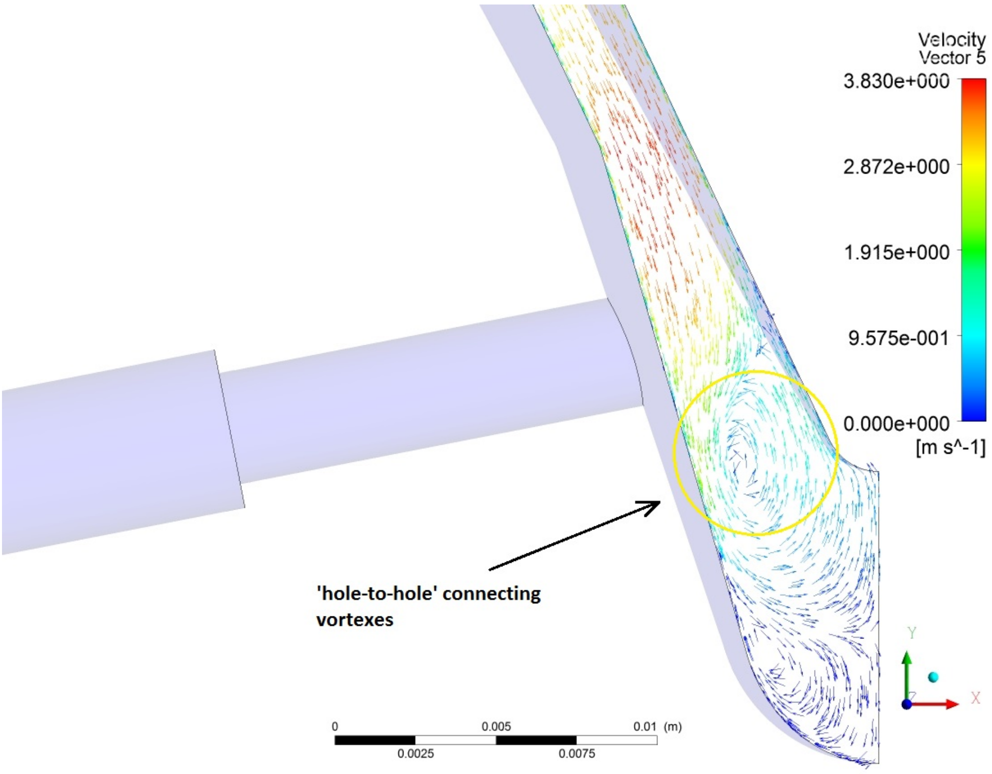

Figure 4.56: 2D vectors plotted on the cyclic plane.

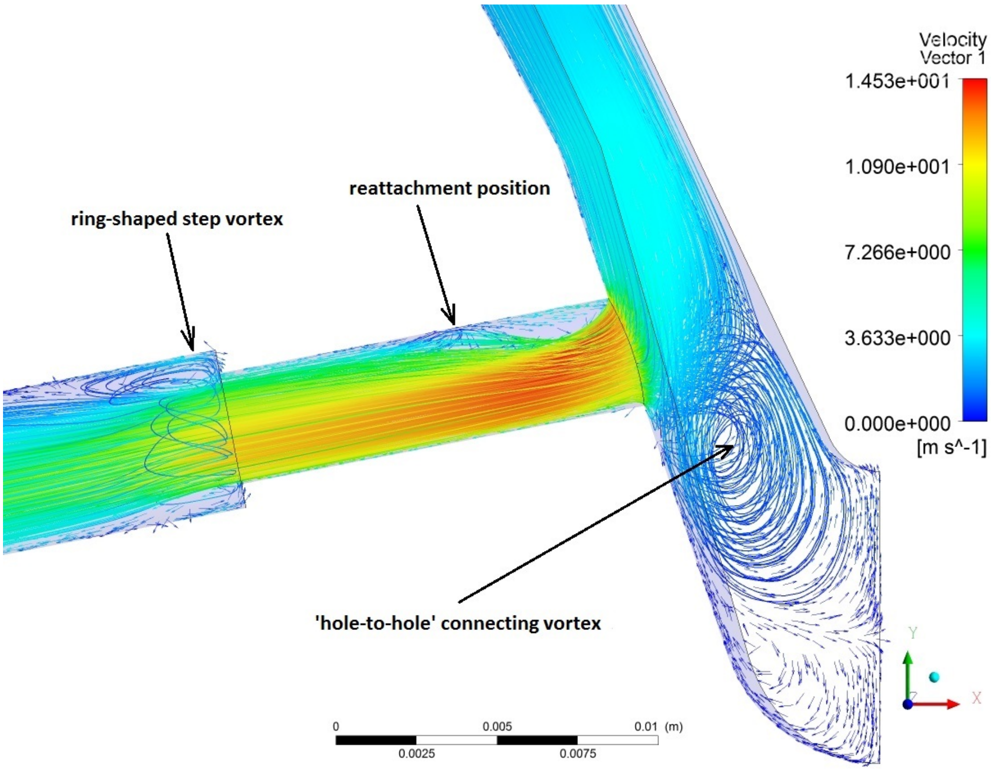

Figure 4.57: 3D velocity streamlines

It was observed that the predicted 'hole-to-hole' vortex at the nominal needle lift (Figure 4.55) has a different direction of rotation than the lower needle lift case (Figure 4.37). In the lower needle lift case, the converging geometry and narrow annulus facilitate higher acceleration hence fluid which does not lie along the injector hole axis tends to go into the sac volume at which the pressure is relatively higher (Figure 4.33). Since the lower pressure in the injector hole causes suction which continuously draws fluid into it and also draws the fluid from the sac volume; Hence, fluid also enters the injector hole from the bottom (Figure 4.32) and sides of the injector hole (Figure 4.42). The volume of fluid which fails to enter the injector collides with the injector wall below the injector hole and results in the formation of the vortex annularly. Nonetheless, due to the lower pressure in the injector hole, it will continue to draw fluid towards it hence would continue to draw fluid into the injector hole from this formed vortex leading to the formation of the 'hole-to-hole' connecting vortex. Therefore, from the Figure 4.37 ($+x, +y, +z$ view), it can be seen that the direction of rotation is clockwise.

Whereas in the nominal needle lift case, the clearance is larger between the needle wall and the injector body than the in the lower lift case, hence at the similar cavitation number the fluid does not accelerate as lower needle lift case. Therefore, fluid streamline which does not pass through the injector hole axis cannot penetrate so well into the sac region as in the lower needle lift case. The volume of fluid which fails to enter the injector hole collides with the injector wall just below the injector hole. The lower pressure in the injector hole would continue to draw the fluid into it and would draw the fluid from the formed vortex which would result in the formation of the hole-to-hole' connecting vortex (Figure 4.55).

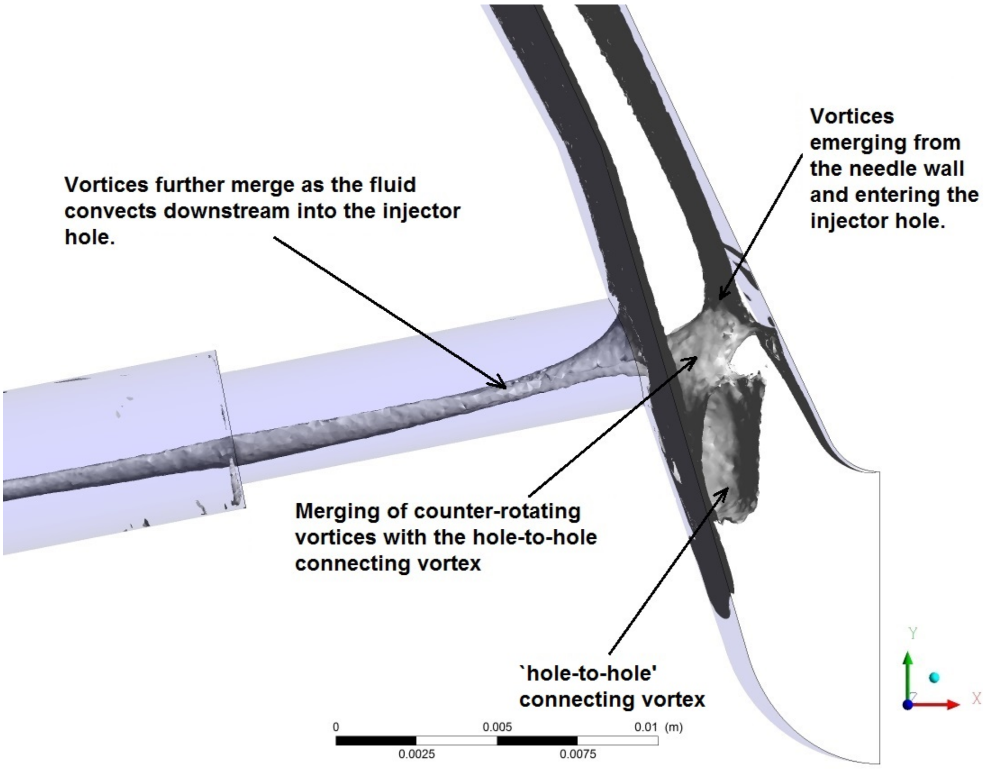
Vortices further merge as the fluid convects downstream into the injector hole.
Vortices emerging from the needle wall and entering the injector hole.
Merging of counter-rotating vortices with the hole-to-hole connecting vortex
`hole-to-hole' connecting vortex
0
0.005
0.01 (m)
0.0025
0.0075
Y
X

Figure 4.58: Side view of the vorticity. Isosurface of vorticity (0.5% of the magnitude) showing the prediction of vortices in the injector.

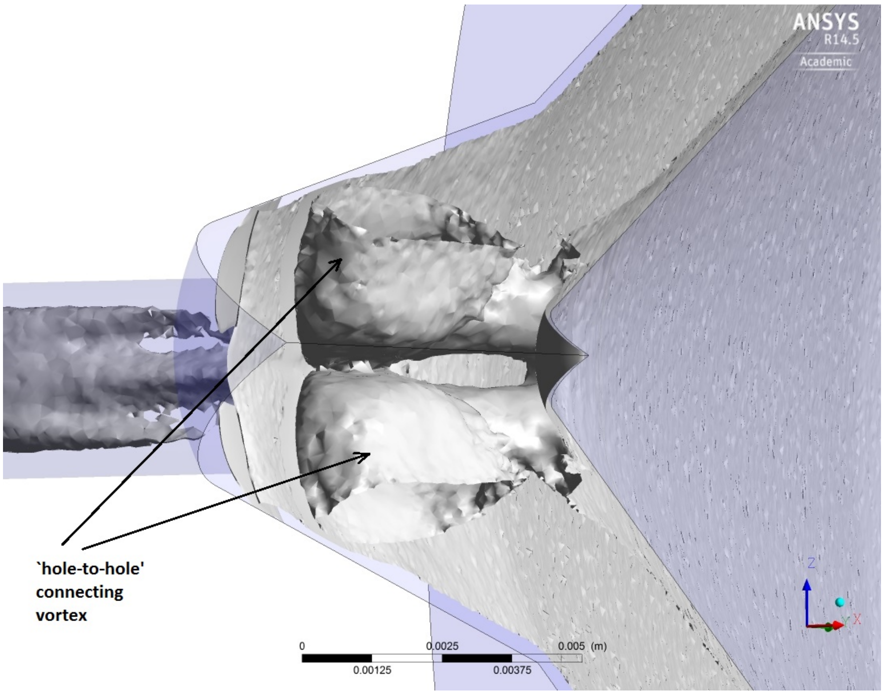
ANSYS
R14.5
Academic
`hole-to-hole'
connecting
vortex
0
0.00125
0.0025
0.00375
0.005 (m)
Z
X

Figure 4.59: Bottom view of the injector. Isosurface of vorticity (0.5% of the magnitude) showing the prediction of vortices in the injector.

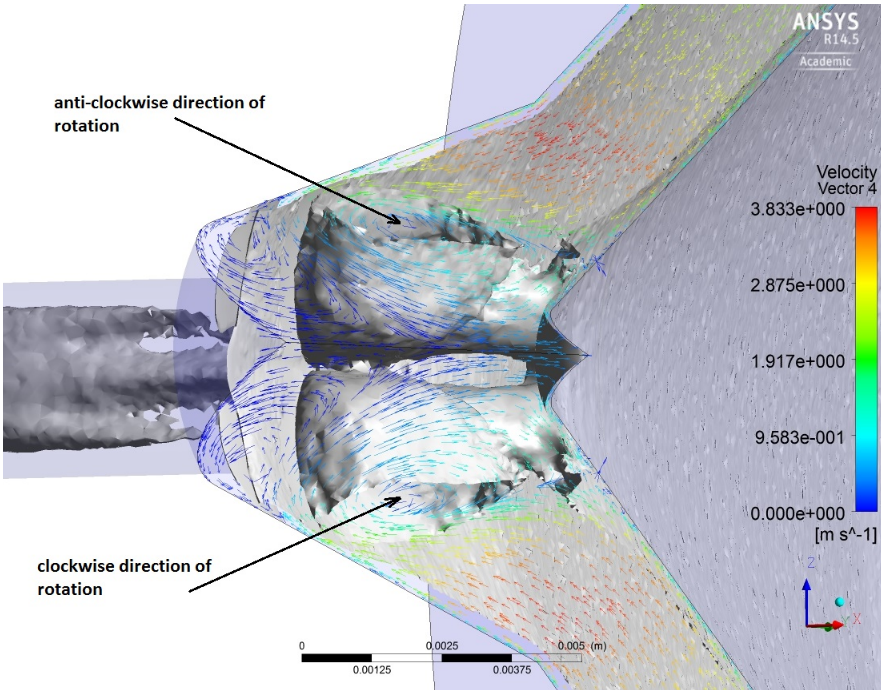
ANSYS
R14.5
Academic
anti-clockwise direction of
rotation
clockwise direction of
rotation
Velocity
Vector 4
3.833e+000
2.875e+000
1.917e+000
9.583e-001
0.000e+000
[m s^-1]
0
0.00125
0.0025
0.00375
0.005 (m)
Z
X

Figure 4.60: Bottom view of the injector. Isosurface of vorticity (0.5% of the magnitude) showing the prediction of vortices in the injector. Velocity vectors have been plotted on the front periodic interface showing the counter-clockwise direction of rotation of 'hole-to-hole' connecting vortex. Velocity vectors have also been plotted on the back side (bottom of the image) of the periodic interface suggesting the clockwise direction of rotation of 'hole-to-hole' connecting vortex.

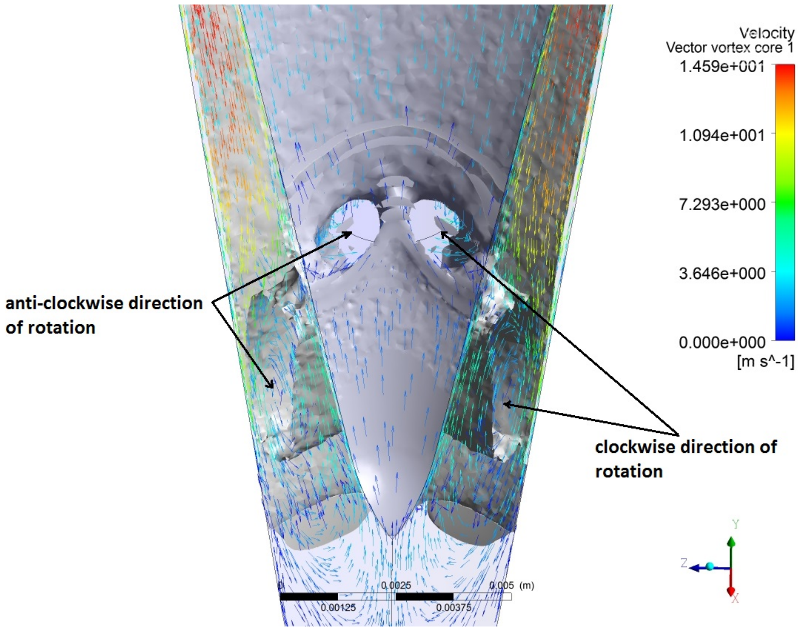
Velocity
Vector vortex core 1
1.459e+001
1.094e+001
7.293e+000
3.646e+000
0.000e+000
[m s^-1]
anti-clockwise direction of rotation
clockwise direction of rotation
0.0025
0.005 (m)
0.00125
0.00375
Y
Z
X

Figure 4.61: Isosurface of vorticity magnitude (0.5% of the magnitude) showing 'counter-rotating' vortices emerging from the needle wall and entering the injector hole just opposite to needle wall. Also, vectors plotted on the cyclic interface to show hole to hole connecting vortex.

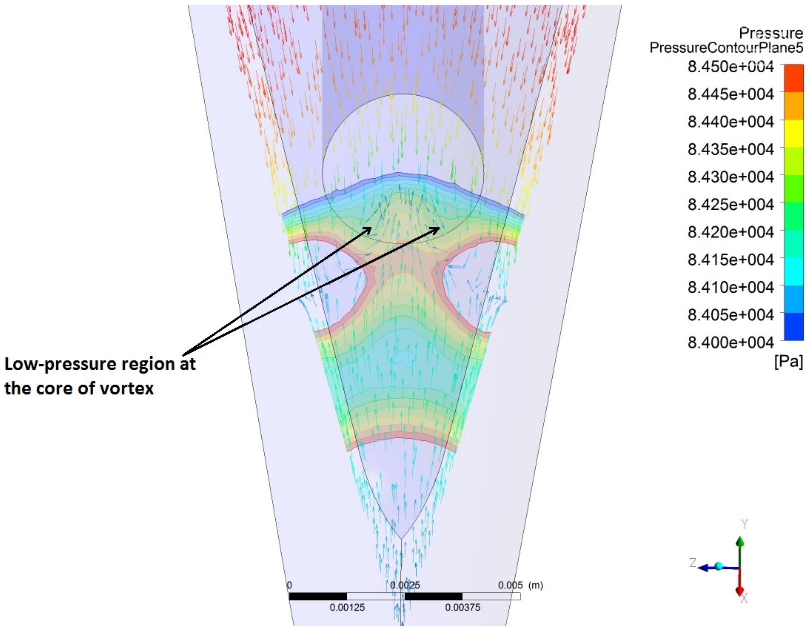

Figure 4.62: Vectors plotted on the plane 4 also reveal the direction of rotation of counter-rotating vortices emerging from the needle wall and entering injector hole opposite to it. Pressure contours reveal corresponding low-pressure region at the core of the vortex.

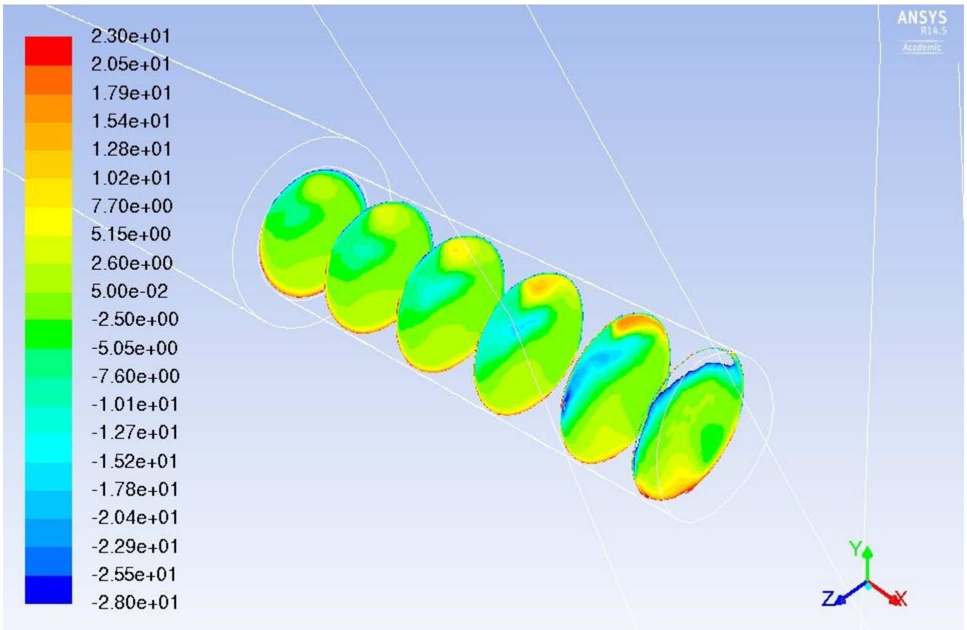

Figure 4.63: Normalised vorticity contours projected on the planes perpendicular to the injector hole. Realizable $k-\epsilon$ model. Positive (red) shows anticlockwise rotation and negative (blue) direction shows clockwise direction.

Isosurface of vorticity magnitude (0.5% of the magnitude) at the nominal needle lift case also indicates the presence of 'hole-to-hole' connecting vortices in the sac volume (Figure 4.58, 4.59 and 4.60). Like in the case of lower needle lift, 'counter-rotating' vortices emerging from the needle wall and entering the injector hole opposite to it. are also detected using isosurface of vorticity and can also be seen in Figure 4.61. The causes for the occurrence of counter-rotating vortices are presented in § 4.7.1.2. Hence, vorticity contours have also been plotted in the different planes in the injector hole which indicate counter-clockwise and clockwise vortices in the injector hole (Figure 4.58 and 4.63). More interestingly for the nominal needle lift vortices emerging from the needle wall can be seen merging with the 'hole-to-hole' connecting vortex. Moreover, it can be seen that when the fluid travels further downstream in the injector hole, the 'hole-to-hole' connecting vortices and 'counter-rotating' vortices further merge and dissipate.

4.7.3 Discussions

- Analysis revealed the presence of 'hole-to-hole' connecting vortices which could be considered as the prerequisite of 'hole-to-hole' connecting vortex cavitation as experimentally observed by Afzal et al. (1999); Arcoumanis et al. (2001); Roth et al. (2002); Roth (2004); Andriotis (2009).

- The analysis also showed the presence of 'counter-rotating' vortices emerging from the needle wall and entering the injector hole facing it. Such vortices are prerequisite for the formation of 'needle strings' or vortex type cavitation structures emerging from the needle wall and entering the injector hole as experimentally observed by Arcoumanis et al. (2001); Roth et al. (2002); Roth (2004).

4.8 Summary

4.8.0.1 Boundary condition errors:

- The $1/6^{th}$ domain with periodic boundary conditions produced similar results as the complete flow domain for the enlarged multi-hole (6) fuel injector nozzle.

4.8.0.2 Numerical errors

- Mean velocity plots for the mean axial velocity for the lower needle lift and nominal needle lift conditions indicate the grid independence is being approached.

4.8.0.3 Physical modelling errors

- More accurate mean axial velocity and RMS velocity has been predicted using the realizable $k - \epsilon$ model than the standard $k - \epsilon$ model.
- The recirculation region is more accurately predicted when ‘Enhanced wall treatment’ method has been used.

4.8.0.4 Flow field analysis

- ‘Hole to hole connecting vortex’ has been predicted in both the lower and nominal needle lift conditions.
- ‘Counter-rotating vortices’ originating from needle wall facing injector hole and entering the injector hole have been predicted for The both lower and nominal needle lift conditions.

4.8.0.5 Contours: lower needle lift

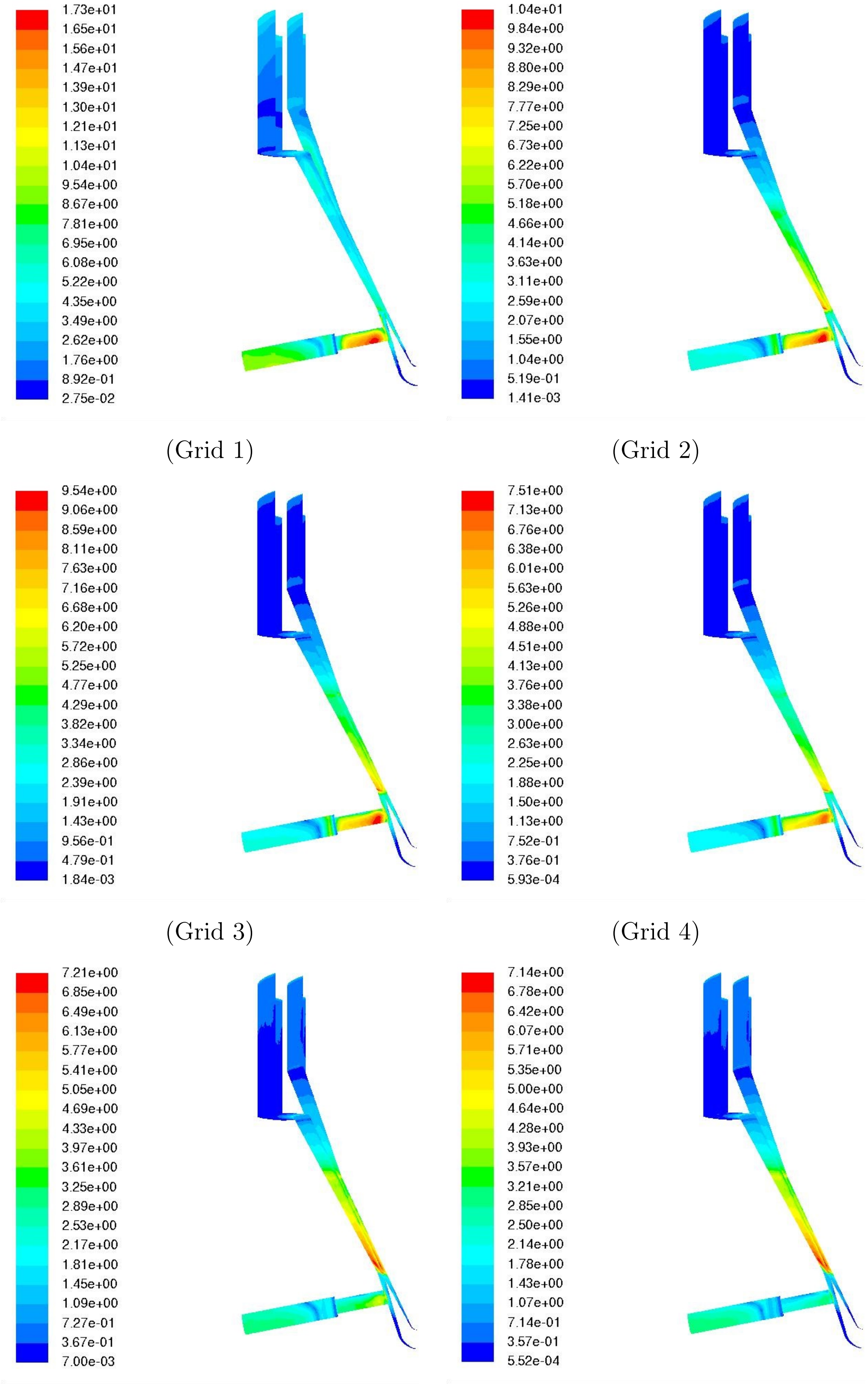

(Grid 1) (Grid 2)

(Grid 3) (Grid 4)

(Grid 5) (Grid 6)

Figure 4.64: Comparison of y^+ for different grids at lower needle lift, +x,+y,+z view.

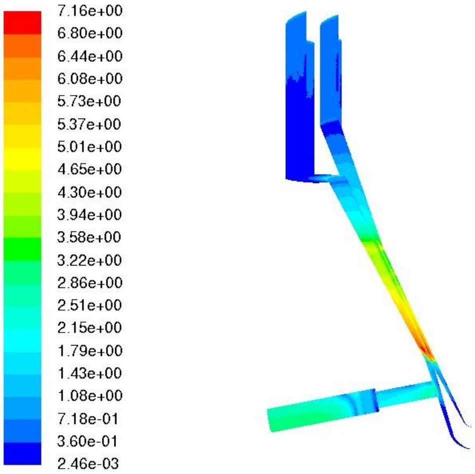

(Grid 7)

Figure 4.65: y^+ contours at grid 7 at the lower needle lift, +x,+y,+z view.

4.8.0.6 Contours: nominal needle lift

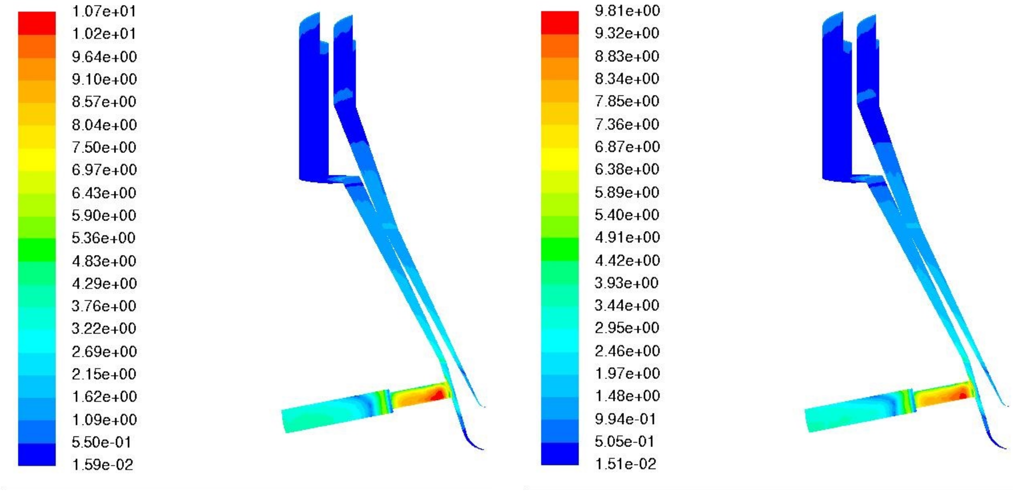

(Grid 1) (Grid 2)

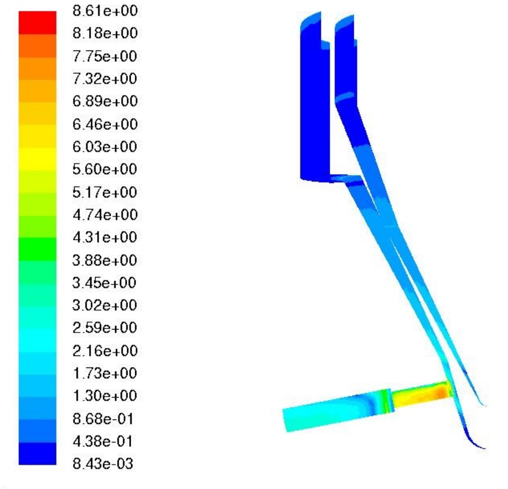

(Grid 3)

Figure 4.66: Comparison of y^+ for different grids at the nominal needle lift, +x,+y,+z view.

Chapter 5

Cavitation simulation in a single-hole injector

5.1 Introduction

The objective of this chapter to assess different turbulence and cavitation models to simulate the cavitating flow in the single-hole injector which could be subsequently applied for simulation of cavitating flow in the multi-hole injector. The impacts of cavitation model parameter and liquid and vapour compressibility would also be assessed. Simulations are performed using commercial CFD code ANSYS FLUENT V14.5. The simulations are evaluated by comparison with experimental measurements.

5.2 Test case description:

Duke et al. (2013a) performed X-ray radiography experiments on a model single-hole nozzle to measure cavitation vapour distribution. The test geometry (Figure 5.1) was a polycarbonate nozzle with a throat diameter of D = 0.5 mm, a length/diameter ratio (L/D) of 5 and inlet/outlet diameter ratio of 5. The working fluid was delivered via a piston accumulator system pressurised with an inert gas. The fluid temperature and pressure were monitored immediately upstream and downstream of the nozzle, and a turbine flowmeter was used to monitor flow rate. The injection pressure P_{inj} and back pressure P_{back} were varied independently. The Reynolds number based on nozzle diameter has been used:

$$Re_D = \frac{4\dot{m}}{\pi \rho_l \nu_l D} \tag{5.1}$$

where D is a diamater of the nozzle, $\dot{m}$ is mass flow rate, ρ_l is density of the liquid, ν_l is kinematic viscosity of liquid. Bergwerk's definition of cavitation number was used:

$$CN = \frac{p_{inj} - p_{back}}{p_{back} - p_v} \tag{5.2}$$

where p_{inj} is the upstream, p_{back} is the downstream pressure and p_v is the vapour pressure of the liquid. The working fluid was a gasoline surrogate (VISCOR 16-BR) with a vapour pressure of 580 Nm^{-2} at 25°C; the fluid was not degasified, more details can be found in Table 5.2. Operating conditions of experiments can be found in Table 5.1.

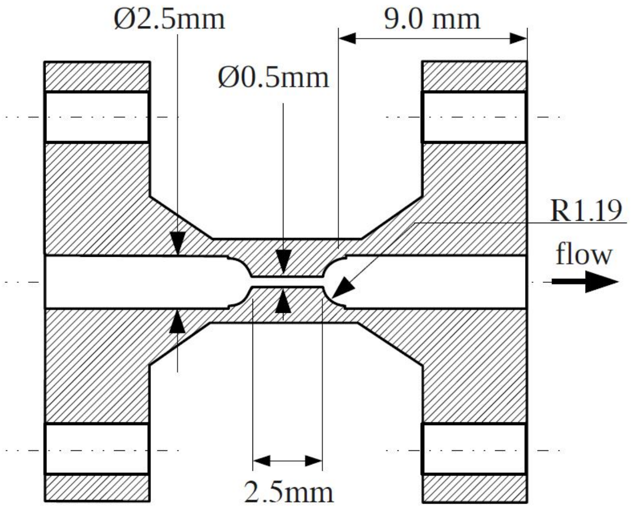

Figure 5.1: Schematic of the cavitating nozzle under study, source: Duke et al. (2013a).

case	P_{Inj} (kPa abs)	P_{back} (kPa abs)	Fuel flow rate (L/hr)	Re	CN	T
1	1060 ± 20	87 ± 2	26.8±0.24	1.58×10^4	11.2	25°C

Table 5.1: Operating conditions for cases.

fluid properties - liquid	
Specific gravity Density Viscosity Saturation pressure[*]	≈ 0.778 $\approx 777.97\ kg\ m^{-3}$ $\approx 8.48 \times 10^{-4}\ kg\ m^{-1}s^{-1}$ $\approx 580\ Nm^{-2}$
fluid properties - vapour	
Density[†] Viscosity[†]	$\approx 1\ kg\ m^{-3}$ $\approx 1.72\ \times 10^{-5}\ N\ m^{-2}s$

[*] The saturation pressure was measured using an Isoteniscope (see Duke et al., 2013a).

[†] The working fluid is a gasoline surrogate is a blend of hydrocarbons typically C_9H_n to $C_{14}H_n$. The physical properties of its vapour state are not known (Duke et al., 2013a). Hence for CFD calculations, density and viscosity of gasoline are used since it is also a mixture of similar hydrocarbons.

Table 5.2: Fluid properties at 25°C

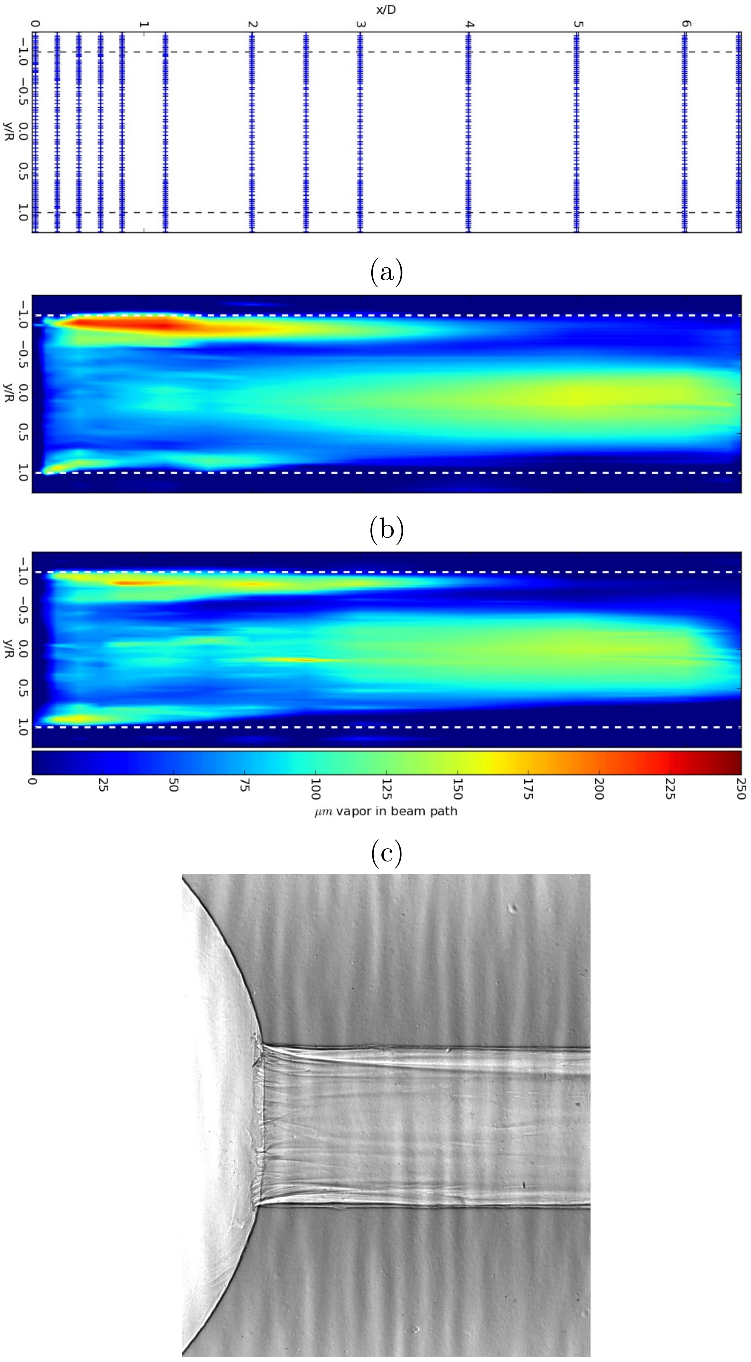

(a)

(b)

(c)

(d)

Figure 5.2: (a) The raster scan grid which shows 100 transverse (y) and 19 streamwise(x) positions where measurements of vapour fraction were taken, (b) Time-averaged X-ray radiography measurement of vapour fraction interpolated onto the contour at $CN = 11.2$, (c) Time-averaged X-ray radiography measurement of vapour fraction interpolated onto the contour at $CN = 10.7$ (d) Time-integrated X-ray images of nozzle inlet, taken with an unfocused X-ray monochromatic X-ray beam at $CN = 11.2$. Source: Duke et al. (2013a)

7-BM beamline of advanced proton source (APS) was used for the X-ray measurements. In the experiment, the focused beam acts as a microprobe, allowing the void fraction to be probed along the small area on the line of site. The nozzle traversed through the fixed beam in a raster scan pattern at 100 transverse positions (y) and 19 streamwise positions (x), the raster scan grid can be seen in Figure 5.2 (a). The time-averaged values were interpolated onto a series of contour plots, one of them can be seen in Figure 5.2 (b). Imaging has also been performed using the conventional X-ray, the Figure 5.2 (d) represents time-averaged X-ray image of the nozzle inlet, in which the presence of vapour can be seen as well. The time-average measurements of vapour quantity achieved an uncertainty of 2%. Time-resolved measurements of cavitation were taken at the different selected positions, at the interest of wall ($x/D = 1.2, y/R = 1$), in the entrainment region ($x/D = 1.2, y/R = 0.9$) and in the freestream ($x/D = 1.2, y/R = 0$), the largest RMS magnitudes in the time-resolved signal were 0.95% of the mean projected vapour quantity. Hence, steady cavitation regime was inferred. More details of the experimental setup can be found in Duke et al. (2013a).

From the experimental results, it was recognised that vapour is being generated at the sharp entrance of the nozzle orifice, as flow travels downstream vapour travels along the wall, shortly thereafter vapour detaches from the wall and mixes with the fluid at the centre line as it travels further downstream. This was in contrast with same research group's later experiment (Duke et al., 2014) in which it was observed that cavitation remained in the vicinity of the wall as fluid travelled downstream. However, the length of the orifice of the nozzle in the later experiments was 3.05 mm compare to 2.5 mm for the present case. The asymmetric vapour distribution was attributed to small machining defects which were acting like additional nucleation sites. Accumulation of vapour in the centre of the flow several diameters downstream was also observed, which has been previously reported by Bauer et al. (2012).

Duke et al. (2013a) proposed that the most likely cause for the presence of vapour along the centre line was due to vapour detachment from the wall and its transportation to the core due to the radially inward negative pressure gradient. This was in contrast with what was proposed by Bauer et al. (2012) who proposed that the isolated nucleation events may have caused vapour accumulation along the centre line. Duke et al. (2013a) also mentioned the possibility of dissolved gases in the fuel which may have caused centre vapour accumulation, which was assumed to be in the order of 10^{-3} moles per unit volume, however, this was not verified in the experiment.

Duke et al. (2013a) further asserted that the projected X-ray data captured all the vapour in the path of the beam, therefore, numerically integrated the total area fraction of vapour across the entire cross-sectional area of the nozzle at different axial locations as specified in Figure 5.2 (a). In this case, it was observed that total quantity of vapour remains constant unless the flow approaches the expansion region of the model nozzle, after which vapour quantity drops as the bubble collapses due to deceleration of the flow. Hence, it was implied that most of the phase change occurs at the sharp entrance of the nozzle orifice. The vapour observed around the nozzle axis few diameters away from the entrance ($0.1 < x/L < 1$) was due to the transport of vapour from the wall via due to the radially inward negative pressure gradient because of the possible vorticity.

The experimentalists (Duke et al., 2013a) did not investigate the possibility of choking due to the local sonic conditions. At choking the mass flow rate is not increased by the further decrease of downstream pressure at constant upstream pressure. Choked flow is said to occur when the flow velocity is greater than the speed of sound in the fluid in converging-diverging nozzles and venturi tubes (Shames and Shames, 1982). Choked flow in cavitating fuel injector has been previously reported by Soteriou et al. (1995); Winklhofer et al. (2001). However, the speed of sound in the liquid is generally in the region around 1300 ms^{-1} and speed of sound in air is in the region of 350 ms^{-1}, hence it can be argued that mean flow may never have exceeded the supersonic speed of both phases. Nevertheless, experimentally it has been shown that a small amount of gas causes a drastic reduction in the sonic speed of liquid-gas or liquid-vapour mixture (Karplus, 1957; Semenov and Kosterin, 1964; Henry et al., 1971). Therefore the mean flow easily becomes supersonic in the two-phase region. However, just downstream of the cavitation region, the fluid reattains the sonic speed of liquid and therefore the mean flow becomes subsonic, producing a shock. Due to this shock, no signal is propagated upstream from the downstream, causing a choked flow. Therefore, it is highly recommended for experimentalists and CFD engineers to investigate the choking phenomenon in multi-phase flows, especially in nozzles.

5.3 Numerical errors (Grid sensivity analysis)

In this section, the influence of grid density in the flow domain on numerical results is assessed.

5.3.0.1 Case setup:

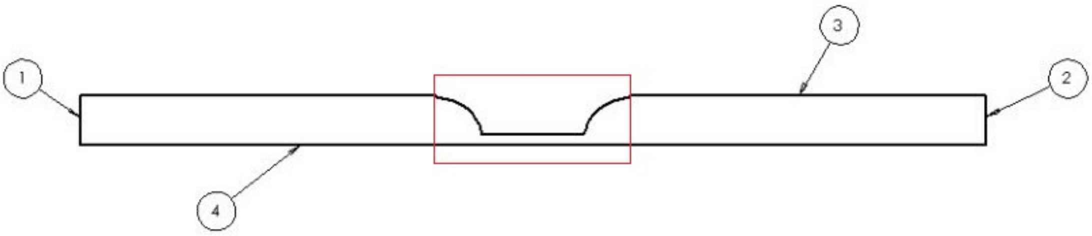

Figure 5.3: 2D flow domain for the present case: The numbers represent boundaries of flow domains, (1) inlet (2) outlet (3) wall (4) axis.

The first simulation was performed using a relatively coarse grid; the grid was then successively refined with each simulation until further refinement did not influence the solution. Operating condition as described for case 1 in Table 5.1, is simulated. Considering that the nozzle was axisymmetrical (Figure 5.1), the 2D axisymmetrical flow domain (Figure 5.3) has been used and was discretized into hexahedral type grid (Figure 5.4 (a)). In addition, 10 inflation layers (2D prism cells) have been added to the wall to resolve near wall turbulence. The grid has been locally refined in the nozzle orifice, convergent circular region before the entrance of the orifice and within the circular expansion after the orifice exit as highlighted using the red box in Figure 5.3, followed by near wall (y^+) refinements (Figure 5.4 (b) & (d)) for low-Re turbulence model simulations. Steady-state simulations have been performed. Turbulence effects are introduced using the standard $k - \epsilon$ model (see Launder and Spalding, 1972) and near wall turbulence is resolved using the 'enhanced wall treatment' method (see § 3.8.3). For cavitation modelling, Zwart et al. (2004) cavitation model has been used with a mixture multi-phase model (see Manninen et al., 1996). Physical properties of working fluid are listed in Table 5.2. Boundary conditions are listed in Table 5.3.

Case	Inlet	Outlet	interface	Walls
$CN = 11.2$	mass-flow rate liquid= 0.00572 $kg\ s^{-1}$ vapour= 0 $kg\ s^{-1}$	constant pressure 87000 Nm^{-2}	cyclic	Enhanced wall treatment method (no slip wall)

Table 5.3: Boundary Conditions

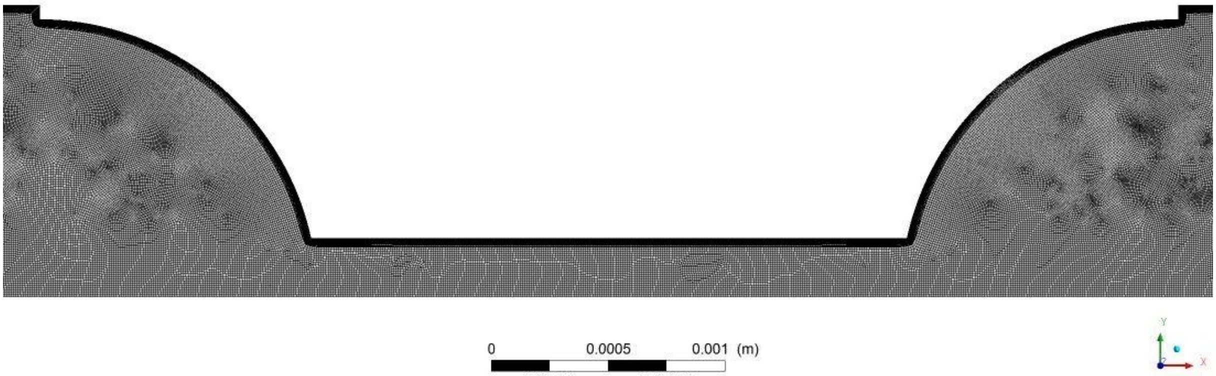
0
0.0005
0.001 (m)
0.00025
0.00075
Y
X

(a) grid 1

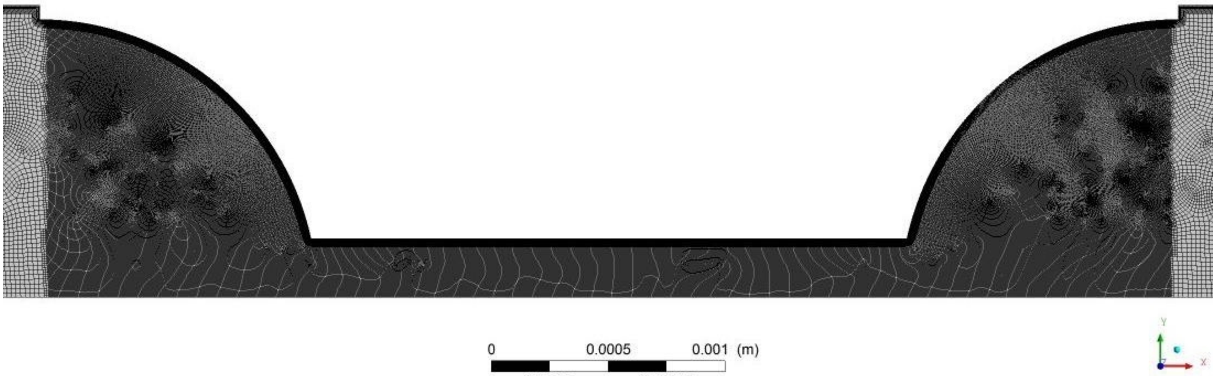
0
0.0005
0.001 (m)
0.00025
0.00075
Y
X

(b) grid 5

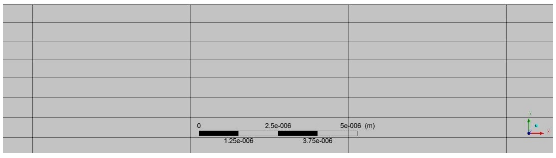
0
2.5e-006
5e-006 (m)
1.25e-006
3.75e-006

(c) Zoom of near wall region of grid 3

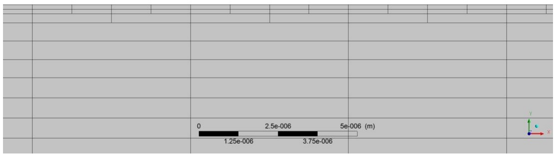
0
2.5e-006
5e-006 (m)
1.25e-006
3.75e-006

(d) Zoom of near wall region of grid 5

Figure 5.4: (a) 2D hexahedral mesh for the flow domain. 10 inflation cells were added to the wall in order to accurately capture near wall flow regime. (b) Grid 5 which has been locally refined successively from the grid 1 within the orifice, circular convergent section of the nozzle and circular expansion section of the nozzle, the mesh concentration near wall was further increased to ensure $y^+ < 1$ using y^+ adaptation, (c) Grid without y^+ adaptation (grid 3) (d) Grid with y^+ adaptation (grid 5).

5.3.0.2 Results:

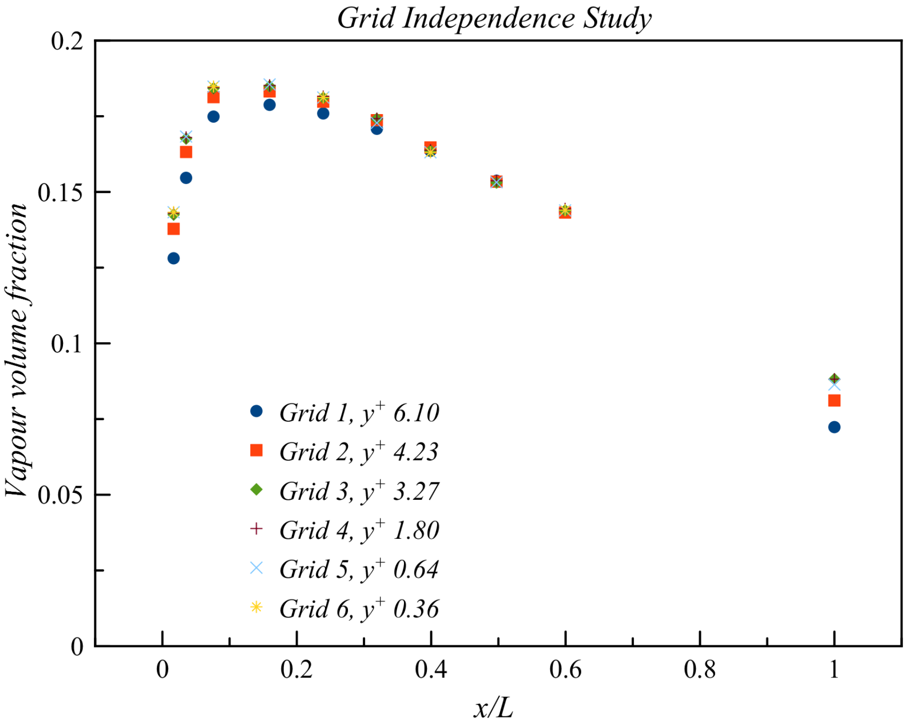

(a)

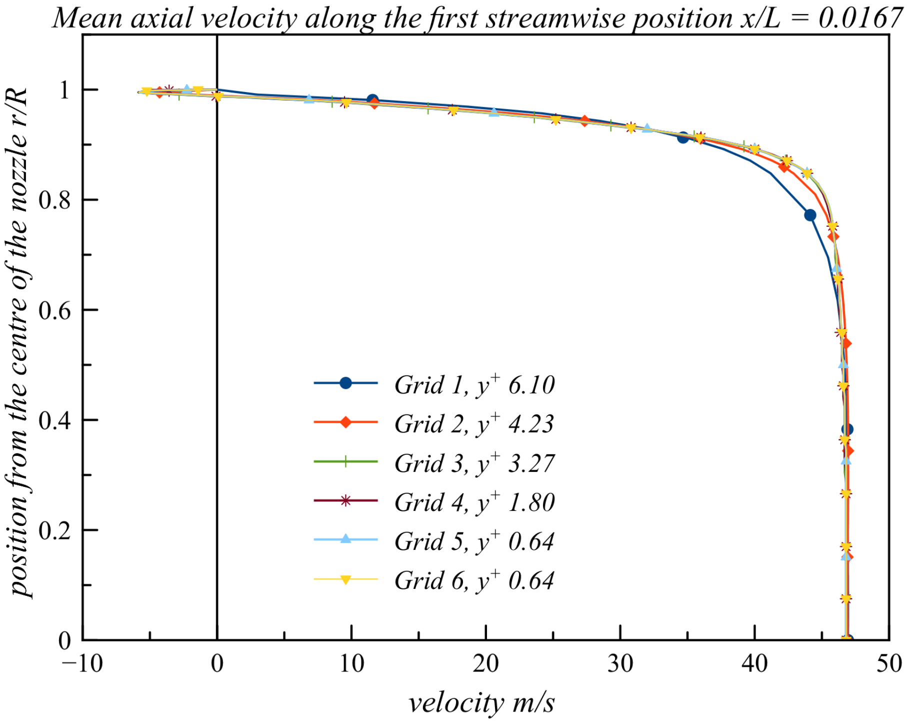

(b)

Figure 5.5: (a) Grid independence study - vapour volume fraction, (b) Grid independence study - velocity.

Grid	(CV)*	Refinement method	Refinement factor (global)**	Maximum y^+
1	89,189	global sizing	1	6.10
2	121,526	locally refined region adaptation †	1.36	4.23
3	251,039	locally refined region adaptation	2.81	3.27
4	253,142	locally refined y^+ adaptation ‡	2.832	1.80
5	260,153	locally refined y^+ adaptation	2.916	0.64
6	273,563	locally refined y^+ adaptation	3.067	0.36

[*] Control Volumes

[†] Region adaption: Mesh is refined over the area as shown in Figure 5.3.

[‡] y^+ adaptation: Mesh refined near wall as shown in Figure 5.4 (a), (b), (c) and (d).

[**] Refinement factor: Refinement factor is defined as the ratio of numbers of cells of the current grid and the first grid.

Table 5.4: Grid description

The grid was first locally refined in the nozzle orifice, convergent circular region before the entrance of the orifice and within the circular expansion after the orifice exit (Figure 5.4 (b)). Following this, grid was refined at the nozzle wall to ensure $y^+ < 1$ for Low-Re turbulence models (see Figure 5.4 (c) and (d) and Table 5.4).

In Figure 5.5, the normalised axial locations represent the streamwise (x) locations in raster scan grid where X-ray measurements of cavitation were taken as shown in Figure 5.2. Simulation results for the vapour volume fraction at these streamwise (x) locations are presented in Figure 5.5 (a) and the axial velocity at the first axial location $x/L = 0.0167$ are presented in Figure 5.5 (b) indicates that grid independence is being approached with grid 5 and 6.

5.3.0.3 Discussions:

- Grid independence is being approached with grid 5 and 6, and hence grid 5 would be used in later analysis.

5.4 Physical modelling errors

5.4.1 Turbulence models comparison

In this section, we evaluate and identify the most well-behaved turbulence model in RANS modelling environment for cavitation prediction for the present test case. Turbulence models which have been evaluated are: 1) Standard $k - \epsilon$ model, 2) Realizable $k - \epsilon$ model, 3) Launder and Sharma $k - \epsilon$ model 4) SST $k - \omega$ model.

5.4.1.1 Case setup:

Operating condition as described for the case 1 in Table 5.1 is simulated. Steady-state simulations have been performed using the above-mentioned turbulence models. 'Enhanced wall treatment' method has been used with the standard and realizable $k - \epsilon$ models for near wall modelling. For cavitation modelling Zwart et al. (2004) model has been used with a mixture multi-phase model. Both liquid and vapour phase are assumed incompressible. Physical properties of the working fluid are listed in Table 5.2. Boundary conditions are listed in Table 5.3.

5.4.1.2 Results:

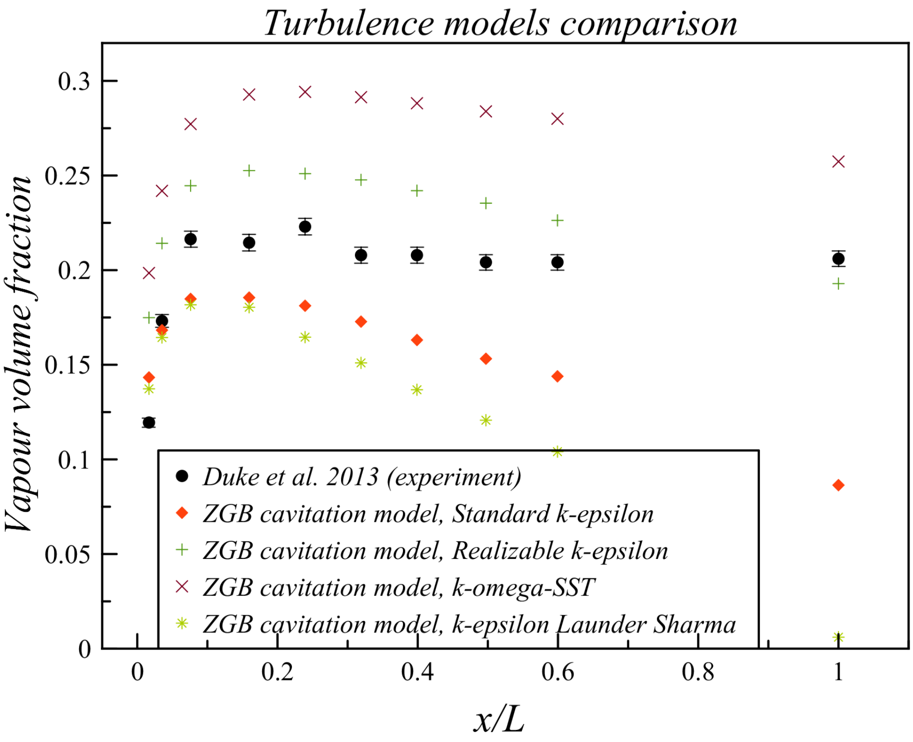

Figure 5.6: Comparison of the predicted total volume fraction of vapour in slices across the nozzle and experimentally measured the total vapour volume fraction of vapour in slices across the nozzle.

Figure 5.7 (a) represents projections of void fraction of the X-ray radiography measurements at CN=11.2. On observing the projected void fractions, it can be seen that vapour is generated at the sharp entrance of the nozzle orifice. The vapour then separates from the wall and mixes with the flow as it travels further downstream. Accumulation of vapour along the centre-line, several diameters downstream can be seen as well. The observed asymmetric vapour distribution has been attributed to small machining defects which may have provided additional nucleation sites to the nozzle (Duke et al., 2013a). The total quantity of vapour was further integrated over the nozzle cross section at different axial locations (x/L) and is represented in Figure 5.6.

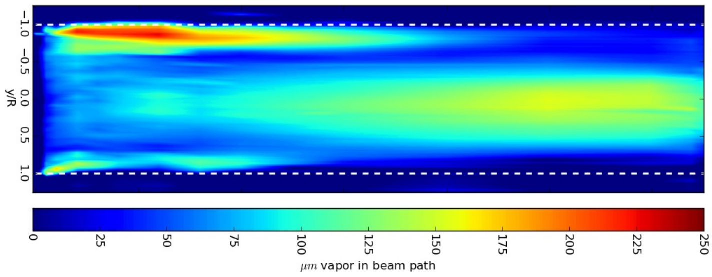

(a) Time-averaged X-ray radiography measurement of vapour fraction interpolated onto the contour at $CN = 11.2$ (Duke et al., 2013a)

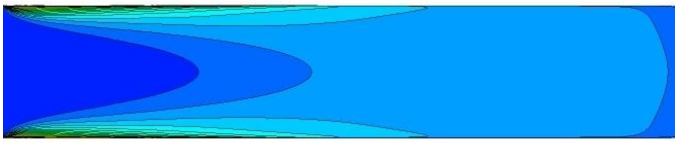

(b) standard $k - \epsilon$ model

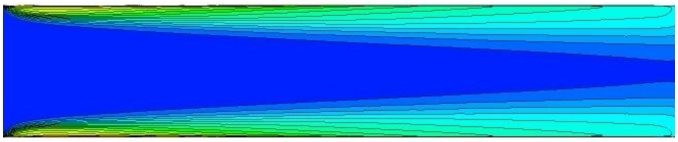

(c) realizable $k - \epsilon$ model

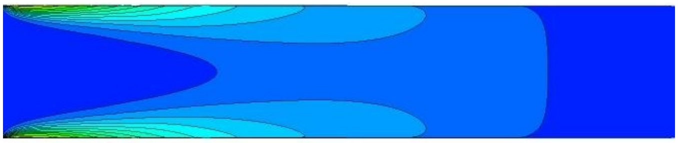

(d) Launder and Sharma low-Re $k - \epsilon$

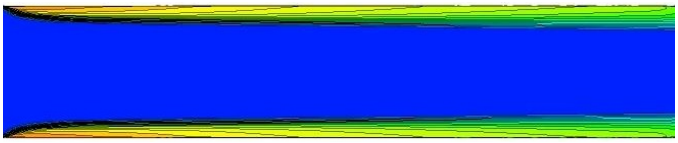

(e) SST $k - \omega$ model

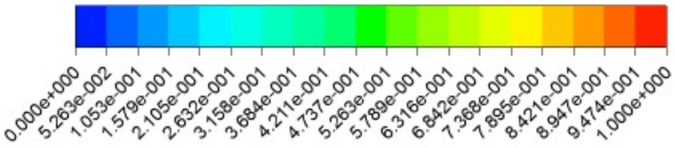

Figure 5.7: Qualitative comparison between the experimental and CFD results.

On comparison of the predicted results using the realizable $k - \epsilon$ and standard $k - \epsilon$ model in Figure 5.6, it can be seen that more cavitation has been predicted using realizable $k - \epsilon$ model. This can be correlated with the larger recirculation zone predicted using the realizable $k - \epsilon$

model at the axial location $x/L = 0.0167$ as shown in Figure 5.9 (a) which presents the mean axial velocity profiles. Larger recirculation zone corresponds to the larger saturated pressure region (Figure 5.9 (b)) leading to the larger prediction of vapour volume.

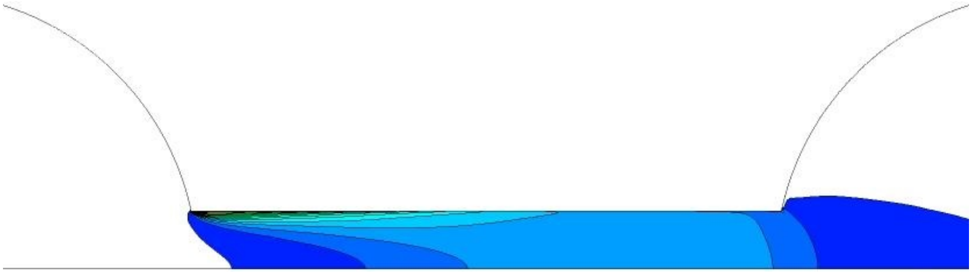

(a) standard $k-\epsilon$ model

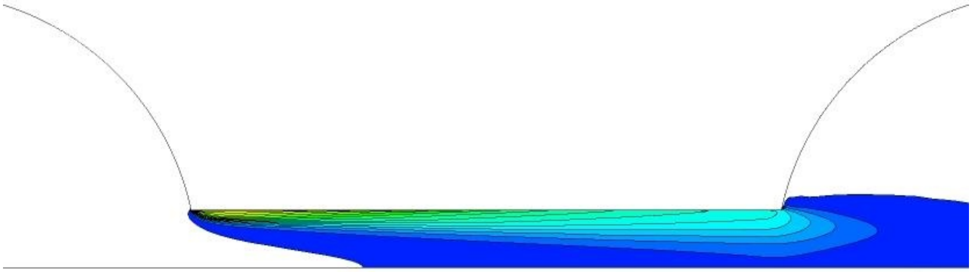

(b) realizable $k-\epsilon$ model

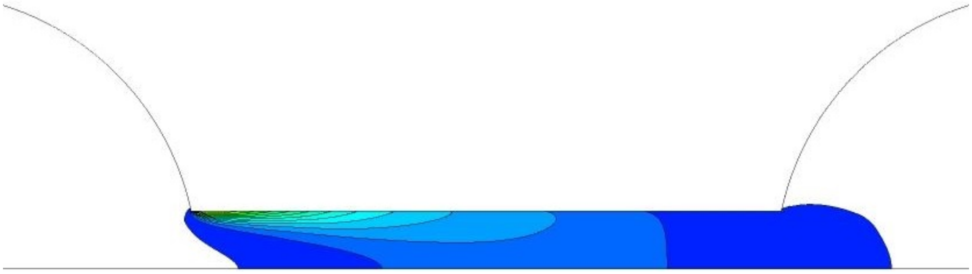

(c) Launder and Sharma low-Re $k-\epsilon$ model

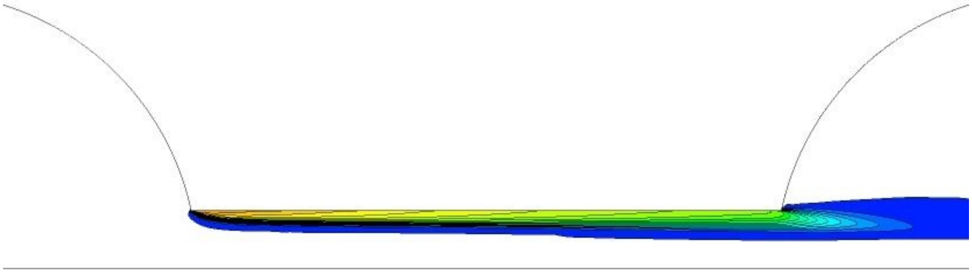

(d) SST $k-\omega$ model

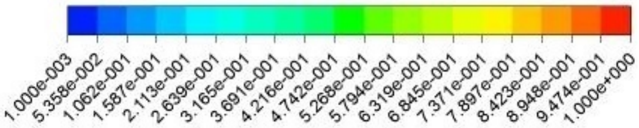

Figure 5.8: Vapour volume fraction predicted using different turbulence models.

On the contrary, by qualitative comparison of the prediction results, results that better agree have been obtained using standard $k-\epsilon$ model (Figure 5.7 (b)) than the realizable $k-\epsilon$ model (Figure 5.7 (c)). The CFD results suggest that vapour is generated at the sharp entrance of the nozzle orifice. The large volume of vapour is seen in the vicinity of the wall and is seen mixing with the liquid as convected further downstream. The cavitation structure ends at the orifice exit (Figure 5.8 (a)). The contours obtained using the realizable $k - \epsilon$ model (Figure 5.7 (c)) also indicate vapour formation at the sharp entrance of the nozzle orifice, however, the vapour remains in the vicinity of the orifice wall, unlike the standard $k - \epsilon$ model. The cavitation contours obtained using the realizable $k - \epsilon$ model (Figure 5.8 (b)) suggests cavitation entering the circular expansion region of the orifice where it finally terminates.

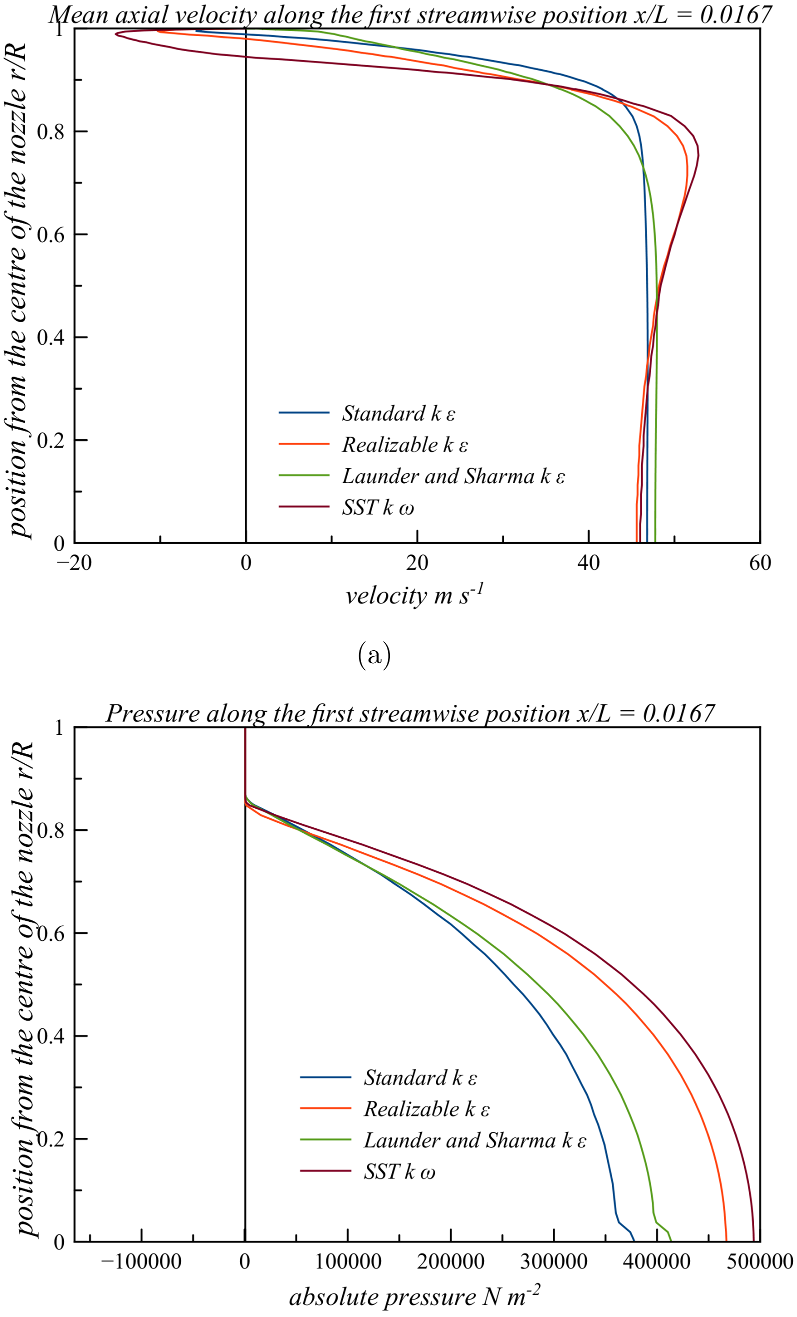

(a)

(b)

Figure 5.9: Predicted mean axial velocity on plane 1 using different turbulence models.

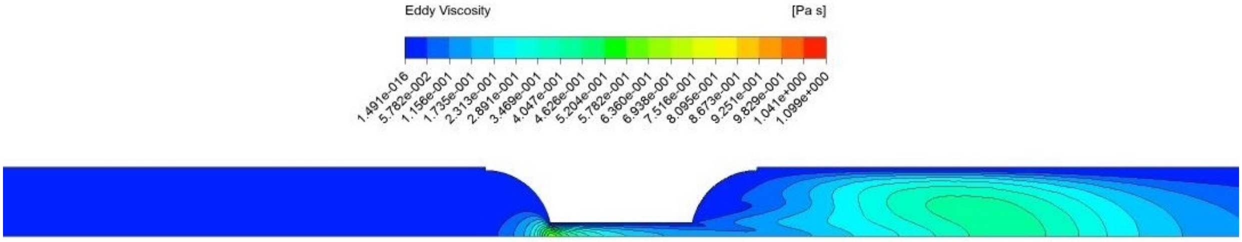

(a) Turbulent viscosity μ_t obtained using standard $k-\epsilon$ model (overall range)

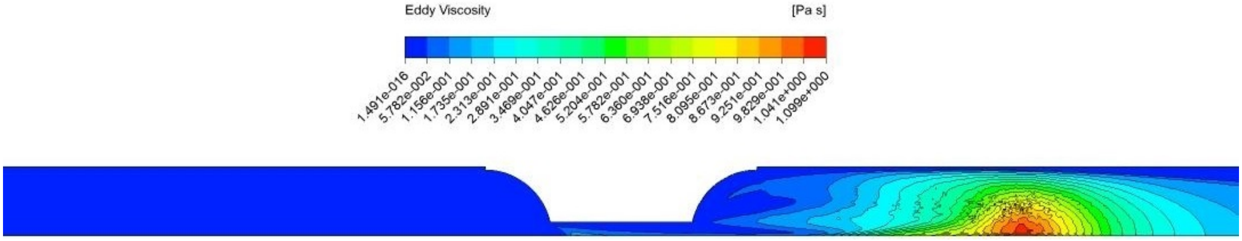

(b) Turbulent viscosity μ_t obtained using realizable $k-\epsilon$ model (overall range)

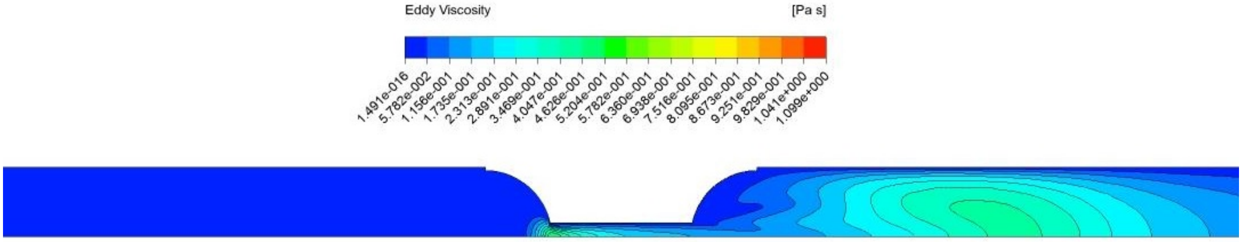

(c) Turbulent viscosity μ_t obtained using Launder and Sharma Low-Re $k-\epsilon$ model (overall range)

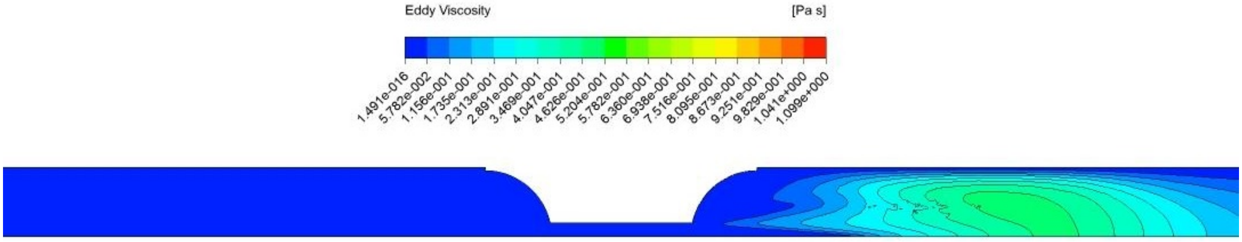

(d) Turbulent viscosity μ_t obtained using SST $k-\omega$ model (overall range)

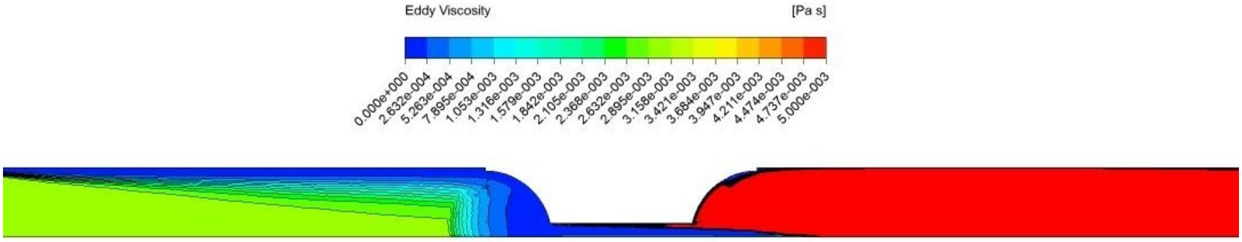

(e) Turbulent viscosity μ_t obtained using SST $k-\omega$ model (specific range)

Figure 5.10: Turbulent viscosity contours obtained using different turbulence models.

It should be noted that the same near wall modelling approach (enhanced wall treatment) has been used with the standard $k-\epsilon$ and realizable $k-\epsilon$ models, therefore, similar maximum y^+ values have been obtained for both models (see Table 5.5). Nevertheless, the difference in the behaviour of both model can be attributed to the variable C_μ in the realizable $k-\epsilon$ model which is constant in the standard $k-\epsilon$ model. The C_μ directly influences the turbulent viscosity μ_t (see Figure 5.10 (a) and (b)) and, therefore, the flow field. It can also be seen in Figure 5.10 (a) and (b) that lower turbulent viscosity is predicted using the realizable $k-\epsilon$ model than the standard $k-\epsilon$ model. Therefore, the larger recirculation region (Figure 5.9 (a)) predicted using the realizable $k-\epsilon$ at the orifice entrance can be attributed to the lower turbulent viscosity predicted and has resulted in the prediction of the larger saturated pressure region (Figure 5.9 (b)).

While higher turbulent viscosity predicted using the standard $k-\epsilon$ has resulted in more diffusion between phases (see Figure 5.7 (a) and (b)). Nevertheless, from the present analysis, it can be stated that the different turbulent viscosity formulation in realizable $k-\epsilon$ model has resulted in a more accurate prediction of the recirculation region, flow reattachment and this resulted in a more accurate prediction of vapour volume fraction in the present case. More accurate prediction of the recirculation region and the flow reattachment using the realizable $k-\epsilon$ model was also observed in the case of an enlarged multi-hole injector in the chapter 4, § 4.5.1.

The vapour volume fraction has been underpredicted using the Launder and Sharma low-Re turbulence model (Figure 5.6, 5.7 (d) and 5.8 (c)). The model has the same transport equations for k and ϵ as the standard $k-\epsilon$ model, as well as has the same formulation for turbulent viscosity. However, the model has additional source terms in the transport equations for k and ϵ and damping functions which are active only close to the wall allowing the model to predict k and ϵ in the viscous sublayer, therefore, the model does not use wall functions. Nevertheless, results indicate that the model's low-Re approach has failed to completely capture the flow regime for the present case. The model has predicted a smaller recirculation region (Figure 5.9 (a)) which resulted in the smaller low-pressure region (Figure 5.9 (b)), therefore, lesser cavitation is predicted. The obtained contours using the Launder and Sharma low-Re turbulence model (Figure 5.7 (d) and 5.8 (c)) indicate vapour is generated at the sharp entrance of the nozzle orifice. As fluid convects downstream the cavitation is largely seen in the vicinity of the wall and ends around two-third of the orifice length.

The vapour volume fraction is overpredicted using the SST $k-\omega$ model (Figure 5.6). The SST $k-\omega$ model uses features of the standard $k-\epsilon$ model (Launder and Spalding, 1972) in the far-field region and the $k-\omega$ model (Wilcox et al., 1998) in the near wall region. The $k-\omega$ terms are integrated throughout the viscous sublayer hence the model does not require wall functions. The model also has a different formulation for turbulent viscosity (see Equation (3.85)) than the $k-\epsilon$ family of models. The model predicts the generation of vapour at the sharp entrance of the nozzle orifice (Figure 5.7 (e) and 5.8 (d)) where liquid pressure reaches its saturated vapour pressure (Figure 5.9 (b). The cavitation contour (Figure 5.8 (d)) suggest that vapour remains in the vicinity of the wall, as fluid convects downstream and can also be seen entering the circular expansion region of the nozzle. On comparing the mean axial velocity profiles at the axial position $x/L = 0.0167$ (Figure 5.9 (a)), it can be seen that the largest recirculation region at the sharp entrance of the nozzle orifice has been predicted using SST $k-\omega$ model leading to a higher vapour prediction. However, it can also be seen that the cavitation does not diffuse and mixes with liquid like the cases of the standard $k-\epsilon$, realizable $k-\epsilon$ and Launder and Sharma $k-\epsilon$ models (see Figure 5.7 (a), (b), (c) and (d) and Figure 5.8 (a), (b), (c) and (d)). This behaviour of the model can be attributed to different turbulent viscosity formulation in the SST $k-\omega$ model, as it can be seen from Figure 5.10 (d) and (e) that very low turbulent viscosity is predicted using a $k-\omega$ model due to which lower diffusion is predicted.

Case	Model	(CV)**	Maximum y^+
1	Standard k ϵ	253,153	0.64
2	Realizable k ϵ	253,153	0.67
3	Launder and Sharma k ϵ	253,153	0.59
4	SST-k ω	253,153	0.75

** Control Volumes

Table 5.5: Maximum y^+ obtained using different turbulence models.

5.4.1.3 Discussions

- Amongst turbulence models evaluated, the best quantitative agreement with the experimental data for cavitation predictions has been achieved using the realizable $k-\epsilon$ model with the 'enhanced wall treatment' method. Therefore, in later studies in this chapter, the turbulence will be modelled using above mentioned approach.

- On comparing results achieved using the standard and realizable $k-\epsilon$ models, higher vapour volume fraction has been predicted using the realizable $k-\epsilon$ model. This may be correlated with a larger recirculation region predicted at the entrance of the orifice using the realizable $k-\epsilon$ model leading to the prediction of a larger saturated pressure region causing higher vapour volume fraction prediction.

- The difference in the results obtained between the standard $k-\epsilon$ model and realizable $k-\epsilon$ model could be attributed to the difference in turbulent viscosity μ_t formulation due to variable C_μ in the realizable $k-\epsilon$ model which resulted in lower turbulent viscosity μ_t. The C_μ is constant in the standard $k-\epsilon$ model.

- The vapour volume fraction has been underpredicted using the Launder and Sharma low-Re $k-\epsilon$ turbulence model. The model has the same transport equations for k and ϵ as standard $k-\epsilon$ model, however, it has additional source terms in the transport equation for k and ϵ and damping functions which are active only close to wall allowing the model to predict k and ϵ in the viscous sublayer, hence the model does not use wall functions. Nevertheless, results indicate that low-Re modelling approach in the model has failed to completely capture the flow regime for the present case. The model predicted a smaller recirculation region at the entrance of the orifice which resulted in the prediction of a small saturated pressure region, leading to the lower prediction of cavitation.

- The highest (may not be the most accurate) cavitation has been predicted using the SST $k-\omega$ model. This may correlate with the largest recirculation zone predicted at the entrance of the orifice. However, it can be seen that cavitation does not diffuse and mixes with liquid like for the cases of the standard $k-\epsilon$, realizable $k-\epsilon$ and Launder and Sharma $k-\epsilon$ models. This behaviour can also be attributed to the turbulent viscosity (Figure 3.49 (e) and (f)) formulation in the model and since less turbulent viscosity has been predicted using the SST $k-\omega$ model, which has resulted in lower diffusion.

- It should be noted that in the present case both liquid and vapour are considered incompressible hence the obtained results may not reflect the true picture of cavitating flows in nozzles.

5.4.2 Cavitation models evaluation

In the present section, we evaluate two cavitation models for cavitation prediction for the present test case. The models which are being assessed are 1) **Schnerr and Sauer (SS)** model and 2) **Zwart, Gerber and Belamri (ZGB)** model.

5.4.2.1 Case setup

Steady-state simulations have been performed. Operating condition as described for the case 1 in Table 5.1 is simulated. Simulations have been performed using Schnerr and Sauer (SS) and Zwart, Gerber and Balamri (ZGB) models with a mixture multiphase model. The model constants have not been changed. The liquid and vapour states are assumed incompressible. a Physical properties of the working fluid are listed in Table 5.2. Boundary conditions are listed in Table 5.3.

5.4.2.2 Results:

Quantitative comparison of predicted results with experimental measurements in Figure 5.11 indicates that higher vapour volume is predicted using the ZGB model then the SS model. The qualitative comparison of predicted contours of vapour fraction with X-ray radiography measurements of vapour volume fraction in Figure 5.13 (a), 5.13 (b) and 5.13 (c) suggests that both models have failed to capture the flow characteristics adequately. Results of both models as shown in Figure 5.12 (a) and 5.12 (b) indicate that cavitation initiates at the sharp entrance of the orifice after which it convects downstream with the liquid. Both models predict that the significant proportion of vapour remains in the vicinity of the wall and can be seen entering into the circular expansion region where it totally collapses due to higher local pressure. Both models have failed to predict vapour along the centre line as found in experimental results.

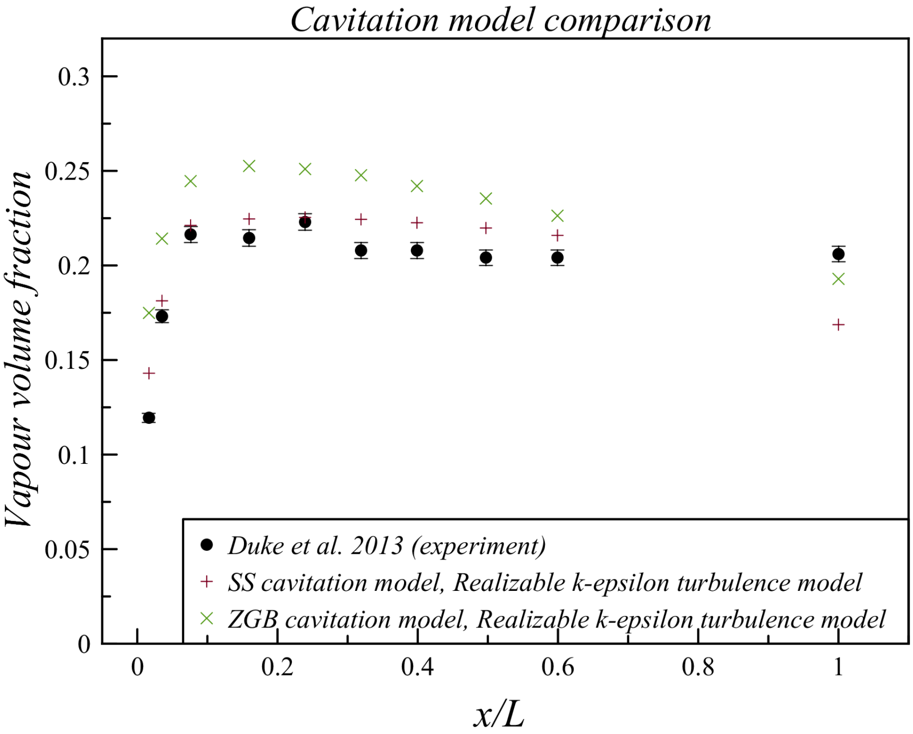

Figure 5.11: Predicted total volume fraction of vapour in slices across the nozzle.

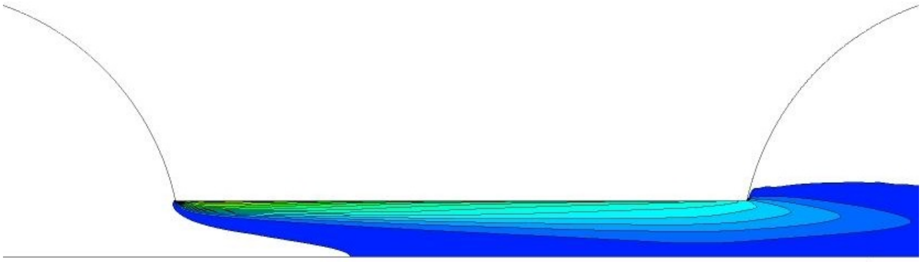

(a) SS model

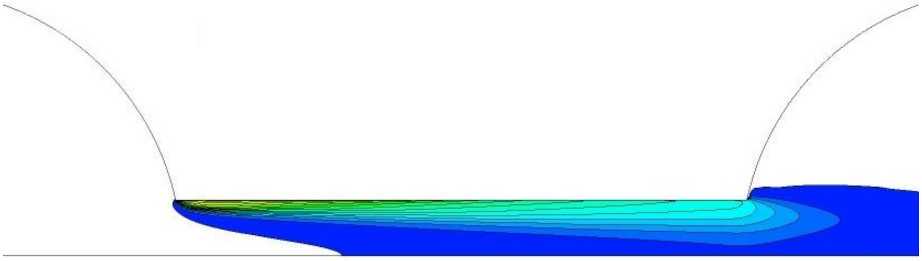

(b) ZGB model

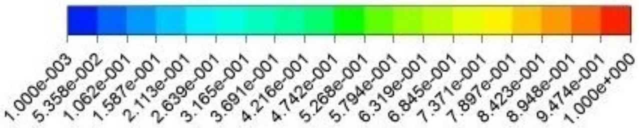
1.000e-003
5.358e-002
1.062e-001
1.587e-001
2.113e-001
2.639e-001
3.165e-001
3.691e-001
4.216e-001
4.742e-001
5.268e-001
5.794e-001
6.319e-001
6.845e-001
7.371e-001
7.897e-001
8.423e-001
8.948e-001
9.474e-001
1.000e+000

Figure 5.12: Visual comparison of vapour volume fraction predicted using two cavitation models.

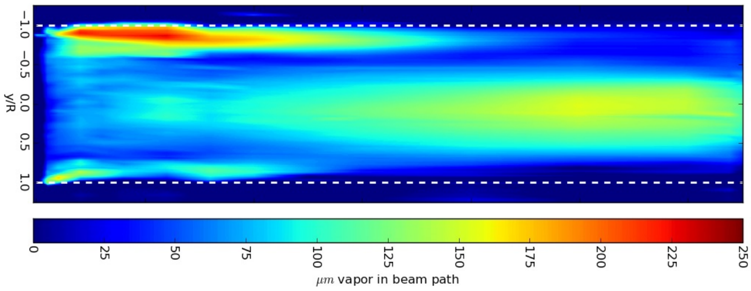

(a)

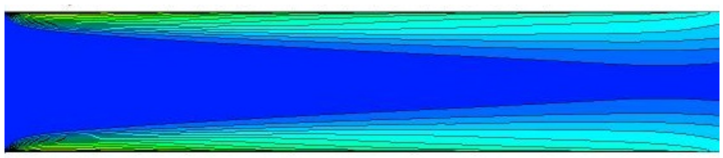

(b) SS model

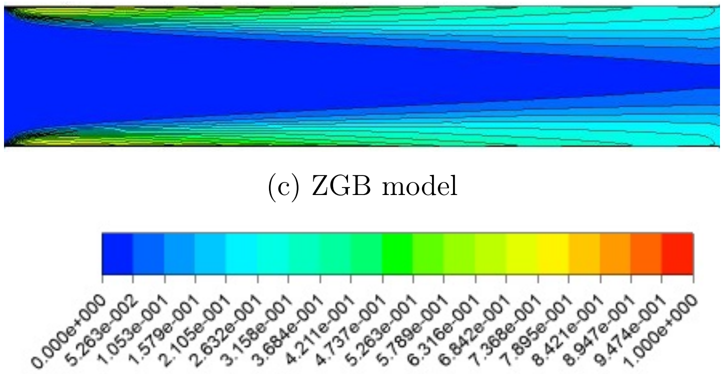

(c) ZGB model

Figure 5.13: Qualitative comparison between the experimental and CFD predicted results. (a) X-ray radiography measurement at $CN = 11.2$, (Duke et al., 2013a), (b) SS model (c) ZGB model.

To further analyse the prediction results, we decided to compare and plot the evaporation and condensation rate terms of both models.

For SS model at $p_v \geq p_{cell}$, we have the following rate term for evaporation:

$$R_e = \frac{\rho_v \rho_l}{\rho_{mixture}} \alpha_v (1 - \alpha_v) \frac{3}{R_B} \sqrt{\frac{2}{3} \frac{|p_v - p_{cell}|}{\rho_l}} \tag{5.3}$$

where R_B is the radius of the bubble and is determined by the following relationship

$$R_B = \left(\frac{\alpha_v}{(1 - \alpha_v)} \frac{3}{4\pi} \frac{1}{n_B} \right)^{\frac{1}{3}} \tag{5.4}$$

For ZGB model at $p_v \geq p_{cell}$, we have the following rate term for evaporation:

$$R_e = F_{vap} \frac{3\alpha_{nuc}(1 - \alpha_v)\rho_v}{R_B} \sqrt{\frac{2}{3} \frac{|p_v - p_{cell}|}{\rho_l}} \tag{5.5}$$

The models constants are:

$$\begin{aligned} R_B &= \text{bubble radius} = 1 \times 10^{-6} m \\ \alpha_{nuc} &= \text{nucleation site volume fraction} = 5 \times 10^{-4} \\ F_{vap} &= \text{evaporation co-efficient} = 50 \end{aligned} \tag{5.6}$$

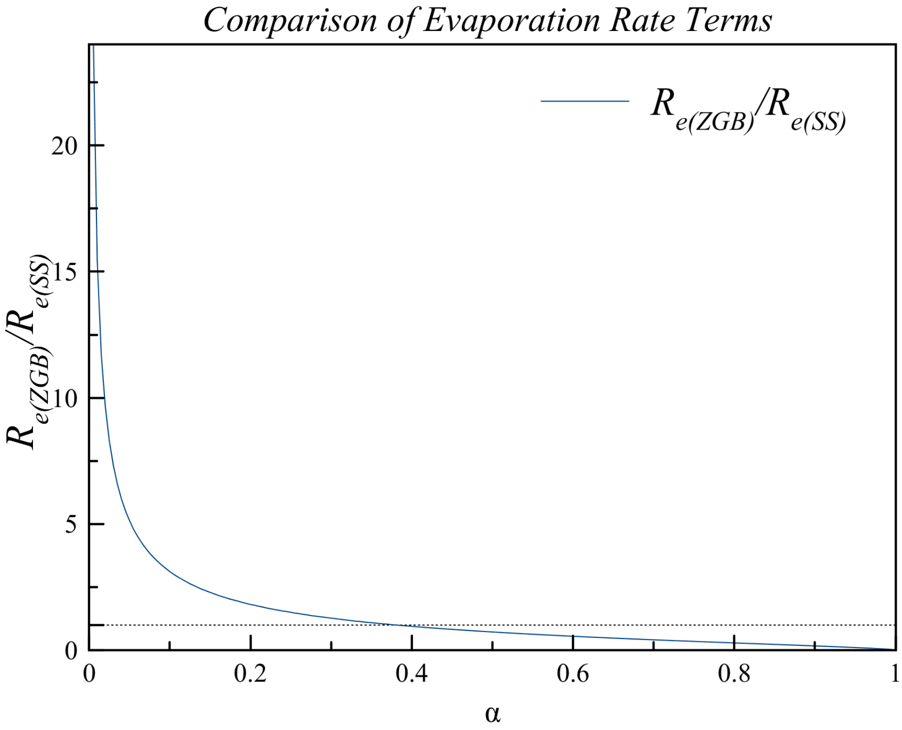

Figure 5.14: Comparison of the evaporation rate of SS and ZGB model. $\rho_l = 777.97 kgm^{-3}$, $\rho_v = 1 kg\ m^{-3}$

For SS model at $p_v \le p_{cell}$, we have the following rate term for condensation:

when $p_v \le p_{cell}$, condensation:

$$R_c = -\frac{\rho_v \rho_l}{\rho_{mixture}} \alpha_v (1 - \alpha_v) \frac{3}{R_B} \sqrt{\frac{2}{3} \frac{|p_v - p_{cell}|}{\rho_l}} \tag{5.7}$$

For ZGB model at $p_v \le p_{cell}$, we have the following rate term for condensation:

$$R_c = -F_{cond} \frac{3 \alpha_v \rho_v}{R_B} \sqrt{\frac{2}{3} \frac{|p_v - p_{cell}|}{\rho_l}} \tag{5.8}$$

where

$$F_{cond} = \text{condensation co-efficient} = 0.01 \tag{5.9}$$

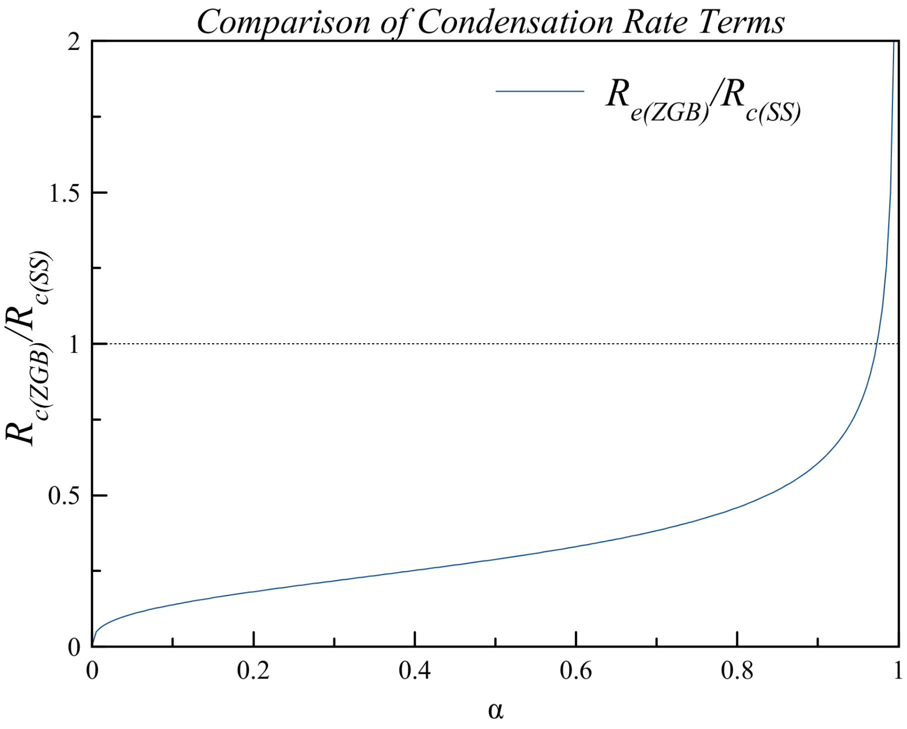

Figure 5.15: Comparison of the condensation rate of SS and ZGB model. $\rho_l = 777.97 kgm^{-3}$, $\rho_v = 1 kg$ m^{-3}

The evaporation and condensation rates in SS model is non-linear and is proportional to $\alpha_v(1 - \alpha_v)$ and has an unusual property; it approaches zero when $\alpha \longrightarrow 0$ and $\alpha \longrightarrow 1$ and is maximum in between. Hence, the SS model requires a particular value of vapour fraction at the inlet boundary. The value used in the present case for SS model is $\alpha_0 = 10^{-5}$ as recommended by Schnerr and Sauer (2001) which is not the case for ZGB model. The evaporation and condensation rates in ZGB model are linear and starts from an initial value.

Hence, the ratio of evaporation and evaporation and condensation rates of both models from range $0.005 < \alpha < 0.995$ are plotted. The evaporation rate ratio indicates that higher values in ZGB model over SS model in the range of $0.005 < \alpha < 0.35$. The condensation rate ratio graph also suggests higher initial values of condensation rate but in a small range $0.995 < \alpha < 0.005$ following which the condensation range is greater of SS model. From this comparison, it can be stated that higher vapour volume fraction is predicted in the ZGB model because of the higher initial evaporation rate in ZGB model over SS model and lesser overall condensation rate of ZGB model.

5.4.2.3 Discussions

- Higher vapour volume fraction is predicted using the ZGB model than SS model which could be due to higher initial values of evaporation rate and lower overall condensation rate in ZGB model than SS model.
- Both models failed to predict cavitation around the orifice centre line.
- Nevertheless, we should note that the cavitation vapour is assumed to be incompressible which may not be in the real situation. Hence, these models are required to be assessed for compressible vapour assumption.

5.4.3 Uncertainties of cavitation models and impact of parameters used in these models

Both cavitation models are based on transport equations for the vapour fraction and have been qualitatively evaluated for cavitating flows and have effectively predicted the mean features of the cavitating flows. The models contain parameters which need to be adjusted to account for the liquid quality. One of the important parameters which affect the liquid quality is the bubble nuclei population (Martynov, 2005). In real liquids, nuclei may comprise of small gas bubbles and impurities. It has been suggested (Brennen, 1995) that nuclei of larger critical value can assist cavitation while smaller ones stay in the liquid.

However, it has also been argued (Brennen, 1995) that it is difficult to characterise these nuclei, the real question arises as how small gas-filled microbubble could exist for any length of time in a body of liquid that is not saturated with that gas. Brennen (1995) also argued that it is not possible to separately assess the number of solid particles and the number of the microparticle with most of existing experimental techniques though both can act like a cavitation site, the probability that microbubble will grow more rapidly is more likely.

However, methods have been developed to measure bubble nuclei concentration in the liquid. One of the methods to measure cavitation nuclei is the use of susceptibility meter (Billet, 1986). The sample fluid containing microbubbles is sucked into the small venturi, and the light is passed over the fluid. The light scattered by a microbubble as it passes through probe volume is collected by a lens and is focussed on the photomultiplier tube. The photomultiplier tube has an aperture which restricts one dimension of the probe volume. The output of the photomultiplier goes through the signal conditioner where it is processed and classified and provides microbubble size range. However, Billet's method tends to be limited to concentrations less than 10 particles cm^{-3}. Studies further revealed that population of nuclei varies from liquid to liquid and depends on the presence of small contaminant particles, free and dissolved gases and also temperature and pressure conditions (Billet, 1985; Brennen, 1995).

Nonetheless, the fuel used in the reference case (Duke et al., 2013a) in the present study contains dissolved gases, however, the nuclei concentration is not known. Nonetheless, the fuel used in the reference case (Duke et al., 2013a) in the present study contains dissolved gases. However, the nuclei concentration is not known. Therefore it becomes essential to assess the cavitation model parameters associated with the liquid quality. Hence, the influence of model parameters associated with liquid quality on cavitation results are assessed: One of the important parameters in Schnerr and Sauer (SS) model is n_B which expresses bubble concentration per unit volume of pure liquid. The effect of n_B has been evaluated by Yuan et al. (2001) and settled for 1.5×10^{14} to be an optimum value for single-hole nozzles. Zwart, Gerber and Balamri (ZGB) model, which is an empirical cavitation model contains parameters such as bubble radius R_B, nucleation site volume fraction α_{nuc}, F_{vap} and F_{cond} that need tuning. Therefore, the objective in this subsection is to assess the influence of these model parameters on cavitation results.

5.4.3.1 Case setup:

Steady-state simulations have been performed. Operating condition as described for case 1 in Table 5.1 is simulated. Simulations have been performed using Schnerr and Sauer (SS) and Zwart, Gerber and Balamri (ZGB) models with a multiphase mixture model, however, model constants have been varied. In SS model, different values of n_B (bubble concentration per unit volume of pure liquid) are used. In Zwart-Gerber-Balamri (ZGB) model, nucleation site volume fraction α_{nuc} has been varied. Physical properties of the working fluid are listed in Table 5.2. Boundary conditions are listed in Table 5.3.

5.4.3.2 Results:

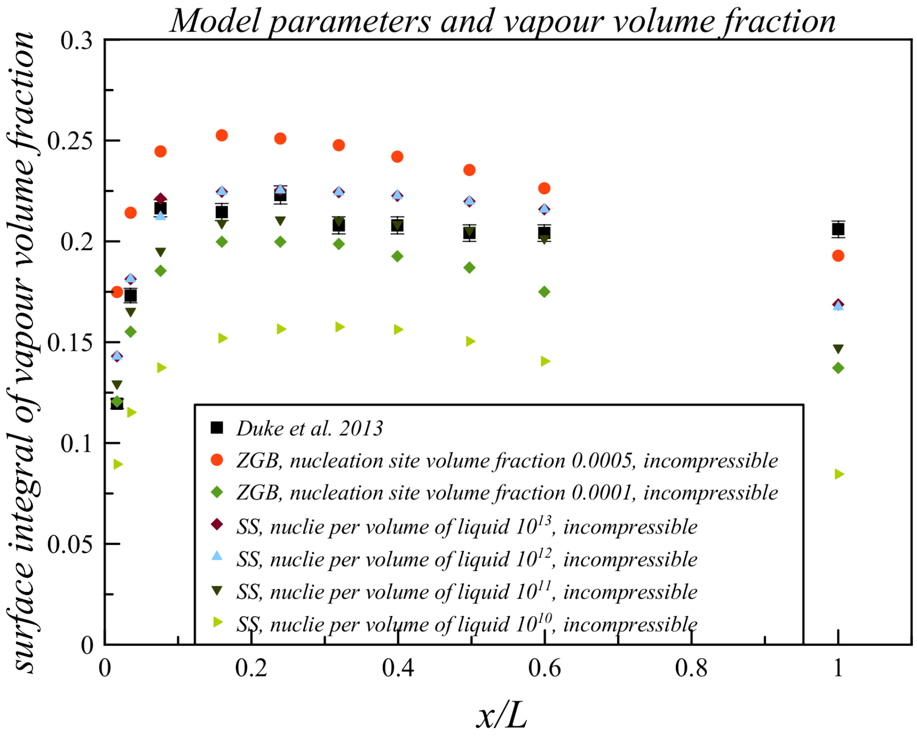

Figure 5.16: Influence of cavitation models parameter on vapour volume fraction.

The results indicate that the amount of cavitation vapour can be varied by changing model parameters. The obtained results allow more elaborate analysis of cavitation models used. Quantitatively the best results are obtained using SS model when the bubble concentration per unit volume of liquid n_B has been kept $10^{13}\ m^{-3}$ (Figure 5.16). Hence, in later cases n_B would be set to $1 \times 10^{13}\ m^{-3}$ in SS model. The ZGB model slightly overpredicts the vapour volume fraction when nucleation site volume fraction α_{nuc} has been kept to 0.0005, however, when α_{nuc} is set to 0.0001, the vapour volume fraction is somewhat underpredicted but in better agreements with the experimental data. Therefore, in the later cases, the value for α_{nuc} would be 0.0001 in the ZGB model. Influence of other empirical parameters i.e. bubble radius R_B, evaporation coefficient F_{vap} and condensation coefficient F_{cond} of ZGB model on cavitation results are not assessed, however, it can be argued that they may achieve similar trends since such parameters are scalars.

5.4.3.3 Discussions:

- Impacts of cavitation model parameters on cavitation results were assessed. The results indicate that model parameters of both SS and ZGB models influence cavitation results. With SS model, the best quantitative agreement with experimental data was achieved when its parameter n_B was set to 1×10^{13}. With ZGB model, the best quantitative agreement with the experimental data was achieved when its parameter α_{nuc} was set to 0.0001. Therefore, in later studies, simulations with these models will be performed with above-specified parameters.

5.4.4 Influence of compressibility on cavitation

Cavitation vapour is assumed to be compressible (Brennen, 1995) and often the ideal gas law is used to model vapour compressibility. Recently Sezal et al. (2009); Neroorkar et al. (2012); Battistoni et al. (2014); Saha (2014) have used the ideal gas law for vapour compressibility. Apart from vapour compressibility, liquid compressibility is also important for cavitating flows. Giannadakis et al. (2008) argued that in locations where cavitation occurs, the liquid should be regarded as compressible due to volume production and destruction caused by cavitation. Therefore, in the present study, the influence of both vapour and liquid compressibility on cavitation results would be assessed. To keep into account the vapour compressibility the ideal gas law is introduced and while the liquid compressibility is modelled via Tait equation. (see Tait, 1888; Dymond and Malhotra, 1988).

The Tait equation has the following form:

$$\left(\frac{\rho}{\rho_0}\right)^n = \frac{K}{K_0} \tag{5.10}$$

where

$$K = K_0 + n\Delta p \tag{5.11}$$

and

$$\Delta p = p - p_0 \tag{5.12}$$

where,

$$\begin{aligned} p_0 &= \text{Reference liquid pressure (Absolute)} \\ \rho_0 &= \text{Reference liquid density (density at the absolute pressure, } p_0\text{)} \\ K_0 &= \text{Reference bulk modulus (Bulk modulus the absolute pressure, } p_0\text{)} \\ n &= \text{Density exponent} \\ p &= \text{Liquid pressure (absolute)} \\ p &= \text{Liquid density at pressure, } p \\ K &= \text{Bulk modulus at pressure, } p \end{aligned} \tag{5.13}$$

The speed of sound is calculated using the following equation:

$$a_l = \sqrt{\frac{K}{\rho}} \tag{5.14}$$

Since the exact composition of working fuel has not been known, bulk modulus K of gasoline has been used as reference bulk modulus which is $1.3 \times 10^9\ Nm^{-2}$. 1 unit of atmospheric pressure is used as the reference pressure which is 101325 Nm^{-2}.
The ideal gas model which is used for vapour compressibility has the following form:

$$\rho = \frac{p_{absolute}}{\frac{R_u}{M_w}T} \tag{5.15}$$

where R_u is the universal gas constant, M_w is the molecular weight and T is the temperature in Kelvin. T is computed from solution of the energy equation (Anderson, 1990).
The speed of sound is calculated from the following equation:

$$a_v = \sqrt{\gamma RT} = \sqrt{\frac{c_p RT}{c_p - R}} = \sqrt{\frac{c_p}{c_p - R}\frac{p}{\rho_v}} \tag{5.16}$$

where γ is the specific heat ratio:

$$\gamma = \frac{c_p}{c_v} = \frac{c_p}{(c_p - R)} \tag{5.17}$$

where R is the specific gas constant R_u/M_w, c_p is the specific heat at the constant pressure and c_v is the specific heat at the constant volume.

5.4.4.1 Case setup

Operating condition, as described the case 1 in Table 5.1, has been simulated. Both the ZGB and SS models are used. For the tait equation, the reference pressure p_0 is assumed to be 1 atm, the reference bulk modulus K_0 is assumed to be $\approx 1.3 \times 10^9\ Nm^{-2}$ which is similar to gasoline at 25° (Vargaftik et al., 1996), the value of density exponent n is set to be 7 considering that such values correspond to weakly compressible substances such as liquids (Ivings et al., 1998). For the ideal gas equation, the molecular weight is assumed to be 114 $g\ mol^{-1}$ which represents the molecular weight of the gasoline. Also, the specific heat of gasoline with the value of 1.6 $kJkg^{-1}K^{-1}$ at 25° has been used. The molecular viscosity of both liquid and vapour is assumed to be constant, and the values set for the present study can be found in the Table 5.2, other physical properties of the working fluid can also are listed in Table 5.2. Boundary conditions are listed in the Table 5.3.

5.4.4.2 Results:

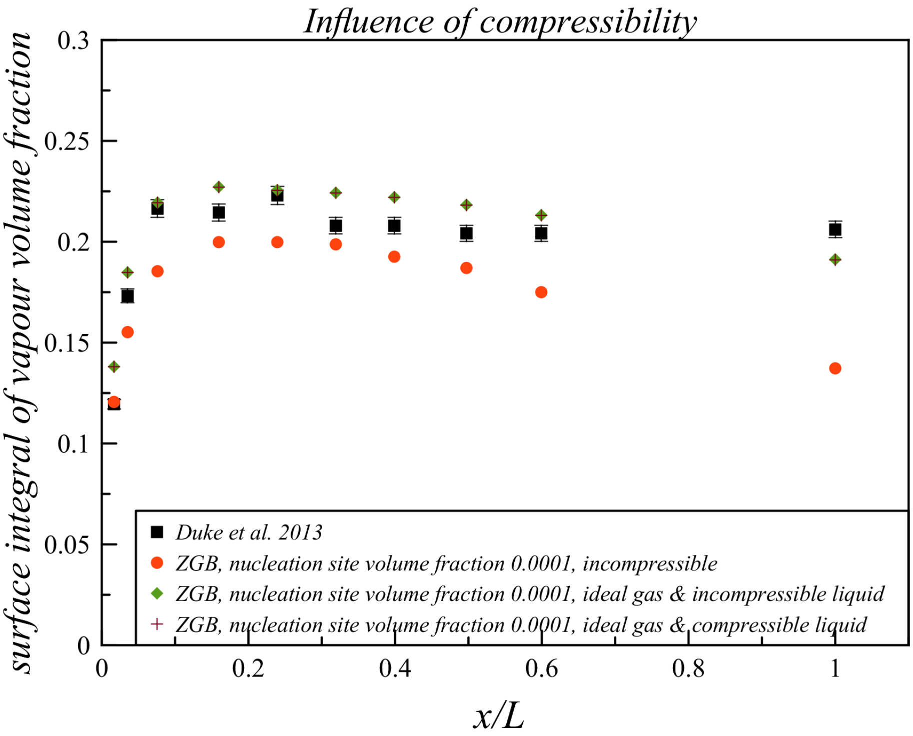

Figure 5.17: Influence of the vapour compressibility on the vapour volume fraction.

When the vapour was assumed to be the ideal gas, contours of vapour volume fraction obtained using the SS model were non-physical and were in complete disagreement with the experimental measurements; which could be due to the nature of the model equations (non-linear evaporation and condensation terms). Hence, results obtained only using the ZGB model presented. The quantitative comparison (Figure 5.17) of the predicted vapour volume fraction indicates an increase in the vapour volume fraction when vapour the is assumed to be the ideal gas. This is because the ideal gas assumption allowed the vapour volume to change with respect to the change in local pressure, therefore, the vapour volume expanded and its density decreased as pressure decreased. The comparison also shows better agreements achieved with the experimental data using the ideal gas assumption for cavitation vapour. In the later simulation, the liquid compressibility was modelled using the Tait equation. However, from Figure 5.17, it can be seen that liquid compressibility assumption made no difference in the cavitation results, implying that liquid compressibility has an insignificant impact in this case.

The qualitative comparison (Figure 5.18 (a) (b) and (c)) of the predicted vapour fraction with the experimental measurements also shows better agreements when the vapour is assumed to be the ideal gas. Predicted results using the ideal gas model shows vapour being generated at the sharp entrance of the nozzle orifice. As the fluid travels further downstream, the vapour separates from the wall and convects to the liquid core around the nozzle centre line few a diameters downstream of the nozzle. The vapour volume can also be seen beyond the orifice as flow goes further downstream entering the circular expansion region of the nozzle (Figure 5.20 (b)). When the vapour is modelled as incompressible, the predicted result shows that vapour is generated at the sharp entrance of the nozzle orifice and remains in the vicinity of the orifice wall. The cavitation is predicted entering the circular expansion region of the nozzle (Figure 5.20 (b)). The density contours are plotted in Figure 5.19 (a) and (b) which corresponds to the vapour volume fraction contours in Figure 5.20 (a) and (b), showing lower density where higher vapour volume fraction is predicted.

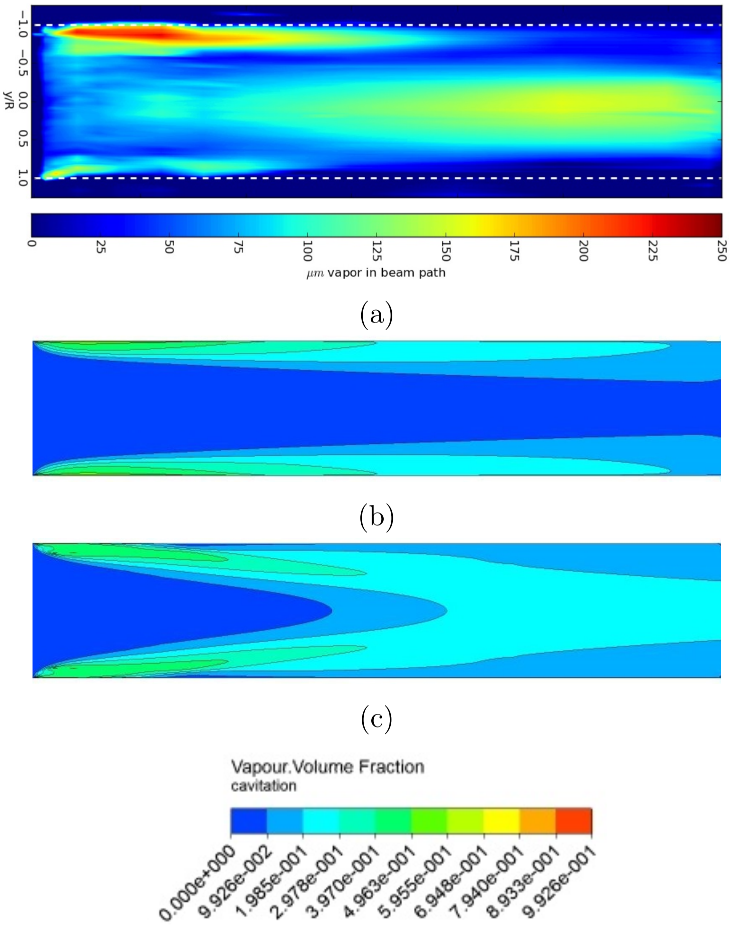

(a)

(b)

(c)

Figure 5.18: Qualitative comparison between the experimental and CFD predicted results to check influences of vapour compressibility. (a) X-ray radiography measurement at $CN = 11.2$, (Duke et al., 2013a), (b) ZGB model, incompressible, $\alpha_{nuc} = 0.0001$, (c) ZGB model, compressible, $\alpha_{nuc} = 0.0001$.

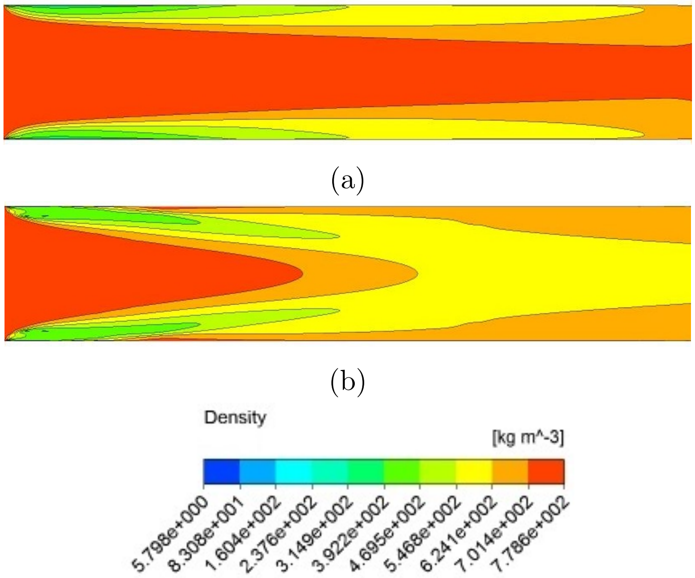

Figure 5.19: Density comparisons: (a) Incompressible vapour (b) Ideal gas formulation for density.

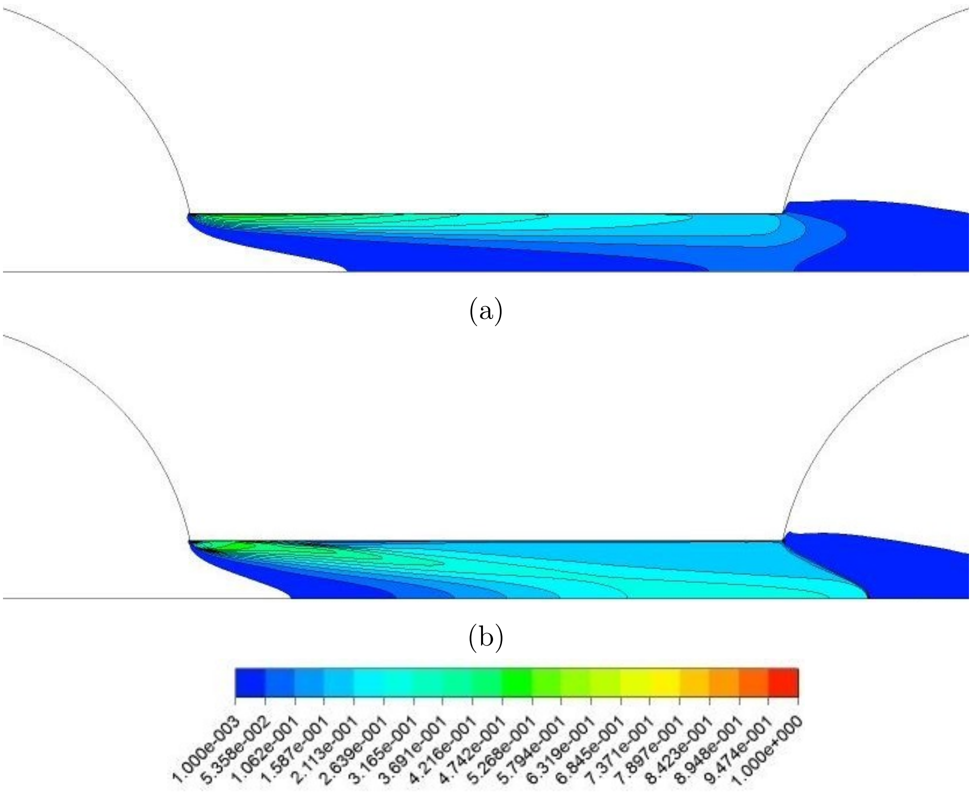

Figure 5.20: Qualitative comparison of the predicted vapour volume fraction to check effects of vapour compressibility. (a) ZGB model, incompressible, $\alpha_{nuc} = 0.0001$, (b) ZGB model, compressible, $\alpha_{nuc} = 0.0001$.

Moreover, on examining the pressure history on the nozzle axis (Figure 5.21 (a)) for the case with the ideal gas assumption for the vapour density, a steep jump in the pressure or shock or a stationary normal shock wave can be noticed. The normal shock wave is predicted due to the sudden change of the fluid velocity (Figure 5.22 (a)) from supersonic to subsonic. Corresponding to it, a sharp drop in the velocity field can also be noticed (Figure 5.21 (b)). The vapour volume fraction contour is presented in Figure 5.25 (a) and the pressure contour is presented in Figure 5.25 (b). From Figures 5.25 (a) and (b) it can be inferred that the shock is predicted just at the downstream of the cavitation region. However, the speed of sound of the liquid has been predicted around 1300 ms^{-1} (Figure 5.22 (a)), using equation (5.14) and the speed of sound of vapour is predicted around of 150 ms^{-1} (Figure 5.22 (a)) using equation (5.16), therefore, from the Figure 5.22 (a) it can be argued that the mean flow has not achieved or exceeded the supersonic speeds of both liquid and vapour.

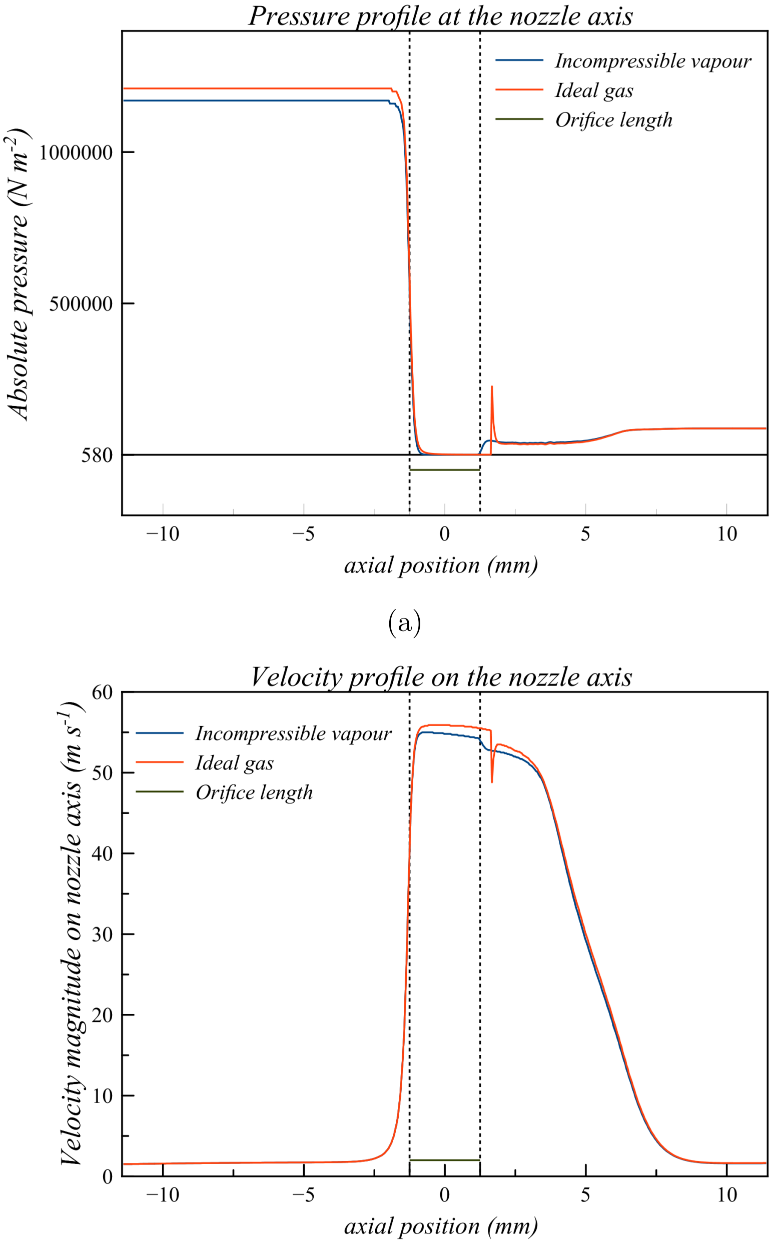

(a)

(b)

Figure 5.21: The predicted pressure and velocity profile on the nozzle axis.

However, it has been experimentally observed (Karplus, 1957; Semenov and Kosterin, 1964;

Henry et al., 1971) that in the two-phase flows, even a small amount of gas or vapour can cause a considerable reduction in the local sonic speed of the two-phase mixture; It is because the liquid-gas mixture is relatively easily compressible owing to the effect of gas bubbles however it remains relatively dense due to the dominant mass of the liquid. (McWilliam and Duggins, 1969). Therefore, in this interest, many attempts (Wallis, 1969; Nguyen et al., 1981; Chung et al., 2004) have been made to model liquid-gas/vapour mixture sonic speed.

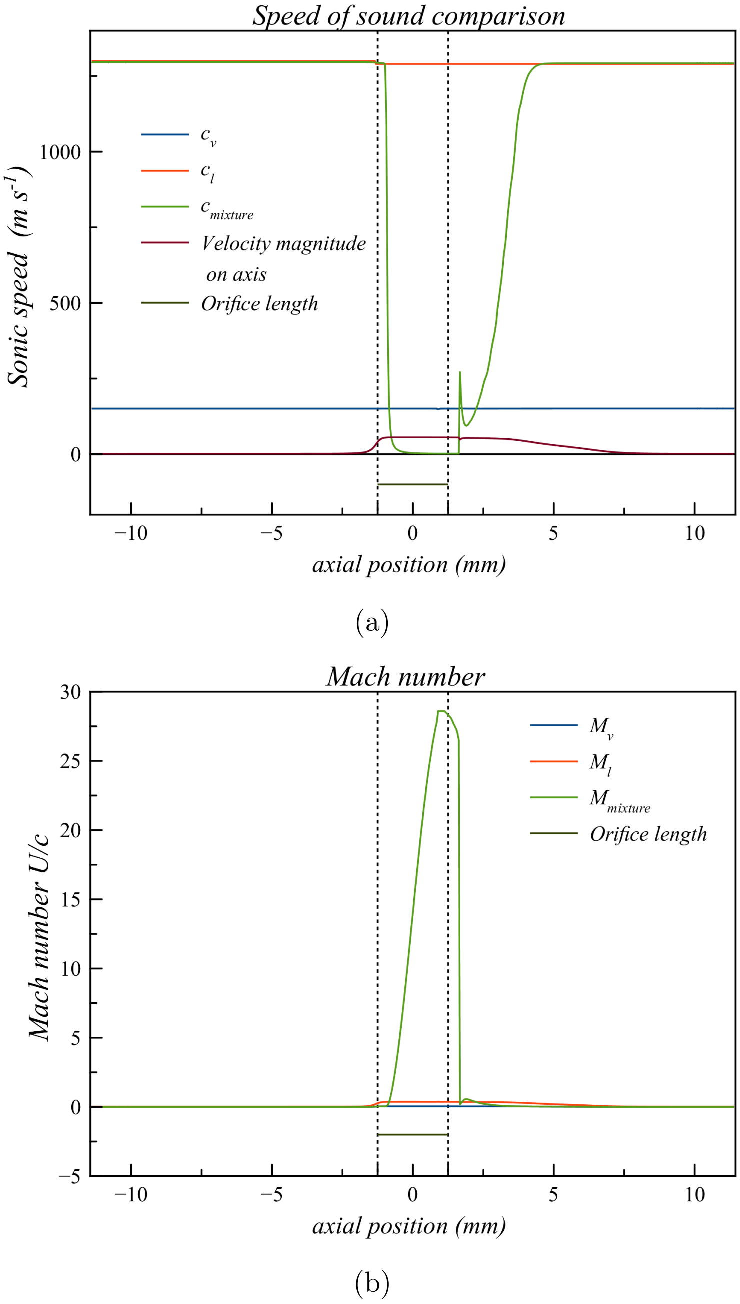

(a)

(b)

Figure 5.22: (a) The predicted speed of sound for vapour, liquid and mixture at nozzle axis, (b) The Mach number of sound for vapour, liquid and mixture at nozzle axis.

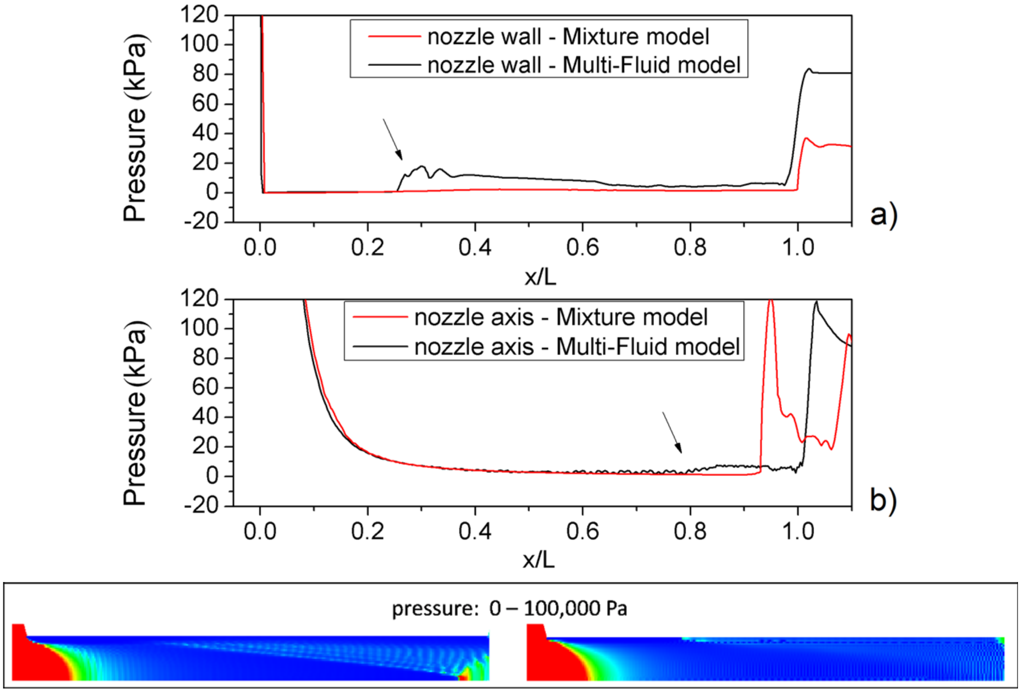

(c)

Figure 5.23: (a) The predicted pressure along the nozzle wall, (b) the predicted pressure along the nozzle axis (c) Pressure contour obtained using the mixture model (left) and multifluid (eulerian multi-phase) model (right). Source: Battistoni et al. (2014).

In the present simulation, Wallis model[1] has been used to compute the sonic speed in the liquid-vapour mixture. The model is based on the 'homogeneous equilibrium' assumption in which velocity, temperature and pressure are equal for all phases. The assumption is based on the notion that difference between these three variable potentials would induce instant momentum, energy and mass transfer between phases so that the thermodynamic equilibrium fluid is maintained (Lagumbay et al., 2007). The model computes the sonic speed in the liquid-vapour mixture much smaller than its constituents (Torvik, 1970) and has been validated against the experimental data (Wallis, 1969). In the present case, Wallis model has computed a very low sonic speed (≈ 1.72 ms^{-1}) in the two-phase region (see Figure 5.22 (a)), therefore, the local flow in the two-phase region became supersonic. However, just downstream of the cavitation region, the fluid re-attains the sonic speed of liquid becoming subsonic. This can be observed in the sonic speed (Figure 5.22 (a)) and Mach number plots (Figure 5.22 (b)) that at the position where there is a change in sonic speed from supersonic to subsonic, a stationary normal shock wave is predicted. Moreover, in the region of the shock wave, there is a sharp change in the mixture sonic speed (Figure

---

[1] The Wallis model has the following form:

$$a_{mixture} = \sqrt{\frac{1}{(\alpha_v \cdot \rho_v + \alpha_l \cdot \rho_l) \cdot \left(\frac{\alpha_v}{\rho_v \cdot a_v^2} + \frac{\alpha_l}{\rho_l \cdot a_l^2}\right)}} \tag{5.18}$$

where, a_l is the speed of sound of liquid, a_v is the speed of sound of vapour and $a_{mixture}$ is the speed of sound of liquid-vapour mixture (Figure 5.22 (a)), α_l represents volume fraction of liquid, α_v represent the volume fraction of vapour (Figure 5.24 (b)), ρ_l is the density of liquid and ρ_v the density of vapour (Figure 5.24 (a)). In the present case, the speed of sound of liquid a_l has been calculated using equation (5.14) and speed of sound of vapour has been calculated using equation (5.16), the liquid density has been calculated using equation (5.10) and density of vapour has been calculated using equation (5.15).

5.22 (a)) which can be attributed to large pressure, velocity and density gradients in this shock region (Anderson, 1990). Similar shock was also predicted by Battistoni et al. (2014) at the same operating conditions as the present case who used their own model (Battistoni et al., 2012) and the 'homogeneous relaxation model' (HRM) (Neroorkar et al., 2012) as shown in Figure 5.23. However, reasons for shock wave predictions were not given in their paper.

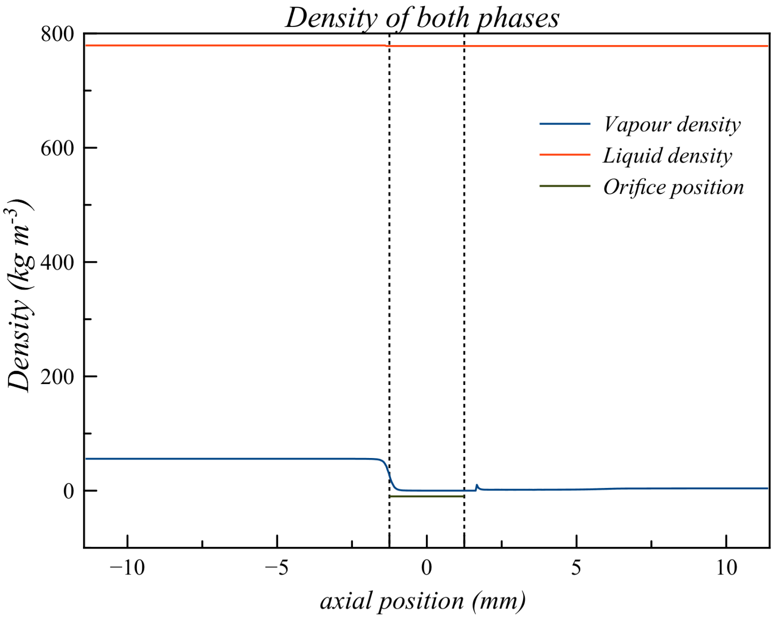

(a)

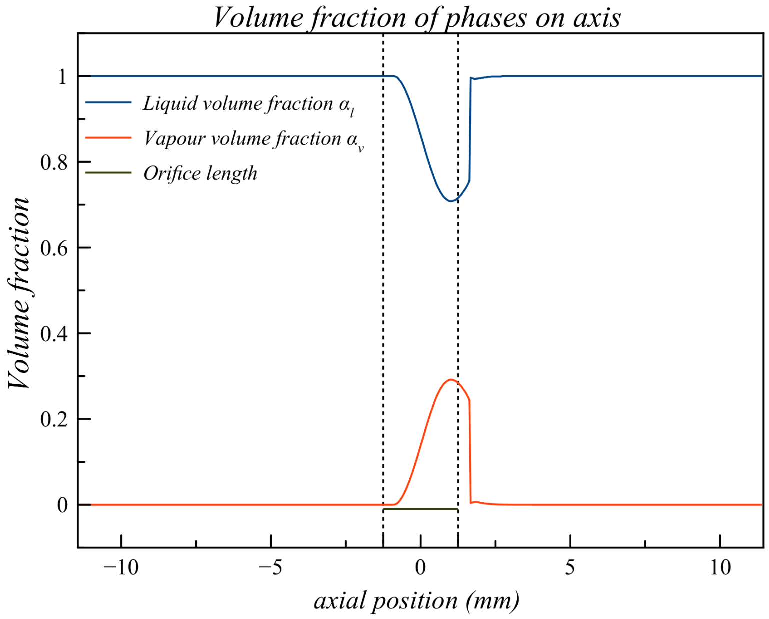

(b)

Figure 5.24: (a) The predicted liquid and vapour density and (b) The predicted liquid and vapour volume fraction on the nozzle axis.

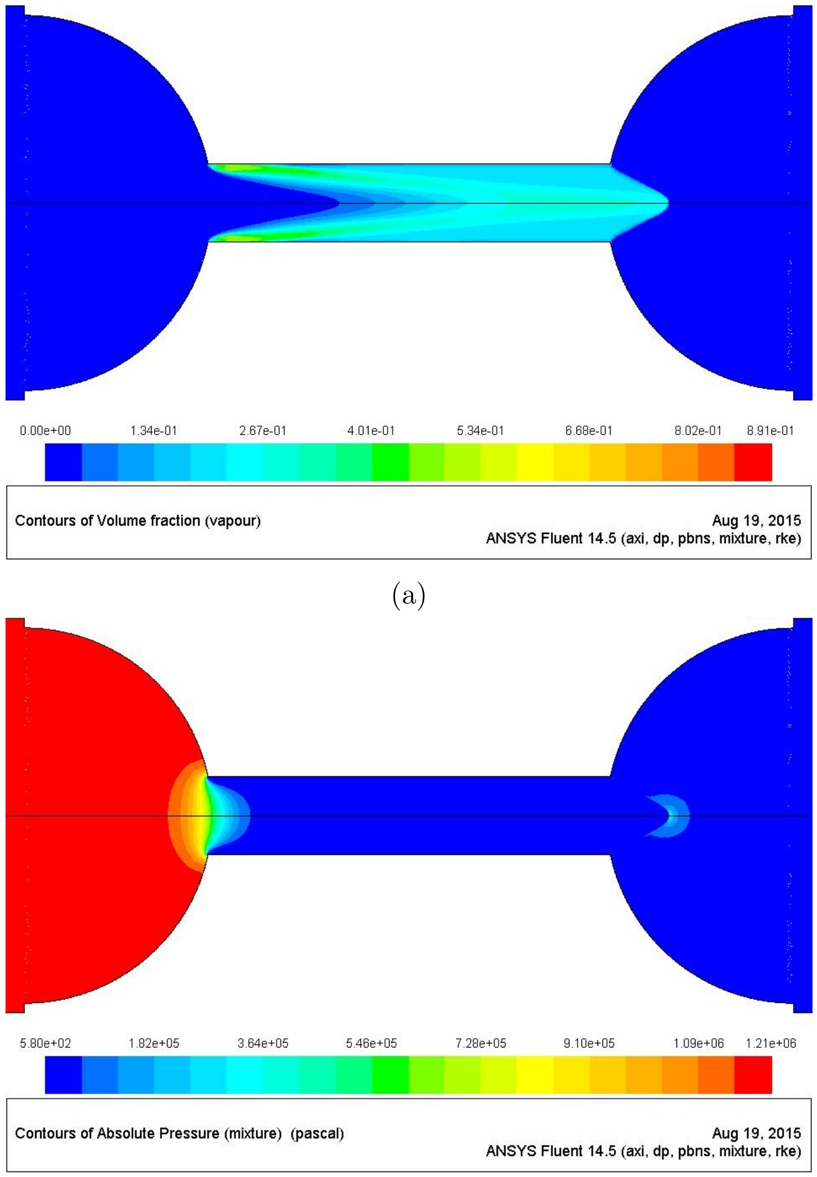

(a)

(b)

Figure 5.25: (a) Vapour volume fraction (b) pressure

5.4.4.3 Discussions:

- When the vapour was assumed to be incompressible, both simulations (using SS and ZGB models) achieved a steady state. However, when vapour was assumed to be an ideal gas, simulations of only ZGB model achieved a steady state. This could be attributed to the nonlinearity added to the model which the SS model could not predict accurately.

- The quantitative comparison indicated an increase in the vapour volume when the ideal gas law was used for vapour compressibility and also resulted in a better agreement with the experimental data. The influence of liquid compressibility on cavitation was insignificant.

- Higher vapour volume was predicted when the vapour was assumed to be an ideal gas. This is because the ideal gas assumption allowed the cavitation vapour volume to change with respect to the change in the local pressure and therefore the vapour volume expanded in the low-pressure regions.

- The qualitative comparison also showed better agreement with experimental data when vapour compressibility is assumed. Vapour is predicted to be generated at the sharp entrance of the nozzle orifice. As the flow travels downstream, the vapour moves away from the wall and convected to the liquid core around the orifice axis few a diameters downstream of the orifice inlet.

- When the vapour is assumed incompressible, vapour is also seen generated at the sharp entrance of the nozzle orifice but remains in the vicinity of the orifice wall as flow convects downstream.

- On examining the pressure profile of the whole nozzle for the case in which the vapour is assumed to be the ideal gas, a steep pressure jump or a stationary normal shock wave was observed at the axial position where the cavitation structure ends. The consequence of the change of mean flow velocity from supersonic to subsonic just downstream of the cavitation region has resulted in the formation of the normal shock wave.

- In the present simulation Wallis (1969) model has been used to compute the sonic speed of the mixture. The model has a produced very low mixture sonic speed ($\approx 1.72\ ms^{-1}$) in the two-phase region. Hence, the local flow velocity became supersonic at the cavitation region. However, at the position where cavitation structure ended the fluid reattained the sonic speed of the liquid and consequently, the flow became subsonic.

5.5 Summary

5.5.1 Numerical errors:

- Similar results for velocity and vapour volume fraction were achieved using grid 5 and 6, hence it was inferred that grid independence is being approached with grid 5 and 6, hence grid 5 was used in later simulations.

5.5.2 Physical modelling errors:

5.5.2.1 Turbulence model evaluation

- The best quantitative agreements for the vapour volume fraction were achieved using the realizable $k - \epsilon$ turbulence model.

5.5.2.2 Cavitation model evaluation

- Similar quantitative and qualitative results were achieved using both the SS and ZGB model.

5.5.2.3 Uncertainties of cavitation models and impact of parameters used in these models

- The model parameters of both cavitation models (SS and ZGB) influenced the cavitation results.

5.5.2.4 Influence of compressibility on cavitation

- The quantitative comparison indicated an increase in the vapour volume fraction of cavitation when the ideal gas model was used for vapour compressibility.
- The results obtained using the ideal gas law for cavitation vapour were also in better agreement with the experimental data. Influence of liquid compressibility on cavitation results was insignificant.
- The qualitative comparison also indicated a better agreement with the experimental data when ideal gas law has been used for vapour density.
- In the present case, when the ideal gas law was used for vapour compressibility, a stationary normal shock wave is predicted downstream of the cavitation region.
- This is because a very low sonic speed is predicted in the cavitation region due to which the local flow in the cavitation region became supersonic. However, just downstream of the cavitation region, the fluid re-attained sonic speed of the liquid.

Chapter 6

Cavitation simulations in an enlarged multi-hole injector

6.1 Introduction

The objective of this chapter is to simulate cavitating flow in the enlarged model of a multi-hole(6) diesel fuel injector. In the present chapter identified approaches of turbulence modelling and cavitation modelling described in the previous chapters are used. The predictions are quantitatively evaluated by comparison with LDV experimental data for mean axial velocity and RMS velocity and qualitatively by comparison with CCD images. Influence of viscosity and density on cavitation are also investigated.

6.2 Test case decription:

Roth et al. (2002); Roth (2004) performed experiments on the transparent enlarged model of a Bosch mini-sac type multi-hole(6) diesel fuel injector at both cavitating and non-cavitating conditions on the steady-state test rig. The LDV (Laser Doppler Velocimetry) was used to measured mean axial velocity and RMS velocity at different axial locations (Figure 6.1) of the injector hole at different cavitation numbers. The still imaging and high-speed video imaging was utilised to capture cavitation occurrence and its development inside the fuel injector. Operating conditions of the test rig at the nominal needle-lift for LDV measurements are described in Table 6.1.

lower needle-lift 1.6 mm						
Case	CN	Re	p_{inj}	p_{back}	U_{inj}	$Flow\ Rate$
1	1.48	26800	2.80 bar	1.19 bar	12.58 ms^{-1}	0.726 ls^{-1}
2	2.39	33200	4.00 bar	1.25 bar	15.56 ms^{-1}	0.898 ls^{-1}
3	5.50	33400	4.00 bar	0.70 bar	15.66 ms^{-1}	0.904 ls^{-1}
nominal needle-lift 6 mm						
1	1.09	30200	2.40 bar	1.20 bar	14.15 ms^{-1}	0.817 ls^{-1}
2	1.48	34100	3.00 bar	1.27 bar	15.97 ms^{-1}	0.922 ls^{-1}
3	4.57	39500	4.00 bar	0.80 bar	18.50 ms^{-1}	1.068 ls^{-1}
			(absolute)	(absolute)		

Table 6.1: Operating conditions of the test rig for LDV measurements at cavitating conditions.

fluid properties - liquid	
Density	895 $kg\ m^{-3}$
Viscosity	$1.4678 \times 10^{-3}\ kg\ m^{-1}s^{-1}$
Vapour pressure	1000 Nm^{-2}
Surface Tension	0.03 Nm^{-1}
Refractive Index	1.49
fluid properties - vapour	
Density*	0.054 $kg\ m^{-3}$
Viscosity†	$1.55\times\ 10^{-5}\ kg\ m^{-1}s^{-1}$

* Ideal gas law has been used to calculate density of vapour.

† The viscosity of vapour has been calculated using model proposed by Lee et al. (1966).

Table 6.2: working-fluid

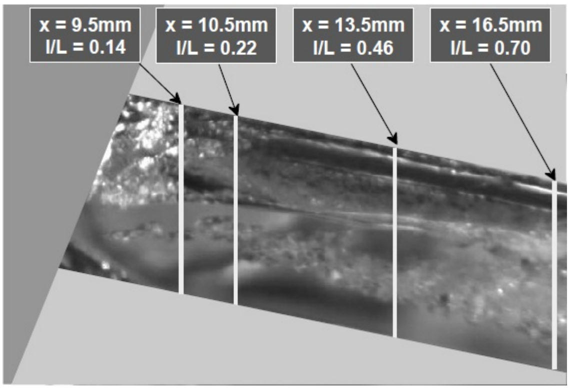

Figure 6.1: Locations inside one of the injector hole for the second series of LDV measurements. Source: Roth et al. (2002)

6.3 Nominal needle lift

6.3.1 Grid sensitivity analysis

In the chapter 4, it was realised that grid sensitivity is being approached for mean axial velocity; in the subsection, the influence of grid density is assessed at the cavitating condition.

6.3.1.1 Case setup

Grids 2 and 3 from the singe-phase simulations at nominal needle lift are used (see Table 6.3). The operating conditions described for the case 2 in the Table 6.1 are simulated. Turbulence is modelled using the realizable $k - \epsilon$ model with "Enhanced wall treatment method" in the near the wall region. For cavitation modelling, Zwart model is used with multi-phase mixture model. Liquid and vapour phases are assumed to be incompressible. Details of boundary conditions can be found in Table 6.4.

Grid	Control Volumes	y^+
2	13,016,832	15.08
3	17,970,861	13.08

Table 6.3: Number of Control volumes (cells) in different grids

Case	Inlet	Outlet	interface	Walls
$CN = 1.48$	mass-flow rate liquid= $0.1375317\ kg\ s^{-1}$ vapour= $0\ kg\ s^{-1}$	constant pressure $127000\ Nm^{-2}$	cyclic	Enhanced wall treatment method (no slip wall)

Table 6.4: Boundary Conditions

6.3.1.2 Results

It can be seen that almost similar profiles of mean velocity in Grid 2 and 3 (Figure 6.2 (a),(c),(e) and 6.3 (a)), suggesting that grid independence is being approached for mean axial velocity. The RMS is calculated using Boussinesq formula; the RMS velocity profiles (Figure 6.2 (b),(d),(f) and 6.3 (a)) indicate that RMS velocity magnitude increases with an increase of grid density owing to increase in mean velocity gradients. The results obtained for vapour volume fraction are following the similar trend. The results indicate that vapour volume fraction is not significantly changing with the increase of grid density (Figure 6.4 (a), (b), (c) and (d)).

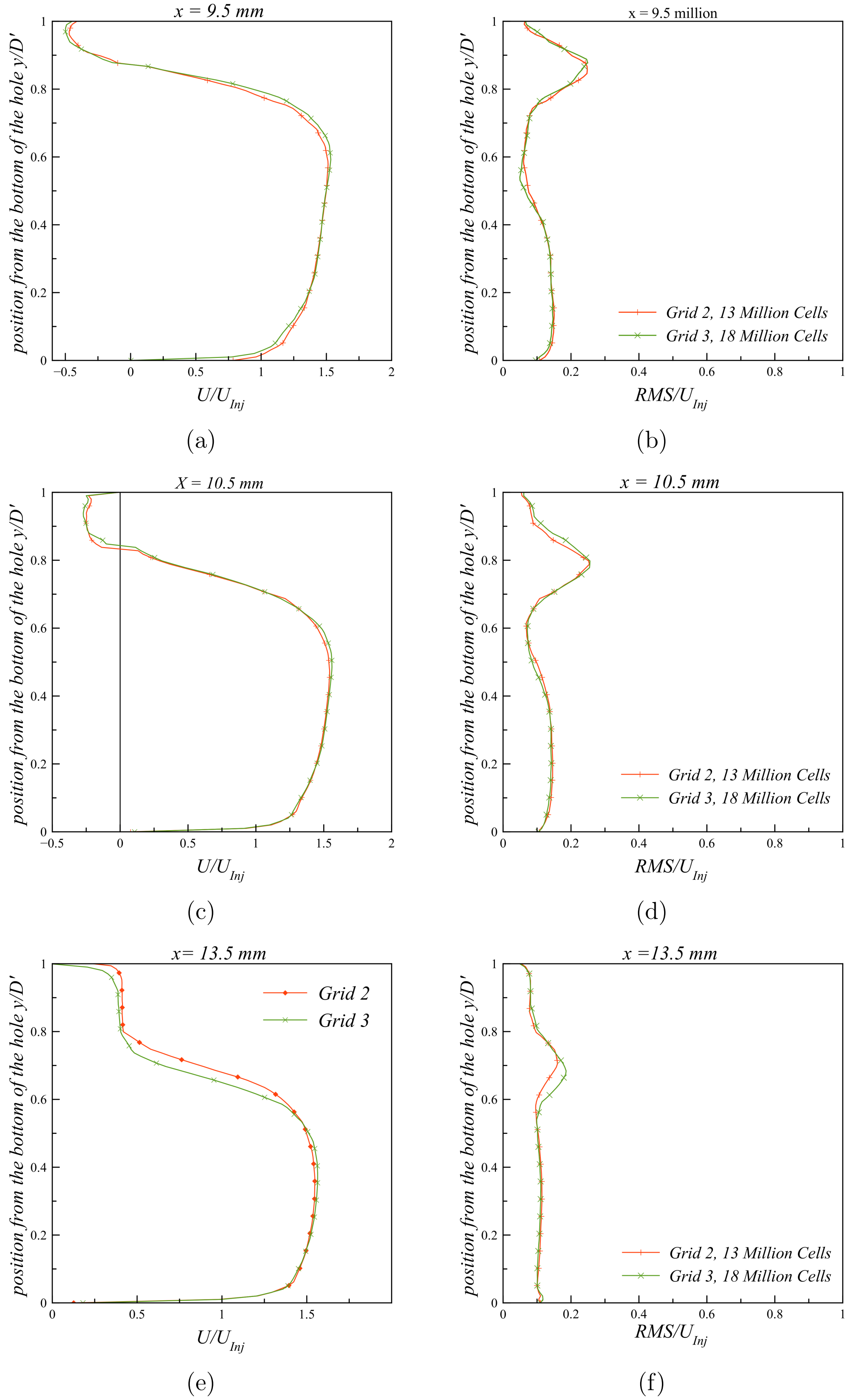

Figure 6.2: Normalized mean axial velocity and RMS comparisons at x = 9.5 mm, x = 10.5 mm and x = 13.5 mm from the origin.

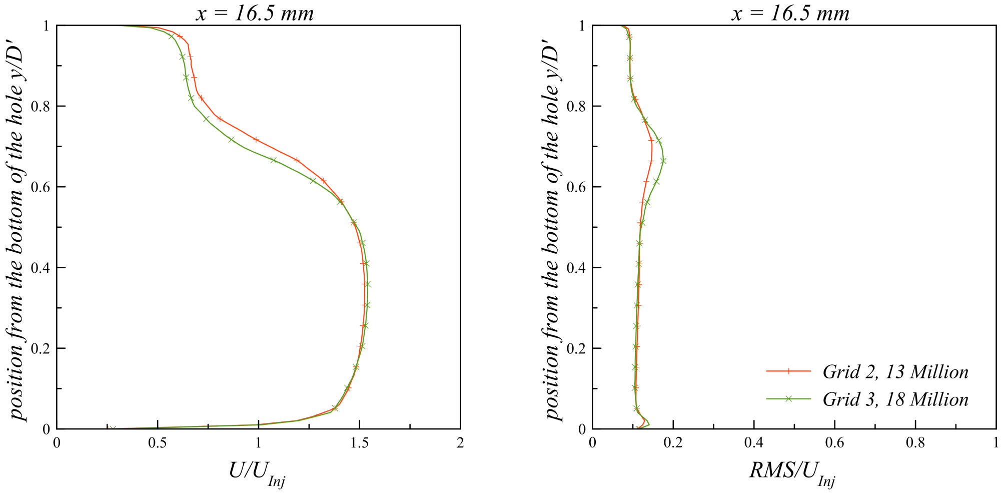

(a) (b)

Figure 6.3: Normalized mean axial velocity and RMS comparisons at x = 16.5 mm from the origin.

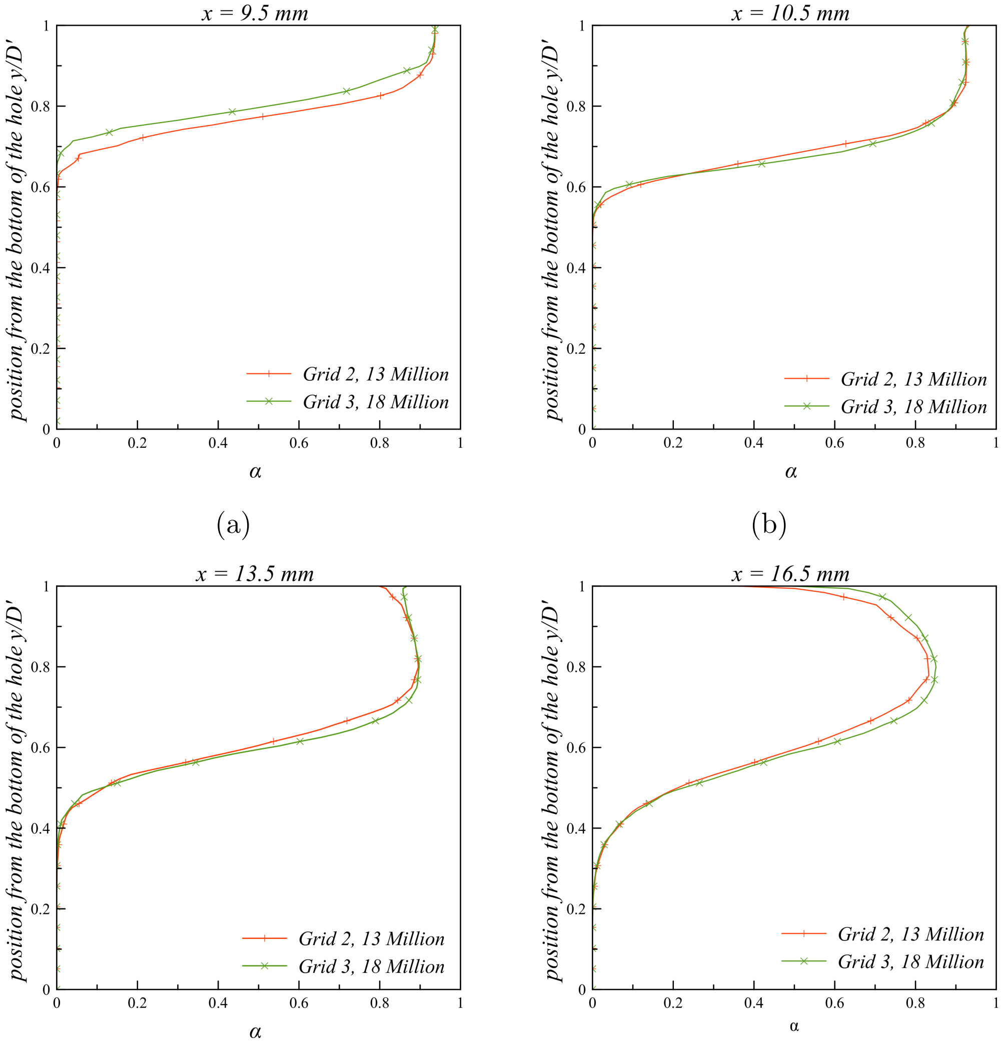

(a) (b)

(c) (d)

Figure 6.4: Predicted vapour volume fraction using different grids at different planes.

6.3.1.3 Discussions

- Grid sensitivity analysis suggests that mean axial velocity, RMS velocity and vapour volume fraction change insignificantly with an increase of grid density. Therefore, grid 2 would be used in further analysis.

6.3.2 Case study 1: Simulation of full-cavitating conditions at CN 1.48 and 4.57.

6.3.2.1 Case setup

Operating conditions as described for case 2 and 3 in table 6.1 at nominal needle lift are simulated. As in chapter 4, it was realised that grid independence is being approached for mean velocity in the single-phase simulations, and in the subsection § 6.3.1, it has been shown that vapour volume fraction did not change significantly with increase in grid density. Hence grid 2 has been used for cavitation simulation (Figure 6.5). In the present study, the best-performed models identified for turbulence and cavitation modelling from chapters 4 and 5 are used. The ideal gas law has been used to model the vapour compressibility, and the Tait equation is used for liquid compressibility; three sets of simulations are performed. In the first simulation, the liquid and vapour phases are assumed to be incompressible. In the second simulation, the liquid is assumed to be incompressible and the vapour compressibility is modelled using an ideal gas law. In the third simulation, the liquid compressibility is modelled using the Tait equation, and the vapour compressibility is modelled using an ideal gas law. Details of the physical models used in this study can be found in the Table 6.5 and of boundary conditions can be found in Table 6.6.

Physical models used	
Turbulence model	Realizable $k - \epsilon$ model (Shih et al., 1994)
Near wall turbulence modelling	‘Enhanced Wall Treatment’ method (Kader, 1981)
Multi-phase modelling approach	mixture model (Manninen et al., 1996)
Vapour compressibility	Ideal gas
Liquid compressibility	Tait equation (Tait, 1888; Dymond and Malhotra, 1988)
Cavitation model*	ZGB model (Zwart et al., 2004)
*Cavitation model constants	
bubble radius R_B	1×10^{-6}
nucleation site volume fraction α_{nuc}	1×10^{-4}
F_{vap} = evaporation co-efficient	50
F_{cond} = condensation co-efficient	0.01

Table 6.5: Physical models used

Case	Inlet	Outlet	interface	Walls
$CN = 1.48$	mass-flow rate liquid= 0.1375317 $kg\ s^{-1}$ vapour= 0 $kg\ s^{-1}$	constant pressure 127000 Nm^{-2}	cyclic	enhanced wall treatment method (no slip wall)
$CN = 4.57$	mass-flow rate liquid= 0.15391 $kg\ s^{-1}$ vapour= 0 $kg\ s^{-1}$	constant pressure 80000 Nm^{-2}	cyclic	enhanced wall treatment method (no slip wall)

Table 6.6: Boundary Conditions

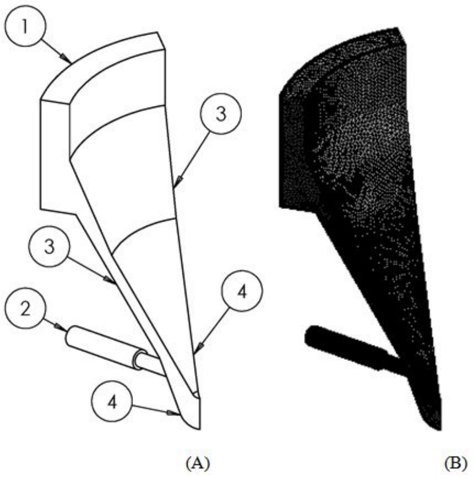

Figure 6.5: (A) One-sixth of the flow domain at the full needle lift with periodic (cyclic) boundary conditions. The numbers represent boundaries of flow domains, (1) inlet (2) outlet (3) walls (4) periodic (cyclic) interface, (B) Mesh for the flow domain.

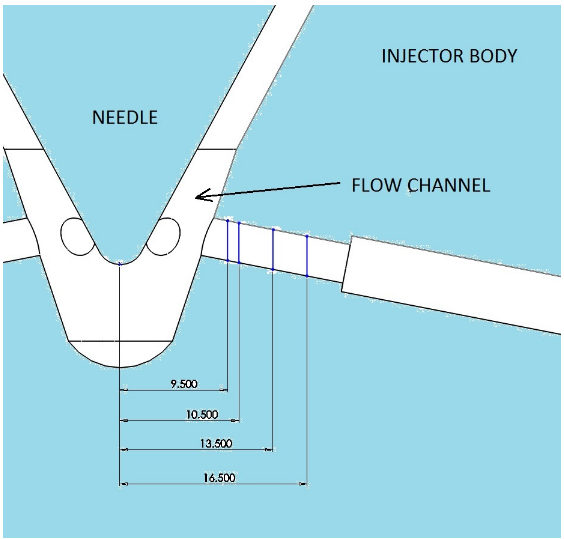

Figure 6.6: Sketch showing needle and injector assembly and the positions where LDV measurements of mean and RMS velocity were recorded. All dimensions are in mm.

6.3.2.2 Results

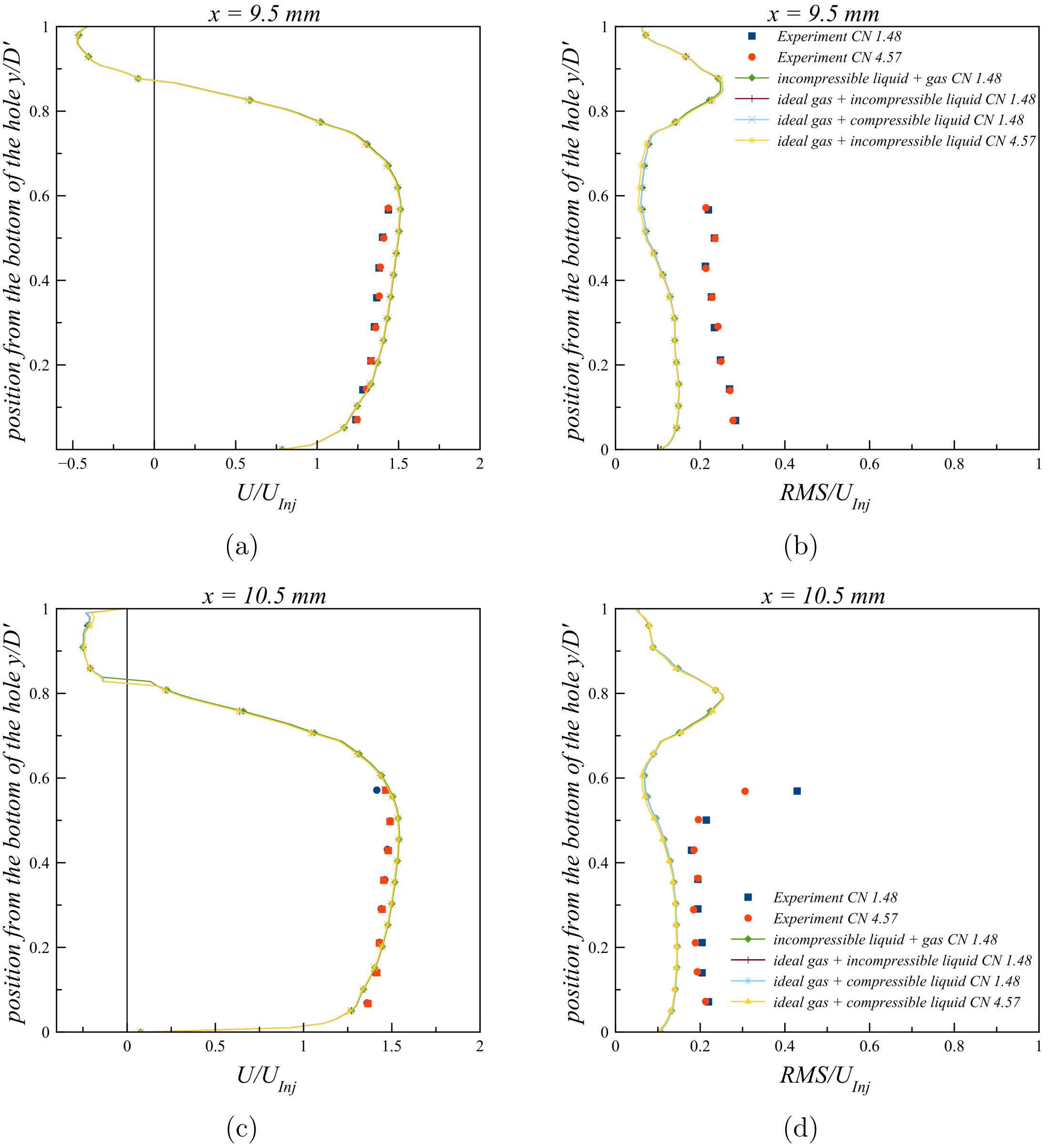

(a) (b)

(c) (d)

Figure 6.7: Normalized mean axial velocity and RMS comparisons at x = 9.5 mm and x = 10.5 mm from the origin.

Quantitative results for the mean axial velocity and the RMS velocity (Figure 6.7 (a), (b), (c), (d) and 6.8 (a), (b), (c), (d)) at $CN = 1.48$ at different planes (see Figure 6.1 and 6.6) reveal the insignificant contribution of the liquid compressibility to the mean and the RMS velocity. On comparing results obtained using the incompressible assumption of vapour and compressible assumption using the ideal gas law, a very small increase in the RMS velocity at the upper section of the hole at axial location x = 9.5 mm can be seen (Figure 6.7 (b) and (d).

In other positions, x = 10.5 mm (Figure 6.7 (c) and (d)), x = 13.5 mm and x = 16.5 mm (Figure 6.8 (a), (b), (c), (d)), almost comparable results were obtained for the mean axial velocity and RMS velocity when the vapour was assumed to be an ideal gas and incompressible at both cases.

However, qualitative comparison of vapour volume fraction on the centre plane $(+x, +y, +z)$ as seen in Figure 6.9 (a) and (b) reveals an increase in the vapour volume fraction when the ideal gas law has been used for the vapour compressibility. The higher vapour volume fraction prediction using the ideal gas law for vapour can be attributed to the change in vapour volume with respect to the change in local pressure. Hence, vapour volume expanded (and density decreased) as pressure decreased. Using the ideal gas assumption the variation in vapour density with respect to the change in local pressure also influenced the velocity field as seen in chapter 5, § 5.4.4 and hence would also influence the mean velocity gradients and this has resulted in a small increase of the RMS velocity.

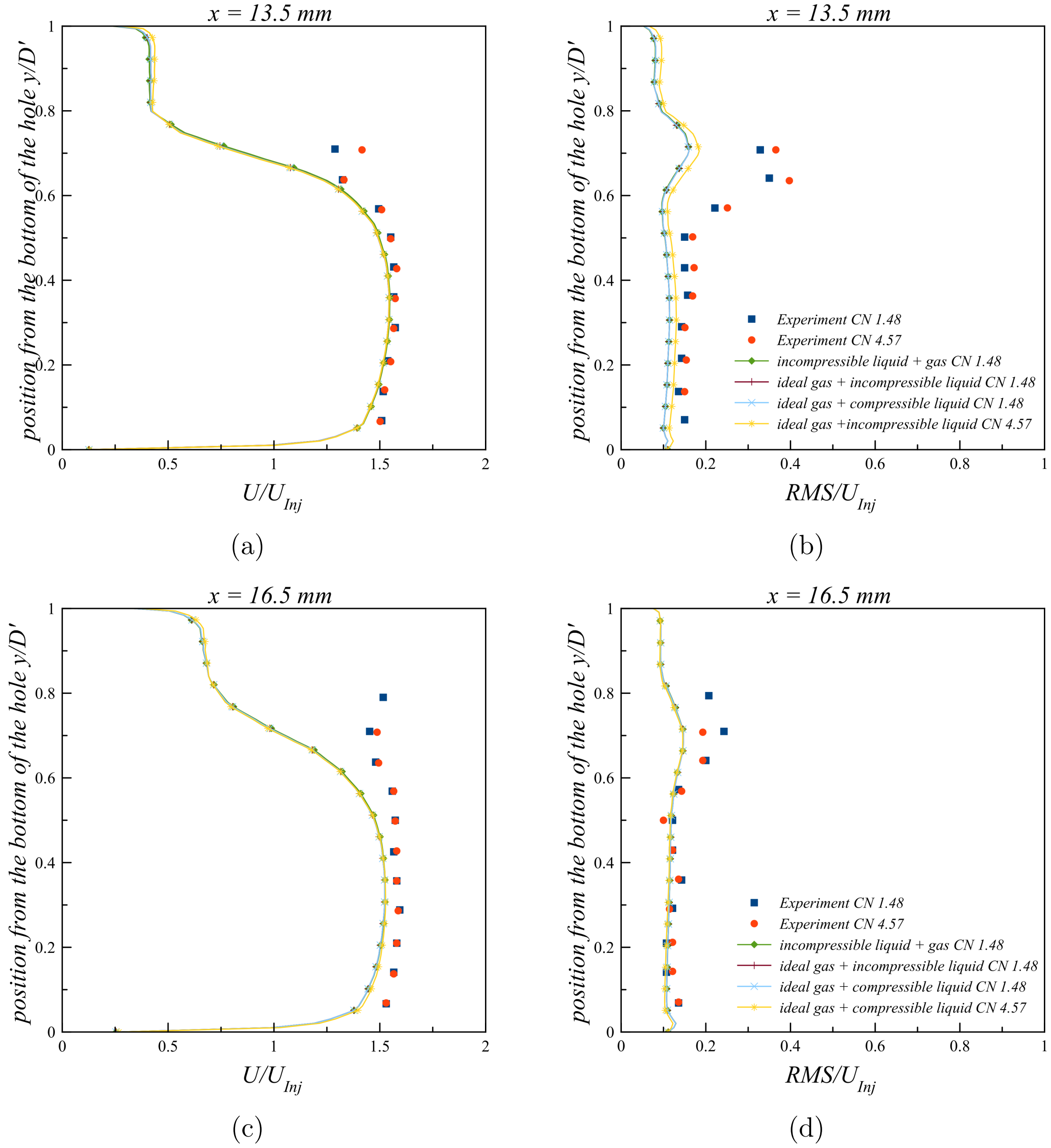

(a) (b)

(c) (d)

Figure 6.8: Normalized mean axial velocity and RMS comparisons at x = 13.5 mm and x = 16.5 mm from the origin.

On observing the mean axial velocity and RMS velocity from the experimental data at the axial position x = 9.5 mm (Figure 6.7 (a) and (b)), it can be seen that the experimental data is only available from bottom to the middle of the hole $y/D' \approx 0.6$, which could have been due to the presence of vapour in the region $0.6 < y/D' < 1$ at both $CN = 1.48$ and 4.57. The presence of vapour is very likely to affect the refractive index of the fluid and hence would affect the quality of the measurements (Nouri et al., 1988), hence measurements are only taken at the positions at which vapour is not present (Roth et al., 2002; Roth, 2004) (see Figure 6.1). The predicted results for the mean axial velocity using all three assumptions (incompressible liquid and incompressible vapour, incompressible liquid and ideal gas for vapour and compressible liquid and ideal gas for vapour) at $CN = 1.48$ indicates a fair agreement with the available experimental data. The comparison of predicted mean axial velocity at $CN = 4.57$ with experimental data at the same plane also indicates reasonable agreements. Similarly on the plane x = 10.5 mm (Figure 6.7 (c) and (d)), experimental results for the mean axial velocity is only available from the bottom to the middle of the plane $(0 < y/D' < 0.6)$. The mean velocity prediction indicates a good agreement with the experimental data at both $CN = 1.48$ and 4.57.

The RMS velocity is underpredicted at the axial position x = 9.5 mm (Figure 6.7 (b)) and x = 10.5 mm (Figure 6.7 (d)) at both $CN = 1.48$ and 4.57. The underprediction of RMS velocity can be attributed to the grid density at the region of interest since it has been realised chapter 4 that the RMS velocity magnitude calculated using Boussinesq formula depends on velocity gradients whose magnitude is highly sensitive to the grid density (increases with the increase of grid density). However, the underprediction of RMS can also be attributed to the modelling errors which could be due to the turbulence model (realizable $k - \epsilon$).

On the plane $x = 13.5$ mm (Figure 6.8 (a) and (b)) it can be again seen that experimental data is available only from the bottom of the hole to the third quarter of the hole $y/D \approx 0.7$. The mean velocity prediction indicates fair a agreement with the experimental data (Figure 6.8 (a)). Reasonable agreements have also been achieved for the RMS velocity from bottom to the middle of the plane $0 < y/D < 0.5$ (Figure 6.8 (b)), however, numerical simulation results indicate that the RMS velocity has been underpredicted in the section of the plane $0.5 < y/D < 0.7$. Since the experimental data are not available at the top section of the plane $0.7 < y/D < 1$, hence no comment can be made regarding the prediction of the RMS velocity of this section. Similarly on the plane $x = 16.5$ mm (Figure 6.8 (c) and (d)), the experimental data for mean axial velocity and RMS velocity the only available from the bottom of the hole to the middle part of the hole $y/D \approx 0.7$. Reasonable agreements are achieved with the available experimental results or mean axial velocity and RMS velocity at both $CN = 1.48$ and 4.57.

The contours (Figure 6.9 (a), (b) and Figure 6.10) and isosurfaces (Figure 6.14 and 6.13) of the vapour volume fraction indicate that vapour is generated at the upper edge of the entrance of the injector hole. From Figure 6.15 and 6.14 it can be inferred that as the fluid enters the injector hole, there is an abrupt change in the flow path and the sudden reduction of cross-sectional area. Due to the sudden reduction of the cross-sectional area, the fluid accelerates and separates from the wall at the upper edge of the entrance of the injector hole which further enhances its velocity (which has been presented using 3d streamlines in Figure 6.15). The fluid then re-attaches to the wall, leading to the formation of the recirculation region at the upper edge of the entrance of the injector hole which the further reduces the cross-sectional area and hence further enhances the fluid acceleration. When the pressure in this recirculation zone becomes lower than the liquid vapour pressure, the liquid starts to cavitate.

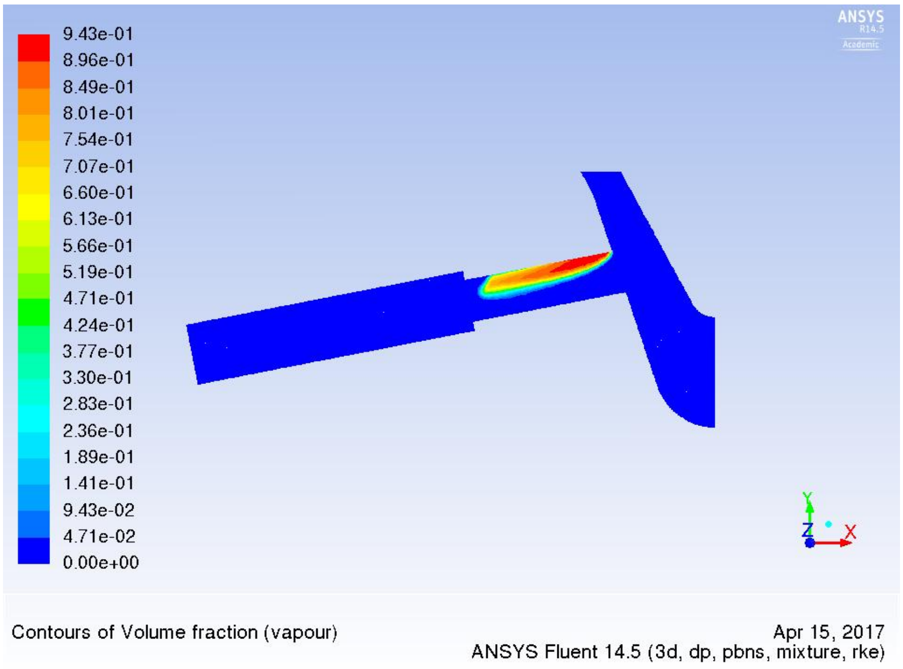

(a) Vapour volume fraction (incompressible vapour assumption)

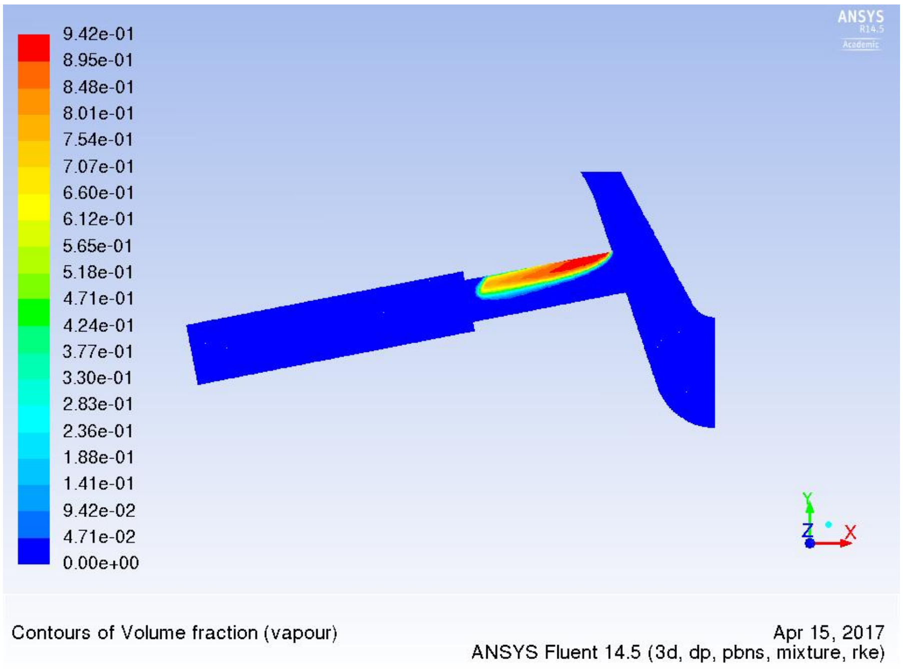

(a) Vapour volume fraction (ideal gas assumption for vapour)

Figure 6.9: The predicted vapour volume fraction using (a) incompressible gas assumption, (b) ideal gas assumption at $CN = 1.48$

From the Figures 6.13 and 6.14, it can be seen that the cavitation vapour convects with the fluid as it travels downstream. At $CN = 1.48$, the cavitation vapour cloud collapses at around 7/8th of the injector hole length. However, at $CN = 4.57$ (see Figure 6.10), the cavitation vapour is seen entering the backflow hole. As the fluid enters the backflow hole, there is an immediate (step) expansion of the cross-sectional area; the step expansion causes the fluid to separate from the wall, this leads to the formation of an annular recirculation region or annular ring-shaped step vortex (Figure 6.15). When the pressure at the core of the annular ring-shaped step vortex goes lower than the vapour pressure of the liquid it starts to cavitate. As the flow goes further downstream the cavitation which has originated at the entrance of the injector hole merges with the cavitation which has originated from the step vortex of the backflow hole (Figures 6.10 and 6.14). The vapour (cavitation) then further mixes with the liquid when it travels downstream, forming a cloudy liquid vapour fluid mixture (cavitation cloud). As the fluid reaches the outlet, the predicted results indicate that the cavitation cloud starts to transform back into liquid state due to the constant pressure outlet boundary conditions. The local sonic conditions can lead to the development of the shocks in the bubbly flows. Hence, for both cases, $CN = 1.48$, and $CN = 4.57$, pressure contours on the centre plane (Figure 6.11 (a) 6.12 (a)) and pressure profile on the injector hole (Figure 6.11 (b) and 6.12 (b) are analysed to investigate any possibility of shock, which does not indicate any possibility of shock.

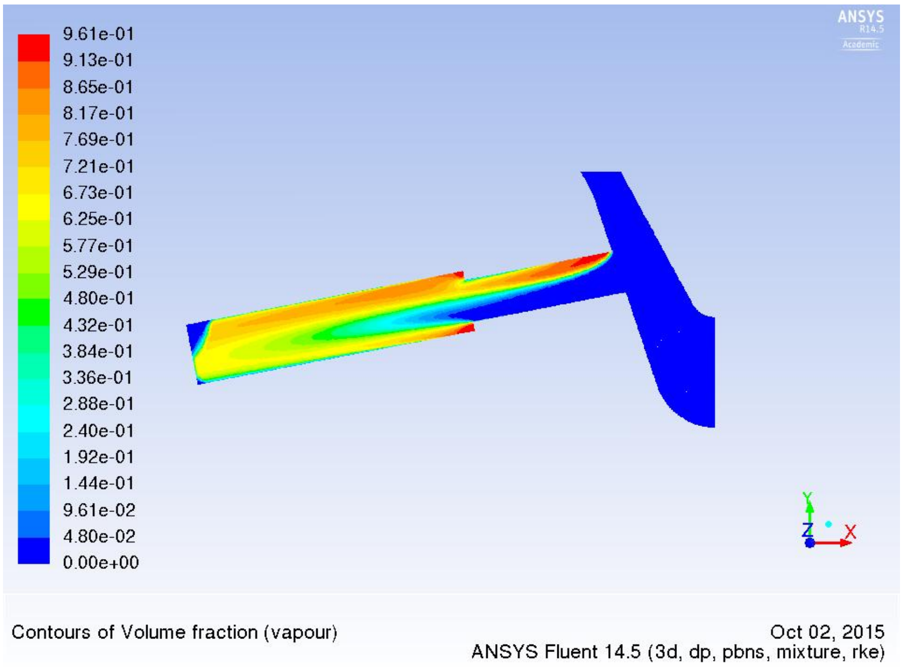

Figure 6.10: The predicted vapour volume fraction at $CN = 4.57$, vapour is assumed to be an ideal gas

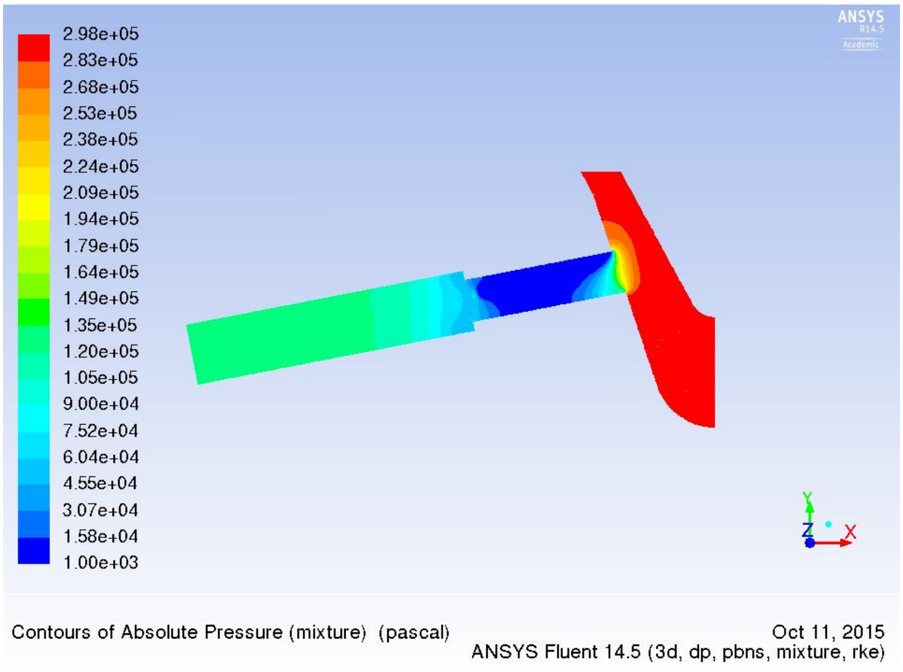

(a) Pressure (absolute) $N\ m^{-2}$

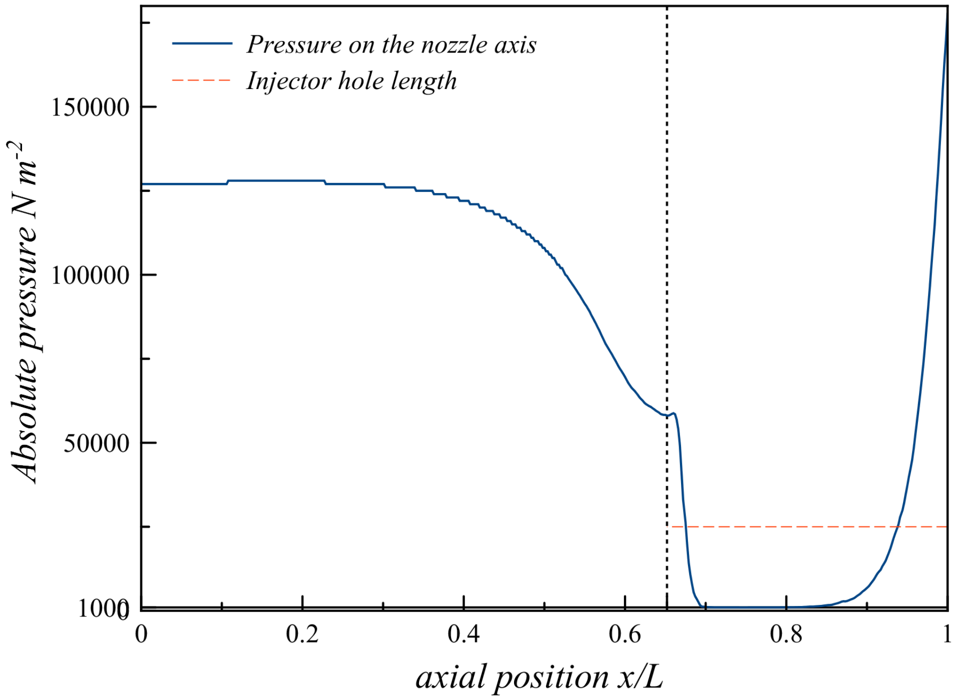

(b) The predicted pressure at the injector hole axis.

Figure 6.11: (a) The pressure contour on the centre plane at $CN = 1.48$. (b) The predicted pressure at the injector hole axis. The direction of flow is from right to left.

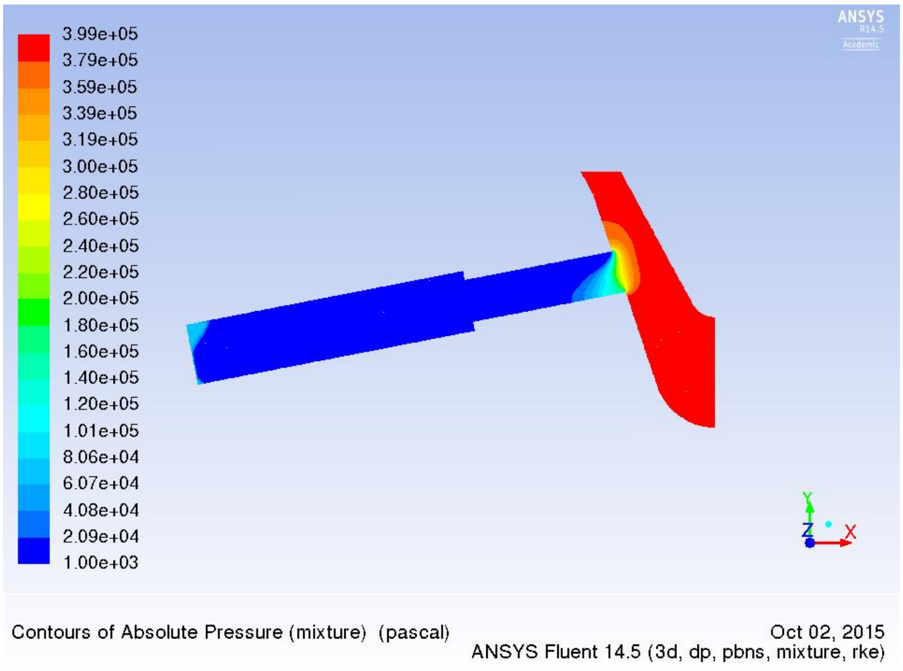
3.99e+05
3.79e+05
3.59e+05
3.39e+05
3.19e+05
3.00e+05
2.80e+05
2.60e+05
2.40e+05
2.20e+05
2.00e+05
1.80e+05
1.60e+05
1.40e+05
1.20e+05
1.01e+05
8.06e+04
6.07e+04
4.08e+04
2.09e+04
1.00e+03
ANSYS
R14.5
Academic
Y
Z
X
Contours of Absolute Pressure (mixture) (pascal)
Oct 02, 2015
ANSYS Fluent 14.5 (3d, dp, pbns, mixture, rke)

(a) Pressure (absolute) $N\ m^{-2}$

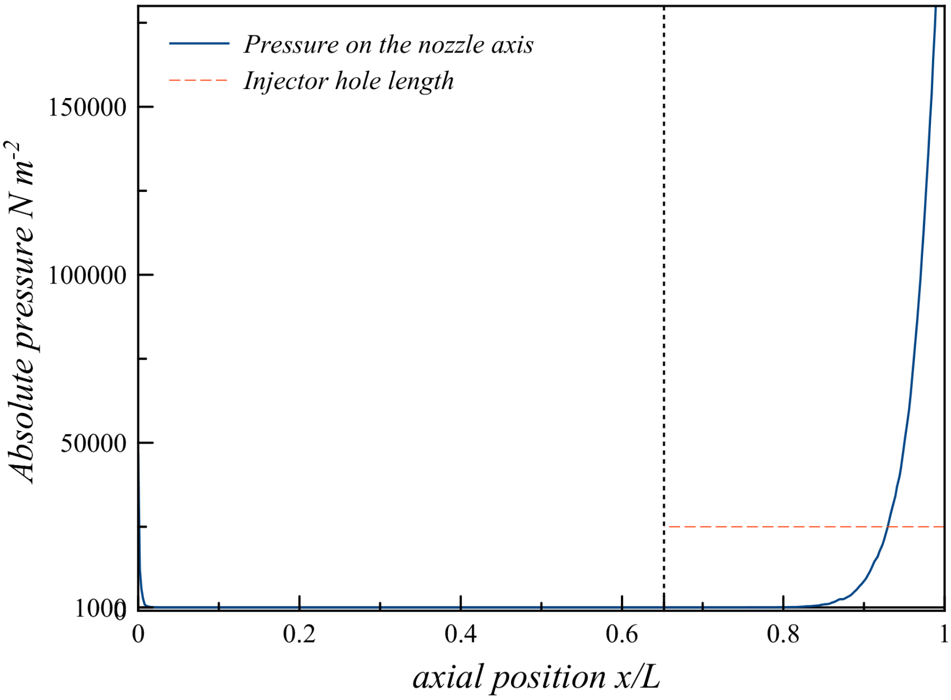

(b) The predicted pressure at the injector hole axis.

Figure 6.12: (a) The pressure contour on the centre plane at $CN = 4.57$. (b) The predicted pressure at the injector hole axis. The direction of flow is from right to left.

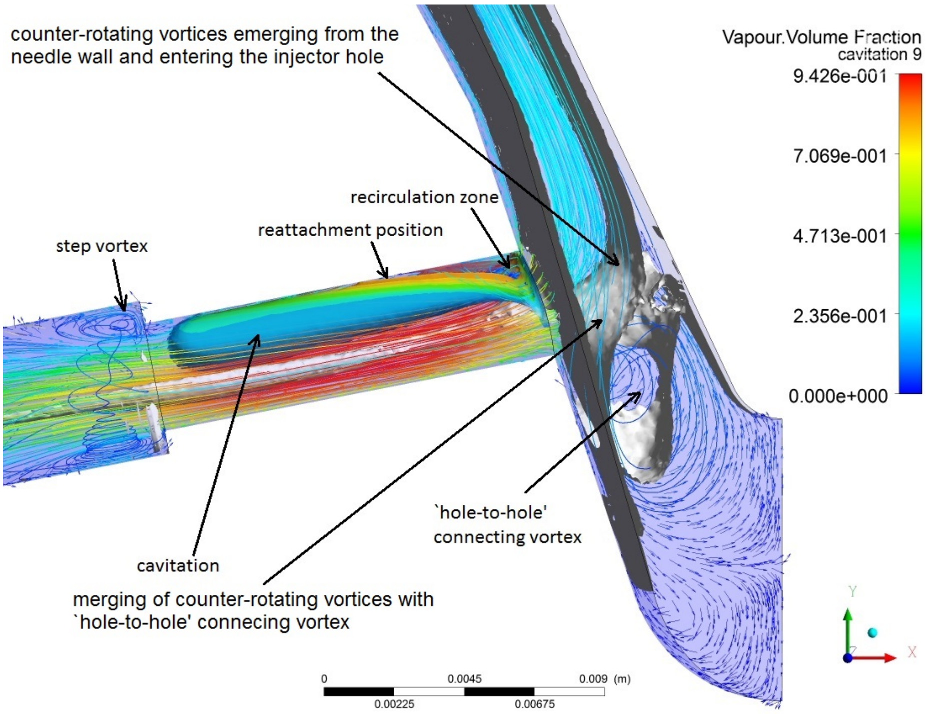
counter-rotating vortices emerging from the needle wall and entering the injector hole
recirculation zone
reattachment position
step vortex
cavitation
merging of counter-rotating vortices with `hole-to-hole' connecing vortex
`hole-to-hole' connecting vortex
Vapour.Volume Fraction
cavitation 9
9.426e-001
7.069e-001
4.713e-001
2.356e-001
0.000e+000
0
0.0045
0.009 (m)
0.00225
0.00675
Y
X

Figure 6.13: Isosurface of vorticity (0.5% of the magnitude) at $CN = 1.48$ indicate vortices; the hole-to-hole connecting vortex can be easily identified, the isosurface of cavitation also indicate cavitation formation at the upper edge of the entrance of the injector hole. The cavitation then travels with the flow and remains in the vicinity of the wall and end at approx 7/8 of the injector hole length. In the cavitation isosurfaces, the red colour represents the maximum concentration of vapour volume fraction and blue represents the minimum.

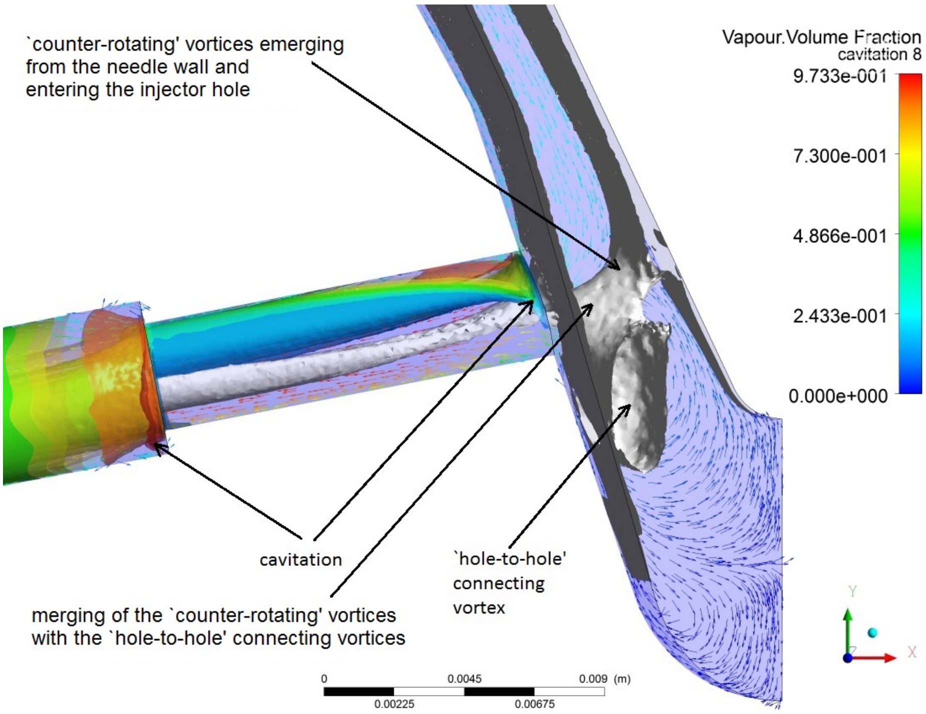
`counter-rotating' vortices emerging from the needle wall and entering the injector hole
cavitation
merging of the `counter-rotating' vortices with the `hole-to-hole' connecting vortices
`hole-to-hole' connecting vortex
Vapour.Volume Fraction
cavitation 8
9.733e-001
7.300e-001
4.866e-001
2.433e-001
0.000e+000
0
0.0045
0.009 (m)
0.00225
0.00675
Y
X

Figure 6.14: Image showing isosurface of cavitation, an isosurface of vorticity magnitude (0.5% of the magnitude), velocity vectors and streamline at $CN = 4.57$. In the cavitation isosurfaces, the red colour represents the maximum concentration of vapour volume fraction and blue represents the minimum.

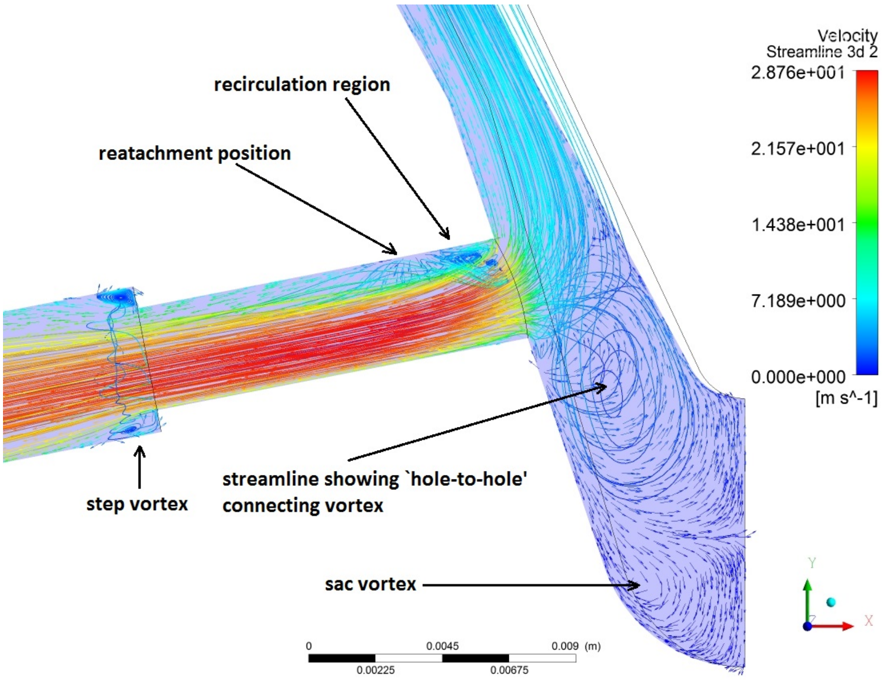

Figure 6.15: Zoom of the sac region showing velocity vectors and 3d velocity streamlines at $CN = 4.57$. The velocity vectors and 3d streamlines indicate the presence of the vortex in the sac region.

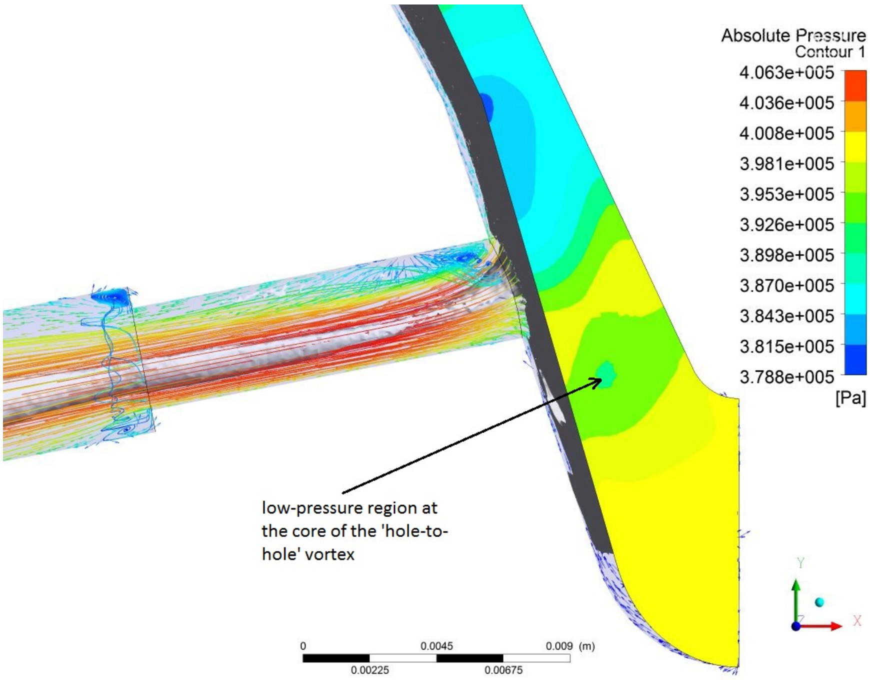

Figure 6.16: Image showing isosurface of vorticity magnitude (0.5% of the magnitude) and pressure contours plotted on the periodic boundary face at $CN = 4.57$. The pressure contour indicates lower pressure at the core of 'hole-to-hole' connecting vortex.

Isosurface of the 0.5% magnitude of vorticity has been generated to detect the presence of vortices at cavitating conditions ($CN = 4.57$). From the iso-surface of vorticity, in the Figures 6.17, 6.18, 6.19 and 6.20 , we can see the 'hole-to-hole' connecting vortices and counter rotating vortices originating from the needle wall and entering the injector hole. From Figures 6.14, 6.17, it can also be seen that these vortices ('hole-to-hole' connecting vortex and 'counter-rotating' vortices) begin to merge as they enter the injector hole and starts to dissipate.

To further investigate the 'hole-to-hole' connecting vortex, vectors have been plotted on the periodic boundary of the injector (Figure 6.19 and 6.20). From the bottom view (y-axis negative) (Figure 6.19) the 'hole-to-hole' connecting vortex appears to have a counter-clockwise direction on the front face and a clockwise direction of rotation on the back face. Pressure contours (Figure 6.16) have also been plotted on the periodic face which indicate a low-pressure region at the core of the vortex, but the pressure never reduces to the vapour pressure of the liquid to initiate cavitation.

Non dimensionalised vorticity contours[1] plotted on the planes normal to the injector hole at different axial positions further assert the presence of 'counter-rotating' vortices emerging from the needle wall and entering the injector hole facing it. Corresponding to vorticity contours, vapour volume fraction contours in Figure 6.22 (a) on the planes in the injector holes indicate that vortices in the injector hole have influenced the shape of the cavitation region as well as the vapour distribution in the cavitation region. The presence of 'counter-rotating' vortices emerging from the needle wall and entering the injector hole is confirmed by the streamlines plotted on the plane which lies in the annular space between the needle wall and the injector hole (plane 4, see chapter 4, § 4.7.1) as shown in Figure 6.21.

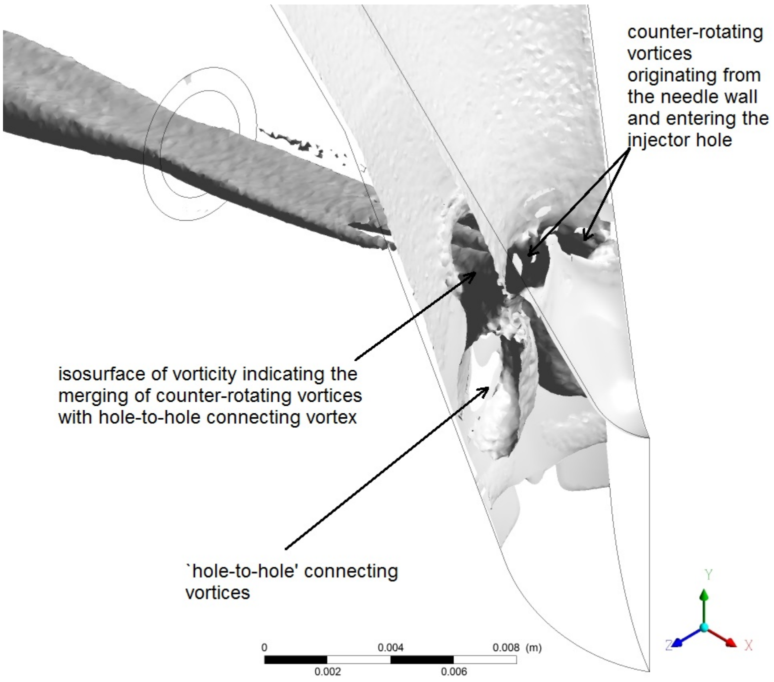
counter-rotating vortices originating from the needle wall and entering the injector hole
isosurface of vorticity indicating the merging of counter-rotating vortices with hole-to-hole connecting vortex
`hole-to-hole' connecting vortices
0
0.002
0.004
0.006
0.008 (m)
Y
Z
X

Figure 6.17: Isometric view of the injector. The isosurface of vorticity magnitude (0.5% of the magnitude) showing the probability of occurrence of vortices in the injector hole at $CN = 4.57$

---

[1] In Figure 4.34 (b) red colour represent a positive (counter-clockwise) and blue indicate a negative vorticity (clockwise)

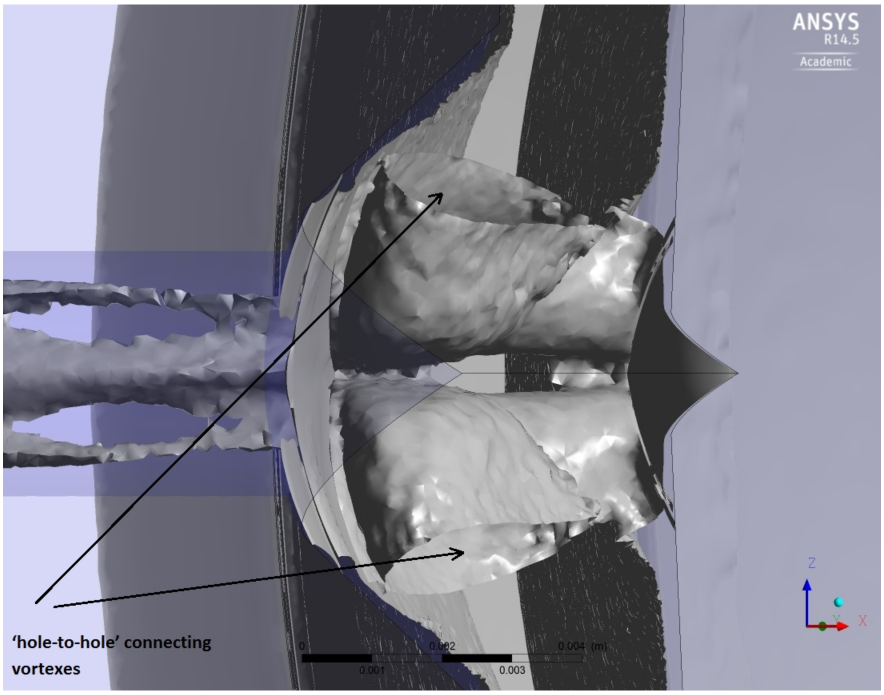
ANSYS
R14.5
Academic
'hole-to-hole' connecting vortexes
0
0.002
0.004 (m)
0.001
0.003
Z
X

Figure 6.18: Bottom view of the injector.The isosurface of vorticity magnitude (0.5% of the magnitude) showing the probability of occurrence of vortices in the injector hole at $CN = 4.57$

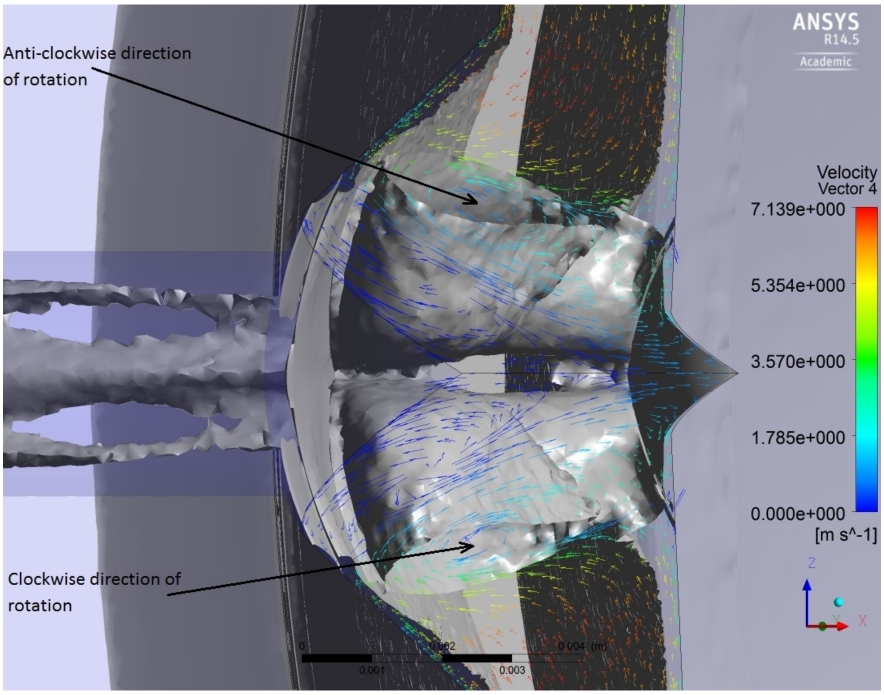
ANSYS
R14.5
Academic
Anti-clockwise direction of rotation
Clockwise direction of rotation
Velocity Vector 4
7.139e+000
5.354e+000
3.570e+000
1.785e+000
0.000e+000
[m s^-1]
0
0.002
0.004 (m)
0.001
0.003
Z
X

Figure 6.19: Bottom view of the injector. The isosurface of vorticity magnitude (0.5% of the magnitude) showing the probability of occurrence of vortices in the injector hole at $CN = 4.57$. Velocity vectors have been plotted on the front periodic plane from which 'hole-to-hole' connecting vortex appears in a counter-clockwise direction and velocity vectors have also been plotted on the back side (bottom of the image) of the periodic interface from which 'hole-to-hole' connecting vortex appears in a counter-clockwise direction.

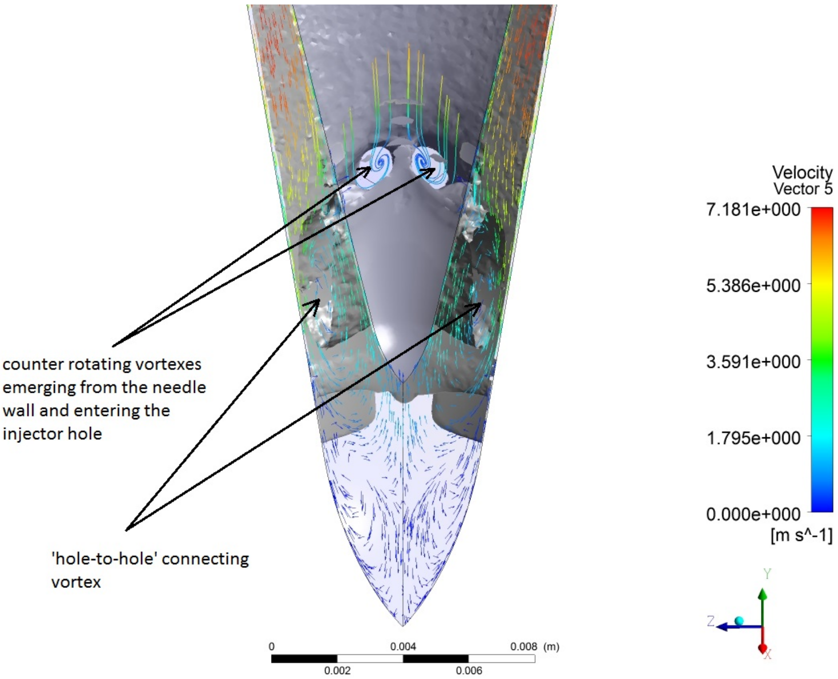
counter rotating vortexes emerging from the needle wall and entering the injector hole
'hole-to-hole' connecting vortex
Velocity
Vector 5
7.181e+000
5.386e+000
3.591e+000
1.795e+000
0.000e+000
[m s^-1]
0
0.002
0.004
0.006
0.008 (m)
Y
Z
X

Figure 6.20: A view of the injector from the centre at $CN = 4.57$. Isosurface of vorticity magnitude (0.5% of the magnitude) indicates vortices emerging from the needle wall and entering the injector hole, isosurface of vorticity magnitude also indicate the presence of 'hole-to-hole' connecting vortex. Vectors plotted on plane 4 indicate opposite direction of rotation. Vectors also plotted on the periodic boundary which also indicate the presence of 'hole-to-hole' connecting vortex.

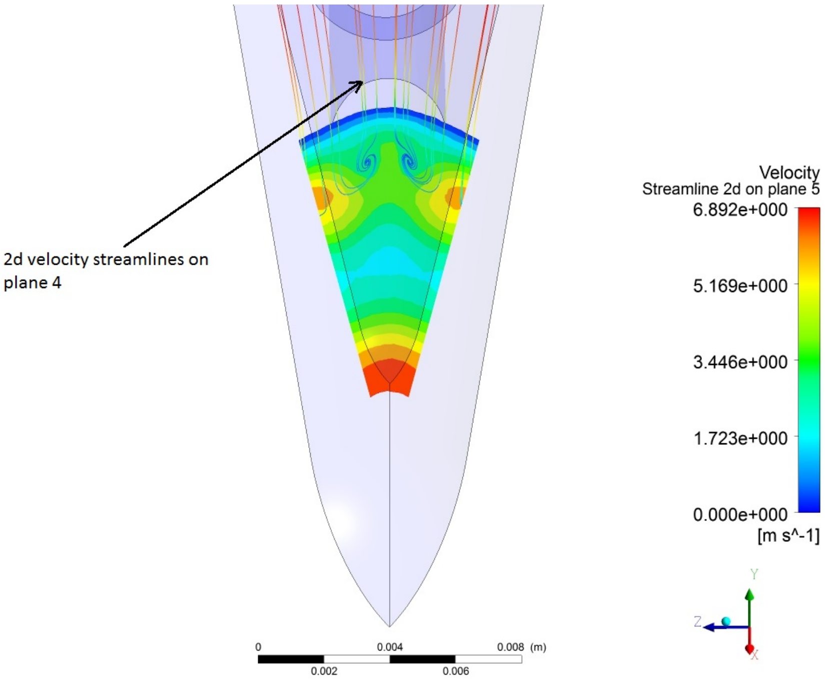
2d velocity streamlines on plane 4
Velocity
Streamline 2d on plane 5
6.892e+000
5.169e+000
3.446e+000
1.723e+000
0.000e+000
[m s^-1]
0
0.002
0.004
0.006
0.008 (m)
Y
Z
X

Figure 6.21: A view of the injector from the centre. Streamlines plotted at $CN = 4.57$, indicate the presence of counter-rotating vortices originating from the needle wall and entering the injector hole. The low-pressure region can also be seen at the core of the vortices.

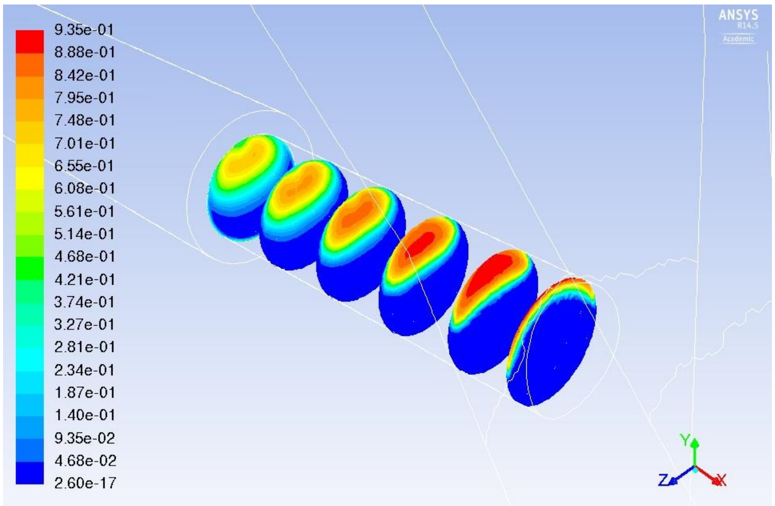

(a) Vapour volume fraction

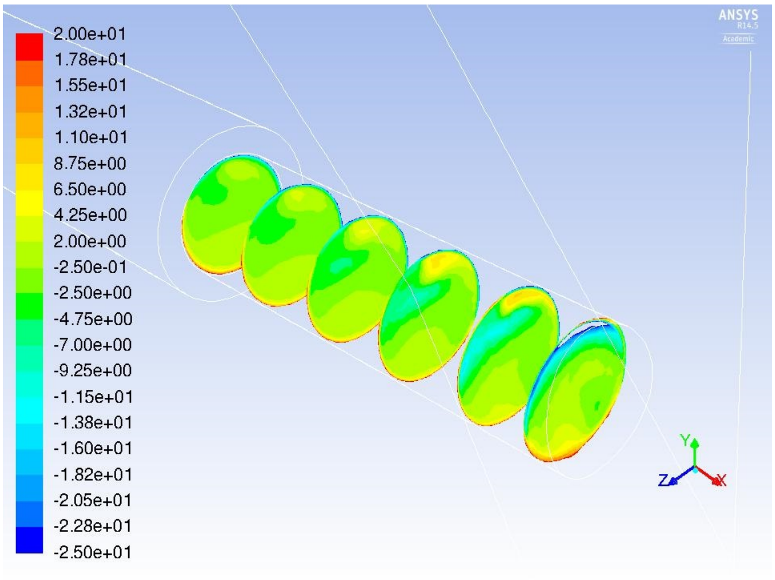

(b) Non-dimensionalised vorticity, $\frac{\vec{\zeta} D}{U_{inj}}$

Figure 6.22: Vapour volume fractions and non-dimensionalised vorticity are plotted at different slices in the injector holes. The vorticity is non-dimensionalised by multiplying with the injector hole diameter which is 3.5 mm and divided by average velocity which is 18.5 $m\ s^{-1}$ at $CN = 4.57$ (Roth et al., 2002; Roth, 2004).

6.3.2.3 Qualitative comparison with experimental data

Since still images and high-speed video images at $CN = 4.57$ of the injector hole for nominal needle lift conditions for mini-sac type enlarged injector are not available (Roth et al., 2002; Roth, 2004) hence results (still images) from Afzal et al. (1999) have been used, which have been taken at similar cavitation number ($CN = 4.57$).

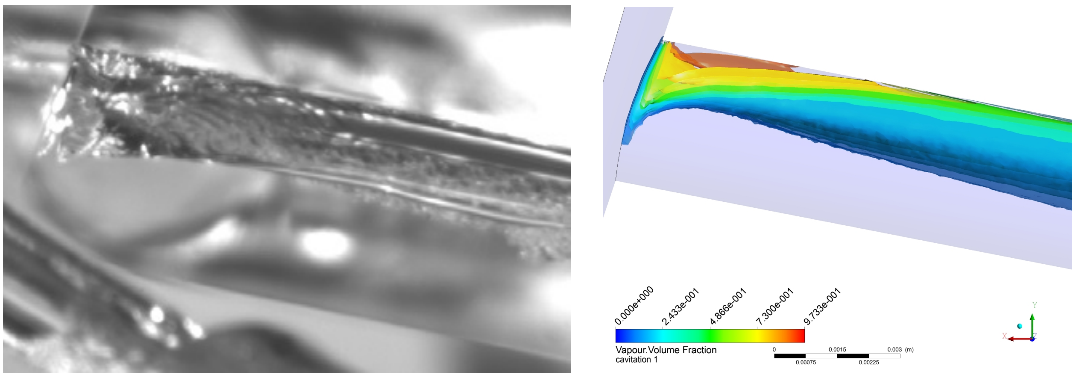
0.000e+000
2.433e-001
4.866e-001
7.300e-001
9.733e-001
Vapour.Volume Fraction
cavitation 1
0
0.0015
0.003 (m)
0.00075
0.00225
Y
X

(a) (b)

Figure 6.23: (a) Still photograph (side view) of the geometry induced cavitation formed at the upper edge of the entrance of the injector hole and travelling downstream, the image indicates that cavitation stays in the vicinity of the injector wall, source: Afzal et al. (1999). (b) isosurface of cavitation prediction at $CN = 4.57$, nominal needle lift (6.00 mm).

Comparison between the side view of a still image of cavitation inside the injector hole at nominal needle lift (6.00 mm) of the mini-sac type multi-hole injector with the isosurface of predicted vapour volume fraction indicates visual similarities between the experimental results and CFD simulations for the vapour distribution. It can also be seen from the comparison of Figure 6.24 (a) and (b) that CFD simulations have resulted in a similar horseshoe-shaped profile of vapour distribution as that of the experiment. Top view of the predicted isosurface of cavitation (Figure 6.25 (b)) and the experimental results (Figure 6.25 (a)) also indicate visual similarities.

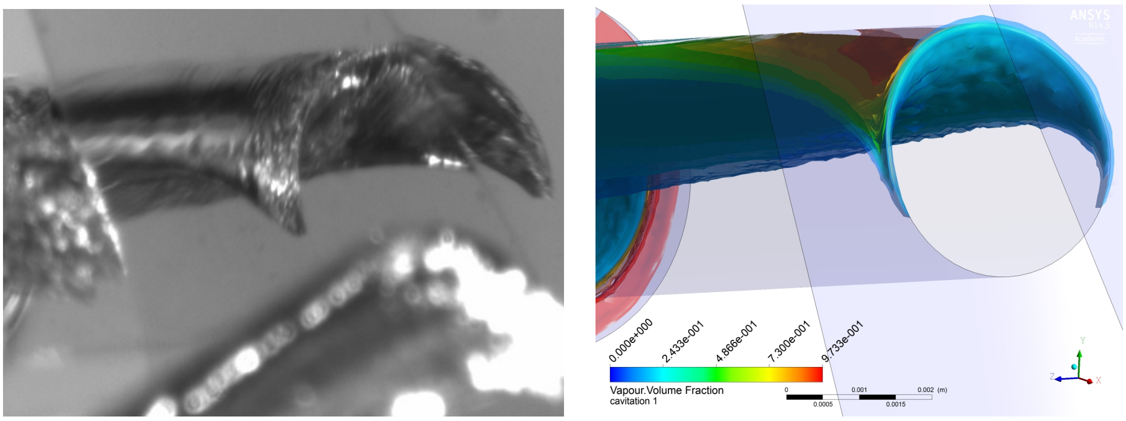
ANSYS
0.000e+000
2.433e-001
4.866e-001
7.300e-001
9.733e-001
Vapour.Volume Fraction
cavitation 1
0
0.001
0.002 (m)
0.0005
0.0015
Y
Z
X

(a) (b)

Figure 6.24: (a) Still photograph of the geometry induced cavitation formed at the upper edge of the entrance of the injector hole and travelling downstream, the image indicates cavitation remains stays in the vicinity of the injector wall, the image also indicates horseshoe appearance of cavitation source: Afzal et al. (1999). (b) isosurface of cavitation prediction at $CN = 4.57$, nominal needle lift (6.00 mm), also indicate horseshoe appearance.

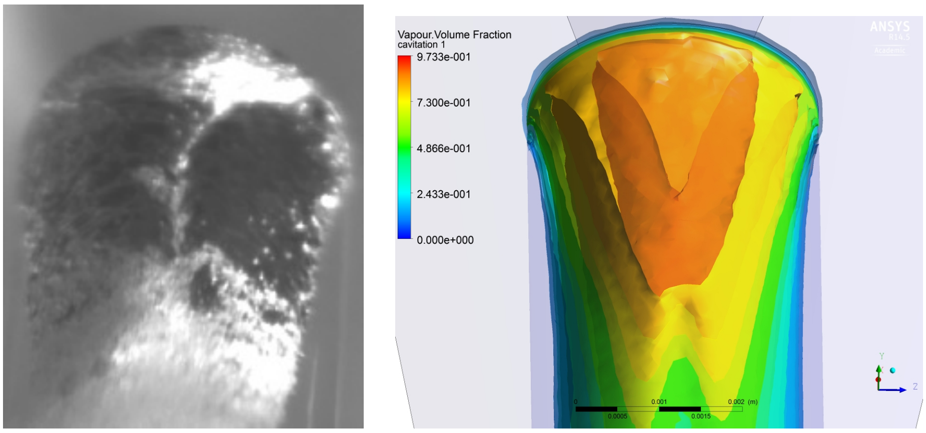

(a) (b)

Figure 6.25: (a) 3D photograph of the geometry induced cavitation formed at the upper edge of the injector hole entrance and travelling downstream, source: Afzal et al. (1999). (b) isosurface of cavitation prediction at $CN = 4.57$, nominal needle lift (6.00 mm).

6.3.2.4 Discussions:

- Fairly accurate results for the mean axial velocity are achieved. The RMS velocity results are also in the reasonable agreements with experimental data.

- Fairly good qualitative agreements with the experimental results for the cavitation are achieved at $CN = 1.48$.

- Flow field analysis indicated that cavitation is generated at the upper edge of the entrance of the injector hole, once vapour forms it travels with the fluid and stays in the vicinity of the injector wall.

- At the $CN = 1.48$, the predicted cavitation structure ends at approx 7/8 of the injector hole length due to the occurrence of higher pressure than the vapour pressure of the liquid at this region.

- At $CN = 4.57$, the predicted the cavitation which originated at the upper edge of the entrance of the injector hole further mixes with the cavitation generated at the backflow hole leading to the formation of cloudy liquid vapour mixture (cavitation cloud).

- Additional cavitation is predicted at the entrance of the backflow hole.

- Flow field analysis also revealed the presence of 'hole-to-hole' connecting vortex and 'counter-rotating' vortices emerging from the needle wall and entering the injector hole facing it.

6.4 Lower needle lift

6.4.1 Case study 2: Simulation of onset conditions at CN 1.48

6.4.1.1 Case setup

Operating condition as described for case 1 in table 6.1 for lower needle lift is simulated. Steady state simulations are performed. Since in the previous chapter 4 it was realised that grid independence at the low needle lift at non-cavitating condition is being approached using for mean axial velocity and and in the subsection § 6.3.1, it has been shown that vapour volume fraction did not change significantly with increase in grid density. Hence, in the present case, the grid 5 from single-phase simulations is used. The same physical models are used with the same models parameters are used as in § 6.3.2 (see Table 6.5). The ideal gas law is used to model the vapour compressibility. The liquid phase is assumed to be incompressible (see § 6.3.2). Boundary conditions are listed in Table 6.7.

	Inlet	Outlet	interface	Walls
	mass-flow rate	constant pressure	cyclic	enhanced wall
liquid	0.108295 $kg\ s^{-1}$	119000 Nm^{-2}		treatment method
vapour	0 $kg\ s^{-1}$			(no-slip wall)

Table 6.7: Boundary Conditions

6.4.1.2 Results

At the axial position x = 9.5 mm (Figure 6.26 (a) and (b)), the experimental data is only available from the bottom of the plane to the 2/3rd of the plane ($0 \leq y/D' \leq 0.7$), because of the presence of cavitation bubble which distorts the laser beam (Nouri et al., 1988), LDV velocity measurements could not be performed at the upper part of the injector hole. Comparison between available experimental data and prediction results for mean axial velocity and RMS velocity with prediction result indicate a reasonable agreement. The simulation results also indicate the presense of a recirculation region at the upper portion of the injector hole.

Similarly at the axial location x = 10.5 mm (Figure 6.26 (c) and (d)) experimental data are only available from the bottom of the plane to 2/3rd of the plane ($0 \leq y/D' \leq 0.7$). Comparison between the experimental data and the predicted result indicates reasonable agreement, however, velocity is underpredicted at the middle section of the plane to 2/3rd of the plane ($0.5 \leq y/D' \leq 0.7$).

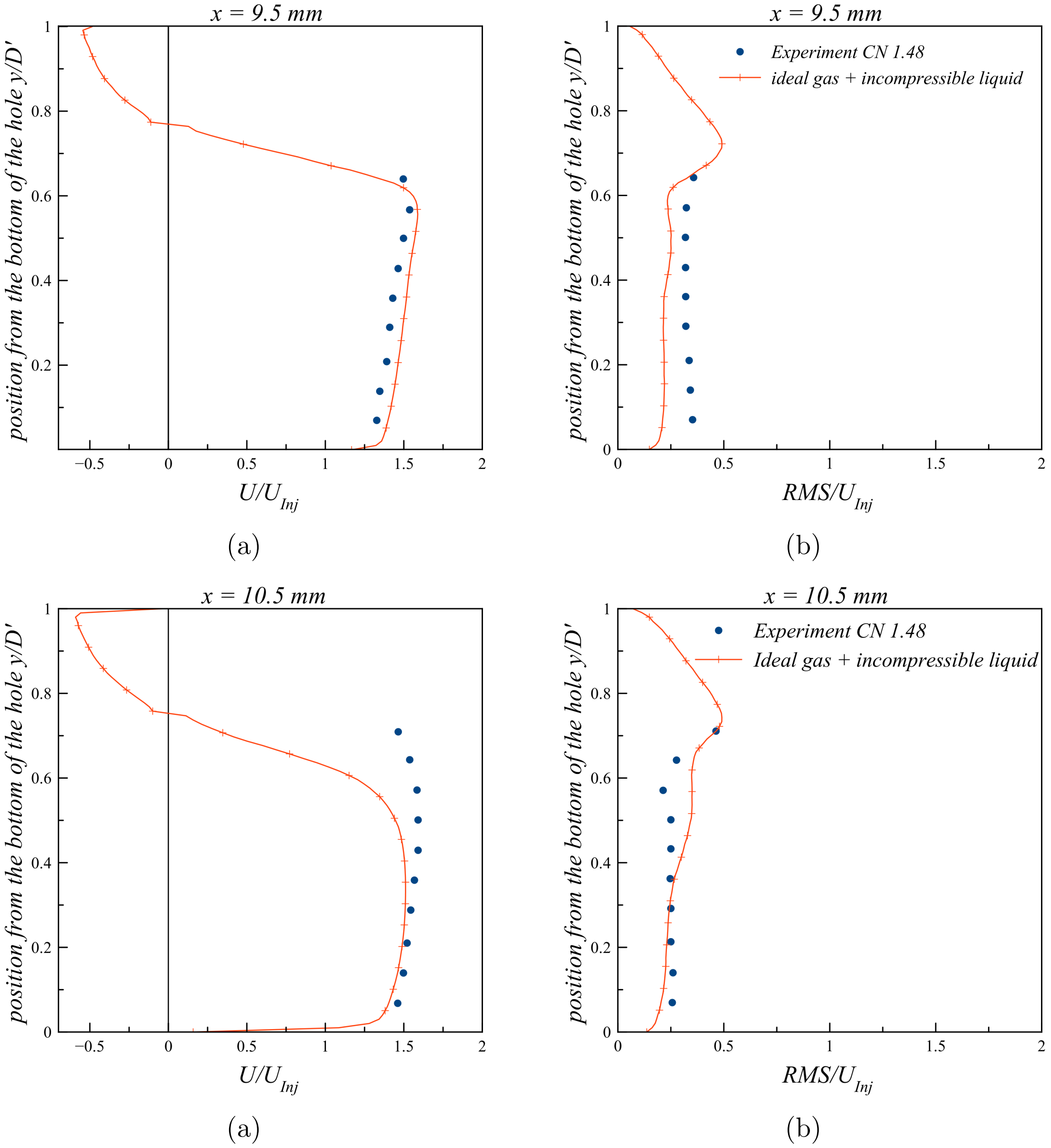

(a) (b)

(a) (b)

Figure 6.26: Normalized mean axial velocity and RMS comparisons at x = 9.5 mm, 13.5 mm and x = 16.5 mm from the origin.

At the axial location x = 13.5 mm (Figure 6.27 (a) and (b)), the experimental data are only available from the bottom of the injector hole to 4/5th of the injector hole ($0 \leq y/D' \leq 0.75$). Comparison between the experimental data and the predicted results indicates underprediction of the mean axial velocity. The mean axial velocity prediction indicates flow recirculation at the very upper region of the plane ($9 \leq y/D' \leq 1$). Comparison of the RMS velocity prediction with experimental data suggests reasonable agreement; which is mainly due to local grid refinement in the injector hole and the sac volume of this grid. The RMS velocity is calculated using the Boussinesq formula; the magnitude of the RMS velocity depends on the magnitude of the mean velocity gradients; which was realised in the chapter 4.

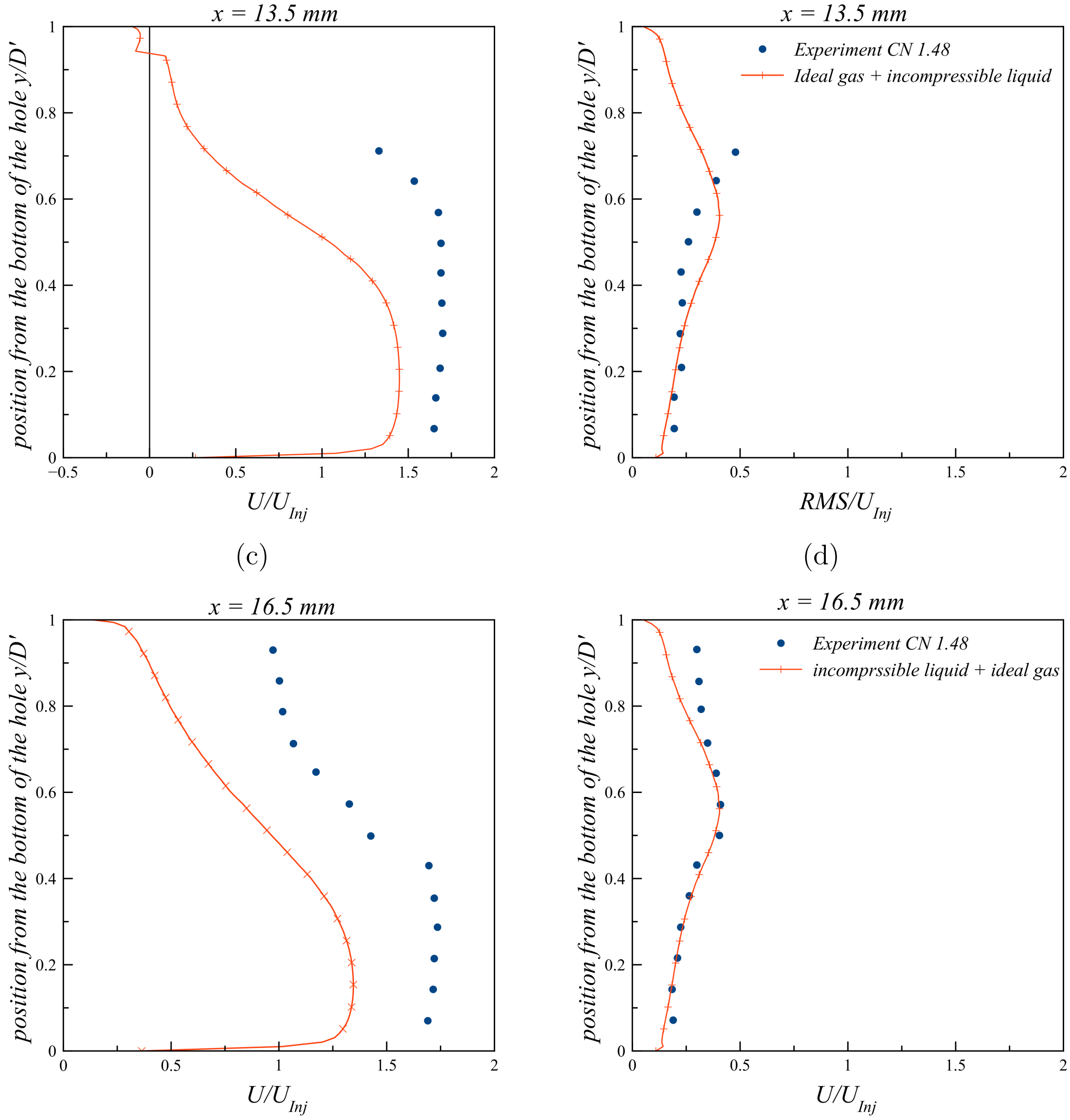

(c) (d)

(c) (d)

Figure 6.27: Normalized mean axial velocity and RMS comparisons at x = 9.5 mm, 13.5 mm and x = 16.5 mm from the origin.

At the axial location x = 16.5 mm (Figure 6.27 (c) and (d)), it can be seen that the experimental data for the mean axial velocity and RMS velocity are available throughout the plane indicating the cavitation bubbles which originated at the entrance of the injector hole have completely collapsed. On the comparison of the experimental data and simulation results for the mean axial velocity it can be seen that the mean axial velocity is underpredicted however has achieved the same profile as of experimental data. Reasonable agreement for the RMS velocity has been achieved and the reasons are stated in the previous paragraph.

The underprediction of the mean axial velocity at positions x = 10.5 mm, 13.5 mm and 16.5 mm is due to underestimation of the vapour volume fraction; hence the cross-sectional area of liquid is larger. However, neither quantitative and qualitative data are available (Roth et al., 2002; Roth, 2004) for the onset of cavitation at the lower lift for the mini-sac type multi-hole enlarged fuel injector and hence quantitative and qualitative comparison and model assessment for the vapour volume cannot be done. Nonetheless, the discrepancies between the predicted and experimental mean axial velocity at cavitation conditions can be attributed to the possibility of needle eccentricity in this particular test rig which has also been previously mentioned by Giannadakis et al. (2008). The needle eccentricity would have caused uneven distribution of fluid in injector holes and possibly because of this reason differences between first and second series of experiments for the mean axial velocity and RMS velocity have been noticed at non-cavitating conditions for both lower (1.6 mm) and nominal lift (6.00 mm) conditions in chapter 4. The isosurface of the vapour volume fraction (Figure 6.28 and 6.30) indicates the occurrence of cavitation 'onset' at the upper edge of the entrance of the fuel injector. 3d velocity streamlines indicate a recirculations region on the upper edge of the entrance of the injector hole. When the pressure in the recirculation regions at the upper of the entrance of the hole decreases to the vapour pressure of the liquid (see Figure 6.29), the liquid starts to cavitate.

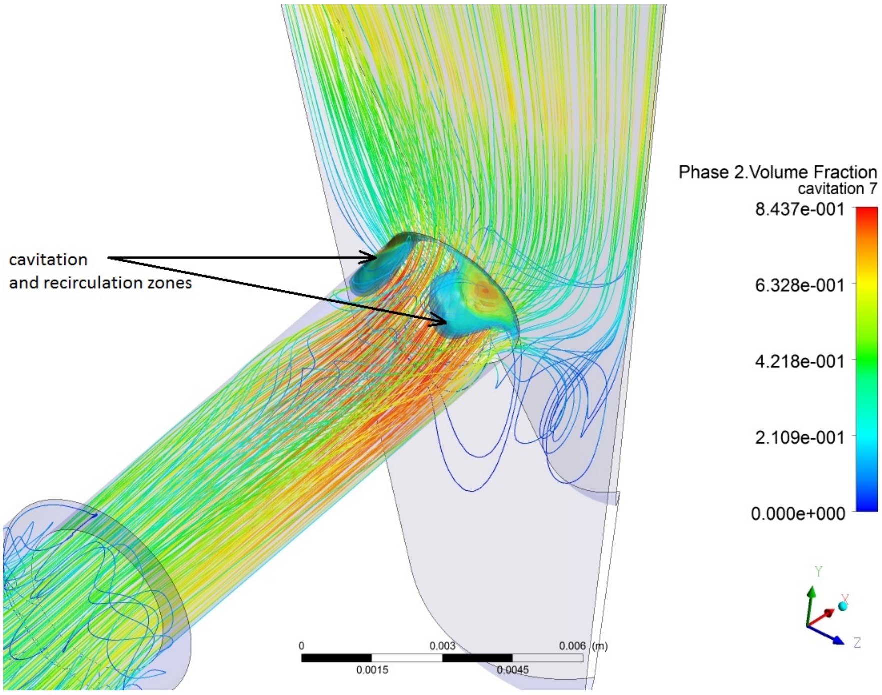

Figure 6.28: The predicted vapour volume fraction and velocity streamline in the injector.

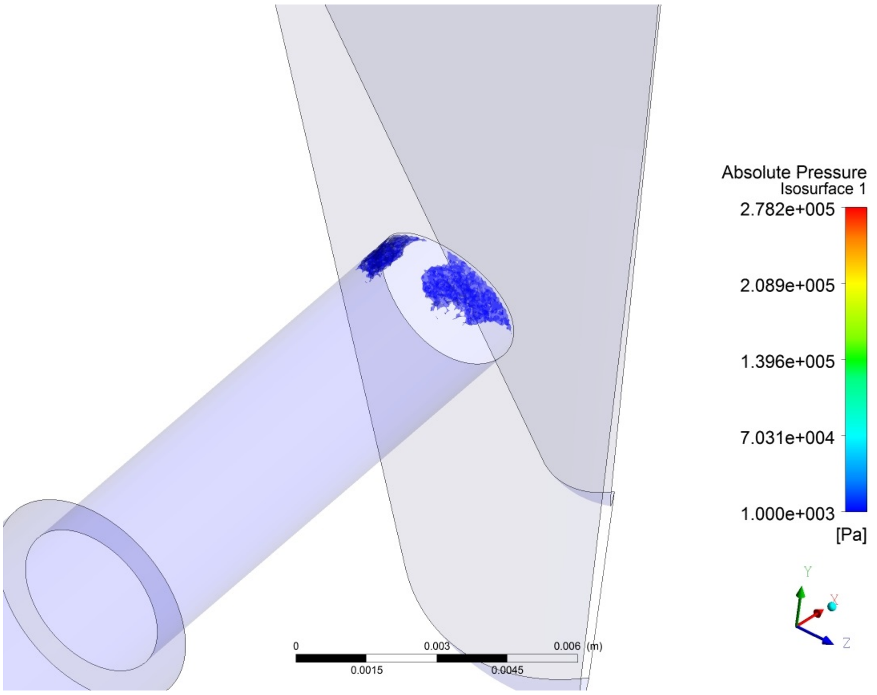
Absolute Pressure
Isosurface 1
2.782e+005
2.089e+005
1.396e+005
7.031e+004
1.000e+003
[Pa]
0
0.003
0.006 (m)
0.0015
0.0045
Y
X
Z

Figure 6.29: Isosurface of vapour pressure

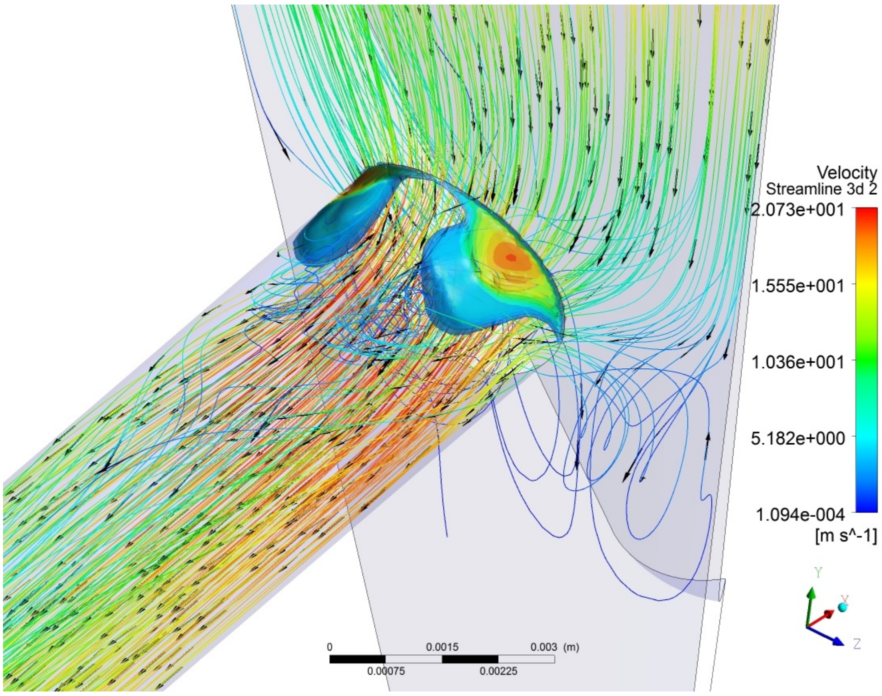
Velocity
Streamline 3d 2
2.073e+001
1.555e+001
1.036e+001
5.182e+000
1.094e-004
[m s^-1]
0
0.0015
0.003 (m)
0.00075
0.00225
Y
X
Z

Figure 6.30: Magnified view of the injector. The predicted vapour volume fraction and velocity streamline can be seen. Velocity streamlines indicate a recirculation region at the upper edge of the injector hole on which 3d velocity vectors have also been plotted.

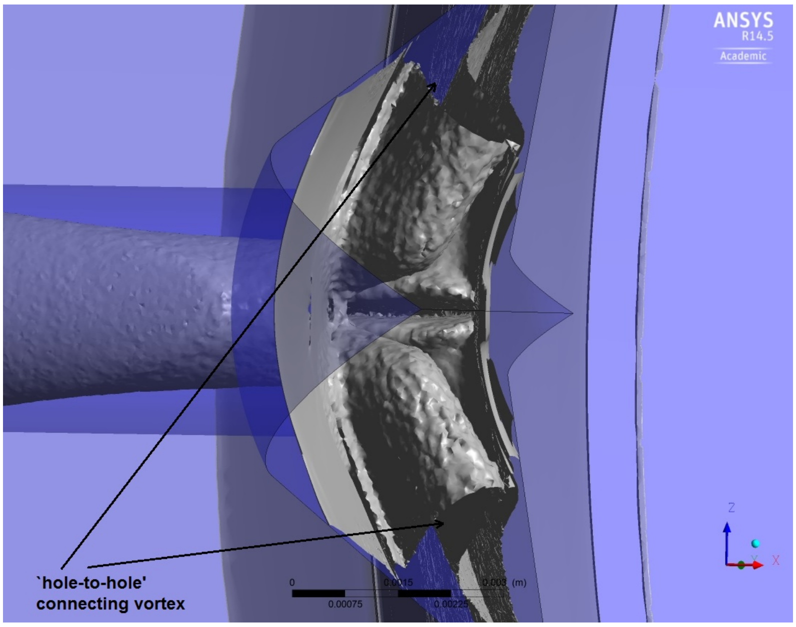
ANSYS
R14.5
Academic
`hole-to-hole'
connecting vortex
0
0.0015
0.003 (m)
0.00075
0.00225
Z
X

Figure 6.31: Bottom view of the injector.The isosurface of vorticity magnitude (0.5% of the magnitude) showing the probability of occurrence of vortices in the injector hole.

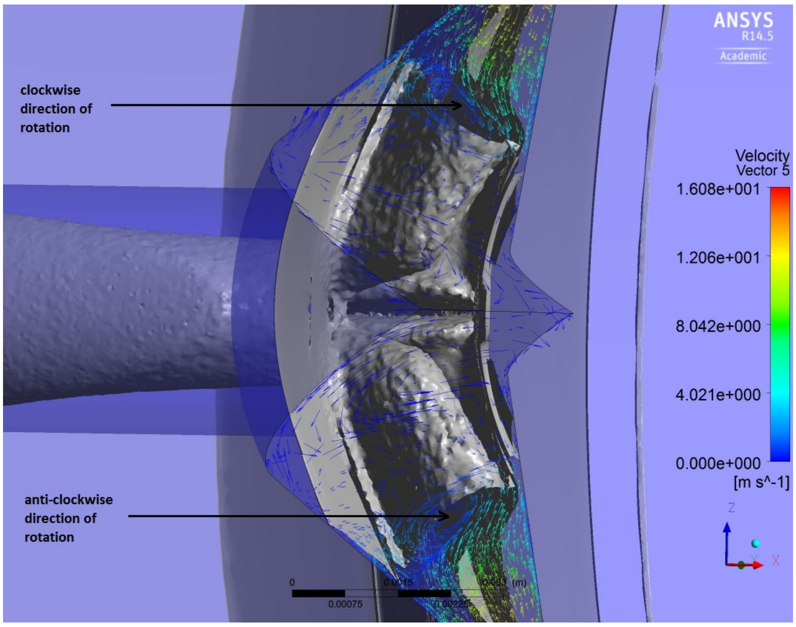
ANSYS
R14.5
Academic
clockwise
direction of
rotation
anti-clockwise
direction of
rotation
Velocity
Vector 5
1.608e+001
1.206e+001
8.042e+000
4.021e+000
0.000e+000
[m s^-1]
0
0.0015
0.003 (m)
0.00075
0.00225
Z
X

Figure 6.32: Bottom view of the injector. The isosurface of vorticity magnitude (0.5% of the magnitude) showing the probability of occurrence of vortices in the injector hole. Velocity vectors have been plotted on the front periodic interface from which ‘hole-to-hole’ vortex appears to be in the clockwise direction of rotation. Velocity vectors have also been plotted on the back side (bottom of the image) of the periodic interface from which ‘hole-to-hole’ connecting vortex appears to be in the counter-clockwise direction of rotation.

To investigate the presence of vortices, the isosurface of vorticity magnitude (0.5% of the magnitude) has been generated to detect vortices. The isosurface likewise in the nominal lift cases § 6.3.2 indicate the presence of the ‘hole-to-hole’ connecting vortex (Figure 6.31 and 6.32) and ‘counter-rotating’ vortices emerging from the needle wall and entering the injector hole (6.33).

Vectors plotted on both faces of the periodic interface (Figure 6.32 and 6.34) and on the plane which lies in the annular space between needle wall and injector hole in Figure 6.34 further confirms the presence of 'hole-to-hole' connecting vortex and 'counter-rotating' vortices emerging from the needle wall and entering the injector hole.

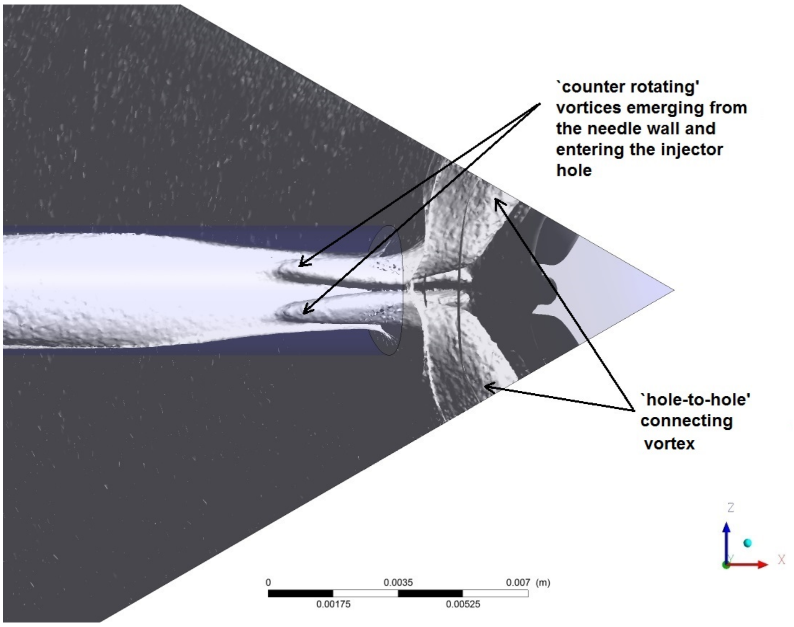
`counter rotating' vortices emerging from the needle wall and entering the injector hole
`hole-to-hole' connecting vortex
Z
X
0
0.0035
0.007 (m)
0.00175
0.00525

Figure 6.33: Bottom view of the injector. Isosurface of vorticity magnitude (0.5% of the magnitude) with the front face removed indicates the probability of occurrence of 'hole-to-hole' connecting vortex and 'counter-rotating' vortices emerging from the needle wall and entering the injector hole'.

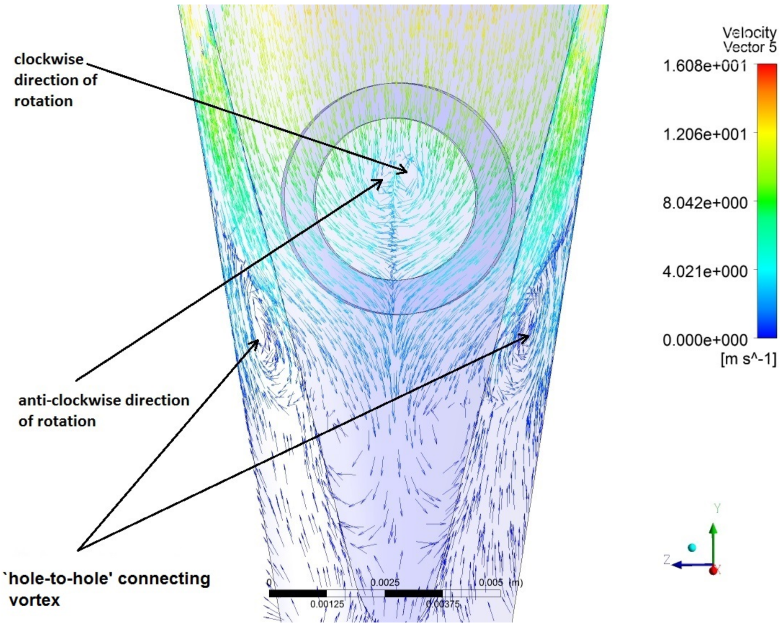

Figure 6.34: A view of the nozzle from the centre. Vectors plotted on plane 4 as well as on both the periodic faces. Vectors indicate the different direction of vortices which emerging from the needle wall and entering the injector hole. Vectors also indicate a presence of 'hole-to-hole' connecting vortex.

6.4.1.3 Discussions:

- Reasonable agreements with the experimental data have been achieved for the mean axial velocity and RMS velocity at the plane 9.5 mm and the 10.5 mm.
- The mean axial velocity is underpredicted at the planes x = 13.5 mm and 16.5 mm. The RMS velocity predictions have achieved a reasonable agreement with experimental data.
- The underprediction of the mean axial velocity at the planes x = 13.5 mm and 16.5 mm indicates the underprediction of vapour volume fraction. However, neither quantitative and qualitative data are available for vapour volume fraction in literature review hence comparison and model assessment for vapour volume could not be performed. Also, differences between the experimental data and the predicted mean axial velocity could be due to a possible needle eccentricity as mentioned by Giannadakis et al. (2008).
- Contours and isosurface of the vapour volume fraction indicated the predicted cavitation ‘onset’ at the upper edge of the entrance of the injector hole.
- Isosurface of vorticity magnitude has indicated the presence of ‘hole-to-hole’ connecting vortex and ‘counter-rotating’ vortices emerging from the needle wall and entering the injector hole facing it.

6.5 Case study 3: influence of viscosity and density on cavitation

The objective of this study (subsection) is to perform a parametric study to investigate the influence of higher viscosity and density on cavitation which is attributed to biodiesel fuel (Sheehan et al., 1998; Knothe et al., 2005). The influence of physical properties would parametrically be investigated. The viscosity and density of vapour and liquid would be parametrically increased by 20% to identify the influence of such individual properties on cavitation.

6.5.0.1 Case setup

Operating conditions as described for case 2 in table 6.1 for nominal needle lift (6 mm) are simulated. Steady state simulations are performed. The same grid as § 6.3.2 has been used. Same physical models are used with same models parameters are used as in § 6.3.2 and § 6.4.1 (see Table 6.5). Four sets of simulations have been performed. In the first simulation, only the viscosity of vapour phase is increased (by 20%), the viscosity of liquid and density of liquid and vapour are unchanged. In the second simulation, the viscosities of both liquid and vapour phase are increased by 20% and while the density of both phases is unchanged. In the third simulation the density of vapour phase is also increased by 20% with a viscosity of liquid and vapour, only the density of the liquid is unchanged. In the fourth simulation the viscosity of both phase has been increased by 20% and the density of both phases is also increased by 20% (see Table 6.8 for details). The simulation from § 6.3.2 at CN = 1.48 is used as a reference case, hence, the same boundary conditions are used as for case with CN =1.48 (see Table 6.6).

Since it has been realised in § 6.3.2 that the liquid compressibility has an insignificant impact to the flow field for this cavitation number ($CN = 1.48$) and for this particular case (20X enlarged Bosch multi-hole (6) axisymmetrical fuel injector), hence the liquid has been assumed incompressible. The ideal gas model has been used for the vapour compressibility is based on a parameter molecular weight, hence in order to increase the density of the vapour, molecular weight has been increasing by 20%.

Case	CN	p_{inj}	p_{back}	p_v	ρ_l	$\rho_v^{\dagger}$	μ_l	$\mu_v^{\ddagger}$
		bar	bar	$N\ m^{-2}$	$kg\ m^{-3}$	$kg\ m^{-3}$	$kg\ m^{-1}s^{-1}$	$kg\ m^{-1}s^{-1}$
1*	1.48	3.00	1.27	1000	895	0.054	1.4678×10^{-3}	1.55×10^{-5}
1	1.48	3.00	1.27	1000	895	0.054	1.4678×10^{-3}	1.86×10^{-5}
2	1.48	3.00	1.27	1000	895	0.054	1.76×10^{-3}	1.86×10^{-5}
3	1.48	3.00	1.27	1000	895	0.0648	1.76×10^{-3}	1.86×10^{-5}
4	1.48	3.00	1.27	1000	1074	0.0648	1.76×10^{-3}	1.86×10^{-5}
		(absolute)	(absolute)	(absolute)				

* The case from § 6.3.2 at $CN = 1.48$ has been used as a reference case.

† Ideal gas law has been used to calculate vapour density.

‡ The viscosity of vapour has been calculated using model proposed by Lee et al. (1966).

Table 6.8: Case setup for the parametric study to check influence of viscosity and density on cavitation.

6.5.0.2 Results:

The results for predicted vapour volume fraction at the $x - y$ plane are presented in Figure 6.35 (a), (c), (d), (e) and (f). On comparing predicted vapour volume fraction contours of Case 1* (Figure 6.35 (a)) and Case 1 (Figure 6.35 (c)), it can be seen that an increase in the vapour molecular viscosity (by 20%) has insignificantly influenced vapour volume fraction. But on comparing contours of the vapour volume fraction of Case 1* (Figure 6.35 (a)) and Case 2 (Figure 6.35 (d)) in which the molecular viscosity of both liquid and vapour are increased, it can be seen that the vapour volume fraction is slightly suppressed. This is because the increase of viscosity has increased the flow resistance and therefore has decreased the velocity (see Figure 6.40 (a) and (d)). This has reduced the size of the recirculation region at the upper edge of the entrance of the injector hole and the saturated pressure region at the same location (Figure 6.41 (a) and (b)). Therefore has resulted in the suppression of the cavitation region.

On further comparing vapour volume fraction of Case 1*, 1, 2 and 3 (Figure 6.35 (a), (c), (d) and (e)) it can be seen that an increase in the vapour density (by 20%) has insignificantly affected the shape and size of vapour volume fraction because the mixture density remains unchanged (Figure 6.38 (d)). However, when the liquid density is increased by 20% (Figure 6.38 (f)) the vapour volume fraction was significantly reduced (Figure 6.35 (f) and 6.36 (f)). The increase of density at the same mass flow rate[2] has resulted in the reduction of velocity (Figure 6.40 (f)) and therefore has reduced the size of recirculation region at the upper edge of the entrance of the injector hole. This has resulted in the prediction of the smaller saturated pressure region (Figure 6.39 (f)) and cavitation region at the same location. The predicted results are in agreement with the experimental results of Suh et al. (2008); Nouri et al. (2012) who showed that 'onset' of cavitation occurs at higher cavitation number for fluids with higher viscosity and density and the previous CFD simulations of Som et al. (2010); Salvador et al. (2011); Battistoni and Grimaldi (2012); Mohan et al. (2014) have also shown suppression of cavitation for biodiesel fuel. From the predicted results, it can be inferred that cavitation suppression occurred because of the increase of liquid viscosity and density.

---

[2] It has to be noted that for present case constant mass flow rate is boundary condition inlet.

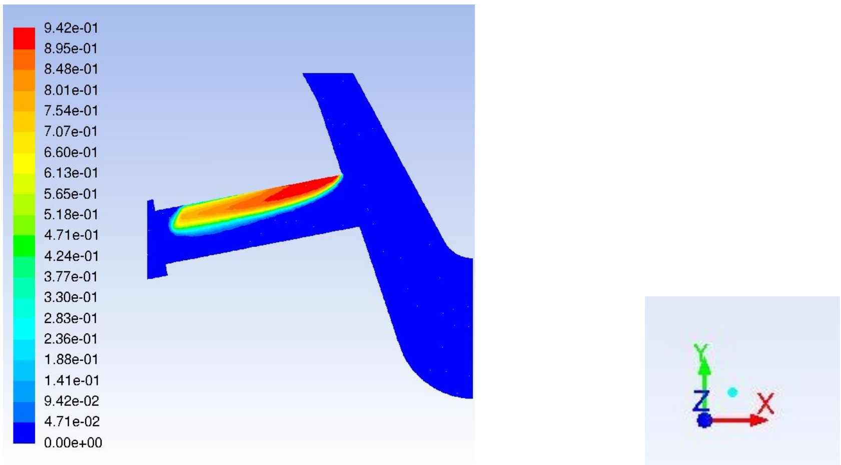

(a) Case 1*
(b) coordinates $(+x, +y, +z)$

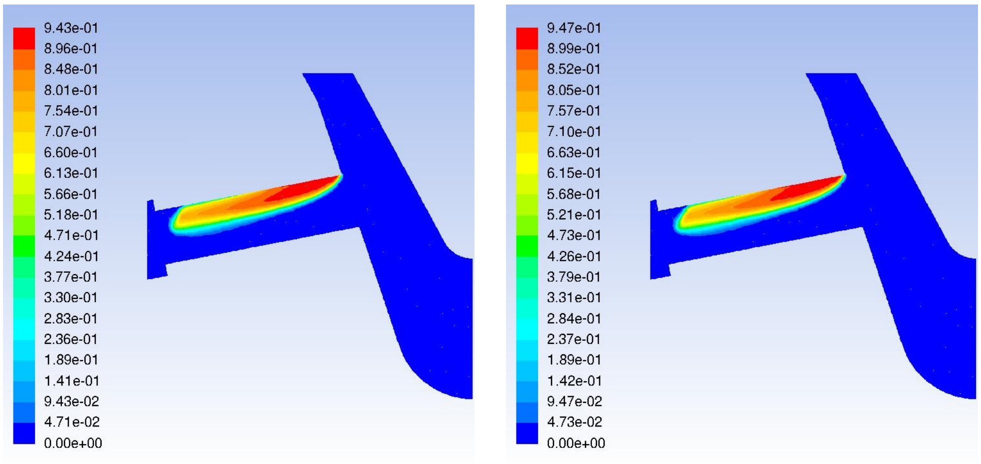

(c) Case 1
(d) Case 2

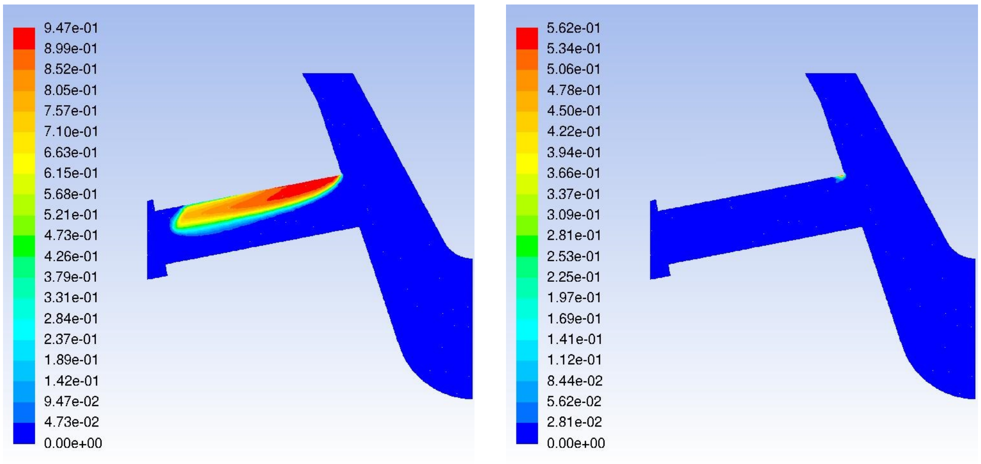

(e) Case 3
(f) Case 4

Figure 6.35: The array of images showing the predicted vapour volume fraction of cases simulated for parametric study. Case 1*: Reference the case (see the case at $CN = 1.48$ in § 6.3.2), Case 1: Viscosity of vapour increased by 20%, Case 2: Viscosity of liquid and vapour increased by 20%, Case 3: Viscosity of liquid and vapour increased by 20% and density of vapour increased by 20%, Case 4: Viscosity and density of both phases are increased by 20%.

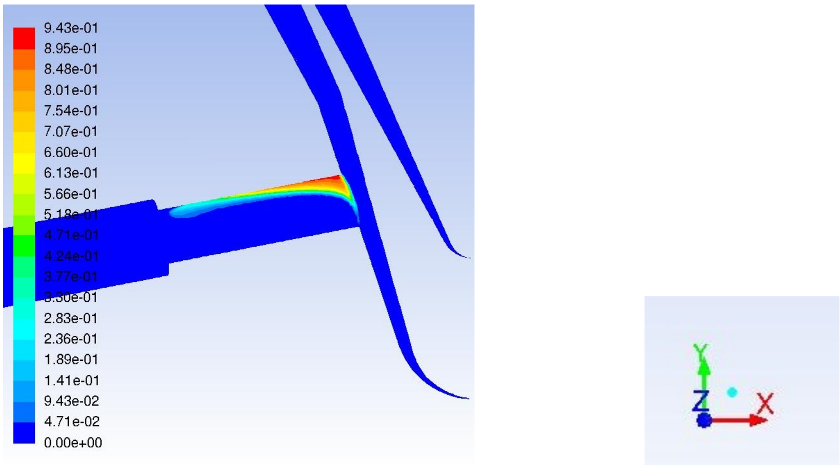

(a) Case 1* (b) coordinates $(+x, +y, +z)$

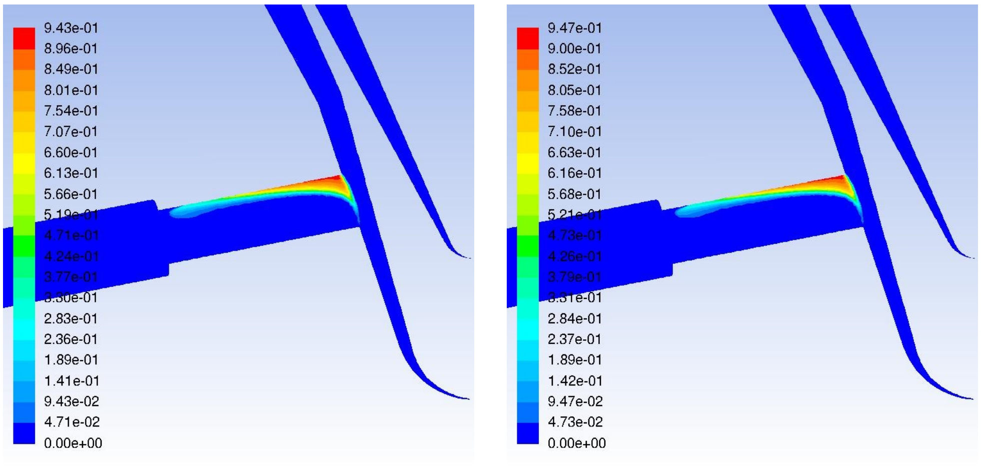

(c) Case 1 (d) Case 2

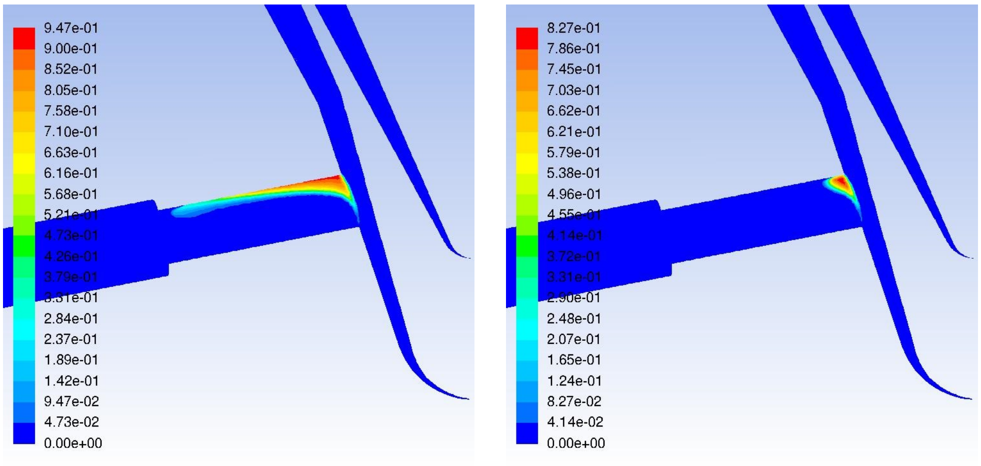

(e) Case 3 (f) Case 4

Figure 6.36: The array of images showingthe predicted vapour volume fraction of cases simulated for parametric study on the nozzle wall. Case 1*: Reference case (see the case at $CN = 1.48$ in § 6.3.2), Case 1: Viscosity of vapour increased by 20%, Case 2: Viscosity of liquid and vapour increased by 20%, Case 3: Viscosity of liquid and vapour increased by 20% and density of vapour increased by 20%, Case 4: Viscosity and density of both phases are increased by 20%.

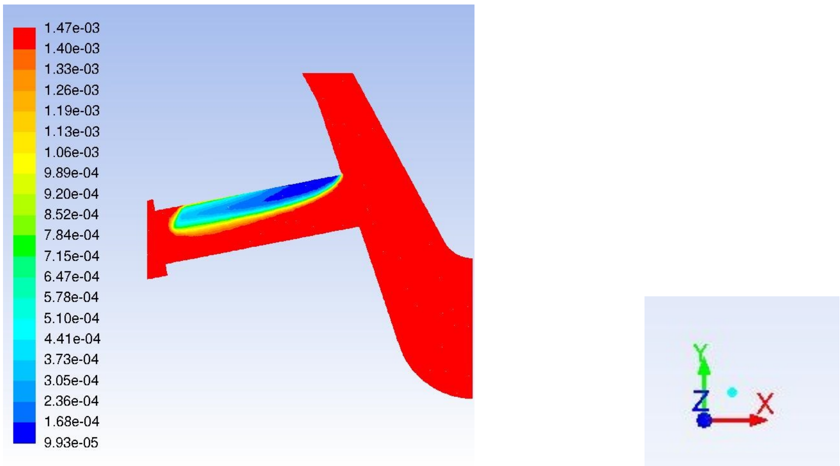

(a) Case 1* (b) coordinates $(+x, +y, +z)$

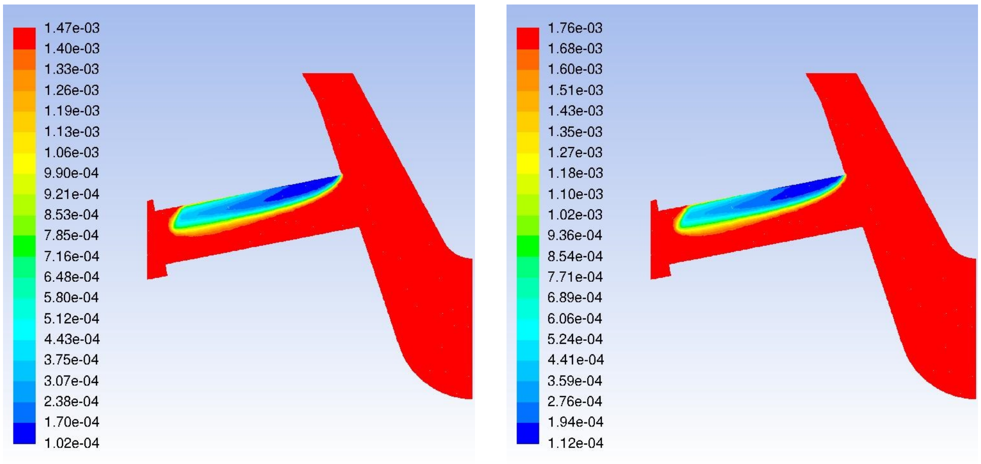

(c) Case 1 (d) Case 2

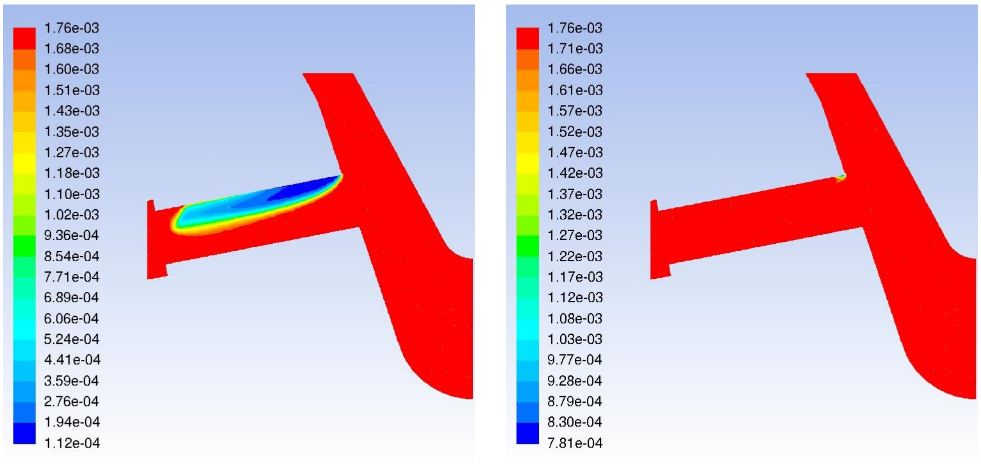

(e) Case 3 (f) Case 4

Figure 6.37: The array of images showing the predicted viscosity of cases simulated for parametric study. Case 1*: Reference case (see the case at $CN = 1.48$ in § 6.3.2), Case 1: Viscosity of vapour increased by 20%, Case 2: Viscosity of liquid and vapour increased by 20%, Case 3: Viscosity of liquid and vapour increased by 20% and density of vapour increased by 20%, Case 4: Viscosity and density of both phases are increased by 20%.

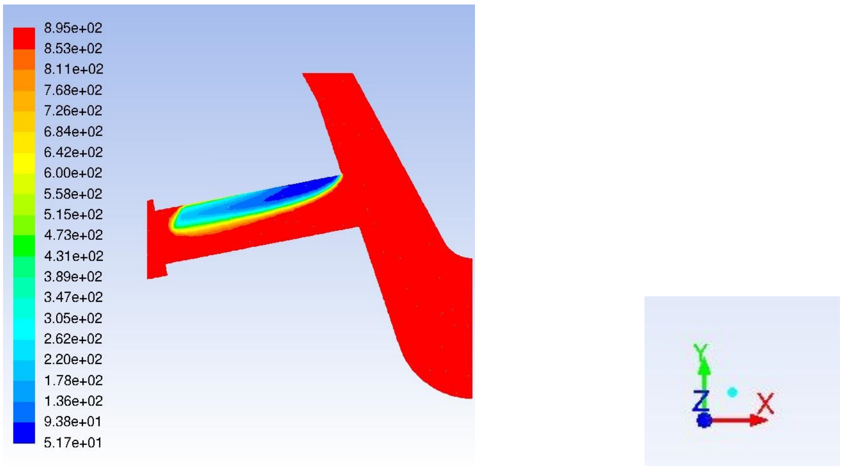

(a) Case 1* (b) coordinates $(+x, +y, +z)$

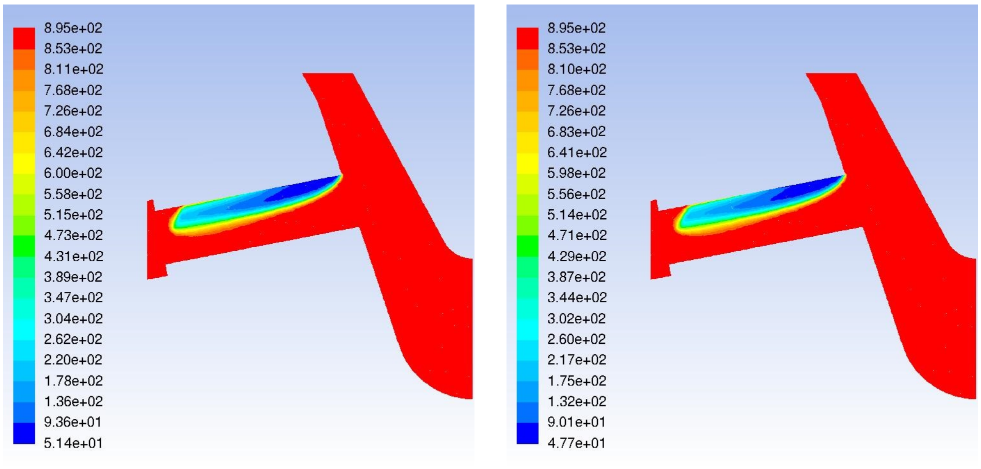

(c) Case 1 (d) Case 2

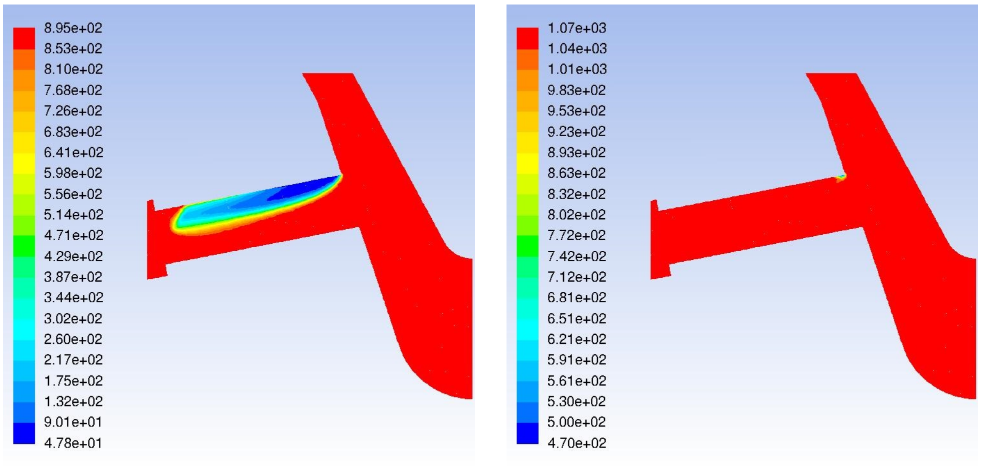

(e) Case 3 (f) Case 4

Figure 6.38: The array of images showing the predicted density of cases simulated for parametric study. Case 1*: Reference case (see the case at $CN = 1.48$ in § 6.3.2), Case 1: Viscosity of vapour increased by 20%, Case 2: Viscosity of liquid and vapour increased by 20%, Case 3: Viscosity of liquid and vapour increased by 20% and density of vapour increased by 20%, Case 4: Viscosity and density of both phases are increased by 20%.

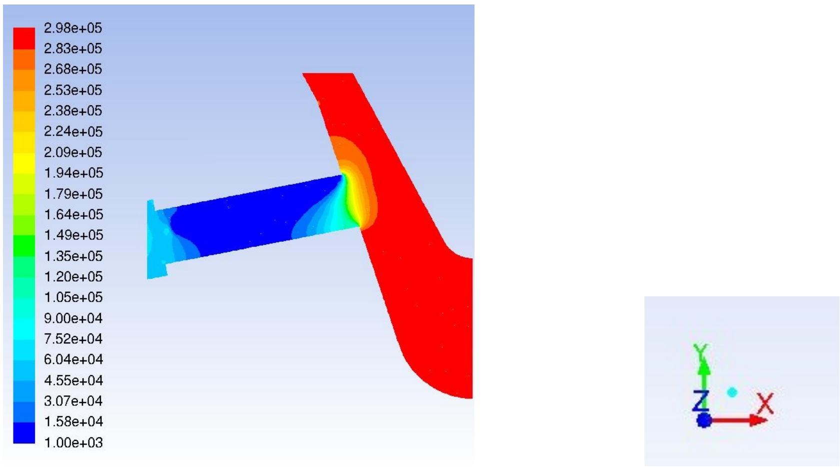

(a) Case 1* (b) coordinates $(+x, +y, +z)$

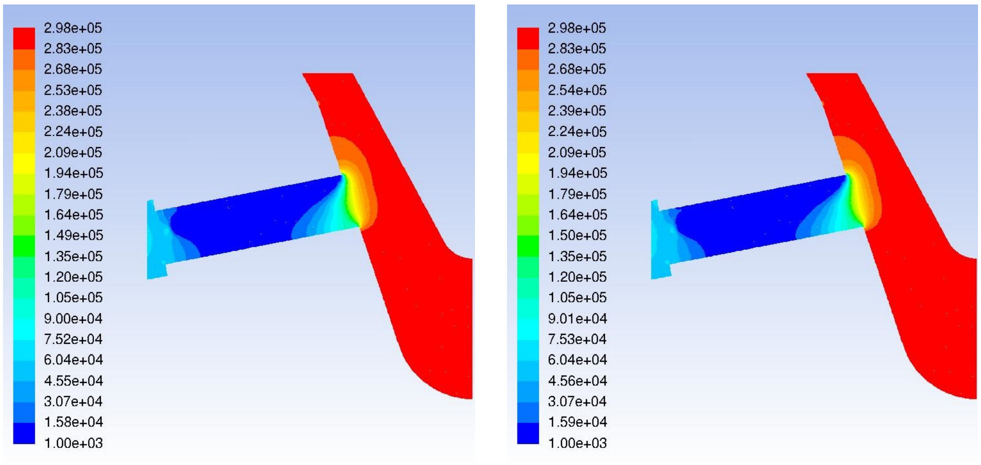

(c) Case 1 (d) Case 2

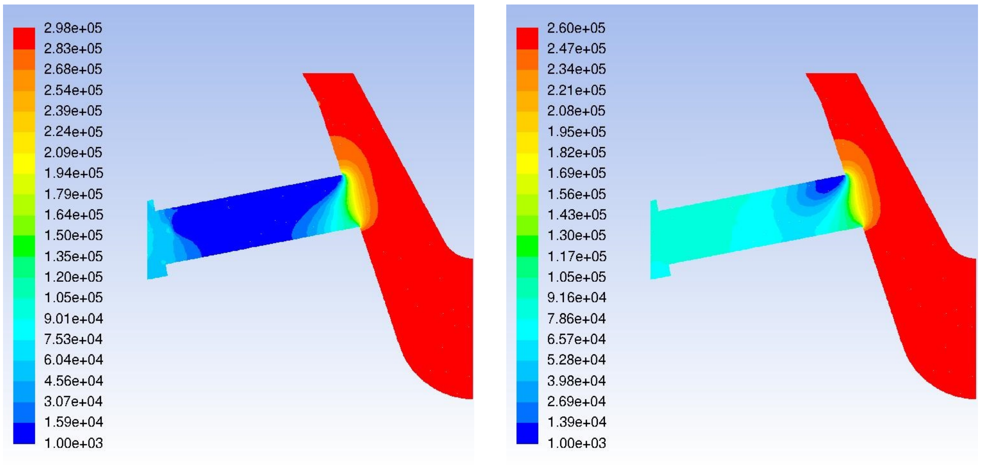

(e) Case 3 (f) Case 4

Figure 6.39: The array of images showing the predicted absolute pressure of cases simulated for parametric study. Case 1*: Reference case (see the case at $CN = 1.48$ in § 6.3.2), Case 1: Viscosity of vapour increased by 20%, Case 2: Viscosity of liquid and vapour increased by 20%, Case 3: Viscosity of liquid and vapour increased by 20% and density of vapour increased by 20%, Case 4: Viscosity and density of both phases are increased by 20%.

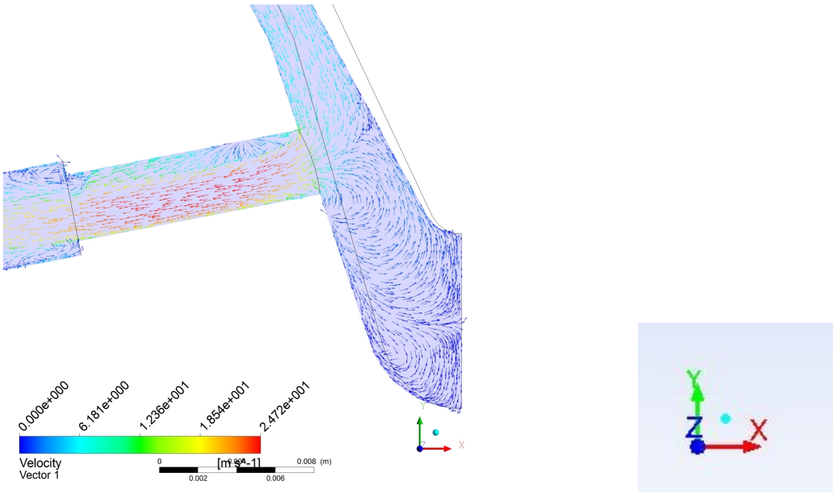

(a) Case 1*

(b) coordinates $(+x, +y, +z)$

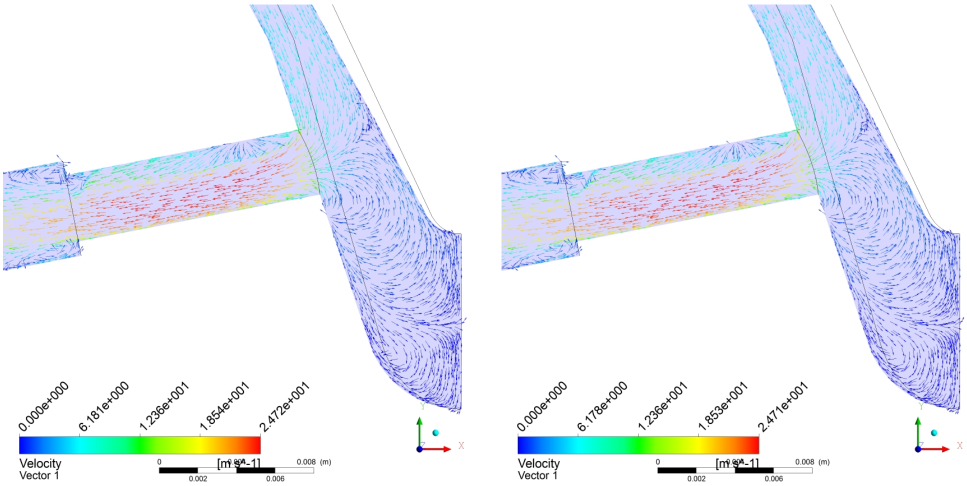

(c) Case 1

(d) Case 2

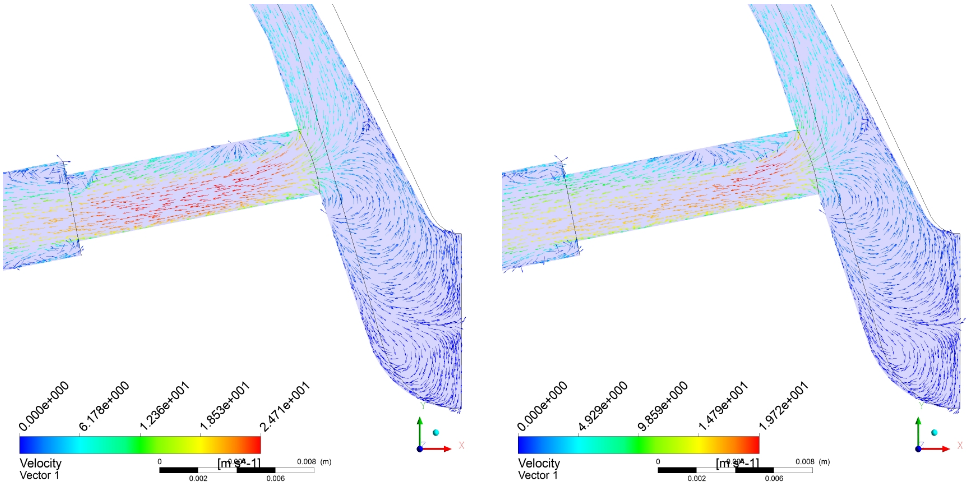

(e) Case 3

(f) Case 4

Figure 6.40: The array of images showing the predicted velocity of cases simulated for parametric study. Case 1*: Reference case (see the case at $CN = 1.48$ in § 6.3.2), Case 1: Viscosity of vapour increased by 20%, Case 2: Viscosity of liquid and vapour increased by 20%, Case 3: Viscosity of liquid and vapour increased by 20% and density of vapour increased by 20%, Case 4: Viscosity and density of both phases are increased by 20%.

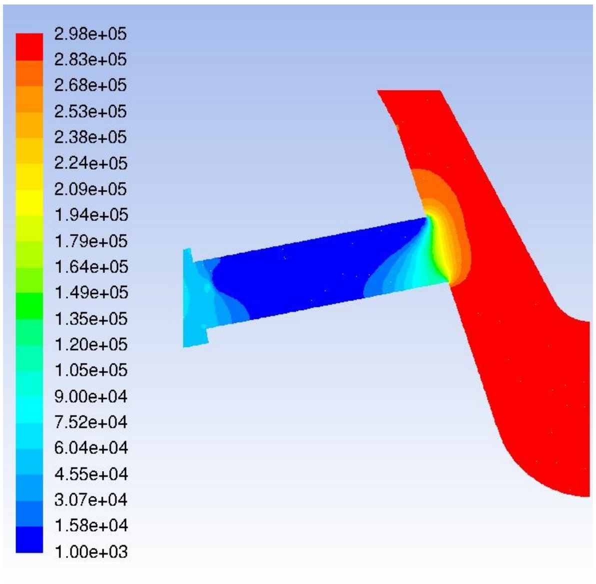

(a) Case 1^*

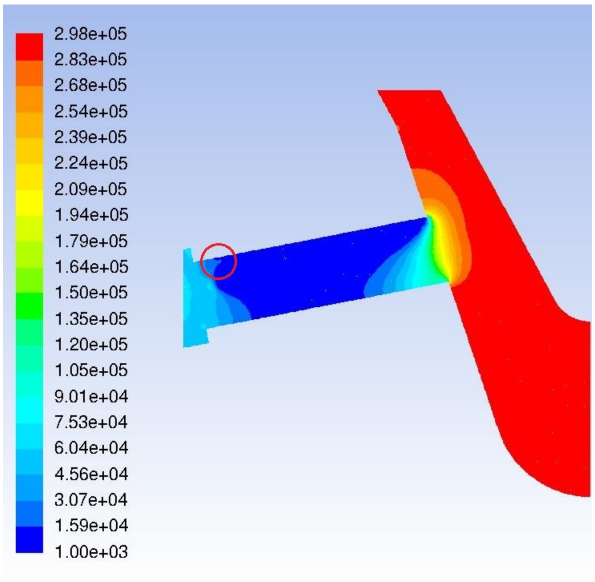

(b) Case 2

Figure 6.41: Zoom of the predicted pressure in sac region for case 1^* and case 2. Comparison of pressure field for case 1 and 2 indicate a very small reduction of lower pressure region for case 2 with an increase of viscosity indicated using a red circle.

6.5.0.3 Discussions:

- The increase in the liquid properties (viscosity and density) have resulted in suppression of cavitation. Insignificant influence on cavitation has been observed when the vapour properties were changed.

6.6 Summary:

6.6.1 Nominal needle lift

- Fairly accurate results are achieved for the mean axial velocity at both $CN = 4.57$ and 1.48. The RMS velocity results also indicate reasonable agreements with the experimental data.
- Qualitative comparison with the experimental data (CCD still images) indicate similar shape of the vapour volume fraction.
- Contours and isosurface of vapour volume indicate cavitation generated at the upper edge of the injector hole. In higher cavitation number case, $CN = 4.57$ additional cavitation being generated at the backflow hole has been predicted.
- Flow field analysis indicates the presence of 'hole-to-hole' vortices and 'counter-rotating' vortices emerging from the needle wall and entering the injector hole facing it.

6.6.2 Low needle lift

- Reasonable agreements have been achieved for the mean axial velocity and RMS velocity at the planes x = 9.5 mm and 10.5 mm.
- The mean axial velocity is underpredicted at the planes x = 13.5 mm and 16.5 mm. The underprediction of mean axial velocity at the planes x = 13.5 mm and 16.5 mm indicates the underprediction of vapour volume fraction or can be associated with a possible needle eccentricity.
- Contours and isosurface of the vapour volume fraction indicated the predicted cavitation 'onset' at the upper edge of the entrance of the injector hole.
- Isosurface of vorticity magnitude has indicated the presence of 'hole-to-hole' connecting vortex and 'counter-rotating' vortices emerging from the needle wall and entering the injector hole facing it.

6.6.3 Influence of viscosity and density on cavitation

- The increase of liquid density and liquid viscosity have resulted in the suppression of cavitation.

Chapter 7

Conclusions and recommendations for future works:

The present chapter is divided into two sections. In the first section conclusions from this work is presented. In the second section, suggestions for future works are outlined.

7.1 Conclusions

7.1.1 Single phase simulations in an enlarged multi-hole injector

In chapter 4, single-phase simulations of the enlarged mini-sac type multi-hole (6) injectors are presented. Single phase simulations were performed in the enlarged mini-sac type multi-hole injector operating at non-cavitating conditions on the steady state test rig. Impacts of boundary condition errors, numerical errors and physical modelling errors are assessed. Flow field analysis is also presented.

- In boundary conditions errors analysis, impacts on the predicted results are shown when a periodic type boundary condition is introduced instead of the complete fluid domain for the enlarged symmetric multi-hole fuel injector. Operating condition similar to steady state test rig at nominal needle lift (6.00 mm) at CN = 0.45, Re = 21000 and volumetric flow rate = 0.568 ls^{-1} was simulated. The errors were assessed by comparing the mean axial velocity results of both cases at different axial locations in the injector holes. From the predicted results, similar mean axial velocity profiles were obtained using one-sixth of the fluid domain with the periodic boundary conditions and the complete flow domain. Hence, it was inferred that impacts of errors were insignificant using one-sixth of the fluid domain with the periodic boundary conditions.
- Numerical errors were assessed by checking the influence of grid density in the fluid domain on simulations results. Simulations were performed at both lower needle lift (CN = 0.44, Re = 18000 and volumetric flow rate = 0.487 ls^{-1}) and nominal lift (CN = 0.45, Re = 21000 and volumetric flow rate = 0.568 ls^{-1}) at non-cavitating operating conditions.

Starting from a relatively coarse grid, the numbers of control volumes were successively increased until similar results were achieved for the mean axial velocity at both lower (1.6 mm) and nominal (6.0 mm) needle-lift. Additionally, the RMS velocity results between the successive grids were also compared. The Results suggested that grid independence is being approached for the mean axial velocity for both lower (1.6 mm) and nominal (6.0 mm) needle-lift cases. The RMS velocity magnitude results increased with the successive grid refinement. This is because the RMS velocity magnitude is dependent on the mean velocity gradients which are more sensitive to successive grid refinements.

- Physical modelling errors were assessed by checking the influences of 'turbulence models' used and 'near wall modelling' approaches used. Two turbulence models; the 'standard k-ϵ' and 'realizable k-ϵ' were evaluated. Simulations were performed at lower needle lift operating condition at $CN = 0.44$, $Re = 18000$ and volumetric flow rate $= 0.487\ ls^{-1}$. Results were assessed by comparing the mean axial velocity and RMS at different axial locations with that of experiment (Roth et al., 2002; Roth, 2004). Comparisons showed more accurate results for both the mean axial velocity and RMS velocity were obtained using the 'realizable k-ϵ' model.

- Two near-wall modelling approaches were assessed. They are 1) Launder and Spalding wall functions' (Launder and Spalding, 1974) and 2) 'Enhanced wall treatment' method. Simulations were again performed at lower needle lift operating conditions at $CN = 0.44$, $Re = 18000$ and volumetric flow rate $= 0.487\ ls^{-1}$. Results were again assessed by comparison of the predicted mean axial velocity with the experimental LDV data (Roth et al., 2002; Roth, 2004). The comparisons showed that better agreements with the LDV measurements were achieved using the 'enhanced wall treatment' method.

- After achieving reasonable agreements with the experimental data, flow field analysis was performed for both the lower and nominal needle lift cases. Isosurface of vorticity magnitude (0.5% of the magnitude) showed vortices in the region between the sac volume and injector holes of the injector. Two types of vortical structures were detected; The 'hole-to-hole' connecting vortex which was predicted entering the injector hole and in the annular volume between the successive injector holes. The predicted 'Hole-to-hole' connecting vortex structure had a noticeable resemblance to the 'hole-to-hole' connecting string type cavitation as observed by Arcoumanis et al. (1999); Afzal et al. (1999); Roth et al. (2002); Roth (2004) (Figure 2.7 (a)) and therefore, can be viewed as the prerequisite for the 'hole-to-hole' connecting string cavitation. Isosurface of vorticity magnitude (0.5% of the magnitude) also showed the 'counter-rotating' vortices emerging from the needle wall and entering the injector hole facing it. These vortices resemble 'needle cavitation' or 'needle cavitation' structure emerging from the needle wall and entering the injector hole facing it as observed by Arcoumanis et al. (2001); Roth et al. (2002); Roth (2004) (see Figure 2.7 (b)) and therefore, can be viewed as a prerequisite for 'needle cavitation'. According to the author's knowledge, these 'counter-rotating' vortices emerging from the needle wall and entering the injector hole have been detected for the first time for mini-sac type multi-hole (6) injector and their previous reference is not available in the literature review. The details of formation and development of such vortices are described in section § 4.7.1.1 and § 4.7.1.2 at the low needle lift and section § 4.7.2 at the nominal needle lift.

7.1.2 Cavitation simulations in a single hole injector

In this chapter simulation results of the single-hole injector are presented. All simulations were performed in the single-hole injector operating at cavitating condition, $CN = 11.2$ and $Re = 1.58 \times 10^4$ and volumetric flow rate $\approx 26.8\ lh^{-1}$ or $0.008\ ls^{-1}$ on the steady state test rig. The objective of this chapter was to evaluate and tune different approaches in order to predict cavitation in the single-hole fuel injector nozzle that can also be applied to multi-hole nozzles. Influence of numerical errors and physical modelling errors were assessed. Simulation results were assessed by quantitative and qualitative comparison with the experimental data (Duke et al., 2013a).

- Numerical errors were assessed by checking the influence of computational mesh density in fluid domain. Grid density was successively increased until similar results were achieved for the mean axial velocity and vapour volume fractions (vapour quantity). Results showed grid independence being approached so, therefore, the penultimate refined grid was used for further simulations.

- Physical modelling errors were assessed by checking the influence of turbulence models, cavitation model including the cavitation model parameters and influence of compressibility on cavitation results. Results were assessed and verified by comparing with qualitative and the quantitative experimental data of Duke et al. (2013a).

- To check the influence of the turbulence models simulations were performed using following turbulence models: Standard $k - \epsilon$ (see Launder and Spalding, 1972), Realizable $k - \epsilon$ (Shih et al., 1994), Launder and Sharma $k - \epsilon$ (Launder and Sharma, 1974) and SST $k - \omega$ (Menter, 1994). The Enhanced wall treatment method was used for near wall modelling with the standard $k - \epsilon$ and realizable $k - \epsilon$ turbulence models. The Launder and Sharma $k - \epsilon$ (Launder and Sharma, 1974) and SST $k - \omega$ (Menter, 1994) models resolve turbulence in the near wall region hence do not require wall functions. The vapour phase and liquid phase were considered incompressible. The cavitation model used was ZGB (Zwart et al., 2004). The prediction results were assessed by quantitatively and qualitatively comparing the predicted vapour volume fraction with experimental data. The best qualitative agreement was achieved using the standard $k - \epsilon$ model, and the best quantitative agreement was obtained using the realizable $k - \epsilon$ model. The analysis also showed that the diffusion between phases was dependent on the magnitude of turbulent viscosity. The highest diffusion was predicted between the liquid and the vapour phases in the standard $k - \epsilon$ due to the highest predicted turbulent viscosity by the standard $k - \epsilon$ and the lowest between both phases in SST $k - \omega$ model due to the lowest predicted turbulent viscosity by the SST $k - \omega$ model.

- Two cavitation models were assessed, SS (Schnerr and Sauer, 2001) and ZGB (Zwart et al., 2004). The vapour phase and liquid phase were considered as incompressible. Since the best quantitative agreements with experimental data was obtained using the realizable $k - \epsilon$ model; hence, the realizable $k - \epsilon$ was used for the turbulence modelling. The Enhanced wall treatment method was used for near wall modelling. The quantitative comparison with experimental data showed good agreements for vapour volume fraction using the SS model; the vapour volume fraction was overpredicted using the ZGB model. The qualitative comparison with experimental data also showed that higher vapour volume fraction is predicted using the ZGB model: however results revealed that both models failed to predict vapour at the nozzle centre line. The higher vapour predicted using the ZGB model can be attributed to higher initial values of evaporation rate and lower overall value of the condensation rate than the SS model.

- Both cavitation models (ZGB and SS) contain parameters which account for liquid quality (the presence of dissolved gases, minute particles and gas-vapour nuclei). Hence, simulations were performed by varying the model parameters. The vapour phase and liquid phase were again considered incompressible. The results showed the vapour quantity can be varied by changing model parameters using both models.
- Influence of compressibility on cavitation was assessed. Vapour was modelled using the ideal gas law and the liquid compressibility was modelled using the Tait equation (Tait, 1888; Dymond and Malhotra, 1988). For turbulence modelling, the realizable $k-\epsilon$ was used with the 'enhanced wall treatment' method to resolve near wall turbulence. Both ZGB and SS models were used; however, the results obtained using the SS model were non-physical which can be attributed to the nature of model equations (nonlinear evaporation and condensation rate terms). Hence, results of only ZGB model were presented. The main key findings were:
    - Vapour compressibility assumptions using the ideal gas resulted in a higher vapour predictions due to the variation of vapour density with respect to the change in local pressure. This allowed vapour's volume to change with respect to the change in the local pressure. Hence, the vapour volume expanded as pressure decreased.
    - Results were also in better agreements when the vapour compressibility was considered.
    - It was found that the influence of liquid compressibility on cavitation results was insignificant.
    - When vapour is assumed to be compressible, the predicted results suggests that vapour is generated at the sharp orifice entrance. As the fluid travels further downstream, the vapour separates from the wall and convects to the liquid core around the axis a few diameters downstream of the nozzle.
    - When vapour is assumed to be incompressible, the predicted results show that vapour is generated at the sharp entrance of the orifice and remained in the vicinity of the wall.
    - When the ideal gas law was used to model the vapour compressibility, the pressure profile on the nozzle axis indicated a normal shockwave just downstream of the cavitation region.

  - In this study, the Wallis (1969) model was used to compute the sonic speed in liquid-vapour mixture and has obtained a very low sonic speed (1.72 m/s) in the liquid-vapour mixture (cavitation region). Therefore, the local flow velocity in the liquid-vapour mixture became supersonic. However, just downstream of the cavitation region, the fluid re-attained sonic speed of the liquid and thus became subsonic. This has resulted in the prediction of the normal shock wave.

7.1.3 Cavitation simulations in an enlarged multi-hole enlarged injector

In chapter 6, simulation results of the enlarged multi-hole injector have been presented. All simulations were performed in the multi-hole injector operating at cavitating conditions on steady state test rig. The Identified turbulence models and cavitation model from previous chapters were used. A parametric study was also performed to investigate the influence of viscosity and density in order to check the influences of biodiesel fuel type physical properties on cavitation.

- At the nominal needle lift (6.00 mm), simulations were performed at $CN = 1.48$, $Re = 34100$ and $CN = 4.57$, $Re = 39500$. Initially, simulations were performed at $CN = 1.48$, $Re = 34100$ and volumetric flow rate of 0.922 ls^{-1}. Grid sensitivity analysis was performed using the selected grids (grid 2 and 3) from the single-phase simulations. The mean axial velocity and RMS velocity trends were similar to those of single-phase simulations. The vapour volume fraction results did not show a significant improvement, with an increase of grid refinement. Hence, the grid 2 from the single-phase simulation were used. Three simulations were performed; in the first simulation, both vapour and liquid were assumed to be incompressible. In the second simulation, vapour was assumed to be an ideal gas (compressible) and liquid to be incompressible. In the third simulation, both liquid and vapour were assumed to be compressible, vapour was assumed to be an ideal gas and the liquid compressibility was modelled using the Tait equation. Simulation results indicated the ideal gas assumption for vapour phase resulted in a slightly higher RMS velocity and cavitation volume fraction. This occurred because the ideal gas assumption allowed vapour density and volume to change on the change in local pressure. So, as vapour density decreased with the drop in pressure, its volume increased. Since it also affected the velocity field and therefore the velocity gradients, so this also resulted in variation in the magnitude of mean velocity gradients. The liquid compressibility assumption did not influence the simulation results (mean axial velocity, RMS velocity and vapour volume fraction). Nonetheless, simulations results for the mean axial velocity and RMS velocity were in reasonable agreement with the experimental data (Roth et al., 2002; Roth, 2004) for all cases. A similar simulations was also performed at $CN = 4.57$, $Re = 39500$ and the volumetric flow of 1.068 ls^{-1}, assuming vapour to be an ideal gas and the liquid to be incompressible. The mean axial velocity and RMS velocity were in the reasonable agreement with the experimental data, following which the predicted vapour volume fraction was compared with the experimental CCD images (Afzal et al., 1999) at the same cavitation number ($CN = 4.57$), which indicated reasonable qualitative agreements.
- Simulations were also performed at lower needle lift (1.60 mm) at $CN = 1.48$ $Re = 26800$

and at volumetric flow rate of 0.726 ls^{-1}. Since, the grid sensitivity study did not show a significant change in mean axial velocity, RMS velocity and the vapour volume fraction at nominal lift conditions, therefore, at lower needle lift, the grid 5 from the single-phase simulation was used. The vapour phase was assumed to be an ideal gas, and the liquid was considered to be incompressible. The predicted mean axial velocity and RMS velocity were compared with the experimental data (Roth et al., 2002; Roth, 2004) and the comparison showed that the mean axial velocity was underpredicted at axial locations at the middle and near the exit of the injector nozzle. The difference between the predicted mean axial velocity and the experimental mean axial velocity may have been due to the possible needle eccentricity as previously mentioned by Giannadakis et al. (2008). This could also be one of the reasons for the discrepancies between the first and second series of experimental data of the mean axial velocity and RMS velocity at the non-cavitating conditions. Isosurface of cavitation indicated the occurrence of cavitation at the upper edge of the inlet of the injector hole. Isosurface of vorticity indicated the presence of 'hole-to-hole' connecting vortices and 'counter-rotating' vortices emerging from the needle wall and entering the injector hole facing it.

- A parametric study to assess the influence of the increase in viscosity and density on the cavitation was performed to check the influences of biodiesel fuel physical properties on cavitation. A previously validated case at the nominal needle at $CN = 1.48$, $Re = 34100$ and volumetric flow rate = 0.922 ls^{-1} was used as a reference case. Hence, simulations were performed at similar operating conditions. Viscosity and density were increased by 20%. Four simulations were performed:

  1. In the first simulation, only the viscosity of vapour phase was increased (by 20%), the viscosity of liquid and density of liquid and vapour were unchanged. The results were compared with the reference case. The comparison showed similarities in terms of pressure, velocity and cavitation with the reference case.
  2. In the second simulation, the viscosity of both liquid and vapour phase was increased by 20% and density of both phases was unchanged. The cavitation was slightly suppressed. The increase of viscosity increased the flow resistance and therefore reduced the velocity. This caused the reduction in the size of recirculation region at the entrance of the injector hole and hence a smaller saturation pressure region was predicted which resulted in the decrease of cavitation volume.
  3. In the third simulation the density of vapour phase is also increased by 20% with a viscosity of liquid and vapour, only the density of the liquid was unchanged. No change on cavitation from the second simulation was observed
  4. In the fourth simulation viscosity of both phases was increased by 20% and the density of both phases was also increased by 20%. The increase in liquid density resulted in the further suppression of cavitation. This is because when the density of liquid increased, the velocity was reduced at the same mass flow rate which further reduced the recirculation region, therefore, reduced the saturation pressure region and the amount of cavitation.

The predicted results were in agreement with the experimental results of Suh et al. (2008); Nouri et al. (2012) who showed that the cavitation onset occurs at higher cavitation number for fluids with higher viscosity and density, also the previous CFD simulations of (Som et al., 2010; Salvador et al., 2011; Battistoni and Grimaldi, 2012; Mohan et al., 2014) have also shown suppression of cavitation for biodiesel fuel. From the predicted results it can be inferred that cavitation suppression occurred because of increase of the liquid viscosity and density.

7.2 Recommendations for future works

7.2.1 Experimental studies

In the enlarged multi-hole injector, the difference between the first and the second series of LDV (Laser Doppler Velocimetry) measurements for mean axial velocity and RMS velocity were noticed for the first time, which were not detected by the experimentalists. Also at the cavitation conditions, only one set of measurements were performed. Additionally, the possibility of needed eccentricity has also been stated by Giannadakis et al. (2008). Therefore it is highly recommended to reperform velocity measurements at non-cavitating and cavitation conditions and perform experiments in the more controlled environment. Apart from LDV, it is recommended to use micro-PIV (Particle image velocimetry) with LIF (Laser-induced fluorescence) for velocity measurements of multi-phase flows in injectors. The LIF can be used to suppress unwanted signals like those from the fluid of different refractive index i.e. vapour, therefore, it can facilitate accurate velocity measurements of the liquid phase. Advanced experimental methods like CT (X-ray computed tomography) scan or X-ray radiography can be used to quantify cavitation in multi-hole fuel injectors.

Since the present CFD simulations and as well as published work by Battistoni et al. (2014) showed a probability of shock wave in a cavitating injector, it is highly recommended to experimentally verify the possibility of shock wave in the cavitating injector. Experimental methods such as shadowgraphy can be used to visualise shock wave in the similar nozzle geometry.

7.2.2 Computational studies

In the multi-hole injectors, RANS simulations at both cavitating and non-cavitating conditions predicted complex vortices; the geometrical shape and positions of these vortices were similar to those of vortex type cavitation structures observed in the experiments in multi-hole injectors. However, RANS could not predict pressure drop accurately in the vortices to initiate cavitation. The use of more sophisticated approaches like LES which can resolve up to 80% of the energy (Pope, 2001) may probably predict lower pressure drop enough to initiate cavitation in these vortical structures. Nevertheless, the Reynolds number is adequately high at full cavitating cases, and the flow is wall bounded, so if the LES solution does not sound to be feasible, researchers may find a good compromise between the computation cost and simulation accuracy using DES (Detached Eddy Simulations).

Likewise, for the case of the multi-hole injector, the Reynolds number is adequately high in the single-hole injector, and the flow is also wall bounded; hence, methods like wall-modelled LES and DES are recommended to obtain more details of flow over RANS.

Bibliography

W. M. Achten, J. Almeida, V. Fobelets, E. Bolle, E. Mathijs, V. P. Singh, D. N. Tewari, L. V. Verchot, and B. Muys. Life cycle assessment of jatropha biodiesel as transportation fuel in rural india. *Applied Energy*, 87(12):3652–3660, 2010.

H. Afzal, C. Arcoumanis, M. Gavaises, and N. Kampanis. Internal flow in diesel injector nozzles: modelling and experiments. *IMechE Paper S*, 492:25–44, 1999.

A. K. Agarwal, D. K. Srivastava, A. Dhar, R. K. Maurya, P. C. Shukla, and A. P. Singh. Effect of fuel injection timing and pressure on combustion, emissions and performance characteristics of a single cylinder diesel engine. *Fuel*, 111:374–383, 2013.

A. Alajbegovic. Three-dimensional cavitation calculations in nozzles. In *Second Annual Meeting of the Institute for Multifluid Science and Technology, Santa Barbara, CA, March*, pages 14–18, 1999.

A. Alajbegovic, H. Grogger, and H. Philipp. Calculation of cavitation in nozzles using the two-fluid model. In *Proc. 7th Annu. Conf. Comp. Fluid Dyn. Soc. Canada, Halifax, NS, Canada (ed. J. Militzer)*, pages 7–3, 1999.

A. Alajbegovic, G. Meister, D. Greif, and B. Basara. Three phase cavitating flows in high-pressure swirl injectors. *Experimental thermal and fluid science*, 26(6):677–681, 2002.

J. D. Anderson. *Modern compressible flow: with historical perspective.* McGraw Hill Higher Education, 1990.

A. Andriotis. *Investigation of cavitation inside multi-hole injectors for large diesel engines and its effect on the near-nozzle spray Structure.* PhD thesis, City University, 2009.

C. Arcoumanis, J. Nouri, and R. Andrews. Application of refractive index matching to a diesel nozzle internal flow. Technical report, DTIC Document, 1992.

C. Arcoumanis, M. Gavaises, J. Nouri, E. Abdul-Wahab, and R. W. Horrocks. Analysis of the flow in the nozzle of a vertical multi-hole diesel engine injector. Technical report, SAE Technical Paper, 1998.

C. Arcoumanis, H. Flora, M. Gavaises, N. Kampanis, and R. Horrocks. Investigation of cavitation in a vertical multi-hole injector. Technical report, SAE Technical Paper, 1999.

C. Arcoumanis, M. Badami, H. Flora, and M. Gavaises. Cavitation in real-size multi-hole diesel injector nozzles. *SAE paper*, pages 01–1249, 2000.

C. Arcoumanis, M. Gavaises, H. Flora, and H. Roth. Visualisation of cavitation in diesel engine injectors. *Mécanique & industries*, 2(5):375–381, 2001.

O. Asi. Failure of a diesel engine injector nozzle by cavitation damage. *Engineering Failure Analysis*, 13(7):1126–1133, 2006.

ASTM. Astm international - standards worldwide. `http://www.astm.org/SNEWS/JF_2009/nelson_jf09.html`, 2009. (Accessed on 04/13/2016).

A. E. Atabani, A. S. Silitonga, I. A. Badruddin, T. Mahlia, H. Masjuki, and S. Mekhilef. A comprehensive review on biodiesel as an alternative energy resource and its characteristics. *Renewable and Sustainable Energy Reviews*, 16(4):2070–2093, 2012.

C. Baker. Banks power | diesel evolution. `http://www.bankspower.com/techarticles/show/28-Diesel-Evolution`, 2016. (Accessed on 022/2/2016).

M. Battistoni and C. N. Grimaldi. Numerical analysis of injector flow and spray characteristics from diesel injectors using fossil and biodiesel fuels. *Applied Energy*, 97:656–666, 2012.

M. Battistoni, C. Grimaldi, and F. Mariani. Coupled simulation of nozzle flow and spray formation using diesel and biodiesel for ci engine applications. Technical report, SAE Technical Paper, 2012.

M. Battistoni, S. Som, and D. E. Longman. Comparison of mixture and multifluid models for in-nozzle cavitation prediction. *Journal of Engineering for Gas Turbines and Power*, 136(6): 061506, 2014.

D. Bauer, H. Chaves, and C. Arcoumanis. Measurements of void fraction distribution in cavitating pipe flow using x-ray ct. *Measurement Science and Technology*, 23(5):055302, 2012.

W. Bergwerk. Flow pattern in diesel nozzle spray holes. *Proceedings of the Institution of Mechanical Engineers*, 173(1):655–660, 1959.

berkeleybiodiesel.org. Advantages and disadvantages of biodiesel fuel, 2015. URL `http://www.berkeleybiodiesel.org/advantages-and-disadvantages-of-biodiesel.html`. (Accessed on 03/03/2016).

M. Billet. Cavitation nuclei measurements with an optical system. *ASME JOURNAL'OF FLUIDS ENGINEERING*, 108:366–372, 1986.

M. L. Billet. Cavitation nuclei measurements-a review. In *Cavitation and multiphase flow forum-1985*, 1985.

BMW. Bmw i3 : At a glance. `http://www.bmw.com/com/en/newvehicles/i/i3/2015/showroom/index.html`, 2015. (Accessed on 04/12/2016).

A. Bonnick. *A practical approach to motor vehicle engineering and maintenance*. Routledge, 2011.

Bosch. Common rail diesel injection from bosch. `http://de.bosch-automotive.com/en/parts_and_accessories/motor_and_sytems/diesel/common_rail_injection/common_rail_diesel_motorsys_parts`, 2016a. (Accessed on 04/12/2016).

Bosch. Gasoline direct injection - fuel injection - high-pressure solenoid injector , high-pressure piezo injector , fuel rail (stainless steel) , high-pressure sensor , high-pressure pump. `http://products.bosch-mobility-solutions.com/en/de/_technik/component/PT_PC_BDI_Fuel-Injection-NEU_PT_PC_Direct-Gasoline-Injection_02_10181.html?compId=7936`, 2016b. (Accessed on 04/12/2016).

Bosch. Gasoline direct injection. `http://products.bosch-mobility-solutions.com/en/de/powertrain/powertrain_systems_for_passenger_cars_1/direct_gasoline_injection/direct_gasoline_injection_23.html`, 2016c. (Accessed on 04/11/2016).

Bosch. Bosch worldwide, 2016d. URL `http://www.bosch.com/en/com/home/index.php#`. (Accessed on 02/03/2016).

R. Bosch. Diesel distributor fuel-injection pumps. Technical report, Robert Bosch GmbH, 1999.

F. Boudy and P. Seers. Impact of physical properties of biodiesel on the injection process in a common-rail direct injection system. *Energy Conversion and Management*, 50(12):2905–2912, 2009.

R. Bray. Ford fiesta 1.0t duratec zetec ecoboost 100ps powershift - newpetrol - co2 114 g/km. `http://www.nextgreencar.com/view-car/49031/ford-fiesta-1.0t-duratec-zetec-ecoboost-100ps-powershift-petrol-automatic-6-speed/`, 2012a. (Accessed on 04/11/2016).

R. Bray. Toyota prius plug-in hybrid 1.8 vvt-i cvt - newplug-in petrol hybrid - co2 49 g/km. `http://www.nextgreencar.com/view-car/45461/toyota-prius-plug-in-hybrid-1.8-vvt-i-cvt-plug-in-petrol-hybrid-continuously-variable/`, 2012b. (Accessed on 04/11/2016).

R. Bray. Vauxhall ampera 1.4 16v vvt v6 earth ecotec e-rev auto - usedplug-in petrol hybrid - co2 27 g/km. `http://www.nextgreencar.com/view-car/45464/vauxhall-ampera-1.4-16v-vvt-v6-earth-ecotec-e-rev-auto-plug-in-petrol-hybrid-automatic/`, 2013. (Accessed on 04/12/2016).

R. Bray. Toyota prius 1.8 vvt-i active cvt - newpetrol hybrid - co2 70 g/km. `http://www.nextgreencar.com/view-car/58542/toyota-prius-1.8-vvt-i-active-cvt-petrol-hybrid-continuously-variable/`, 2016. (Accessed on 04/11/2016).

J. Bredberg. On the wall boundary condition for turbulence model. *Chalmers University of Technology, Department of Thermo and Fluid Dynamics. Internal Report 00/4. G oteborg*, 2000.

C. E. Brennen. *Cavitation and bubble dynamics*, volume 44. Oxford University Press, USA, 1995.

E. Buyukkaya. Effects of biodiesel on a di diesel engine performance, emission and combustion characteristics. *Fuel*, 89(10):3099–3105, 2010.

M. Canakci. Combustion characteristics of a turbocharged di compression ignition engine fueled with petroleum diesel fuels and biodiesel. *Bioresource technology*, 98(6):1167–1175, 2007.

C. Carraretto, A. Macor, A. Mirandola, A. Stoppato, and S. Tonon. Biodiesel as alternative fuel: experimental analysis and energetic evaluations. *Energy*, 29(12):2195–2211, 2004.

D. R. Chapman. Computational aerodynamics development and outlook. *AIAA journal*, 17(12): 1293–1313, 1979.

H. Chaves, M. Knapp, A. Kubitzek, F. Obermeier, and T. Schneider. Experimental study of cavitation in the nozzle hole of diesel injectors using transparent nozzles. *SAE paper*, 950290, 1995.

M.-S. Chung, S.-B. Park, and H.-K. Lee. Sound speed criterion for two-phase critical flow. *Journal of sound and vibration*, 276(1):13–26, 2004.

M. L. Corradini. Homogeneous equilibrium model. `http://wins.engr.wisc.edu/teaching/mpfBook/node12.html`, 1997. (Accessed on 04/19/2016).

L. Davidson et al. An introduction to turbulence models. *Department of Thermo and Fluid Dynamics, Chalmers University of Technology, Gothenburg, Sweden*, 2003.

M. P. Davis. *Experimental investigation of the cavitation of aviation fuel in a converging-diverging nozzle*. ProQuest, 2008.

L. De Nocker, C. Spirinckx, and R. Torfs. Comparison of lca and external-cost analysis for biodiesel and diesel. In *2nd International Conference LCA in Agriculture, Agro-industry and Forestry, Brussels*, pages 3–4, 1998.

A. Demirbas. Biodiesel production from vegetable oils via catalytic and non-catalytic supercritical methanol transesterification methods. *Progress in energy and combustion science*, 31(5): 466–487, 2005.

A. Demirbas. Importance of biodiesel as transportation fuel. *Energy policy*, 35(9):4661–4670, 2007.

A. Demirbas and M. F. Demirbas. Importance of algae oil as a source of biodiesel. *Energy Conversion and Management*, 52(1):163–170, 2011.

Denso. Diesel pumps - denso. `http://www.denso-am.eu/products/automotive-aftermarket/diesel-components/diesel-pumps/`, 2015. (Accessed on 021/2/2016).

J. Desantes, R. Payri, F. Salvador, and J. De la Morena. Cavitation effects on spray characteristics in the near-nozzle field. Technical report, SAE Technical Paper, 2009.

D. A. Drew and S. L. Passman. *Theory of multicomponent fluids*, volume 135. Springer Science & Business Media, 2006.

D. Duke, A. Kastengren, F. Z. Tilocco, and C. Powell. Synchrotron x-ray measurements of cavitation. In *25th Annual Conference on Liquid Atomization and Spray Systems, ILASS-Americas, Pittsburgh, PA, May*, pages 5–8, 2013a.

D. Duke, A. Kastengren, A. Swantek, N. Sovis, K. Fezzaa, K. Neroorkar, M. Moulai, C. Powell, and D. Schmidt. Comparing simulations and x-ray measurements of a cavitating nozzle. In *Proceedings of the ILASS-Americas 26th Annual Conference on Liquid Atomization and Spray Systems*, 2014.

D. J. Duke, D. P. Schmidt, K. Neroorkar, A. L. Kastengren, and C. F. Powell. High-resolution large eddy simulations of cavitating gasoline–ethanol blends. *International Journal of Engine Research*, 14(6):578–589, 2013b.

D. Durante and M. Miltenberger. Net energy balance of ethanol production. *A Publication of Ethanol Across America, October. Available at http://www. ethanol. org/pdf/contentmgmt/Issue_ Brief_ Ethanols_ Energy_ Balance. pdf (accessed May 4, 2008)*, 2004.

J. Dymond and R. Malhotra. The tait equation: 100 years on. *International journal of thermophysics*, 9(6):941–951, 1988.

A. Eisentraut, A. Brown, and L. Fulton. Technology roadmap: Biofuels for transport. *Paris Cedex, France: IEA Publishing*, 2011.

Enginebasics. What is turbo lag? turbo lag explained. `http://www.enginebasics.com/Advanced%20Engine%20Tuning/Turbo%20Lag.html`, 2010. (Accessed on 04/11/2016).

EPA. 2016 chevrolet volt. `https://www.fueleconomy.gov/feg/Find.do?action=sbs&id=36863`, 2016a. (Accessed on 04/12/2016).

EPA. Global emissions | climate change | us epa. `https://www3.epa.gov/climatechange/ghgemissions/global.html`, 2016b. (Accessed on 04/11/2016).

Eur-Lex. Eur-lex - l28186 - en - eur-lex. `http://eur-lex.europa.eu/legal-content/EN/TXT/?uri=URISERV:l28186`, 2015. (Accessed on 04/11/2016).

European-Commission. European commission - press releases - press release - commission and acea agree on co2 emissions from cars. `http://europa.eu/rapid/press-release_IP-98-734_en.htm?locale=en`, 1998. (Accessed on 04/27/2016).

European-Commission. The contribution of transport to ghg emissions | eu transport ghg: Routes to 2050. `http://www.eutransportghg2050.eu/cms/the-contribution-of-transport-to-ghg-emissions/`, 2011. (Accessed on 04/21/2016).

European-Commission. Reducing co2 emissions from passenger cars - european commission. `http://ec.europa.eu/clima/policies/transport/vehicles/cars/index_en.htm`, 2016. (Accessed on 04/27/2016).

A. Fluent. 14.5. *Theory Guide*, 117, 2012.

H. Fukuda, A. Kondo, and H. Noda. Biodiesel fuel production by transesterification of oils. *Journal of bioscience and bioengineering*, 92(5):405–416, 2001.

Y. Gao, J. Deng, C. Li, F. Dang, Z. Liao, Z. Wu, and L. Li. Experimental study of the spray characteristics of biodiesel based on inedible oil. *Biotechnology Advances*, 27(5):616–624, 2009.

M. Gavaises and E. Giannadakis. Modelling of cavitation in large scale diesel injector nozzles. In *Proc. 19th Annual Meeting of the Institute for Liquid Atomization and Spray Systems (Europe) Nottingham*, 2004.

M. Gavaises, D. Papoulias, A. Andriotis, E. Giannadakis, and A. Theodorakakos. Link between cavitation development and erosion damage in diesel injector nozzles. Technical report, SAE Technical Paper, 2007.

M. Gavaises, A. Andriotis, D. Papoulias, N. Mitroglou, and A. Theodorakakos. Characterization of string cavitation in large-scale diesel nozzles with tapered holes. *Physics of Fluids (1994-present)*, 21(5):052107, 2009.

E. Giannadakis, M. Gavaises, H. Roth, and C. Arcoumanis. Cavitation modelling in single-hole diesel injector based on eulerian-lagrangian approach. In *Proc. THIESEL International Conference on Thermo-and Fluid Dynamic Processes in Diesel Engines. Valencia, Spain*, 2004.

E. Giannadakis, D. Papoulias, M. Gavaises, C. Arcoumanis, C. Soteriou, and W. Tang. Evaluation of the predictive capability of diesel nozzle cavitation models. Technical report, SAE Technical Paper, 2007.

E. Giannadakis, M. Gavaises, and C. Arcoumanis. Modelling of cavitation in diesel injector nozzles. *Journal of Fluid Mechanics*, 616(1):153–193, 2008.

GM-Europe. A look into the future of engines and transmissions. `http://mediaassets.gmeuropearchive.info/viewcatalogue.php?catid=108560&lng=EN`, 2008. (Accessed on 04/12/2016).

A. Guide. Release 14.5, ansys. *Inc.< http://www. ansys. com*, 2012.

J. B. Guinée. Handbook on life cycle assessment operational guide to the iso standards. *The international journal of life cycle assessment*, 7(5):311–313, 2002.

C.-T. Ha, W.-G. Park, and C. L. Merkle. Multiphase flow analysis of cylinder using a new cavitation model. In *Proceedings of the 7th International Symposium on Cavitation*, 2009.

K. Hanjalic. Will rans survive les? a view of perspectives. *Journal of fluids engineering*, 127(5):831–839, 2005.

M. K. K. Hannu Jääskeläinen. Common rail fuel injection. `https://www.dieselnet.com/tech/diesel_fi_common-rail.php`, 2015. (Accessed on 021/2/2016).

T. Hayashi, M. Suzuki, and M. Ikemoto. Visualization of internal flow and spray formation with real size diesel nozzle. In *12th Triennial International Conference on Liquid Atomization and Spray Systems, ICLASS*, pages 2–6, 2012.

C. He, Y. Ge, J. Tan, and X. Han. Spray properties of alternative fuels: A comparative analysis of biodiesel and diesel. *International journal of energy research*, 32(14):1329–1338, 2008.

R. Henry, M. Grolmes, and H. K. Fauske. Pressure-pulse propagation in two-phase one-and two-component mixtures. Technical report, Argonne National Lab., Ill., 1971.

J. B. Heywood. *Internal combustion engine fundamentals*, volume 930. Mcgraw-hill New York, 1988.

C. W. Hirt and B. D. Nichols. Volume of fluid (vof) method for the dynamics of free boundaries. *Journal of computational physics*, 39(1):201–225, 1981.

Hitachi. Hitachi construction machinery. `https://www.hitachi-c-m.com/`, 2011. (Accessed on 03/03/2016).

HM-Government. Vehicle tax rate tables - gov.uk. `https://www.gov.uk/vehicle-tax-rate-tables/overview`, 2016. (Accessed on 03/21/2016).

R. Horne, T. Grant, and K. Verghese. *Life Cycle Assessment: Principles, Practice, and Prospects.* Csiro, 2009.

M. Ivings, D. Causon, and E. Toro. On riemann solvers for compressible liquids. *International Journal for Numerical Methods in Fluids*, 28(3):395–418, 1998. doi: 10.1002/(SICI) 1097-0363(19980915)28:3<395::AID-FLD718>3.0.CO;2-S.

J. M. Johnson, M. D. Coleman, R. Gesch, A. Jaradat, R. Mitchell, D. Reicosky, and W. Wilhelm. Biomass-bioenergy crops in the united states: A changing paradigm. *The Americas Journal of Plant Science and Biotechnology*, 1(1):1–28, 2007.

T. Jongen. Simulation and modeling of turbulent incompressible fluid flows. 1998.

S. Joshi, L. B. Lave, H. Maclean, and R. Lankey. A life cycle comparison of alternative transportation fuels. 2000.

B. Kader. Temperature and concentration profiles in fully turbulent boundary layers. *International Journal of Heat and Mass Transfer*, 24(9):1541–1544, 1981.

H. B. Karplus. Velocity of sound in a liquid containing gas bubbles. *The Journal of the Acoustical Society of America*, 29(11):1261–1262, 1957.

F. P. Kärrholm. *Numerical modelling of diesel spray injection, turbulence interaction and combustion.* Chalmers University of Technology, 2008.

F. P. Kärrholm, H. Weller, and N. Nordin. Modelling injector flow including cavitation effects for diesel applications. ASME, 2007.

R. T. Knapp, J. W. Daily, and F. G. Hammitt. Cavitation. 1979.

T. Knopp. On grid-independence of rans predictions for aerodynamic flows using model-consistent universal wall-functions. In *ECCOMAS CFD 2006: Proceedings of the European Conference on Computational Fluid Dynamics, Egmond aan Zee, The Netherlands, September 5-8, 2006*. Delft University of Technology; European Community on Computational Methods in Applied Sciences (ECCOMAS), 2006.

G. Knothe and K. R. Steidley. Kinematic viscosity of biodiesel fuel components and related compounds. influence of compound structure and comparison to petrodiesel fuel components. *Fuel*, 84(9):1059–1065, 2005.

G. Knothe, J. H. Van Gerpen, J. Krahl, et al. *The biodiesel handbook*, volume 1. AOCS press Champaign, IL, 2005.

G. Knothe, C. A. Sharp, and T. W. Ryan. Exhaust emissions of biodiesel, petrodiesel, neat methyl esters, and alkanes in a new technology engine. *Energy & Fuels*, 20(1):403–408, 2006.

P. K. Koukouvinis, G. Bergeles, and M. Gavaises. A new methodology for estimating cavitation erosion: Application on a high speed cavitation test rig. 2013.

B. Kovarik. Environmental history / biofuels |. `http://www.environmentalhistory.org/billkovarik/about-bk/research/cabi/`, 2013. (Accessed on 04/12/2016).

A. Kubota, H. Kato, H. Yamaguchi, et al. A new modelling of cavitating flows: A numerical study of unsteady cavitation on a hydrofoil section. *Journal of fluid Mechanics*, 240(1):59–96, 1992.

R. F. Kunz, D. A. Boger, T. S. Chyczewski, D. Stinebring, H. Gibeling, and T. Govindan. Multi-phase cfd analysis of natural and ventilated cavitation about submerged bodies. In *3rd ASME/JSME Joint Fluids Engineering Conference, San Francisco*, volume 1, page 1, 1999.

R. F. Kunz, D. A. Boger, D. R. Stinebring, T. S. Chyczewski, J. W. Lindau, H. J. Gibeling, S. Venkateswaran, and T. Govindan. A preconditioned navier–stokes method for two-phase flows with application to cavitation prediction. *Computers & Fluids*, 29(8):849–875, 2000.

R. S. Lagumbay, O. V. Vasilyev, and A. Haselbacher. Homogeneous equilibrium mixture model for simulation of multiphase/multicomponent flows. *Contract*, 4(00821):5F–00462, 2007.

B. Launder and B. Sharma. Application of the energy-dissipation model of turbulence to the calculation of flow near a spinning disc. *Letters in heat and mass transfer*, 1(2):131–137, 1974.

B. E. Launder and D. Spalding. The numerical computation of turbulent flows. *Computer methods in applied mechanics and engineering*, 3(2):269–289, 1974.

B. E. Launder and D. B. Spalding. Lectures in mathematical models of turbulence. 1972.

A. L. Lee, M. H. Gonzalez, B. E. Eakin, et al. The viscosity of natural gases. *Journal of Petroleum Technology*, 18(8):997–1000, 1966.

C. Lilly. Peugeot 208 1.6 bluehdi active 75 s&s - newdiesel - co2 79 g/km. `http://www.nextgreencar.com/view-car/55690/peugeot-208-1.6-bluehdi-active-75-s&s-diesel-manual-6-speed/`, 2016. (Accessed on 04/11/2016).

J. L. Lumley. Computational modeling of turbulent flows. *Advances in applied mechanics*, 18: 123–176, 1979.

H. L. MacLean and L. B. Lave. Peer reviewed: A life-cycle model of an automobile. *Environmental science & technology*, 32(13):322–330, 1998.

H. L. MacLean, L. B. Lave, R. Lankey, and S. Joshi. A life-cycle comparison of alternative automobile fuels. *Journal of the air & waste management association*, 50(10):1769–1779, 2000.

M. Manninen, V. Taivassalo, S. Kallio, et al. On the mixture model for multiphase flow. 1996.

S. Martynov. *Numerical simulation of the cavitation process in diesel fuel injectors*. PhD thesis, The University of Brighton, 2005.

S. Martynov, D. Mason, and M. Heikal. Numerical simulation of cavitation flows based on their hydrodynamic similarity. *International Journal of Engine Research*, 7(3):283–296, 2006.

D. McWilliam and R. Duggins. Speed of sound in bubbly liquids. In *Proceedings of the Institution of Mechanical Engineers, Conference Proceedings*, volume 184, pages 102–107. SAGE Publications Sage UK: London, England, 1969.

F. R. Menter. Two-equation eddy-viscosity turbulence models for engineering applications. *AIAA journal*, 32(8):1598–1605, 1994.

C. L. Merkle, J. Feng, and P. E. Buelow. Computational modeling of the dynamics of sheet cavitation. In *3rd International symposium on cavitation, Grenoble, France*, volume 2, pages 47–54, 1998.

M. Mirshahi, J. M. Nouri, Y. Yan, and M. Gavaises. Link between in-nozzle cavitation and jet spray in a gasoline multi-hole injector. 2013.

N. Mitroglou, J. Nouri, M. Gavaises, and C. Arcoumanis. Spray characteristics of a multi-hole injector for direct-injection gasoline engines. *International Journal of Engine Research*, 7(3): 255–270, 2006.

N. Mitroglou, M. Gavaises, J. Nouri, and C. Arcoumanis. Cavitation inside enlarged and real-size fully transparent injector nozzles and its effect on near nozzle spray formation. In *DIPSI Workshop*, 2011.

M. Mittelbach and C. Remschmidt. *Biodiesel: the comprehensive handbook*. Martin Mittelbach, 2004.

B. Mohan, W. Yang, and S. Chou. Cavitation in injector nozzle holes–a parametric study. *Engineering Applications of Computational Fluid Mechanics*, 8(1):70–81, 2014.

A. Monyem and J. H. Van Gerpen. The effect of biodiesel oxidation on engine performance and emissions. *Biomass and Bioenergy*, 20(4):317–325, 2001.

W. C. Moss. Understanding the periodic driving pressure in the rayleigh–plesset equation. *The Journal of the Acoustical Society of America*, 101:1187, 1997.

M. N. Nabi, M. M. Rahman, and M. S. Akhter. Biodiesel from cotton seed oil and its effect on engine performance and exhaust emissions. *Applied Thermal Engineering*, 29(11):2265–2270, 2009.

K. Neroorkar, B. Shields, R. O. Grover Jr, A. P. Torres, and D. Schmidt. Application of the homogeneous relaxation model to simulating cavitating flow of a diesel fuel. Technical report, SAE Technical Paper, 2012.

K. D. Neroorkar. Modeling of flash boiling flows in injectors with gasoline-ethanol fuel blends. 2011.

D. Nguyen, E. Winter, and M. Greiner. Sonic velocity in two-phase systems. *International Journal of Multiphase Flow*, 7(3):311–320, 1981.

A. Niederl and M. Narodoslawsky. Life cycle assessment–study of biodiesel from tallow and used vegetable oil. *Institute for Resource Efficient and Sustainable Systems. Graz*, 2004.

Nissan. Electric car range - nissan leaf - electric car nissan. `http://www.nissan.co.uk/GB/en/vehicle/electric-vehicles/leaf/charging-and-battery/range.html`, 2016. (Accessed on 04/11/2016).

NNFCC. Anaerobic digestion | the official information portal on anaerobic digestion. `http://www.biogas-info.co.uk/`, 2016. (Accessed on 04/15/2016).

W. F. Noh and P. Woodward. Slic (simple line interface calculation). In *Proceedings of the Fifth International Conference on Numerical Methods in Fluid Dynamics June 28–July 2, 1976 Twente University, Enschede*, pages 330–340. Springer, 1976.

J. Nouri, J. Whitelaw, and M. Yianneskis. A refractive-index matching technique for solid/liquid flows. In *Laser anemometry in fluid mechanics, selected papers from the 3rd international symposium on application of laser-doppler anemometry to fluid mechanics*, 1988.

J. Nouri, S. Mackenzie, C. Gaskell, and A. Dhunput. Effect of viscosity, temperature, needle lift and nozzle length-to-diameter ratio on internal flow and cavitation in a multi-hole injector. In *IMechE Presentation*, 2012.

W. Nurick. Orifice cavitation and its effect on spray mixing. *ASME Transactions Journal of Fluids Engineering*, 98:681–687, 1976.

C. Öner and Ş. Altun. Biodiesel production from inedible animal tallow and an experimental investigation of its use as alternative fuel in a direct injection diesel engine. *Applied Energy*, 86(10):2114–2120, 2009.

D. Papoulias. *Cavitation Bubble-Dynamics Modelling and CFD Simulations In High-Pressure Diesel Nozzles*. PhD thesis, City University London, 2013.

A. Papoutsakis, A. Theodorakakos, E. Giannadakis, D. Papoulias, and M. Gavaises. Les predictions of the vortical flow structures in diesel injector nozzles. Technical report, SAE Technical Paper, 2009.

S. H. Park, H. K. Suh, and C. S. Lee. Effect of cavitating flow on the flow and fuel atomization characteristics of biodiesel and diesel fuels. *Energy & Fuels*, 22(1):605–613, 2007.

S. H. Park, H. J. Kim, H. K. Suh, and C. S. Lee. Experimental and numerical analysis of spray-atomization characteristics of biodiesel fuel in various fuel and ambient temperatures conditions. *International journal of heat and fluid flow*, 30(5):960–970, 2009.

L. M. Pascual and R. R. Tan. Comparative life cycle assessment of coconut biodiesel and conventional diesel for philippine automotive transportation and industrial boiler application. *Technological Forecasting & Social Change*, 58:83–103, 2004.

J. Pignon. Diesel engines: Design and emissions. *Platinum Metals Review*, 49(3):119–121, 2005.

U. Piomelli. Large-eddy and direct simulation of turbulent flows. 1997.

U. Piomelli. Large-eddy simulation: achievements and challenges. *Progress in Aerospace Sciences*, 35(4):335–362, 1999.

M. Plesset. The dynamics of cavitation bubbles. *J. Appl. Mech.*, 16:277, 1949.

T. Poinsot and D. Veynante. *Theoretical and numerical combustion*. RT Edwards, Inc., 2005.

S. B. Pope. Turbulent flows, 2001.

E. Porpatham, A. Ramesh, and B. Nagalingam. Investigation on the effect of concentration of methane in biogas when used as a fuel for a spark ignition engine. *fuel*, 87(8):1651–1659, 2008.

A. Pradhan, D. Shrestha, A. McAloon, W. Yee, M. Haas, J. Duffield, and H. Shapouri. Energy life-cycle assessment of soybean biodiesel. *Agricultural Economic Repoert*, (845), 2009.

L. Rayleigh. Viii. on the pressure developed in a liquid during the collapse of a spherical cavity. *The London, Edinburgh, and Dublin Philosophical Magazine and Journal of Science*, 34(200): 94–98, 1917.

A. Read and R. Piccioli. Introduction to multiphase flows, June 2015.

Z. Rewse-Davies. *Near Nozzle Phenomena of Gasoline Direct Injection Sprays*. PhD thesis, City University London, 2015.

W. Reynolds. Fundamentals of turbulence for turbulence modeling and simulation. In *Modern Theoretical and Experimental Approaches to Turbulent Flow Structure and its Modelling*, volume 1, 1987.

E. Roohi, A. P. Zahiri, and M. Passandideh-Fard. Numerical simulation of cavitation around a two-dimensional hydrofoil using vof method and les turbulence model. *Applied Mathematical Modelling*, 37(9):6469–6488, 2013.

H. Roth. *Experimental and computational investigation of cavitation in diesel injector nozzles.* PhD thesis, Imperial College London (University of London), 2004.

H. Roth, M. Gavaises, and C. Arcoumanis. Cavitation initiation, its development and link with flow turbulence in diesel injector nozzles. Technical report, SAE Technical Paper, 2002.

K. Saha. *Modelling of cavitation in nozzles for diesel injection applications.* PhD thesis, University of Waterloo, 2014.

F. Salvador, J.-V. Romero, M.-D. Roselló, and J. Martínez-López. Validation of a code for modeling cavitation phenomena in diesel injector nozzles. *Mathematical and Computer Modelling*, 52(7):1123–1132, 2010.

F. Salvador, J. Martínez-López, J.-V. Romero, and M.-D. Roselló. Influence of biofuels on the internal flow in diesel injector nozzles. *Mathematical and Computer Modelling*, 54(7):1699–1705, 2011.

J. Sauer. *Instationar kavitierende Stromungen: ein neues Modell, basierend auf front capturing (VoF) und Blasendynamik.* PhD thesis, Karlsruhe, Univ., Diss., 2000, 2000.

D. Schmidt, S. Gopalakrishnan, and H. Jasak. Multi-dimensional simulation of thermal non-equilibrium channel flow. *International journal of multiphase flow*, 36(4):284–292, 2010.

D. P. Schmidt, C. J. Rutland, and M. L. Corradini. A fully compressible, two-dimensional model of small, high-speed, cavitating nozzles. *Atomization and Sprays*, 9(3):255–276, 1999.

G. Schnerr and J. Sauer. Physical and numerical modeling of unsteady cavitation dynamics. In *Fourth International Conference on Multiphase Flow, New Orleans, USA*, volume 1, 2001.

U. Schumann. Realizability of reynolds-stress turbulence models. *Physics of Fluids (1958-1988)*, 20(5):721–725, 1977.

N. Semenov and S. Kosterin. Results of studying the speed of sound in moving gas-liquid systems. *Teploenergetika*, 11(6):46–51, 1964.

I. H. Sezal et al. *compressible dynamics of cavitating 3-D multi-phase flows.* PhD thesis, Technische Universität München, 2009.

I. H. Shames and I. H. Shames. *Mechanics of fluids.* McGraw-Hill New York, NY, 1982.

J. Sheehan, V. Camobreco, J. Duffield, M. Graboski, and H. Shapouri. Life cycle inventory of biodiesel and petroleum diesel for use in an urban bus. final report. Technical report, National Renewable Energy Lab., Golden, CO (US), 1998.

T.-H. Shih, W. Liou, A. Shabbir, Z. Yang, and J. Zhu. A new k-epsilon eddy viscosity model for high reynolds number turbulent flows: Model development and validation. *NASA STI/Recon Technical Report N*, 95:11442, 1994.

A. K. Singhal, M. M. Athavale, H. Li, and Y. Jiang. Mathematical basis and validation of the full cavitation model. *TRANSACTIONS-AMERICAN SOCIETY OF MECHANICAL ENGINEERS JOURNAL OF FLUIDS ENGINEERING*, 124(3):617–624, 2002.

G. Sivakumar, D. R. Vail, J. Xu, D. M. Burner, J. O. Lay, X. Ge, and P. J. Weathers. Bioethanol and biodiesel: Alternative liquid fuels for future generations. *Engineering in Life Sciences*, 10 (1):8–18, 2010.

R. Slade and A. Bauen. Micro-algae cultivation for biofuels: cost, energy balance, environmental impacts and future prospects. *Biomass and Bioenergy*, 53:29–38, 2013.

J. Smagorinsky. General circulation experiments with the primitive equations: I. the basic experiment*. *Monthly weather review*, 91(3):99–164, 1963.

S. Som, D. Longman, A. Ramirez, and S. Aggarwal. A comparison of injector flow and spray characteristics of biodiesel with petrodiesel. *Fuel*, 89(12):4014–4024, 2010.

C. Soteriou, R. Andrews, and M. Smith. Direct injection diesel sprays and the effect of cavitation and hydraulic flip on atomization. Technical report, SAE technical paper, 1995.

R. Spikes and G. Pennington. Discharge coefficient of small submerged orifices. *Proceedings of the Institution of Mechanical Engineers*, 173(1):661–674, 1959.

T. F. Stocker. *Climate change 2013: the physical science basis: Working Group I contribution to the Fifth assessment report of the Intergovernmental Panel on Climate Change.* Cambridge University Press, 2014.

H. Suh, S. Park, and C. Lee. Experimental investigation of nozzle cavitating flow characteristics for diesel and biodiesel fuels. *International Journal of Automotive Technology*, 9(2):217–224, 2008.

P. Tait. Physics and chemistry of the voyage of hms challenger. *Vol. II, Part IV, SP LXI*, 1888.

N. Takenaka, T. Kadowaki, Y. Kawabata, I. Lim, and C. Sim. Visualization of cavitation phenomena in a diesel engine fuel injection nozzle by neutron radiography. *Nuclear Instruments and Methods in Physics Research Section A: Accelerators, Spectrometers, Detectors and Associated Equipment*, 542(1):129–133, 2005.

H. Tennekes and J. L. Lumley. *A first course in turbulence.* The MIT press, 1972.

A. Theodorakakos. *Numerical simulation of flow in IC engines.* PhD thesis, National Technical University of Athens, 1997.

P. Thomas. Bmw i3 electric car 127kw auto - newelectric (av uk mix) - co2 0 g/km. `http://www.nextgreencar.com/view-car/49674/bmw-i3-electric-car-127kw-auto-electric-(av-uk-mix)/`, 2015. (Accessed on 04/12/2016).

P. J. Torvik. Note on the speed of sound in two-phase mixtures. *The Journal of the Acoustical Society of America*, 48(2A):432–433, 1970.

K. Varatharajan and M. Cheralathan. Influence of fuel properties and composition on no x emissions from biodiesel powered diesel engines: a review. *Renewable and Sustainable Energy Reviews*, 16(6):3702–3710, 2012.

N. B. Vargaftik, Y. K. Vinogradov, and V. S. Yargin. Handbook of physical properties of liquids and gases. *Pure Substances and Mixtures*, pages 663–717, 1996.

H. K. Versteeg and W. Malalasekera. *An introduction to computational fluid dynamics: the finite volume method*. Pearson Education, 2007.

T. Von Karman. Mechanical similitude and turbulence. 1931.

G. B. Wallis. *One-dimensional two-phase flow*, volume 1. McGraw-Hill New York, 1969.

X. Wang, Z. Huang, O. A. Kuti, W. Zhang, and K. Nishida. Experimental and analytical study on biodiesel and diesel spray characteristics under ultra-high injection pressure. *International journal of heat and fluid flow*, 31(4):659–666, 2010.

J.-P. Wauquier. *Petroleum Refining: Crude oil, petroleum products, process flowsheets*, volume 1. Éditions Technip, 1995.

D. C. Wilcox et al. *Turbulence modeling for CFD*, volume 2. DCW industries La Canada, CA, 1998.

E. Winklhofer, E. Kull, E. Kelz, and A. Morozov. Comprehensive hydraulic and flow field documentation in model throttle experiments under cavitation conditions. In *ILASS-Europe 2001, 17 International Conference on Liquid Atomization and Spray Systems*, 2001.

M. Wolfshtein. The velocity and temperature distribution in one-dimensional flow with turbulence augmentation and pressure gradient. *International Journal of Heat and Mass Transfer*, 12(3):301–318, 1969.

W. Yuan, J. Sauer, and G. H. Schnerr. Modeling and computation of unsteady cavitation flows in injection nozzles. *Mécanique & industries*, 2(5):383–394, 2001.

H. Zhao. *Advanced Direct Injection Combustion Engine Technologies and Development: Diesel Engines*, volume 2. Elsevier, 2009.

P. J. Zwart, A. G. Gerber, and T. Belamri. A two-phase flow model for predicting cavitation dynamics. In *Fifth International Conference on Multiphase Flow, Yokohama, Japan*, 2004.